EXPLORING THE EFFECT OF ACTIVE GALACTIC NUCLEI ON QUENCHING, MORPHOLOGICAL TRANSFORMATION AND GAS FLOWS WITH SIMULATIONS OF GALAXY EVOLUTION

By

RYAN BRENNAN

A dissertation submitted to the

Graduate School—New Brunswick

Rutgers, The State University of New Jersey

in partial fulfillment of the requirements

for the degree of

Doctor of Philosophy

Graduate Program in Physics and Astronomy

written under the direction of

Dr. Rachel Somerville

and approved by

_____

_____

_____

_____

_____

New Brunswick, New Jersey

October, 2017

ABSTRACT OF THE DISSERTATION

Exploring the Effect of Active Galactic Nuclei on Quenching, Morphological Transformation and Gas Flows with Simulations of Galaxy Evolution

By RYAN BRENNAN

Dissertation Director:

Dr. Rachel Somerville

We study the evolution of simulated galaxies in the presence of feedback from active galactic nuclei (AGN). First, we present a study conducted with a semi-analytic model (SAM) of galaxy formation and evolution that includes prescriptions for bulge growth and AGN feedback due to galaxy mergers and disk instabilities. We find that with this physics included, our model is able to qualitatively reproduce a population of galaxies with the correct star-formation and morphological properties when compared with populations of observed galaxies out to $z \sim 3$. We also examine the characteristic histories of galaxies with different star-formation and morphological properties in our model in order to draw conclusions about the histories of observed galaxies. Next, we examine the structural properties of galaxies (morphology, size, surface density) as a

function of distance from the "star-forming main sequence" (SFMS), the observed correlation between the star formation rates (SFRs) and stellar masses of star-forming galaxies. We find that, for observed galaxies, as we move from galaxies above the SFMS (higher SFRs) to those below it (lower SFRs), there exists a nearly monotonic trend towards more bulge-dominated morphology, smaller radius, lower SFR density, and higher stellar density. We find qualitatively similar results for our model galaxies, again driven by our prescriptions for bulge growth and AGN feedback.

Next, we conduct a study of the effect of AGN feedback on the gas in individual galaxies using a suite of cosmological hydrodynamical simulations. We compare two sets of 24 galaxies with halo masses of 10^{12} - $10^{13.4} M_{\odot}$ run with two different feedback models: one which includes stellar feedback via UV heating, stellar winds and supernovae, AGN feedback via momentum-driven winds and X-ray heating, and metal heating via photoelectric heating and cosmic X-ray background heating from accreting black holes in background galaxies (MrAGN), and another model which is identical except that it does not include any AGN feedback (NoAGN). We find that our AGN feedback prescription acts both "ejectively," removing gas from galaxies in powerful outflows, and "preventatively", suppressing the inflow of gas onto the galaxy. The histories of MrAGN galaxies are gas ejection-dominated, while the histories of NoAGN galaxies are gas recycling-dominated. This difference in gas cycles results in the quenching of star formation in MrAGN galaxies, while their NoAGN counterparts continue to form stars until z=0. Finally, we examine how this change in the baryon cycle affects the metal content of MrAGN galaxies relative to NoAGN galaxies and find that a combination of gas removal from and metal injection into the hot gas halo results in higher average halo metallicities in MrAGN galaxies.

Acknowledgments

First, I would like to thank my advisor, Rachel Somerville, for all of her support and guidance over the last six years. I would also like to thank my thesis committee (Alyson Brooks, Tad Pryor, Wim Kloet, and Thorsten Naab) for their insightful questions and suggestions.

I would like to thank the Rutgers astronomy group: faculty, postdocs and graduate students past and present who have created a great atmosphere in which to work, even when things were difficult. Joel: Thanks for all of the office conversations and Babylon 5. Ena: Thanks for all of your help and never getting annoyed at how many emails I sent you. Sheehan, Jon, Carl, Jesse, Anna and especially Catie: thanks for everything. It was pretty fun most of the time.

Thank you to my family, Patrick, Tracy and Daniel, for supporting me even when they weren't exactly sure what it was I was doing.

Portions of this work have appeared or will appear in publication elsewhere. Chapter 3 has been published as Brennan et al. (2015) and Chapter 4 has been published as Brennan et al. (2017). Chapter 5 has been submitted to MNRAS and Chapter 6 will soon be submitted. I would like to thank the CANDELS team for all of their advice and comments on Chapters 3 and 4, and I would like to thank all of my collaborators and co-authors (Viraj Pandya, Guillermo Barro, Ned Taylor, Stijn Wuyts, Eric Bell, Avishai Dekel, Harry Ferguson, Dan McIntosh, Casey Papovich, Joel Primack, Asa Bluck, Sandy Faber, Anton Koekemoer, Peter Kurczynski, Jeffrey Newman, Michaela Hirschmann, Thorsten Naab and Jerry Ostriker).

These works have been supported by HST Theory grant HST-AR-13270-A and the Downsbrough Fund, as well as by the Simons Foundation through a Simons Investigator grant to rss.

Support for HST Programs GO-12060 and GO-12099 was provided by NASA through grants from the Space Telescope Science Institute, which is operated by the Association of Universities for Research in Astronomy, Inc., under NASA contract NAS5-26555.

Dedication

For Zorp the Surveyor

Table of Contents

List of Tables

List of Figures

Chapter 1

Introduction

1.1 Galaxy Formation

The local, present-day galaxy population is the result of hierarchical structure formation. In the very early universe, quantum fluctuations were made macroscopic by inflation. Initial dark matter overdensities attracted more material and became more overdense, while initial underdensities experienced the opposite. The accreted material took the form of both additional dark matter as well as baryonic matter. The dark matter collapsed into "haloes" in overdense regions of the universe, and baryonic matter, which was too hot initially to form self-gravitating objects on its own, accreted onto these haloes.

This baryonic matter eventually cooled and settled into rotating disks at the centers of the dark matter haloes, where it became dense enough to undergo further gravitational collapse and form stars. These first galaxies continued to have new gas accrete onto them, some of which continued to form stars. Stars at the end of their lifetimes exploded as supernovae, injecting energy into surrounding gas, removing it or heating it up. Galaxies also merged with each other to form even larger galaxies. The disruption of gas by merging could feed supermassive black holes at the centers of galaxies, which could also release energy into the surrounding gas. The interplay of all of these processes (and more) led to the galaxy population that we observe today.

The Lambda Cold Dark Matter (ΛCDM) cosmological paradigm, our current best model for the universe at large, describes this buildup of larger structures as a result of gravitational

collapse and merging of smaller systems into larger ones, as well as the accelerating expansion of the universe. This model is extremely well-tested. However, there are still many questions about the physics on galactic scales, where non-linearity takes over and small-scale processes begin to dominate evolution (Mo et al. 2010, Section 1.2).

Many observational and theoretical studies have been undertaken in order to capture the intricacies of galaxy evolution by linking galaxies at high redshift (which are farther away and which we are seeing at a time earlier in the universe's history) to those at low redshift. Throughout this work we will use both models and observations to try to understand how galaxies evolve with time, specifically as a result of accretion of material onto their central supermassive black holes. We will now briefly discuss in more detail some of the galactic processes mentioned above.

1.2 Star Formation, Chemical Enrichment, and Morphology

Studies of galaxies out to high redshift have shown us how the galaxy population as a whole has evolved over time, both in terms of star formation and morphology, or shape.

1.2.1 Star Formation

As mentioned above, star formation can take place when gas streams onto a dark matter halo, collapsing and cooling. Star formation takes place in cold, dense gas complexes called molecular clouds. These clouds are made up mainly of neutral molecular hydrogen, H_2. If the cloud is massive enough, the gas pressure within is not enough to halt gravitational collapse, at which point the gas will collapse and form stars. This process may occur naturally in a cold gas disk, or it may be stimulated by gas compression due to nearby energy injection by supernovae or the galaxy's central supermassive black hole. Gas compression and star formation can also be stimulated by galaxy interactions and mergers (Mo et al. 2010, Sections 9.1-9.3, 12.4).

The peak of cosmic star formation occurred at z∼2-3 (Madau & Dickinson 2014). The star formation rate of a galaxy is generally defined as the mass in new stars being produced per year, in units of solar masses per year ($M_{\odot}/yr$). Galaxies span the range of possible star formation rates, but can generally be divided into two classes: star forming galaxies, which are actively forming stars, as their name implies, and quiescent galaxies, which are no longer forming stars. In the local universe, the distribution of star formation rates is bimodal and dominated by these two populations. These two types of galaxies can be identified by their color, which is a difference of their luminosities in two different passbands. Galaxies which are actively forming stars are dominated by the light of young, hot, massive stars, which gives them a blue color, while quiescent galaxies are dominated by the light of old stars, giving them a red color (Kauffmann et al. 2003; Baldry et al. 2004; Brinchmann et al. 2004). The bimodal distribution of color in the local universe can be seen in Figure 1.1.

Star-forming galaxies, or galaxies in the "blue cloud", tend to be lower mass than quiescent galaxies, or galaxies on the "red" sequence. The number density of blue, star forming galaxies has been decreasing since the peak of star formation, while the number density of red, quiescent galaxies has increased (Bell et al. 2004b; Borch et al. 2006; Bell et al. 2007; Faber et al. 2007). The star formation rates of star forming galaxies also tend to be correlated with their stellar masses, forming a tight relation in SFR-M_* space colloquially known as the "star-forming main sequence" (Noeske et al. 2007; Rodighiero et al. 2011).

Examining the buildup of red and blue galaxies across cosmic time has led to the conclusion that blue galaxies are being turned into red galaxies, i.e. the star formation in blue galaxies is being shut off (Bell et al. 2007; Brammer et al. 2011). This phenomenon is referred to as star formation "quenching".

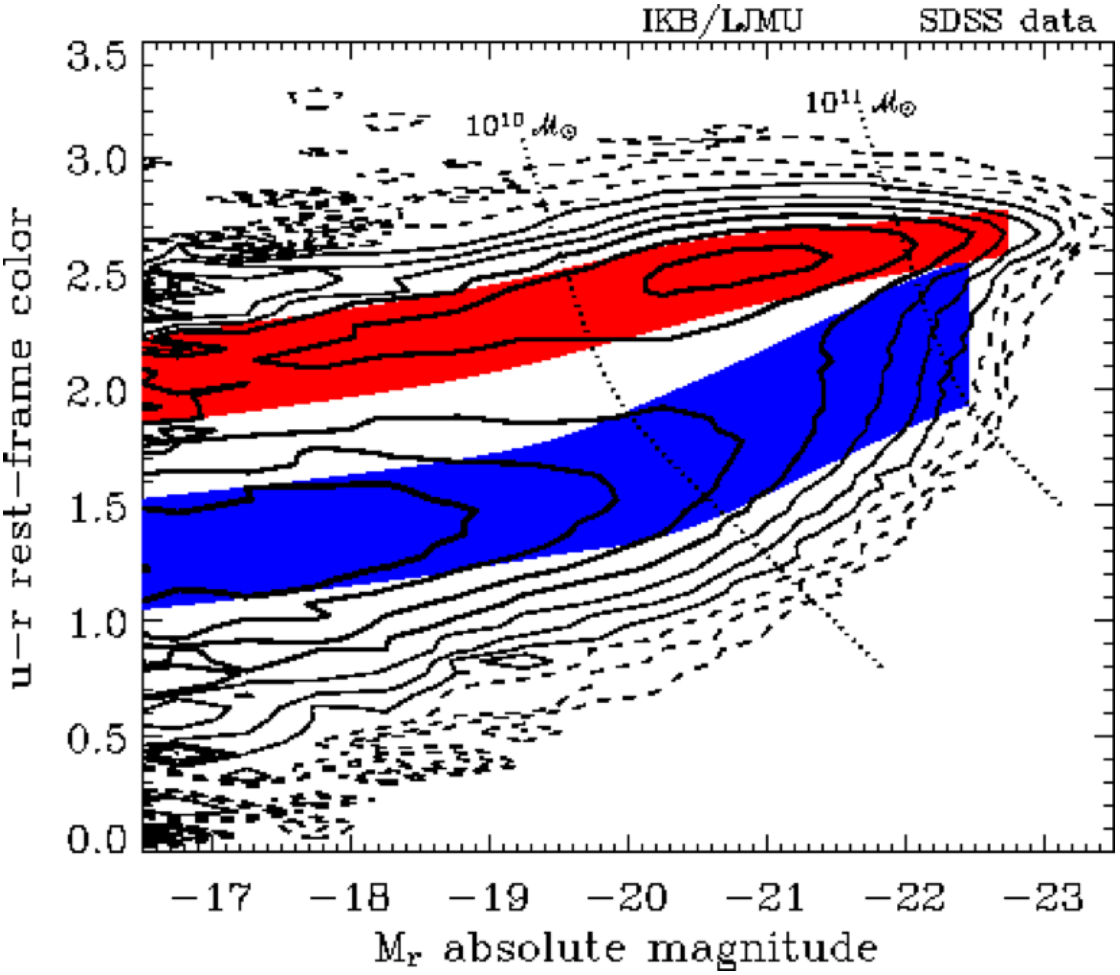

Figure 1.1: Population density of galaxies from SDSS in color-magnitude space. Blue and red bands show the peaks in the population representing the blue cloud and the red sequence, corresponding to star forming and quiescent galaxies, respectively. Figure taken from Baldry et al. (2004).

1.2.2 Chemical Enrichment

In astronomy, the periodic table is very simple. First, there is Hydrogen, which makes up $\sim 74\%$ of the baryonic material by mass in the universe. Helium makes up another $\sim 24\%$. All other elements, which make up the remaining $\sim 2\%$, are referred to as "metals". Hydrogen and Helium have been the most abundant elements since the Big Bang, and while some other elements were created in trace amounts in the very early universe, most of the metal content of the universe today was created within stars or in supernova explosions. Heavier elements are created through fusion reactions in the cores of stars, then released into the universe through stellar winds and supernovae, the latter of which produce even heavier metals.

The metal content of a star or parcel of gas is usually presented in one of two ways. The mass fraction of elements heavier than Helium is expressed as Z=1-X-Y, where X and Y are the Hydrogen and Helium mass fractions respectively. More often, the metal content is expressed as an abundance of iron relative to hydrogen, which is referred to as an abundance ratio. This value is given relative to the value found in the Sun, and is defined as

$$[\mathrm{F/He}] = \log_{10}\left(\frac{\mathrm{N_{Fe}}}{\mathrm{N_H}}\right)_{\mathrm{star/gas}} - \log_{10}\left(\frac{\mathrm{N_{Fe}}}{\mathrm{N_H}}\right)_{\mathrm{sun}}$$

where $\mathrm{N_x}$ is the number of atoms of element x. Both of these definitions (mass fraction and heavy element abundance ratios relative to hydrogen) are informally referred to as "metallicity." Other common abundance ratios are [O/Fe] and [α/Fe], where α refers to the number density of all α-elements, whose most abundant isotopes have atomic masses which are multiples of 4, and are created by successively adding helium nuclei by fusion.

Due to the interrelated nature of stellar mass buildup and metallicity (both being the result of star formation), there is an observed correlation between stellar mass and metallicity known as the mass-metallicity relation (Tremonti et al. 2004). Studies of the radial dependence of

metallicity, known as metallicity gradients, can also give us insight into the star formation history and incidence of inflows and outflows in individual galaxies.

1.2.3 Morphology

There are nearly as many galaxy shapes as galaxies themselves, but as a first broad approximation we say that galaxies can be represented as a combination of a disk component and a bulge component. The disk component is rotationally supported and is generally where star formation takes place. The bulge component consists of stars traveling in random orbits and is dispersion supported. There are galaxies which are nearly pure disks, others which are pure bulges, and still others which are combinations of both. Pure bulge galaxies are also called elliptical galaxies (Mo et al. 2010, Section 2.3).

There are many different ways to classify the relative contributions of disk and bulge components, but two of the most popular are bulge-to-total ratio (B/T) and Sérsic index. B/T is a ratio of the mass (or luminosity) of the bulge component divided by the total mass (or luminosity) of the galaxy. The Sérsic profile is a function of how the light intensity of a galaxy changes with radius from its center, R, and is given as

$$\ln \mathrm{I(R)} = \ln \mathrm{I_0} - \mathrm{kR}^{1/\mathrm{n}}$$

where I_0 is the intensity at R=0, k is a parameter that depends on n, and n is the Sérsic index, which controls the curvature of the function and serves as proxy for concentration of light. Pure exponential disks are described by n=1, and pure bulges are well-described by n=4 (Sérsic 1963).

Galaxy morphology tends to correspond to star formation rate, such that blue star forming galaxies are often disk-dominated and red, quiescent galaxies are often bulge-dominated (Wuyts

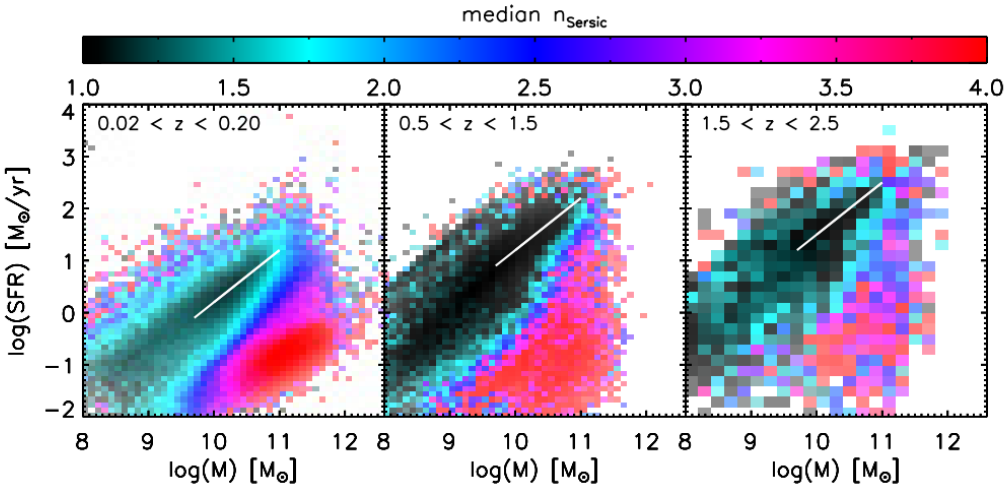

Figure 1.2: The distribution of galaxies in the SFR-M_* plane color-coded by their mean Sérsic index in three redshift bins. Taken from Wuyts et al. (2011).

et al. 2011; Bluck et al. 2014), as can be seen in Figure 1.2. Next, we will discuss a possible reason for this correlation.

1.3 AGN Feedback

1.3.1 Active Galactic Nuclei

Active galaxies make up a small but vital fraction of the galaxy population. Active galaxies have a bright nuclear region that is far more luminous than regions of the same size in inactive galaxies. Often, this inner region outshines the rest of the galaxy by a large amount. This region is referred to as the active galactic nucleus (AGN). Not only is the AGN bright, but it generates continuum emission across the entire electromagnetic spectrum, which sets the spectral energy distribution of active galaxies apart from those of normal galaxies whose spectra are dominated by stars. This non-stellar, non-thermal continuum emission extends all the way from the X-ray (or even gamma ray) to the radio. AGN are also characterized by strong emission lines, as well as variability in both the emission lines and continuum. Variability can occur on relatively short

timescales, due to the compactness of the AGN. With the discovery of Seyfert galaxies, quasars and radio galaxies in the middle of the last century, the issue facing astronomers was "explaining how a region the size of the solar system can produce the light of a trillion stars" (Peterson 2008). It is now accepted that accreting supermassive black holes at the centers of galaxies are the engines which power these AGN (Lynden-Bell 1969).

It is believed that almost all spheroid-dominated galaxies host a supermassive black hole at their centers, and the masses of these black holes are correlated with properties of the galaxy's bulge component such as mass and velocity dispersion (Magorrian et al. 1998). Figure 1.3 shows the relationship between black hole mass and central velocity dispersion. This suggests that black holes and their host galaxies co-evolve, and makes it likely that the local galaxy population is made up of galaxies that have gone through an AGN phase in the past. Considering that the energy released by accretion onto a supermassive black hole is at least on the order of a galaxy's binding energy, it seems likely that if most galaxies did indeed host AGN at some point in their lifetimes, that the energy release associated with that phase would have an important effect on the host galaxy (Silk & Rees 1998).

Basic Model of AGN Activity

The gravitational potential energy of a mass M at a distance r from a black hole is $U = \frac{GM_{\rm BH}M}{r}$, so the luminosity of the AGN can be written as $L = \frac{GM_{\rm BH}}{r}\dot{M_{\rm BH}}$, where $\dot{M_{\rm BH}}$ is the mass accretion rate. Since the luminosity will depend on how much of the accreted mass's rest energy is converted into radiation, we can also write the luminosity as $L = \eta\dot{M_{\rm BH}}c^2$, where η is the efficiency with which rest mass is converted to radiation. It is believed that most of the continuum radiation from the AGN is emitted at $\sim 5r_s$ from the black hole, where $r_s = \frac{2GM_{\rm BH}}{c^2}$ is the Schwarzschild radius, from within which nothing can escape the black hole's gravitational pull. Writing $\eta = \frac{L}{\dot{M_{\rm BH}}c^2} = \frac{1}{2}\frac{r_s}{r}$, we see that we can take $\eta \sim 0.1$, which is the standard value often

adopted (Peterson 2008).

We can also look for the maximum luminosity of a black hole by using arguments of hydrostatic equilibrium; the radiation pressure from a source cannot overpower its self gravity or else it would blow itself apart. We can write $P_{\rm rad} = \frac{F}{c} = \frac{L}{4\pi c r^2}$, where F is the radiation flux (and we have assumed spherical symmetry). In the radiation field of the AGN, it is a safe bet that the surrounding material is fully ionized, so the radiation pressure will be felt mostly by electrons and the cross section we use to find the radiation force is the Thomson cross section: $F_{\rm rad} = P_{\rm rad}\sigma_{\rm T} = \frac{L\sigma_{\rm T}}{4\pi c r^2}$ is the force on each electron. Meanwhile the gravitational force will act mainly on the protons since $m_p >> m_e$. We assume that $n_e \cong n_p$ and apply our condition to find that $\frac{L\sigma_{\rm T}}{4\pi c r^2} \leq \frac{GM_{\rm BH}m_p}{r^2}$, or:

$$L \leq L_{\rm Edd} = \frac{4\pi G c m_p}{\sigma_{\rm T}} M_{\rm BH} \approx 1.26 \times 10^{38} \Big(\frac{M_{\rm BH}}{M_\odot}\Big) erg/s \tag{1.1}$$

where the black hole mass has been normalized to one solar mass and an erg is equivalent to 10^{-7} Joules (Peterson 2008). This limit is known as the Eddington limit. The assumption of spherical symmetry is almost surely not an accurate one. It is likely that accretion is preferred along some directions, while radiation pressure dominates in others, so mildly super-Eddington accretion rates are possible. The Eddington luminosity is still a convenient quantity to use when talking about radiation from an AGN and is often used as a limit to find constraints on quantities like black hole mass and accretion rate.

1.3.2 Feedback

As described above, star formation in some galaxies is being turned off somehow. One theory as to the cause of this "quenching" of star formation is the release of gravitational energy by an AGN, also described above, which can remove or heat gas within the galaxy, preventing it

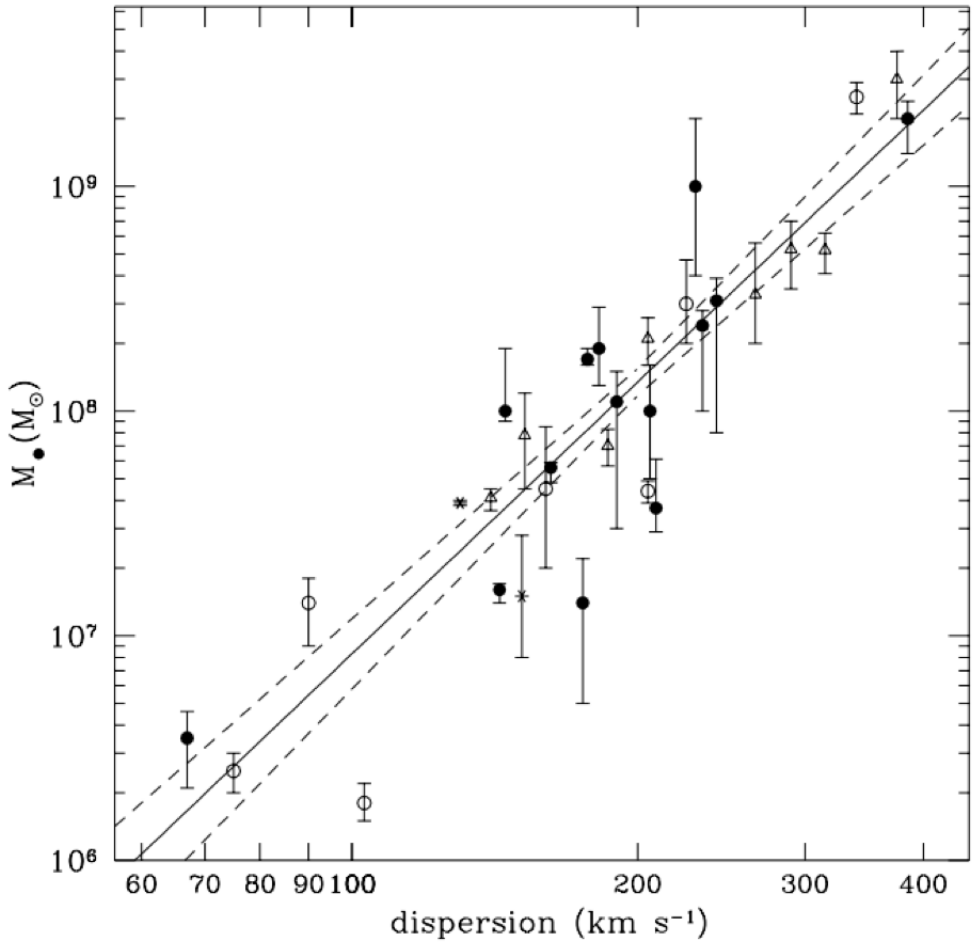

Figure 1.3: A fairly tight correlation exists between the masses of central supermassive black holes and their host galaxies' bulge velocity dispersions. Taken from Tremaine et al. (2002).

from forming stars (Peterson 2008). While supernova feedback may be able to achieve this in lower mass galaxies, AGN feedback is invoked in galaxies more massive than our Milky Way ($M_{halo}>10^{12}M_{\odot}$) (Somerville & Davé 2015).

Additionally, we expect that processes that disrupt the gas content of a galaxy, thereby feeding the black hole and leading to a bout of AGN feedback, would also disrupt the disk of the galaxy, leading to the observed correlation between star formation rate and morphology.

This feedback may take the form of the AGN heating the surrounding gas to its escape temperature or energetic photons near the source applying radiation pressure to dust or resonance transitions in the gas. These processes are called "radiative" feedback and are theoretically invoked in order to remove gas from galaxies and drive outflows like those observed in quasar and Seyfert host galaxies. There are many broad absorption line and integral field unit observations which suggest very high velocity outflows which seem impossible to drive by stellar and supernova feedback alone (Somerville & Davé 2015).

Another type of feedback is called "jet" mode, or "radio" mode. This is a kinetic type of feedback that involves the launching of relativistic radio jets generated in the inner regions of the AGN, which then inflate "kinetic bubbles" which act to heat the gas that remains in the galaxy, keeping it from cooling and forming stars. These jets and radio bubbles are observed in some quasars but are most dynamically important in massive elliptical radio galaxies (Somerville & Davé 2015).

These types of feedback are theoretically invoked in order to shut off star formation in galaxies and prevent it from starting up again. In order to constrain these theoretical models for galaxy evolution, we use models, two types of which are briefly described now.

1.4 Semi-analytic Models

Semi-analytic models (SAMs) are an extremely useful tool to gain an understanding of galaxy evolution in the presence of different kinds of physics. A dark matter halo merger tree is taken from a dark matter-only N-body simulation; this represents the hierarchical CDM backdrop against which galaxies form, merge and evolve. Galaxies are then "placed" into these dark matter haloes and evolved forward in time. Relatively simple but physically motivated "recipes" are used to represent physical processes such as gas cooling, star formation, metal enrichment and feedback due to supernovae and AGN. Bulk quantities like galaxy stellar mass, hot and cold gas mass and metallicity, among others, are solved for using a series of coupled equations at each timestep and tracked.

SAMs are extremely computationally efficient and can produce large ensembles of galaxies which can be compared with observational catalogs. The recipes for physical processes are governed by several parameters which can be varied, allowing one to vary and isolate the effect of a given physical process on individual galaxies and the population as a whole. Because of the computational efficiency, large volumes of parameter space can be explored relatively easily. SAMs have been successful in reproducing many fundamental properties of the galaxy population, such as the stellar mass and luminosity functions, gas fraction versus stellar mass relation, and the evolution of stellar mass and star formation rate density with redshift (Kauffmann et al. 2003; Somerville & Primack 1999; De Lucia et al. 2006; Guo et al. 2011; Somerville et al. 2012). One of the latest additions to SAMs has been the incorporation of prescriptions for AGN feedback, which has helped greatly in reproducing the evolution of the quiescent fraction of galaxies with redshift. An example of such a model is described in detail in Chapter 2 and used extensively in Chapters 3 and 4.

1.5 Hydrodynamical Simulations

Hydrodynamical simulations (specifically smoothed particle hydrodynamics, or SPH, simulations, which are used in this work), divide a fluid into discrete particles. These particles have a "smoothing length" over which their properties are smoothed by a kernel function; this allows physical properties to be calculated for each particle based on other particles within its smoothing length. The motion and behavior of these particles are then governed by the equations of hydrodynamics and thermodynamics. This approach is useful because denser areas naturally contain more particles, providing better resolution where it is needed.

Small-scale processes such as star formation and feedback must still be implemented with "sub-grid" recipes analogous to those used in SAMs, as the mass and spatial scales at which these processes take place in real galaxies are still unresolved in simulations.

SPH simulations have also been able to reproduce basic properties of the galaxy population (Oppenheimer et al. 2010; Hirschmann et al. 2013; Christensen et al. 2016) and recent studies have begun to add processes associated with AGN feedback in order to capture its effect on the evolution of galaxies (Choi et al. 2014, 2015; Weinberger et al. 2017). Details of the SPH simulation used in this work can be found in Chapter 2. The simulation is used as part of the studies in Chapters 5 and 6.

1.6 The Contents of This Thesis

While much progress has been made in understanding the evolution of the galaxy population over time, the exact mechanisms responsible for star formation quenching and morphological change, as well as the effect of AGN feedback on host galaxies, are still debated. In this work, we employ different models of galaxy formation and evolution which contain prescriptions for AGN feedback in an effort to see how this AGN feedback affects individual galaxies and the galaxy

population as a whole. We ask the questions: 1) Can a model prescription for AGN feedback in conjunction with a simple recipe for bulge growth recreate the star formation and morphology demographics of large galaxy surveys? 2) What do the histories of such model galaxies look like? 3) How are inflows and outflows affected by the fast-moving winds observed around AGN in the real universe? 4) How is the production and distribution of metals affected by these AGN-driven winds?

In Chapter 2, which is mainly reproduced from parts of Brennan et al. (2015), Brennan et al. (2017), and additional work submitted for publication, we describe the models used throughout the rest of this work. We present the "Santa Cruz" semi-analytic model, which contains prescriptions for basic processes such as gas cooling and star formation, as well as prescriptions for AGN feedback through winds and jets and morphological transformation due to mergers and disk instabilities (Somerville et al. 2008a, 2012; Porter et al. 2014a). Also presented is a version of the SPH code GADGET, which includes a prescription for mechanical and radiation-driven AGN feedback meant to drive strong outflows like those seen around quasars (Springel 2005; Choi et al. 2012, 2014, 2015).

We then present the observations with which we compare the results from the SAM. These are galaxies observed as part of the CANDELS (Grogin et al. 2011; Koekemoer et al. 2011) and GAMA (Driver et al. 2009) surveys, providing us with a wealth of star formation and morphological information in both the local universe and at high redshift.

With the semi-analytic model we can generate a statistical population of galaxies, the ensemble properties of which we can compare with real galaxies in an effort to assess the success of our AGN feedback model. In Chapter 3, published elsewhere as Brennan et al. (2015), we examine the evolution of the star formation rate and morphological properties of galaxies out to high redshift. We examine the quiescent fraction and spheroid-dominated fraction of galaxies, both for our simulated sample and for a sample of observed galaxies. We then subdivide galaxies

further into four populations based on their star formation rate and morphology: star forming disk-dominated galaxies, star forming spheroid-dominated galaxies, quiescent disk-dominated galaxies and quiescent spheroid-dominated galaxies. We examine the buildup of these four populations with redshift. We next examine the processes responsible for moving simulated galaxies into these different subpopulations, and study some individual simulated galaxy histories in order to explain the behavior of our observational sample.

We refine this analysis in Chapter 4, published elsewhere as Brennan et al. (2017), examining the structural properties of galaxies as a function of their distance from the star forming main sequence, as opposed to grouping galaxies into large bins. We compare the distributions of median Sérsic index, effective radius, star formation rate surface density and stellar surface density in the SFR-M_* plane for our SAM sample versus a sample from CANDELS and GAMA. We also compare the median values of these quantities as a function of distance from the main sequence. In both of the above studies, we examine where our model succeeds and fails in creating a realistic galaxy population.

In Chapter 5, which has been submitted for publication elsewhere, we shift focus to the effect of AGN feedback on individual galaxies. Specifically, we examine the effect of AGN feedback on the inflow and outflow of gas in a suite of 24 SPH cosmological zoom simulations. The simulations include stellar feedback via UV heating, stellar winds and supernovae, AGN feedback via momentum-driven winds and X-ray heating, and metal heating via photoelectric heating and cosmic X-ray background heating. We examine how the inflow and outflow rates of gas are affected by momentum-driven AGN feedback. We track inflowing and outflowing gas particles in order to determine how often gas is recycled, as well as to record the timescales and distances associated with gas recycling and ejection events. In this study we see how feedback meant to mimic large scale outflows observed in the universe affects the gas cycle in these simulated galaxies.

In Chapter 6, we focus on the same 24 SPH cosmological zoom simulations, this time examining the metal content of our galaxies in order to see how the addition of mechanical and radiation-driven AGN feedback affects the chemical enrichment of gas both inside the galaxy and in the galactic gas halo. In Chapter 7, we summarize our results.

Chapter 2

Simulations and Observational Data

In the following work, we employ two different simulations of galaxy formation and evolution: a semi-analytic model in Chapters 3 and 4, and a smoothed-particle hydrodynamics simulation in Chapter 5. We also compare explicitly with observations from the CANDELS (Grogin et al. 2011; Koekemoer et al. 2011) and GAMA (Liske et al. 2015) surveys in Chapters 3 and 4. The details of these models and observations are given here.

2.1 Simulations

2.1.1 Semi-analytic Model

The SAMs used in Chapters 3 and 4 were first presented in Somerville & Primack (1999) and Somerville et al. (2001), and significantly updated in Somerville et al. (2008a, S08), Somerville et al. (2012, S12) and Porter et al. (2014a, P14). The model includes prescriptions for the following physical processes: the hierarchical growth of structure in the form of dark matter merger trees, the heating and cooling of gas, star formation as governed by the empirical Kennicut-Schmidt law, the evolution of stellar populations, supernova feedback, chemical evolution of the interstellar medium (ISM) and intracluster medium (ICM) due to supernovae, AGN feedback, and starbursts and morphological transformation due to galaxy mergers and disk instabilities. Here we will briefly summarize these processes, focusing mainly on the processes relevant to the evolution of star formation and morphology, including our AGN feedback prescription. For a

more in depth description of the model, see S08 and P14. We assume a standard ΛCDM cosmology ($\Omega_m = 0.27$, $\Omega_\Lambda = 0.73$, $h = 0.7$) and a Chabrier (2003) initial mass function. Our adopted baryon fraction ($\Omega_{\rm b}/\Omega_{\rm m}$, or the density of baryons divided by the total density of matter) is 0.1658. Our cosmology was chosen to match that adopted by the Bolshoi simulation (detailed below) and is consistent with the Wilkinson Microwave Anisotropy Probe (WMAP) 5/7-year results (Komatsu et al. 2009, 2011).

In this work, we use the CANDELS lightcones (Somerville et al. in prep) extracted from the Bolshoi dark-matter only N-body simulation (Klypin et al. 2011; Trujillo-Gomez et al. 2011). Dark matter haloes are identified using the ROCKSTAR algorithm of Behroozi et al. (2013a). The Bolshoi simulation is complete down to haloes with $V_{\rm circ} = 50$ km/s, and has a force resolution and mass resolution of $1h^{-1}$ kpc and $1.9 \times 10^8 M_\odot$, respectively. Merger trees are constructed for each halo in the lightcone using the method of Somerville & Kolatt (1999). There is no appreciable difference in results when using merger trees extracted from the N-body simulation (as done in Porter et al. 2014) as opposed to EPS (as we do here). For our lowest redshift bin, the lightcones represent a very small volume so we simply use a low-z snapshot from the Bolshoi volume.

When dark matter haloes merge, the central galaxy of the largest progenitor becomes the new central galaxy, while all other galaxies become satellites. Satellite galaxies are able to spiral in and merge with the central galaxy, losing angular momentum to dynamical friction as they orbit. The merger time-scale is estimated using a variant of the Chandrasekhar formula from Boylan-Kolchin et al. (2008). Tidal stripping and destruction of satellites as described in S08 are also included.

Before the universe is reionized, each halo has a hot gas mass equal to the virial mass of the halo times the universal baryon fraction. The collapse of gas into low-mass haloes is suppressed after reionization due to the photoionizing background. We assume the universe is fully reionized

by $z = 11$ and use the results of Gnedin (2000) and Kravtsov et al. (2004) to model the fraction of baryons that can collapse into haloes of a given mass following reionization. Due to the galaxy mass range selected in this work, we do not expect our results to be sensitive to this prescription.

When dark matter haloes collapse or are involved in a merger, the hot gas is shock-heated to the virial temperature of the new halo. The rate at which this gas can cool is determined by a simple spherical cooling flow model. Assuming a monotonically decreasing density profile for the gas, and that denser gas cools faster, we can define a "cooling radius", within which all gas is able to cool within some time $t_{\rm cool}$, which we have defined as the halo dynamical time. The initial density profile is assumed to be that of a singular isothermal sphere, and the cooling radius is found by using the atomic cooling curves of Sutherland & Dopita (1993). The cooling radius may be larger or smaller than the virial radius of the halo; when the cooling radius is larger, the cooling rate is limited only by the rate at which gas is infalling. The transition from $r_{\rm cool} > r_{\rm vir}$ to $r_{\rm cool} < r_{\rm vir}$ is associated with the transition from "cold flows", where cold gas streams into the halo along dense filaments without being heated, to "hot flows", where gas is shock heated on its way in, forming a diffuse hot gas halo before cooling (Birnboim & Dekel 2003; Dekel & Birnboim 2006; Kereš et al. 2005). Note that in this way, virial shock heating (sometimes referred to as 'halo mass quenching') is included in our SAMs. However, it has been shown by many studies (both numerical and semi-analytic) that this effect alone is insufficient to create the observed population of massive quiescent galaxies (Somerville & Davé 2015, and references therein).

Newly cooled gas collapses to form a rotationally supported disk, the scale radius of which is estimated based on the initial angular momentum of the gas and the profile of the halo. We assume that angular momentum is conserved and that the self-gravity of the collapsing baryons causes the inner part of the halo to contract (Blumenthal et al. 1986; Flores et al. 1993; Mo et al. 1998). This method was shown to reproduce the observed size-stellar mass relations of disks out

to $z \sim 2$ in Somerville et al. (2008b).

Spheroids can be created by mergers or disk instabilities. The sizes of spheroids formed in mergers are determined by the stellar masses, sizes and gas fractions of the two progenitors, as described in P14. The size of spheroids formed in disk instabilities is determined by assuming that they form from the center of the exponential stellar disk; the radius is simply the radius that contains the amount of mass that is to be transferred from the disk to the bulge (again, see P14 for details).

There are two modes of star formation in the model: a "normal" mode that occurs in isolated disks and a "starburst" mode that occurs as a result of a merger or internal disk instability, which will be discussed in more depth below. The normal mode follows the Schmidt-Kennicutt relation (Kennicutt 1998) and assumes that gas must be above some fixed critical surface density (the adopted value here is $6\,M_{\odot}/\mathrm{pc}^2$) in order to form stars.

Exploding supernovae and massive stars are capable of depositing energy into the ISM, which can drive outflows of cold gas from the galaxy. We assume that the mass outflow rate is proportional to the SFR and decreases with increasing galaxy circular velocity, in accordance with the theory of "energy-driven" winds. Some ejected gas is removed from the halo completely, while some is deposited into the hot gas reservoir of the halo and is eligible to cool again. The gas that is driven from the halo entirely is combined with the gas that has been prevented from cooling by the photoionizing background and may later reaccrete back into the halo. The fraction of gas which is retained by the halo versus the amount that is ejected is a function of halo circular velocity as decribed in S08.

Heavy elements are produced by each generation of stars, and chemical enrichment is modelled simply using the instantaneous recycling approximation. For each parcel of new stars dm_*, a mass of metals $dM_{\mathrm{Z}} = y dm_*$ is also created, which is immediately mixed with the cold gas in the disk. The yield y is assumed to be constant and is treated as a free parameter. Supernova

driven winds act to remove some of this enriched gas, depositing a portion of the created metals into the hot gas or outside of the halo.

Mergers and Starbursts

Mergers between galaxies are assumed to remove angular momentum from stars and gas in the disk and drive material towards the center, building up a spheroidal component. In our model, this spheroidal component is formed instantaneously. In principle this could affect our results by forming bulges more quickly than they should form in the real universe. However, actual bulge formation time scales ($\sim t_{\rm dyn}$, after which we expect a disturbed galaxy to settle) are quite short compared with the times associated with our redshift bins, so we don't expect this to have much of an effect.

Mergers also trigger a starburst, the efficiency of which depends on the gas fraction of the central galaxy and the mass ratio of the two progenitors. The time scale of the burst is also determined by properties of the progenitor galaxies. The parameterization is based on hydrodynamical simulations of binary mergers between disks (Hopkins et al. 2009b). Simulations show that the closer the mass ratio of the progenitors is to one (or how "major" the merger is) and the more gas-poor the merger is, the more efficient it is at removing angular momentum from the gas and driving it into the nucleus, and scattering disk stars into a hot spheroid component (Cox et al. 2006; Robertson et al. 2006). The gas fraction dependence can be understood as follows: if the progenitors are very gas-rich, there is not enough stellar mass to create a torque on the gas, making it difficult for the gas to shed angular momentum and collapse inward (Hopkins et al. 2009b). S08 parameterized the burst efficiency only as a function of mass ratio, but S12 and P14 introduced the gas fraction dependence in accordance with Hopkins et al. (2009a). Stars that are formed as part of the starburst are added to the spheroidal component, as are 80% of the stars from the merging satellite galaxy. The other 20% are deposited into a diffuse stellar halo

component.

Disk Instabilities

Disk material can also be converted into a spheroidal component as a result of internal gravitational instabilities. A pure disk without a dark matter halo is very unstable to the formation of a bar or bulge, while massive dark matter haloes tend to stabilize a thin, cold galactic disk (Ostriker & Peebles 1973; Fall & Efstathiou 1980). When the ratio of dark matter mass to disk mass falls below a critical value, the disk can no longer support itself and material collapses into the inner regions of the galaxy (Efstathiou et al. 1982). Here we adopt an avenue for bulge growth due to disk instability, based on a Toomre-like stability criterion. Following Efstathiou et al. (1982), Mo et al. (1998), P14 and many other works, we define the stability parameter as

$$\epsilon_{\rm disk} = \frac{V_{\rm max}}{(GM_{\rm disk}/r_{\rm disk})^{1/2}} \tag{2.1}$$

where $V_{\rm max}$ is the maximum circular velocity of the halo (used as a proxy for the maximum circular velocity of the disk), $r_{\rm disk}$ is the scale length of the stellar disk and $M_{\rm disk}$ is the stellar mass of the disk. This is identical to the "**Stars DI**" disk instability criterion introduced in P14. Whenever $\epsilon_{\rm disk} < \epsilon_{\rm crit}$, the disk is considered to be unstable. The value of $\epsilon_{\rm crit}$ in numerical simulations of isolated disks has been found to be in the range of $0.6 - 1.1$, with disks containing stars and cold gas having a lower threshold than pure stellar disks (Efstathiou et al. 1982; Mo et al. 1998). We set $\epsilon_{\rm crit} = 0.75$ as in P14, where this value was chosen to match the observed fraction of spheroid-dominated galaxies at $z = 0$. When the disk becomes unstable, stellar mass is moved from the disk to the bulge until $\epsilon_{\rm disk} = \epsilon_{\rm crit}$. The gas in the disk is not affected. The "**Stars+Gas DI**" model of P14 included gas in determining the stability of the

disk and also moved some gas to the bulge component to feed the central supermassive black hole when the disk became unstable. However, the results for the two approaches were very similar. Again, the creation of the bulge component is instantaneous. While we are aware that this implementation of disk instability is crude and perhaps does not capture all of the relevant physics, this is an approach that is commonly used in the literature. One of the goals of Chapter 3 is to explore how important bulge growth through disk instabilities might be, in order to guide future investigations. We discuss in Chapter 3 more physical models of disk instability and how including them might affect our results.

It is worth noting that we also do not account for the possibility that a previously existing bulge may help stabilize the disk against another instability. Because of this (and the fact that we only move as much material as needed to restabilize the bulge) it is possible for disks to develop chronic instabilities which lead to the steady growth of a bulge component.

In Chapter 3 we present our results for versions of the SAM both with the disk instability prescription turned on (DI model) and off (noDI model). The DI model is our fiducial model, however, and unless otherwise noted, it is the DI model that is shown.

Black Hole Accretion and Feedback

Galaxies are initially seeded with a massive black hole of $10^4\,M_\odot$ (Hirschmann et al. 2012). When two galaxies merge as described above, their central black holes are assumed to merge as well, after which the new central black hole of the merger remnant engages in a bout of feeding and radiatively efficient, or "quasar" mode, AGN activity. During this time, the black hole accretes at its Eddington limit. As the black hole accretes and radiates, it deposits energy into the surrounding medium until it reaches a critical mass which corresponds to the energy which would stop accretion and begin driving an outflow, such as those seen in many recently merged systems (Rupke & Veilleux 2013; Emonts et al. 2014). The black hole effectively starves itself of

material, as its accretion rate declines as a power law, in accordance with the results of Hopkins et al. (2006). We follow the hydrodynamical binary merger simulations of Hopkins et al. (2007) for our definition of the critical mass, $M_{\rm crit}$, at which the black hole accretion rate enters the declining phase, and $M_{\rm final}$, at which the black hole stops feeding. If the newly merged black hole is already more massive than $M_{\rm final}$, there is no accretion event. We note that our predicted final black hole and bulge masses are consistent with the observed $M_{\rm BH} - M_{\rm bulge}$ relation (Somerville et al. 2008a; Hirschmann et al. 2012).

A bout of black hole accretion and AGN activity can also be triggered by a disk instability. When disk mass is transferred to the bulge as previously described, we assume the black hole accretes a gas mass equivalent to some fraction of that mass. Following Hirschmann et al. (2012), we set this term to be $f_{\rm fuel,DI} = 0.002$, which leads to good agreement with the observed number density of low-luminosity AGN. The black hole can continue to accrete until this fuel is consumed.

The black hole is also able to feed and effect feedback in the "radio" or "maintenance" mode. In this mode the black hole feeds via Bondi-Hoyle accretion from the hot halo (Bondi 1952). The accretion is usually significantly sub-Eddington. This feedback mode is associated with giant radio jets which heat the surrounding gas, preventing it from cooling and forming stars. Once the accretion rate is determined, a coupling constant determines how effectively the energy released couples to the surrounding gas. The radio mode heating rate is then calculated and subtracted from the cooling rate described above.

Computing Sérsic Indices and Composite Sizes for Model Galaxies

In Chapters 3 and 4 we compare the structural properties of model galaxies to those of observed galaxies. Our main basis of comparison is the Sérsic index; although disk-dominated and spheroid-dominated galaxies at high redshift become less morphologically distinct, the Sérsic index should still provide us with information about whether we are dealing with an extended

or more compact galaxy. Our model directly computes the bulge luminosity, total luminosity, bulge stellar mass, total stellar mass, the 3D half-mass radius of stars in the bulge, and the 3D scale radius of stars and cold gas in the disk for each galaxy, allowing us to compute the bulge-to-total H-band flux ratio, the bulge-to-total stellar mass ratio, and the 3D mass-weighted bulge radius-to-disk radius ratio.

In Chapter 3, in an initial attempt to put our model and the observations on equal footing, we have converted our mass-weighted outputs (stellar mass bulge-to-total ratio and mass-weighted bulge radius-to-disk radius ratio) to a Sérsic index using a lookup table which takes in the bulge-to-total mass ratio and bulge radius to disk radius ratio and gives an effective radius and Sérsic index. This lookup table was generated by fitting Sérsic indices and effective radii to synthetic bulge+disk systems (n=1 for disks and n=4 for bulges) for a range of different bulge-to-total mass ratios and bulge radius to disk radius size ratios (see Lang et al. (2014) for details). The values that come out of the lookup table are discrete for obvious reasons, so we use a 2D interpolation of the table to generate our Sérsic indices and effective radii. More information and some tests of our approach can be found in Appendix A.

In Chapter 4, we go a step further in making our model outputs more like the observations by converting our mass-weighted quantities to light-weighted quantities. For our high redshift galaxies (z>0.5), we convert our mass-weighted disk and bulge radii to projected rest-frame V-band half-light radii (the projection done according to Prugniel & Simien (1997)) in order to use the stellar mass and redshift dependent wavelength correction provided by van der Wel et al. (2014a) to get observed frame H-band sizes to go with our H-band bulge-to-total ratio (and to match the observed H-band Sérsic indices and sizes from CANDELS). The sizes of our low redshift model galaxies are left in the rest-frame V-band, which should be comparable to the r-band from which the structural properties of GAMA galaxies are derived. We then utilize the lookup table described above to calculate the effective Sérsic index and effective radius for each

system. The Sérsic index and effective radius that we derive here are light-weighted, in contrast with the stellar mass weighted quantities used in Chapter 3, and should provide a more accurate comparison to the Sérsic indices and sizes derived from light for our observed sample. However, we note that we do not attempt to include the effects of dust attenuation in our light-weighted quantities.

2.1.2 Hydrodynamical Simulation

In Chapter 5 we present simulated massive galaxies from cosmological zoom-in runs performed with a version of the parallel SPH code GAGDET-3 (Springel 2005). Specifically, we use the modified code, SPHGAL which mitigates previous problems SPH codes have traditionally had with fluid mixing (Hu et al. 2014). A detailed description of the code can be found in Hu et al. (2014) and relevant updates can be found in Choi et al. (2017), but below we will give a brief overview of the physics relevant to our study.

Code Basics and Setup

The code employs the pressure-entropy SPH formulation of Hopkins et al. (2013) and also has improved force accuracy due to the use of the Wendland C^4 kernel with 200 neighboring particles (Dehnen & Aly 2012). We also include the improved artificial viscosity implementation presented by Cullen & Dehnen (2010) and an artificial thermal conductivity according to Read & Hayfield (2012) in order to reduce the noise in pressure estimates in the presence of strong shocks. Finally, a timestep limiter is employed according to Saitoh & Makino (2009) and Durier & Dalla Vecchia (2012) to ensure that neighboring particles have similar timesteps and that ambient particles do not remain inactive when a shock is approaching.

Star Formation and Stellar/Supernova Feedback

Star formation and chemical evolution are modeled as described in Aumer et al. (2013); chemical enrichment is achieved via winds driven by Type I and II supernovae and asymptotic giant branch (AGB) stars. Eleven species of metals are tracked explicitly and cooling rates are calculated based on abundances, as well as the temperature and density of the gas. Redshift-dependent metagalactic UV/X-ray and cosmic microwave backgrounds are included with a modified Haardt & Madau (2012) spectrum.

Stars are formed stochastically where the density is greater than the density threshold for star formation. This threshold is given as $n_{\rm th} \equiv n_0(T_{\rm gas}/T_0)^3(M_0/M_{\rm gas})^2$ where $n_0 = 2.0$ cm^{-3} and $T_0 = 12000$ K, with M_0 being the gas particle mass. This corresponds to the density value for the Jeans gravitational instability of a mass $M_{\rm gas}$ at temperature $T_{\rm gas}$. The star formation rate is calculated as $d\rho_*/dt = \eta\rho_{\rm gas}/t_{\rm dyn}$, where ρ_*, $\rho_{\rm gas}$, and $t_{\rm dyn}$ are the stellar density, gas density and local dynamical time for the gas particle, respectively. η is the star formation efficiency and is set to 0.025.

Stellar feedback is included in the form of stellar winds and heating by ionizing radiation from young massive stars. Momentum from stellar winds is added to the surrounding gas particles, while cold gas within the Strömgren radius of hot stars is heated to $T = 10^4$ K.

Supernova feedback takes the form of momentum ejection with a velocity of $v_{\rm out,SN} = 4,500$ km s^{-1}. Gas particles which receive the initial kick then impart momentum to their neighbors in a free-expansion phase until at a certain radius, corresponding to the Sedov-Taylor blast-wave supernova remnant phase, the supernova energy is transferred as 30% kinetic and 70% thermal. Finally at larger radii, the snowplow phase kicks in and radiative cooling becomes significant. An allowance is also made for more efficient propagation of the remnant in a multi-phase interstellar medium where appropriate. A detailed description of the early stellar and supernova feedback

prescription can be found in Núñez et al. (2017).

Feedback from low- and intermediate-mass stars is also included in the form of slow winds as from AGB stars. Energy and momentum are transferred to surrounding gas particles such that momentum is conserved. The initial outflowing wind velocities are assumed to be $v_{\rm out,AGB} = 10$ km s^{-1}, which is typical for AGB stars (Nyman et al. 1992). Metal-enriched gas from all of these prescriptions is continuously added to the ISM. We also include metal diffusion, which allows for the mixing and spreading of metals in the enriched gas (see Aumer et al. (2013) for details).

Black Hole Growth and Feedback

Seed black holes are treated as collisionless sink particles and are placed in the centers of haloes that reach a mass threshold ($10^{5.15} M_\odot$ black holes are placed in $10^{11.15} M_\odot$ haloes). These black holes can then grow by gas accretion or by merging with another black hole, as soon as the two black holes fall within each other's local SPH smoothing lengths and their relative velocities are smaller than the local sound speed. In the case of gas accretion, infall onto the black hole is governed by the Bondi-Hoyle-Littleton rate (Bondi 1952). The size of the SPH gas particles is taken into account so that full accretion is allowed when the entire volume of a particle is within the Bondi radius. Gas particles which fall only partially inside the Bondi radius are given a probability of being absorbed by the black hole based on the volume within the Bondi radius (Springel et al. 2005; Choi et al. 2012, 2014).

Processes on scales below our resolution limit (such as radiation pressure) are assumed to impart momentum to the gas. Winds are launched from the central region around the black hole with a fixed wind velocity of 10,000 km/s; the number of particles selected to receive a kick due to this wind is determined by a parameter for feedback efficiency. The total momentum flux carried by the wind is $\dot{E_{\rm w}} \equiv \epsilon_{\rm w} \dot{M_{\rm acc}} c^2$, where the efficiency parameter $\epsilon_{\rm w}$ is set to 0.005 (Ostriker et al. 2010; Choi et al. 2015). The selected gas particles receive the wind kick in a direction parallel

or anti-parallel to their angular momentum vectors and share momentum with their two nearest neighbors. The momentum is split between the gas particles and is conserved, and the excess kinetic energy of the particles before the collision is deposited into the gas particles as thermal energy.

Radiation feedback from Compton and photoionization heating due to X-ray radiation from the accreting black hole, radiation pressure associated with the heating, and the Eddington force are also included. We utilize the AGN spectrum and metal line heating prescription of Sazonov et al. (2004). X-ray radiation is coupled to surrounding gas using an approximation from Sazonov et al. (2005). The radiation pressure on each gas element is also calculated. Accretion is not artificially capped at the Eddington rate, but the Eddington force acting on electrons is included such that super-Eddington accretion can occasionally occur but naturally reduces inflow while stimulating outflows.

Also included are metallicity-dependent heating prescriptions due to photoelectric emission and metal line absorption. The emmissivity of background AGN is calculated as $\varepsilon(z) = \epsilon \frac{d\rho_{\rm BH}(z)}{dt} c^2$, where the radiative efficiency ϵ is set to 0.1. From this the heating by the cosmic X-ray background is derived. More details about these and all of our feedback prescriptions can be found in Choi et al. (2017).

We note here that these feedback prescriptions have been shown to produce galaxies with fairly realistic observable properties (Choi et al. 2017). Without AGN feedback, our model produces galaxies with stellar to halo mass ratios which are too high by a factor of three, and continue to form stars until $z = 0$, in conflict with observations of galaxies of this mass, which are predominantly quenched. This results in compact stellar cores, effective radii which fall a factor of five below the observed size-mass relation and high velocity dispersions (Choi et al. 2017). The addition of AGN feedback alleviates all of these problems, resulting in quiescent galaxies with observationally consistent sizes and velocity dispersions. AGN feedback also removes gas

from halos, resulting in lower, more physical X-ray luminosities and gas mass fractions (Choi et al. 2017). Post-processing the simulations with newly developed nebular emission line models additionally shows that the evolution of optical nebular emission line-ratios of massive galaxies is widely consistent with observations (Hirschmann et al. 2017). Satisfied that our model produces galaxies which compare favorably with observed high-mass elliptical galaxies, in Chapters 5 and 6, we turn to analyze the wind properties, gas cycle, and gas metallicity in these systems.

Zoom Simulations

The "zoom-in" initial conditions that we use are described in detail in Oser et al. (2010) and Oser et al. (2012). We run our zooms in dark matter haloes picked from a 72 Mpc h^{-1} dark matter only simulation which employed the parameters from WMAP3 (Spergel et al. 2007) and assumed a flat cosmology: $h = 0.72, \Omega_{\rm b} = 0.044, \Omega_{\rm dm} = 0.216, \Omega_{\Lambda} = 0.74, \sigma_8 = 0.77$, and an initial power spectrum slope $n_{rms} = 0.95$. We trace back the dark matter particles close to the haloes of interest in each snapshot and then replace those dark matter particles with high-resolution dark matter and gas particles. The high-resolution zoom is then evolved from $z = 43$ to today.

The selected dark matter haloes have final virial masses between $1.4{\times}10^{12} M_{\odot}$ and $2.3{\times}10^{13} M_{\odot}$ and are made up of dark matter particles with a mass of $m_{\rm dm}{=}3.57{\times}10^{7} M_{\odot}$. The final central galaxy masses in these halos (for our runs with AGN) are between $8.2{\times}10^{10} M_{\odot}$ and $1.5{\times}10^{12} M_{\odot}$, with gas and star particles both having a mass of $m_{*,\rm gas}{=}6.0{\times}10^{6} M_{\odot}$. We use comoving gravitational softening lengths of $\epsilon_{\rm gas,star}{=}.556$ kpc and $\epsilon_{\rm halo}{=}1.236$ kpc for gas/star particles and dark matter particles, respectively.

In Chapters 5 and 6, we will examine zoom regions run with two different models: MrAGN and NoAGN. MrAGN is the fiducial model which includes all of the physics described above, including the different ways in which AGN can effect feedback on their surrounding galaxies. NoAGN is the same in every way except it contains no black holes and thus no AGN feedback.

In this way the effects of the different feedback mechanisms can be isolated. Out of our initial sample of 30 pairs of zoom runs, we focus on the 24 of which we can use to make a direct comparison between the two models, as described in Chapter 5.

2.2 Observational Data

2.2.1 High Redshift: CANDELS

Our high redshift dataset in Chapters 3 and 4 (spanning $0.5 < z < 3.0$) consists of observations taken as part of the Cosmic Assembly Near-infrared Deep Extragalactic Legacy Survey (CANDELS; Grogin et al. 2011; Koekemoer et al. 2011). The CANDELS data span five different fields. In Chapter 3, we utilize data from two of these fields: GOODS-S (Guo et al. 2013) and UDS (Galametz et al. 2013). In Chapter 4, we use data from all five fields, including COSMOS (Nayyeri et al. 2017), GOODS-N (Barro et al. (in prep.)), and EGS (Stefanon et al. 2017) (see all of these references for details about data processing and catalog creation for each of the CANDELS fields.) With this multiwavelength data we are able to study the star formation properties and structure of galaxies out to $z \sim 2.5$ at high resolution.

We make use of data catalogs generated by several previous studies. Here we give a very brief overview of the derivation of physical parameters which applies generally to all of the CANDELS fields. For a given field, the template-fitting method TFIT (Lee et al. 2012; Laidler et al. 2007) was used to merge datasets of different wavelengths with different resolutions in order to construct the observed-frame multi-wavelength photometric catalog. The Bayesian framework of Dahlen et al. (2013) was used to derive photometric redshifts. Spectroscopic redshifts are used where available and reliable. 3D-HST grism redshifts are used for GOODS-S galaxies where available (Morris et al. 2015). The EAZY code (Brammer et al. 2008 and Kocevski et al. in prep.) was used to fit templates to the observed-frame SEDs in order to derive rest-frame photometry.

Several independent codes, such as FAST (Kriek et al. 2009), were used to derive stellar masses under fixed assumptions, but allowing for some variation of assumed star formation histories. We assume the following: Bruzual & Charlot (2003) stellar population synthesis models, Chabrier (2003) initial mass function, exponentially declining star formation histories, solar metallicity and a Calzetti (2001) dust attenuation law. A ladder of SFR indicators prescribed in Barro et al. (2011) and Wuyts et al. (2011) is used to derive star formation rates for galaxies in each field. Finally, structural parameters were derived using GALFIT (Peng et al. 2002), fitting to the HST/WFC3 F160W H-band images using a one-component Sérsic model as described in van der Wel et al. (2012).

We make the following selection cuts on our data: stellar mass $> 10^{10} M_{\odot}$ (to ensure completeness) and GALFIT quality flag=0 (to ensure good fits and robustness of our galaxy morphologies). We cut at a stellar mass of $10^{10} M_{\odot}$ for continuity with our low-redshift GAMA sample, which starts to become incomplete below this mass range. Because of this, we employ a relatively conservative mass cut throughout Chapters 3 and 4.

2.2.2 Low Redshift Sample: GAMA

At low redshift CANDELS probes a very small volume, so we supplement with observations from Data Release 2 (DR2) of the Galaxy and Mass Assembly survey (GAMA;Liske et al. 2015). Our low redshift range spans $0.005 < z < 0.12$, sometimes referred to as $z = 0.06$ in the text. GAMA has an area of 144 square degrees and goes two magnitudes deeper (r<19.8 mag) than SDSS while maintaining high spectroscopic completeness ($\gtrsim 98\%$). GAMA also has a rich supplementary multi-wavelength dataset (Liske et al. 2015). The backbone of GAMA is deep optical spectroscopy with the Anglo-Australian Telescope (AAT), while its multi-wavelength catalogs are bolstered by collaborations with several other independent surveys (for a review, see Driver et al. (2011)).

Again we make use of derived properties generated by previous work. Bulk flow-corrected redshifts are adopted from Baldry et al. (2012) and rest-frame photometry and stellar masses were derived from SED fitting as described in Taylor et al. (2011). GAMA's high spectroscopic completeness allows the derivation of $H\alpha$-based star formation rates from extinction-corrected $H\alpha$ line luminosities. Structural properties of GAMA galaxies are provided via multi-band measurements using GALFIT (Peng et al. 2002). We adopt the structural fits in the r-band so as to analyze the structural properties of GAMA galaxies in the same band in which they were selected (as with the H-band for CANDELS galaxies).

We also employ the following selection cuts as we did with our CANDELS data: stellar mass $> 10^{10}\,M_{\odot}$ (again to ensure our sample is complete), and GALFIT quality flag = 0.

Chapter 3

Quenching and Morphological Transformation in CANDELS and a Semi-analytic Model

3.1 Introduction

As described in Chapter 1, the mechanisms by which galaxies are transformed and evolve over time, both in terms of their star formation rates and their morphologies, are still not clearly known. At low redshift, the distribution of galaxy colors is bimodal (Baldry et al. 2004; Bell et al. 2004b). This division of galaxies into the star forming "blue cloud" and the quiescent "red sequence" can be observed most clearly in the color-magnitude and specific star formation rate (sSFR)-stellar mass planes (Baldry et al. 2004; Brinchmann et al. 2004; Kauffmann et al. 2003; Strateva et al. 2001). Additionally, star forming galaxies can be said to occupy a "star forming main sequence," a correlation between the star formation rate and the stellar mass of star forming galaxies (Noeske et al. 2007; Daddi et al. 2007; Elbaz et al. 2007; Rodighiero et al. 2011). Galaxies that are part of the red sequence have a wider range of star formation rates, although they do exhibit a correlation between mass (or luminosity) and color, where more massive galaxies tend to be redder (Bernardi et al. 2003; Gallazzi et al. 2006; Peng et al. 2010; Brammer et al. 2011; Muzzin et al. 2013b).

In addition to the bimodality due to stellar populations, there is also a bimodality in the structure of galaxies (Kauffmann et al. 2003). Often characterized by the bulge-to-total luminosity or mass ratio, or light profile parameterizations such as the Sérsic index, galaxy morphology

tends to be correlated with the star formation activity in the galaxy. Galaxy disks tend to be bluer than bulges (Peletier & Balcells 1996; Bell et al. 2004a) and galaxies that are part of the blue cloud are more likely to be disk-dominated, while galaxies that are members of the red sequence are more likely to have more prominent bulges, or to have the concentrated light profiles that are characteristic of early type galaxies (Blanton & Moustakas 2009; Schiminovich et al. 2007; Bell 2008; Cheung et al. 2012).

Large surveys have shed light on how the galaxy population evolved over a large fraction of the age of the universe. These observations have shown that the bimodality seen in the local universe is in place even at $z \sim 2-3$ (Brammer et al. 2009, 2011; Muzzin et al. 2013b). Analysis of the buildup of stellar populations from high redshift to the present reveals that the stellar mass contained in objects in the blue cloud has remained relatively constant, while the stellar mass represented by galaxies on the red sequence has grown significantly; this implies that blue star forming galaxies are in fact being transformed into red, quiescent ones (Bell et al. 2004b; Borch et al. 2006; Bell et al. 2007; Faber et al. 2007). The mechanism responsible for this "quenching" (or turning off of star formation) is not so clear. New information about the evolution of galaxy structure and morphologies has recently been gleaned from observations using the Hubble Space Telescope. Recent work suggests that quiescence is intimately tied to the presence of a bulge component (Wuyts et al. 2011; Lang et al. 2014; Bluck et al. 2014; McIntosh et al. 2014). Moreover, observations have revealed a population of compact spheroid-dominated star forming galaxies at $z \sim 2$, which may be the progenitors of the quiescent, elliptical galaxies we see today (Wuyts et al. 2011; Whitaker et al. 2012b; Barro et al. 2013; Williams et al. 2014; Barro et al. 2014; Williams et al. 2015). It seems likely that the mechanisms responsible for quenching, morphological, and size evolution are connected.

There have been several mechanisms proposed to explain galaxy quenching. One of the most popular scenarios involves feedback due to active galactic nuclei (AGN). AGN feedback

can be broadly divided into two regimes: the radiatively efficient "quasar" or "bright" mode, which is proposed to drive a powerful wind which expels gas from the galaxy, and the "radio" or "maintenance" mode, which heats gas in the galactic halo, preventing it from cooling and forming stars (Somerville & Davé 2015, and references therein). This AGN activity can be driven either by galaxy mergers (Ellison et al. 2011; Silverman et al. 2011) or in situ processes such as disk instabilities (Bournaud et al. 2011; Dekel & Burkert 2014). Both of these processes lead to rapid transfer of angular momentum and the growth of a bulge component. Virial shock heating is another proposed mechanism: during collapse, gas can be heated via the conversion of gravitational potential energy into kinetic energy (White & Rees 1978). Above a (redshift dependent) critical halo mass of $\sim 10^{12} M_{\odot}$, this shock heating may be able to keep a substantial fraction of the halo gas hot, leading to quenching (Birnboim & Dekel 2003; Kereš et al. 2005).

While this does not seem directly related to the presence of a bulge component, it is clear from observations that galaxies residing in halos above $10^{12} M_{\odot}$ are more likely to be bulge-dominated than disk-dominated (Dekel et al. 2009; Woo et al. 2015a). There is also the possibility that the presence of a (significant) bulge may itself stabilize the disk against local instabilities, thus making star formation less efficient, an effect known as morphological quenching (Martig et al. 2009). Finally, there is a suite of processes connected with dense environments, including tidal and ram pressure stripping and harrassment. These are often collectively referred to as "environmental quenching" (Oemler 1974; Dressler 1980; Balogh et al. 2004; Tinker & Wetzel 2010; Peng et al. 2010), and they likely primarily affect satellites orbiting within a larger halo. These processes probably operate on a different timescale, and lead to different sorts of morphological transformation, than the ones described above. In this work, we focus on field galaxy environments, so environmental processes are likely to be sub-dominant. See also McIntosh et al. (2014) for a summary of proposed quenching processes.

If quenching and morphological transformation are (in most cases) intimately tied to each

other, then galaxies which seem to be the "outliers" in this picture may be of particular interest: the quiescent disk-dominated galaxies and star forming spheroid-dominated galaxies. These populations are smaller than those of star forming disk-dominated and quiescent spheroid-dominated galaxies, although they are not insignificant in size (McGrath et al. 2008; van der Wel et al. 2011). Schawinski et al. (2014) did an analysis of galaxies in the local universe that occupy the "green valley," the region in between the blue cloud and the red sequence on the color-magnitude diagram, using observational data from SDSS (York et al. 2000) and GALEX (Martin et al. 2005). They used morphology classifications from Galaxy Zoo (Lintott et al. 2008, 2011) and determined that there were two distinct paths through the green valley, one taken by galaxies that leave the blue cloud as disk dominated systems, the other by galaxies that transition as bulge-dominated systems (see also the work of (Smethurst et al. 2015)). The path associated with spheroid-dominated galaxies is consistent with work that suggests that bulge growth precedes quiescence (Wuyts et al. 2011; Wong et al. 2012; Lang et al. 2014), while the path taken by disk-dominated galaxies may explain the slowly growing population of quiescent disk galaxies in the local universe which have been cut off from their gas supply but suffered nothing catastrophic to destroy or use up their existing gas reservoirs. Barro et al. (2013) and Woo et al. (2015a) similarly identify different scenarios of quenching based on structural evolution. McIntosh et al. (2014) also describe a path associated with spheroid-dominated galaxies when examining what they call "recently quenched ellipticals" in the Sloan Digital Sky Survey. In this light, these "outlying" populations are possibly much more important to the overall picture than originally suspected, and may be an indication that quenching is caused by multiple physical processes.

Aiding in the investigation of galaxy formation and evolution are state of the art numerical simulations and semi-analytic models. N-body dark matter simulations such as Bolshoi (Klypin et al. 2011) are an invaluable tool when testing the predictions of our currently favored Lambda Cold Dark Matter cosmological model, ΛCDM. Semi-analytic models, or SAMs, plant galaxies

in merger trees assembled in dark matter N-body simulations or constructed using techniques based on the Extended Press Schechter formalism. By following the evolution of these galaxies within the backbone of the dark matter history, accounting for physical processes such as gas accretion and cooling, star formation, merging and feedback with physically motivated recipes, population statistics for a cosmological sample of galaxies can be generated quickly and with minimal computational resources (Kauffmann et al. 1993; Cole et al. 1994; Somerville & Primack 1999; De Lucia et al. 2006; Somerville et al. 2008a; Guo et al. 2011; Somerville et al. 2012; Porter et al. 2014a). SAMs have been used to study the evolution of star formation and the buildup of spheroid-dominated galaxies and to gauge which processes are especially important. De Lucia et al. (2006) and Benson & Devereux (2010) have investigated the buildup of spheroid-dominated galaxies in SAMs with cosmic time. These analyses and others have reiterated that bulge growth often appears to be connected to the cessation of star formation and also demonstrate that the two main channels for bulge growth are mergers and disk instabilities, both of which appear to be important, although their degree of importance may change with redshift, galaxy mass and environment, and is also model dependent (Parry et al. 2009; De Lucia et al. 2011; Fontanot et al. 2012; Porter et al. 2014a).

Recently, Porter et al. (2014a) compared the predictions of the latest version of the "Santa Cruz" SAM (Somerville & Primack 1999; Somerville et al. 2008a) for the $z = 0$ stellar mass function divided by morphology with available observations, and found fairly good agreement. They found that adding a prescription for bulge growth via disk instabilities brought the model into better agreement with the observed galaxy stellar mass function of spheroid-dominated galaxies at intermediate masses ($10.5 < \log(M_*/M_\odot) < 11.5$). In addition, Porter et al. (2014a) developed a new model for predicting the radial *sizes* and velocity dispersions of bulges formed via mergers or disk instabilities, based on a simple analytic model calibrated using numerical

hydrodynamic simulations of binary galaxy mergers. Their model reproduces the observed size-mass relation for spheroids and disks, and the evolution of this relation from $z \sim 2$ to the present day (see also Somerville et al. in prep). Porter et al. (2014b) investigated the predictions of the same models for the correlation of the age and metallicity of stars in local spheroid-dominated galaxies with structural parameters such as size and velocity dispersion. They found a strong correlation between both stellar population parameters (age and metallicity) and internal velocity dispersion, in agreement with observations. They found no correlation between age and radius, and a weak correlation between metallicity and radius, also in agreement with observations of nearby early type galaxies. In this work we follow up on the work by Porter and collaborators by directly studying the build-up of the spheroid-dominated population over cosmic time, and comparing with observations of high-redshift galaxies.

The conclusions of previous studies in the literature regarding the spheroid-dominated fraction of galaxies in SAMs and the agreement with observations are difficult to synthesize, because different analyses use different criteria to define spheroid-dominated galaxies both in the models and in the observations. The bulge-to-total mass ratio (B/T) that is readily predicted in SAMs is difficult to measure observationally. Therefore it has been difficult to make a direct comparison between model predictions and observations previously. One of the important new features of this study is that we extend our models to predict a morphological quantifier that can be compared more directly with observations. Our method for converting model quantities to an observed morphological indicator is described in Chapter 2.

In this chapter, we present results quantifying the evolution of quenching and spheroid growth in observations from $z \sim 3$ to the present, and also present new predictions of these same quantities from state-of-the-art semi-analytic models. We split galaxies according to their star formation rates and morphologies and examine the buildup of the quiescent and spheroid-dominated fractions of galaxies. We then go further than studies in the past by subdividing into four populations:

star forming disk-dominated galaxies (SFDs), star forming spheroid-dominated galaxies (SFSs), quiescent disk-dominated galaxies (QDs) and quiescent spheroid-dominated galaxies (QSs). We examine the evolution of the fraction of galaxies in each of these populations. Our low redshift observational data ($z \sim 0.06$) come from the Galaxy and Mass Assembly Survey (GAMA Driver et al. 2009) and our higher redshift data ($0.5 < z < 3.0$) come from the Cosmic Assembly Near-infrared Deep Extragalactic Legacy Survey (CANDELS; Grogin et al. 2011; Koekemoer et al. 2011). We use the Santa Cruz SAM of Somerville et al. (2008a) with updates as described in Somerville et al. (2012) and Porter et al. (2014a). Our semi-analytic model includes the effects of AGN feedback and bulge growth triggered by mergers and (optional) disk instabilities. Another way in which our study is unique is the way we characterize the morphologies of our model galaxies: we convert our model output, bulge-to-total mass ratio, to Sérsic index as described in Chapter 2 and Appendix A in order to facilitate a more direct comparison between model and observed galaxy morphologies than has been carried out before. We will also examine in detail the histories of galaxies selected from each population in order to shed light on the individual tracks that different types of galaxies move along as they evolve. The structure of this chapter is as follows. In Section 2 we present a comparison of the evolution of these populations in the model and the observations. We present our discussion, in part informed by studying individual evolutionary tracks of galaxies from the model, in Section 3 and our summary and conclusions in Section 4.

3.2 Results

We examine here how well our model (with the disk instability prescription described in Chapter 2 turned both on and off) matches the buildup of the quiescent and spheroid-dominated fraction of observed galaxies. We then subdivide the model and observed populations further and examine

the buildup of the four quadrants of the sSFR-Sérsic index plane. In this way we can assess where our model is succeeding and failing in transforming galaxies in terms of their star formation rates and morphologies.

3.2.1 Quiescent Fraction

Dividing by sSFR

Our first step is to split galaxies into star forming and quiescent populations. We preferred not to simply divide our population by eye and sought an automated process which would divide our galaxies in each redshift bin in a reasonable way. One approach used in the literature is to divide at a specific star formation rate $sSFR(z) = 1/[3t_{\rm H}(z)]$, where $t_{\rm H}(z)$ is the Hubble time at the redshift of interest. This divider in sSFR is roughly equivalent to the division of galaxies into star forming and quiescent on the UVJ color-color diagram as described in Whitaker et al. (2012a) and Muzzin et al. (2013b). This division line, as well as others that we attempted to use, all shared the same problem: the distribution of sSFRs in the model and from observations is somewhat different, especially at z>2.2, so dividing lines which made a reasonable cut for model galaxies did not work as well for observed galaxies and vice versa. The sSFR distribution of model galaxies is not as bimodal as it is for the observations; rather than having a second peak at very low sSFR, our model distribution tails off. We don't expect this to significantly affect the results of this work as the star formation rates in question are already very low (our model galaxies *are* being quenched; their sSFRs just aren't distributed in quite the same way as the observations) and any new stars formed shouldn't change the structural parameters with which we concern ourselves later. Still, this makes defining quiescence by examining the trough between populations somewhat difficult. We instead seek to define our dividing line in relation to the star forming main sequence, which leads us to a slightly different issue.

The star formation rates of the observed galaxies are systematically slightly higher than those of the model galaxies, so a typical observed star forming galaxy (one which we would say occupies the main sequence of star formation) has a different sSFR than a corresponding model galaxy. The dependence of sSFR on stellar mass for star forming galaxies is also steeper for observed galaxies than for model galaxies. This may point to a deficiency in some of our prescriptions for star formation and/or stellar feedback (see the discussion in Somerville & Davé 2015, and references therein). However, in this work we are concerned with broadly distinguishing between star forming and quiescent, and with the processes responsible for moving galaxies fairly dramatically off of the main sequence. Therefore as long as we define our dividing line relative to the main sequence in the models and in the observations, our analysis should be robust.

To deal with these issues, we introduce a method to calculate a dividing line between star forming and quiescent galaxies which we apply to both the observations and the model galaxies; however, the actual normalization, slope, and redshift dependence of the dividing line are not the same for the model and the observational samples. Geha et al. (2012) has shown that, in the local universe, essentially all isolated galaxies with $m_{\rm star} \lesssim 10^9 M_\odot$ show active star formation. This is also the case in our models. Therefore, at low stellar masses we should be able to measure the "native" star-forming main sequence (SFMS), unaffected by internal quenching processes. We cannot reliably reach such low mass limits, but we use galaxies with stellar masses between 10^9 and $10^{9.5} M_\odot$ to measure the baseline SFMS (we restrict our sample in the models to central galaxies for reasons mentioned in Section 3.3.4). We then find the mean log(sSFR) of galaxies in this mass range in time bins, tracking the evolution of the sSFR of typical star forming galaxies across cosmic time. Once this evolution is known, we calculate the main sequence slope by measuring the change in the mean log(sSFR) between stellar masses of 10^9 and $10^{10} M_\odot$. In a given redshift bin, we use the mean low-mass sSFR and derived slope to define a mass-dependent main sequence line. We then define quiescent galaxies as having less than 25% of the sSFR of

Table 3.1: Coeffients for $MS(z) = a_3t^3(z) + a_2t^2(z) + a_1t(z) + a_0$, the mean log(sSFR) of the main sequence, where $t(z)$ is the age of the universe in Gyrs at the redshift of interest.

Dataset	a_3	a_2	a_1	a_0
SAM	-0.0012	0.039	-0.499	-7.640
GAMA & CANDELS	-0.0017	0.039	-0.398	-7.513

Table 3.2: Slope derived as described in the text for each of our redshift bins.

Redshift	SAM b	GAMA & CANDELS b
$0.006 < z < 0.12$	0.021	-0.303
$0.5 < z < 1.0$	-0.105	-0.400
$1.0 < z < 1.4$	-0.054	-0.144
$1.4 < z < 1.8$	-0.241	-0.130
$1.8 < z < 2.2$	-0.377	-0.236
$2.2 < z < 2.6$	-0.408	-0.256
$2.6 < z < 3.0$	-0.487	-0.370

the main sequence line. Our quiescence divisor for a given redshift and stellar mass is given by

$$sSFR(z, M_*) = 0.25[10^{MS(z)+b(log(M_*/M_\odot)-9.25)}] \tag{3.1}$$

where b is the slope we derived and MS is the mean log(sSFR) measured in the low mass bin ($10^9 M_\odot \leq M_* \leq 10^{9.5} M_\odot$). The values of these quantities are determined separately for the model galaxies and for the observed galaxies. The coefficients for $MS(z)$ and the values of b in each of our redshift bins are listed in Tables 3.1 and 3.2, respectively.

Figure 3.1 shows the division of star forming and quiescent galaxies for the model (including disk instability) and from the observations in the redshift bins $z \sim 0.06$, $0.5 < z < 1.0$ and $2.2 < z < 2.6$. Although the galaxy sample we will use for the remainder of this work includes only galaxies with $\log(M_*/M_\odot) > 10.0$, here we plot galaxies down to stellar masses of $10^9\, M_\odot$, since these are the galaxies from which our dividing lines are derived. The green line indicates our split between star forming and quiescent galaxies. The red line is drawn at $sSFR = 1/(3t_{\rm H})$,

where $t_{\rm H}$ is the Hubble time at the median redshift of the bin, for comparison with alternate dividing lines commonly used in the literature. We apply the cut derived for the DI model to the noDI model as well, since we would like to see how the disk instability affects the sSFRs of galaxies within the model and that information would be lost if we allowed the cut to move between the two models. It is worth noting, however, that $MS(z)$ and b are very similar between the two models. We can see in all three bins that the dividing line has a different slope and normalization for the models than for the observations.

Evolution of the Quiescent Fraction

Figure 3.2 shows the evolution of the quiescent fraction of galaxies with redshift for galaxies from the SAM, both the DI and noDI models, and from observational data taken from GAMA and CANDELS. We compute 1-σ uncertainties due to field-to-field variance and uncertainty in observed galaxy properties (stellar mass, Sérsic index and star formation rate) as follows. Our lightcones are about nine times larger than the CANDELS fields that we are comparing with, so we select a model sample from a subsection of the lightcone that has comparable area. If we select different CANDELS-sized areas from our lightcone to do our analysis, we get a measure of the effect of cosmic variance. We also calculate the 1-σ error in the quiescent fraction due to uncertainties in the estimates of galaxy properties in the observational sample. We use quoted uncertainties in Sérsic index, assume an uncertainty of 0.25 dex for star formation rates and use the redshift-dependent stellar mass uncertainty of Behroozi et al. (2013b). The separate uncertainties due to cosmic variance and parameter estimation can be seen in the top panel. We add the uncertainty due to each in quadrature and apply them to the observations. In the lowest redshift bin, the error estimates reflect only the uncertainties due to errors in the physical parameters; these uncertainties dominate over the cosmic variance due to the large volume probed by GAMA. We note here that we are still likely underestimating uncertainties due to systematics

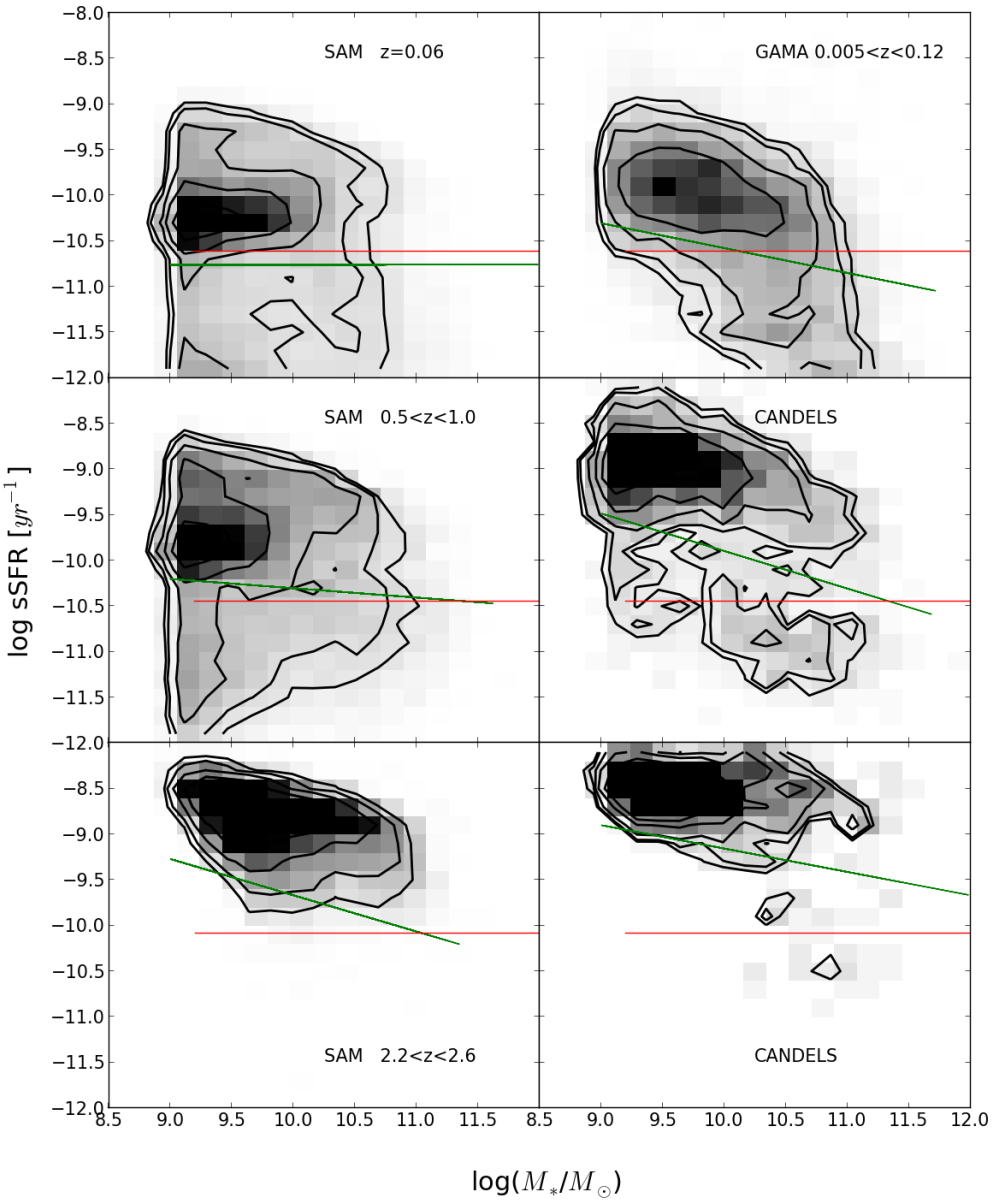

Figure 3.1: The distribution of observed and model galaxies ($\log(M_*/M_\odot)$>9.0) in the plane of stellar mass and specific star formation rate (sSFR) in the redshift bins $z \sim 0.06$, $0.5 < z < 1.0$ and $2.2 < z < 2.6$. The greyscale shows the population density with contours overplotted in black. The green line shows our adopted dividing line between star forming and quiescent galaxies. In practice, the dividing line is calculated for each galaxy individually based on its stellar mass and redshift; the green line is a least mean squares fit to the stellar masses and threshold sSFRs of each galaxy. The red line is the $1/3t_{\rm H}$ dividing line sometimes used in the literature. It is clear that the normalization and slope for the model SFMS is different from those for the observations, necessitating the use of a different dividing line. Left panel: Galaxies from the SAM. Right panel: Galaxies from the GAMA or CANDELS survey.

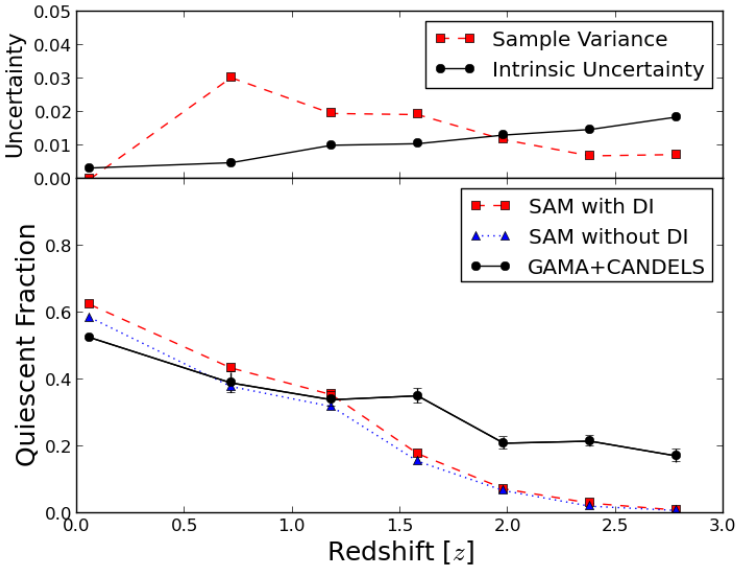

Figure 3.2: The evolution of the quiescent fraction of galaxies ($\log(M_*/M_\odot)$>10.0) with redshift. The top panel is the predicted 1-σ uncertainty due to sample variance (red, dashed) and due to uncertainty in galaxy parameter estimation (black, solid). These are added together in quadrature and shown plotted on the observational measurements in the bottom panel. In the bottom panel the red dashed line with squares corresponds to the model including disk instabilities, the blue dotted line with triangles to the model without disk instabilities, and the black solid line with circles to the observations. This convention is used throughout this work. Field-to-field variance is expected to be negligible in the lowest redshift bin, so here the plotted error is entirely due to uncertainties in galaxy properties. Overall, the agreement between the model predictions and observational results is quite good. Below $z \sim 1.2$, the fractions predicted by the model differ from the observational fraction by no more than 0.1, although at $z \gtrsim 1.2$ they begin to differ by as much as 0.2, with the model predicting almost no quiescent galaxies. The predicted quiescent fraction is affected very little by the inclusion of disk instabilities in the model.

such as the assumed star formation histories of CANDELS galaxies, possible variations in the IMF, etc.

The quiescent fraction of galaxies in the model is relatively insensitive (changing by <10% in all redshift bins) to the inclusion of disk instabilities in our models; as we will see, the net effect of the disk instability is mainly to create more bulge-dominated galaxies. This is due in part to the fact that our disk instability prescription does not affect gas and limits the amount of low-level AGN feedback that is triggered by disk instabilities. Both models agree well with observations at low redshift; for $z \lesssim 1.2$, the fractions differ by no more than $0.05 - 0.1$. Above this redshift, however, the fractions begin to differ by about 0.2, with the model predicting fewer quiescent galaxies than are observed. Overall, the model exhibits a steeper evolution than the observed galaxies, predicting basically no quiescent galaxies at $z \sim 3$. It seems that the model is not quenching galaxies early enough. We will discuss possible reasons for this discrepancy later.

In Figure 3.3, we examine the mass dependence of the quiescent fraction evolution. The behavior is similar in each mass bin to the overall behavior in Figure 3.2. At redshifts above ~ 1.2 the model predicts a smaller quiescent fraction than is observed for all three mass bins. This discrepancy gets worse as the stellar mass increases. In the highest mass bin, the fractions can differ by as much as 40 %. This is an extension of the overall high redshift discrepancy in Figure 3.2; since our model predicts no quiescent galaxies (in any mass range) and in general more massive galaxies are likely to be considered quiescent, the gulf between our model quiescent fraction and the observed fraction widens as the masses considered become larger. In the two lower mass bins, the DI model actually overproduces quiescent galaxies by as much as 0.15 at $z \lesssim 1.2$, but it is in better agreement (within 0.05) with observations in the highest mass bin. As expected, the quiescent fraction increases for galaxies with higher stellar mass for both the model and the observations. The model also captures the steeper evolution of the quiescent fraction for higher masses, although again, the evolution in the model is steeper than observations for all

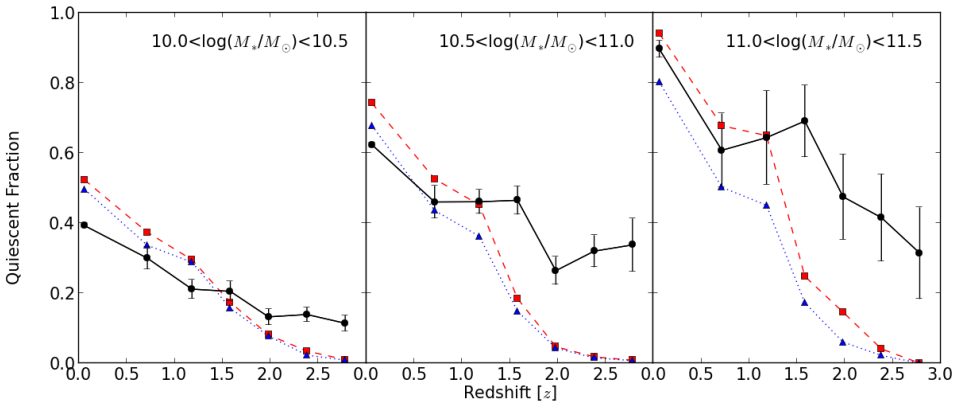

Figure 3.3: Each panel is like Figure 3.2, but for different bins in stellar mass. Line types and colors are the same as Figure 3.2. The quiescent fraction increases with stellar mass for both the models and observations, with disk instabilities contributing more of the quenched galaxies at higher masses. The discrepancy between the model predictions and observations is larger in the two higher stellar mass bins.

mass bins.

3.2.2 Spheroid-Dominated Fraction

We now split galaxies into spheroid-dominated and disk-dominated populations. We define spheroid-dominated galaxies as having Sérsic indices greater than 2.5, the average of a pure disk ($n = 1$) and pure bulge ($n = 4$), as has been done in many other studies (Shen et al. 2003; Lange et al. 2015; Bruce et al. 2014; Mortlock et al. 2015). We discuss later how making this spheroid-domination cut less stringent (at $n = 2$) affects our results. We have also done the same analysis by dividing galaxies at a bulge-to-total mass ratio of 0.5. These results are very similar and can be found in Appendix B. Figure 3.4 shows the evolution with redshift of the spheroid-dominated fraction of galaxies. Here, we see the main effect of the disk instability. The noDI model severely underpredicts the fraction of spheroid-dominated galaxies at almost all redshifts, with the disagreement becoming worse towards lower redshifts. The DI model does a much better job of matching the observed spheroid-dominated fraction, increasing our prediction

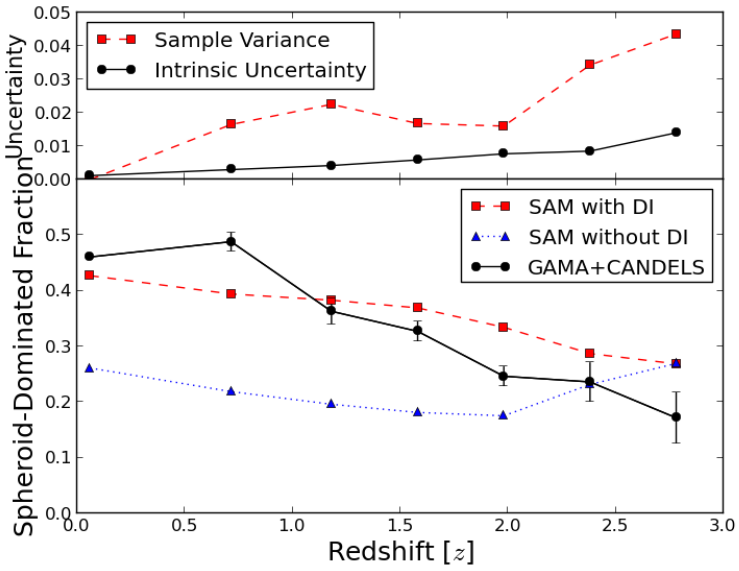

Figure 3.4: The evolution of the spheroid-dominated fraction of galaxies with redshift. Error bars are the $1-\sigma$ uncertainties due to sample variance and uncertainties in observed galaxy properties added in quadrature, as in Fig. 3.2. The separate contributions are plotted in the top panel. The model in which spheroids form only via mergers underproduces the fraction of spheroid dominated galaxies at $z \lesssim 2$ and does not reproduce the build-up of the spheroid-dominated population seen in the observations. The model with additional spheroid growth via disk instabilities (DI model) is qualitatively in fairly good agreement with observations (the two agreeing to within ~ 0.1 at all redshifts), though the predicted evolution in spheroid fraction is still a bit too shallow, with the model overpredicting spheroid-dominated galaxies at high redshift and underpredicting them at low redshift.

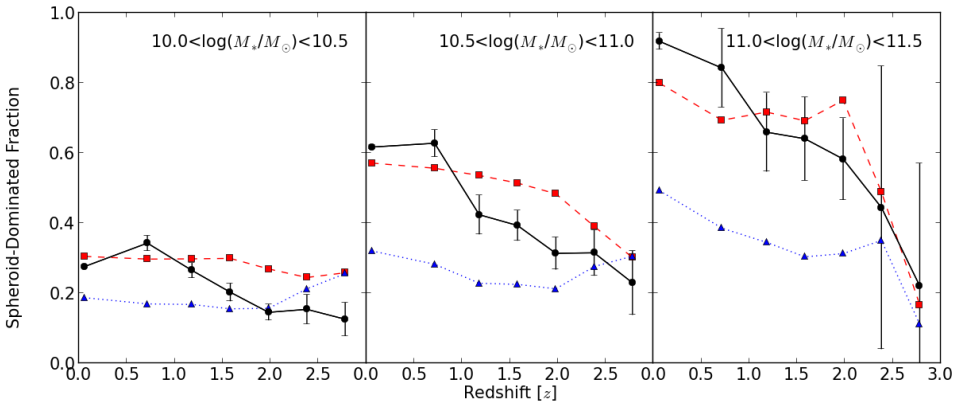

Figure 3.5: Same as Figure 3.3, but for the spheroid-dominated fraction.

by almost a factor of two at low redshift; within the uncertainties, the fractions do not disagree by more than 0.1 at any redshift. However, the evolution of the spheroid-dominated fraction in the model is somewhat shallower than in observations, so we overpredict the spheroid-dominated fraction at $z \gtrsim 1$ and underpredict it at $z \lesssim 1$.

We once again investigate the mass dependence in Figure 3.5. Again, as expected, at larger masses, the spheroid-dominated fraction is greater at almost all redshifts, and the spheroid-dominated fraction increases more rapidly with redshift for massive galaxies. There appears to be a population of massive, disk-dominated galaxies at high redshift in both the observations and the model. The behavior in all three mass bins is reminiscent of the overall behavior in Figure 3.4, except for the high mass, high redshift case. As in Figure 3.4, the disk instability brings the model mainly into better agreement, although in the two lower mass bins at $z \gtrsim 1$ the fractions can differ by as much as $0.15 - 0.2$, which is slightly more than for the overall population.

3.2.3 Comparison with Previous Results

We take a moment here to compare with previous work that has probed the evolution of the quiescent and spheroid-dominated fractions of galaxies. Brammer et al. (2011) and Muzzin et al.

(2013b) both examine the dependence of the quiescent fraction on stellar mass across a range of redshifts. Brammer et al. (2011) examine galaxies from the NEWFIRM Medium-Band Survey (NMBS) (van Dokkum et al. 2009; Whitaker et al. 2010) while Muzzin et al. (2013b) observe a sample of galaxies in the COSMOS/UltraVISTA field (Muzzin et al. 2013a) over a similar redshift range. Our observational results are in good agreement with both studies. The quiescent fraction is higher at larger stellar masses and lower redshifts and the quiescent fraction of high stellar mass galaxies increases more steeply with redshift than that of low mass galaxies. The quiescent fraction evolution of our high mass bin ($10^{11} M_{\odot} \lesssim M_{*} \lesssim 10^{11.5} M_{\odot}$) is in good agreement with Brammer et al. (2011); in both cases, the fraction increases from ~ 0.5 at $z \sim 2$ to ~ 0.8–0.9 at $z \sim 0.5$. Muzzin et al. (2013b) is in good agreement with our high mass quiescent fraction as well, but also investigates the quiescent fraction down to lower stellar mass so we can compare our lower mass bins. These also agree very well. For galaxies with $10^{10} M_{\odot} \lesssim M_{*} \lesssim 10^{10.5} M_{\odot}$, the quiescent fraction increases from ~ 0.2 at $z \sim 2$ to ~ 0.4 at $z \sim 0.2$–0.5. Meanwhile, the quiescent fraction of galaxies with $10^{10.5} M_{\odot} \lesssim M_{*} \lesssim 10^{11} M_{\odot}$ increases from ~ 0.4 at $z \sim 2$ to ~ 0.5–0.6 at $z \sim 0.2$–0.5.

In terms of spheroid-dominated fraction, Buitrago et al. (2013) examines the fraction of spheroid-dominated galaxies with masses $>10^{11} M_{\odot}$ from $z \sim 3$ to the present day. They cover this range by combining several different surveys: SDSS DR7 (Abazajian et al. 2009), POWIR/DEEP2 (Bundy et al. 2006; Conselice et al. 2007) and the GOODS NICMOS Survey (GNS;Conselice et al. 2011). They find a steady increase in the fraction of spheroid-dominated galaxies ($n > 2.5$) whereas, when the same mass cut is applied (as can be seen in the right panel of Figure 3.5), we predict a sharper increase in spheroid-dominated fraction from $\sim 20\%$ at $z \sim 2.5$ to $\sim 60\%$ at $z \sim 1.5$. Because of this, we predict a somewhat larger spheroid-dominated fraction than theirs between $z \sim 1$ and 2. Bruce et al. (2014) observe galaxies with $M_{*}>10^{11} M_{\odot}$ in the COSMOS and UDS fields from the CANDELS survey over the redshift range $1<z<3$. They

use bulge-disk decompositions to sort galaxies by B/T and compute the spheroid-dominated fraction. They find a spheroid-dominated fraction of ~ 0.6 for $z \sim 1.5$ and a fraction of ~ 0.45 for $z \sim 2.5$. This is in very good agreement with our results (again cutting at $10^{11} M_{\odot}$ and now defining spheroid-dominated as having B/T>0.5); we find a spheroid-dominated fraction of ~ 0.45 for $z \sim 2.5$ and ~ 0.6 for $z \sim 1.5$.

3.2.4 Dividing into Quadrants

Having divided the sSFR-Sérsic plane in halves, we now further divide the plane into four quadrants to examine the evolution of the populations in each one: SFDs, QSs, SFSs and QDs. Figure 3.6 shows an example of the division of galaxies into quadrants for both the model and the observations in the redshift bins $z \sim 0.06$, $0.5 < z < 1.0$ and $2.2 < z < 2.6$. The star formation division line is a least mean squares fit to the individual star formation thresholds for each galaxy in the redshift bin according to its stellar mass and specific redshift. Figures 3.7 and 3.8 show the distributions of Sérsic index and sSFR for our DI models and for the observations in the redshift bin $0.5 < z < 1.0$. In both cases, the distributions are similar, but not exactly the same. Our model has trouble reproducing the strong observed bimodality in both quantities; our disk instability creates many galaxies of intermediate Sérsic index. As we move toward lower redshift, the differences between the distributions of model and observed galaxies become more significant. We will return to this point in the discussion.

Figure 3.9 shows the evolution of the fraction of all galaxies in each quadrant with redshift for the DI model, the noDI model and the observations. We see here again the reason for the difference in how the quiescent and spheroid-dominated fractions change with the disk instability: the disk instability decreases the fraction of QDs while increasing the fraction of QSs, leaving the quiescent fraction relatively unchanged. The two spheroid-dominated populations, however, are both increased, leading to the large change in the overall spheroid-dominated fraction. The DI

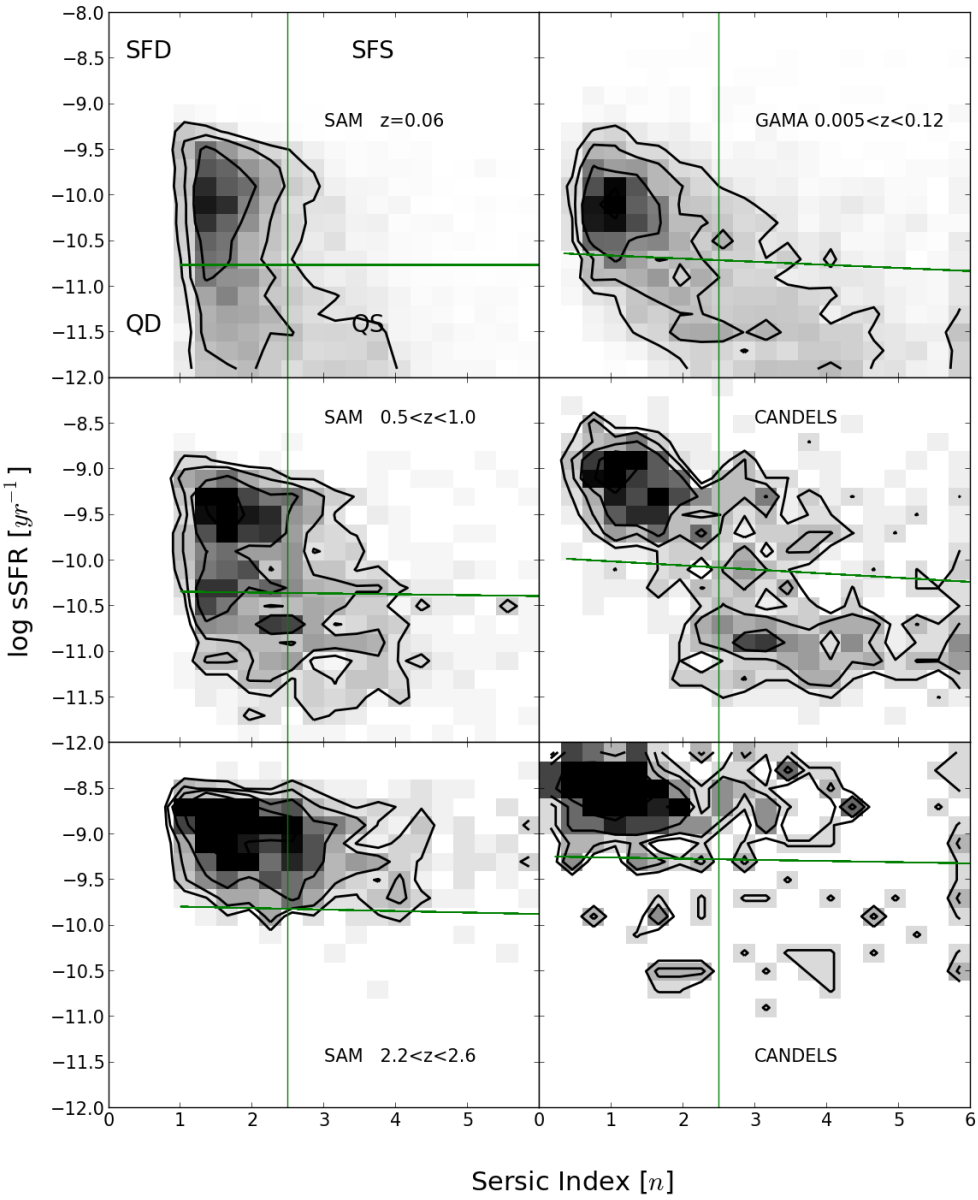

Figure 3.6: The distribution of galaxies in the sSFR-n plane in the redshift bins $z \sim 0.06$, $0.5 < z < 1.0$ and $2.2 < z < 2.6$. Left panel: Galaxies from the SAM. Right panel: Galaxies from GAMA and CANDELS. The greyscale shows the population density in the sSFR-n plane, with contours in black overplotted. The green lines are the dividing lines used in this work to identify the four "quadrants" (see text).

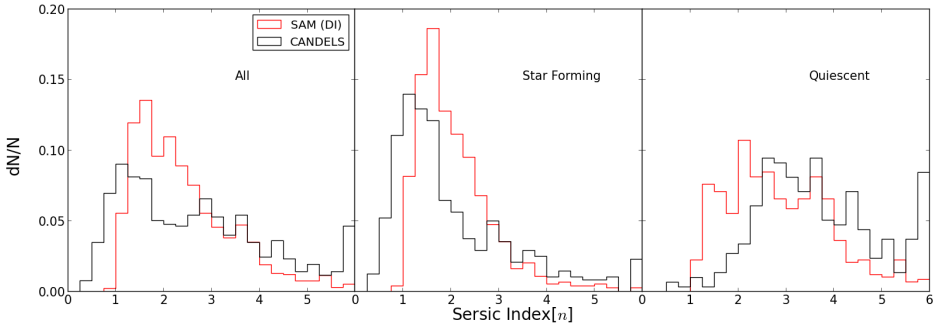

Figure 3.7: Distribution of Sérsic indices for model galaxies and CANDELS galaxies in the redshift bin 0.5<z<1.0. Left panel: All galaxies. Middle Panel: Star forming galaxies. Right panel: Quiescent galaxies.

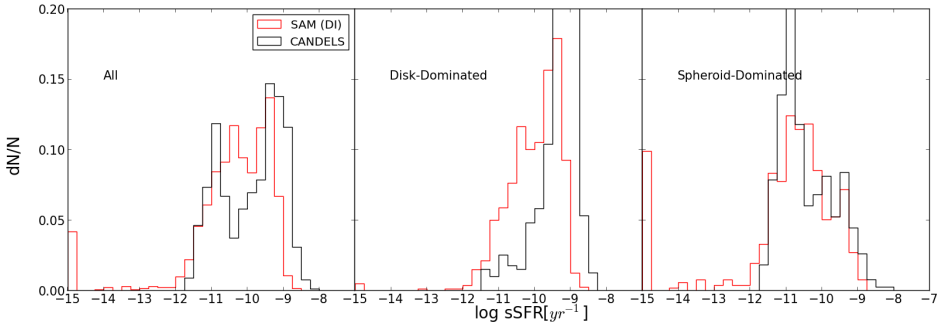

Figure 3.8: Same as previous figure, but now showing the distribution of sSFR. Left panel: All galaxies. Middle Panel: Disk-dominated galaxies. Right panel: Spheroid-dominated galaxies.

model reproduces the evolution of SFDs to within a few percent as their numbers dwindle due to various transformative processes. The noDI model predicts too many SFDs, the model and observed fractions differing by as much as 0.2. The DI model reproduces the observed fraction of QSs at $z \sim 0.1$, but slightly underproduces QSs at higher redshifts, although the fractions do not differ by more than ~ 0.1. The noDI model underproduces QSs at all redshifts, to an even larger degree. Both models underpredict the fraction of QDs at $z \gtrsim 1.5$ (which is again an extension of the overall issue seen in Figure 3.2) and overpredict them at $z \lesssim 1.5$. Once again, the disagreement is worse when the model with no disk instability is considered. While the models match the observed fraction of SFSs to a few percent at redshifts $\lesssim 1$, they predict too many at high redshift, in some cases by a factor of two. It becomes clear when comparing the two models that the disk instability is mostly responsible for the excess of SFSs that we predict at redshifts $z \sim 1.5 - 2.5$. At redshifts higher than this, mergers seem to become increasingly important as a channel for bulge growth. We expect some SFSs in the universe to have disturbed morphologies due to the process responsible for making them an SFS. It is possible that some of the CANDELS galaxies that would be classified as SFSs are dust obscured and are either not detected or not considered star forming, leading to an underestimate of the fraction of SFSs. While we do include the effect of dust extinction in our model, as well as make the same H-band magnitude cut as is used for CANDELS, the possibility remains that we are underestimating dust extinction. This would cause objects that are missed in CANDELS due to the H-band magnitude limit to be included in our model catalogs. It is not unreasonable that we would be underestimating the effects of dust in these objects in particular, as our prescription is based on an undisturbed disk geometry and does not account for the possibly heavily-obscured starbursting systems we are concerned with in the SFS quadrant.

We also note here that changing our cut in Sérsic index from $n = 2.5$ to $n = 2$, which still distinguishes systems with significant bulge components, does change our results somewhat

as the distribution of n in the models is different from the observed distribution (as seen in Figures 3.6 and 3.7). The spheroid-dominated fraction increases more for the DI model than for the observations, especially at higher redshifts. The noDI model is changed very little. When looking at different mass bins as in Figure 3.5, the change of the spheroid-dominated fraction of the DI model relative to the observations is more pronounced in the two lower mass bins than in the highest one. Figure 3.10 shows the evolution of the fraction of all galaxies in each quadrant for the morphology cut at $n = 2$. The DI model now underpredicts the fraction of SFDs by about 0.1-0.15 at all redshifts and overpredicts SFSs at high redshift by an even larger amount (as much as 0.4). The fraction of QSs matches the observational results well at $z \lesssim 1.5$ but still underpredicts these objects at higher redshifts. However, qualitatively the results are very similar, so we continue to use our $n = 2.5$ cut for the rest of this work.

Now, knowing both where our model succeeds and fails in matching the buildup of these populations, we can dig into the model to see which mechanisms are responsible for moving our simulated galaxies in the sSFR-n plane.

3.3 Discussion

The SAM can provide us with details about galaxy formation histories which we cannot glean directly from observations; we now examine the statistics of events that drive galaxy tranformation and quenching (mergers and disk instabilities) in our models, and provide representative examples of how individual galaxies trace out their histories in the sSFR-n plane.

Figure 3.11 shows density contours for galaxies from the SAM ($0.5 < z < 1.0$) in the sSFR-n plane. Overlaid arrows show how different physical processes might move galaxies in this diagram. SFDs may merge with each other or suffer disk instabilities to form bulge-dominated galaxies which then undergo gas depletion by AGN feedback, leading to quenching of star formation. In

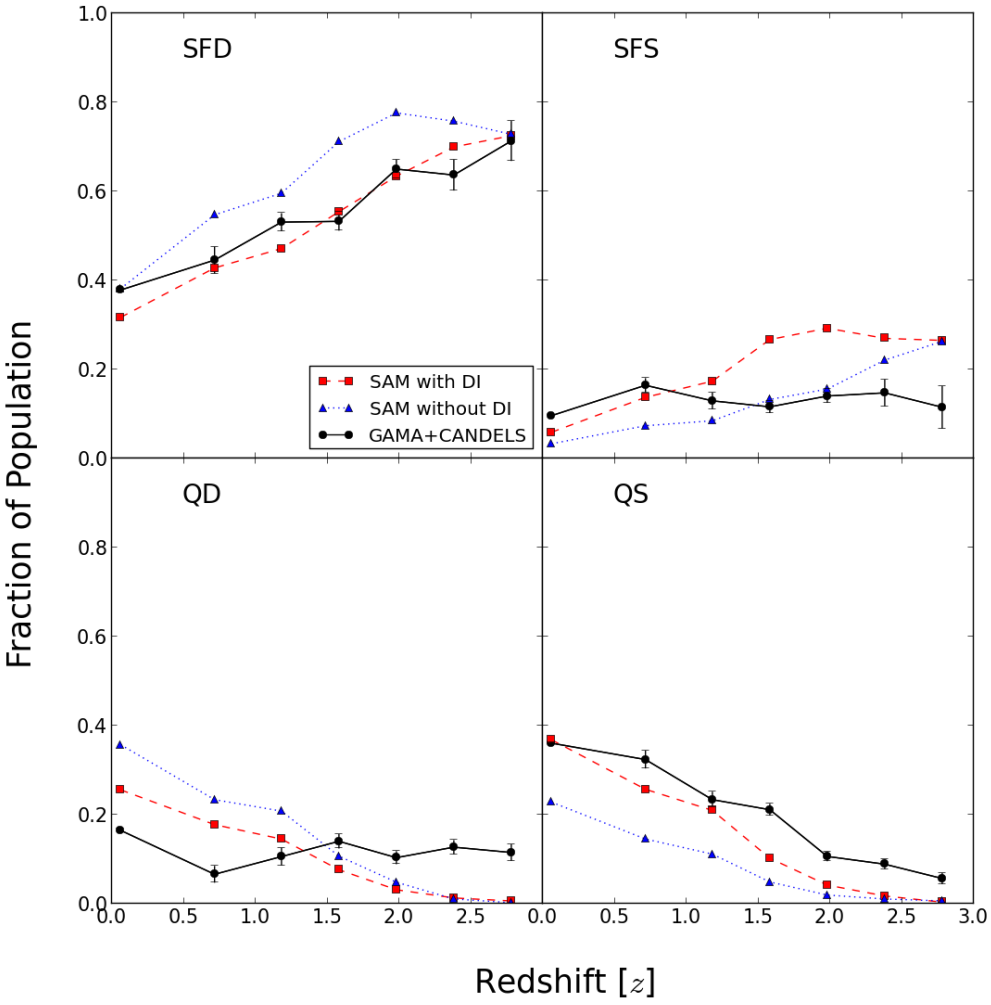

Figure 3.9: The evolution of the fraction of galaxies in each quadrant of the sSFR-Sérsic plane with redshift. Top left: Star forming disk-dominated galaxies (SFD). Top right: Star forming spheroid-dominated galaxies (SFS). Bottom left: Quiescent disk-dominated galaxies (QD). Bottom right: Quiescent spheroid-dominated galaxies (QS). Our models qualitatively reproduce the trends of a decreasing fraction of SFD galaxies and the increasing fraction of QS galaxies with cosmic time, with the DI model in general producing better agreement with the observations. Our models do less well at reproducing the observed trends for SFS and QD, predicting mild decrease and increase in these populations, respectively, with cosmic time, while in the observations their fractions are nearly constant from $3 \gtrsim z \gtrsim 0.1$.

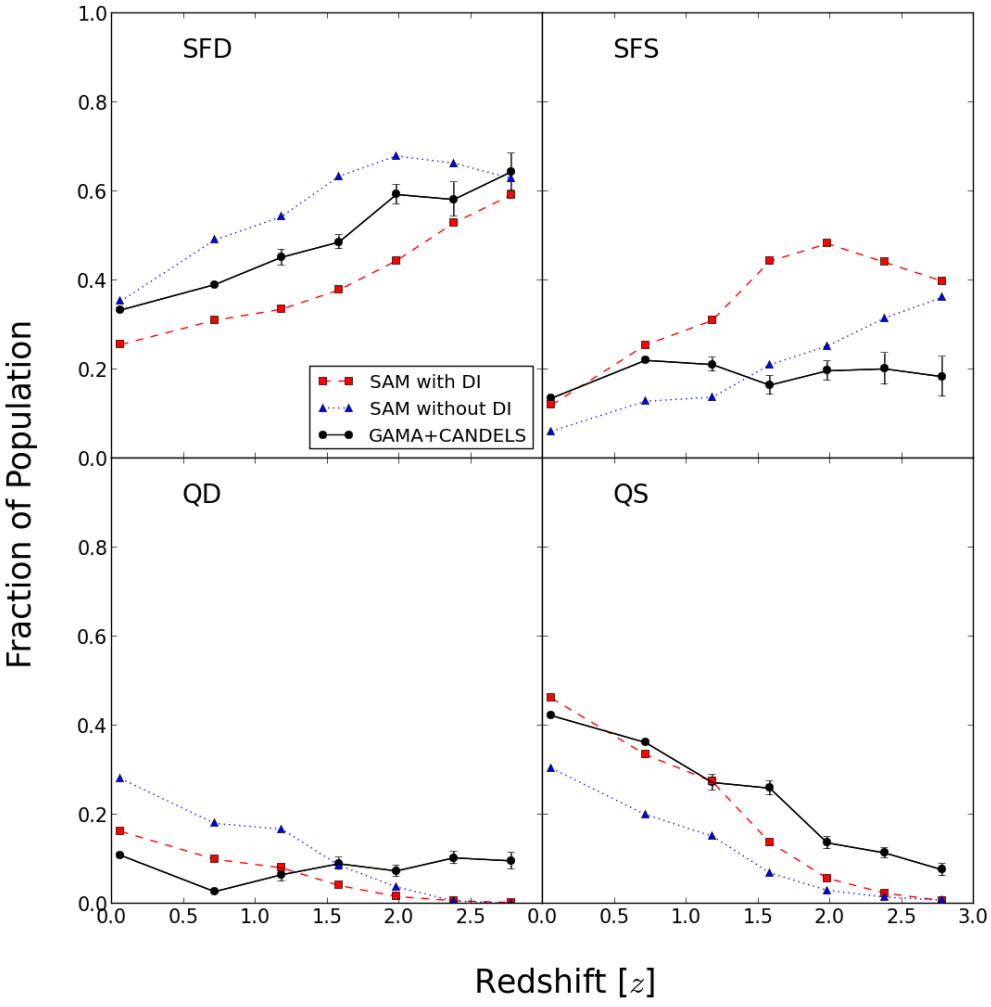

Figure 3.10: Same as Figure 3.9, but now with a morphology cut at $n = 2$.

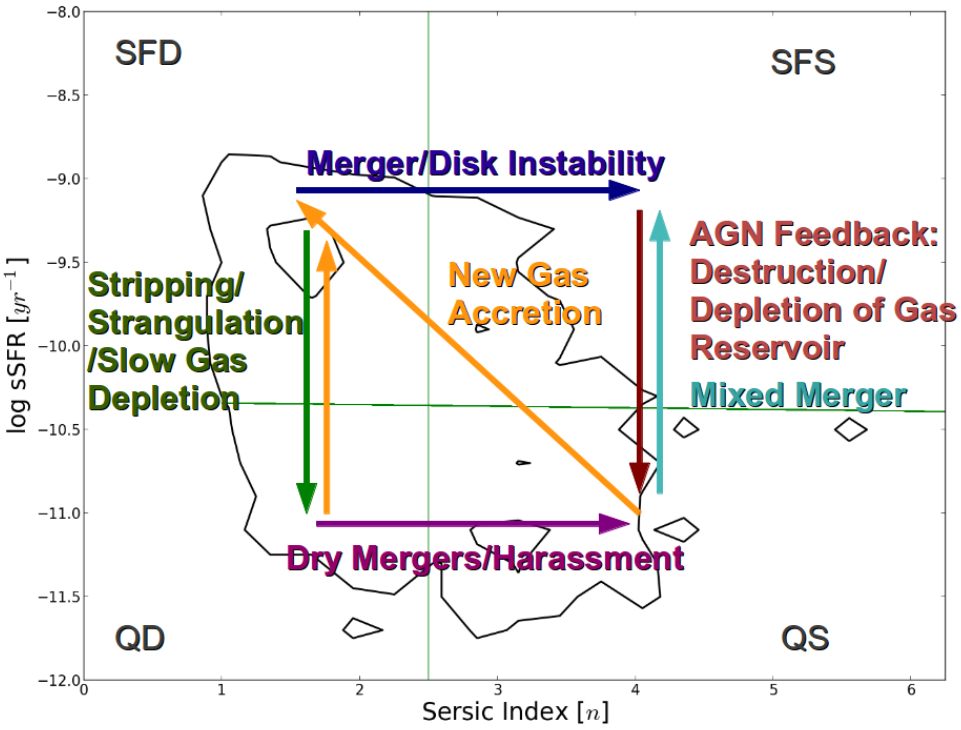

Figure 3.11: Schematic representation of how different physical processes might cause galaxies to migrate in the sSFR-n plane. The density distribution of galaxies in the SAM (DI model) for $0.5 < z < 1.0$ is shown with contours.

the SAM this occurs over relatively short time scales of several hundred million years. Meanwhile, other SFDs may passively evolve, depleting their gas reservoirs over much longer time scales of a Gyr or more, eventually becoming QDs, which may then experience dry (gas-poor) mergers which puff them up and form QSs. Quiescent galaxies may then accrete new gas which allows regrowth of a disk component. We now examine the importance of some of these processes in the SAM in a bit more detail.

3.3.1 How Recently Have Different Types Been Disturbed?

We would like to know how galaxies in different quadrants in the sSFR-Sérsic plane are formed or evolve to their current state and with the SAM we can directly measure the time since traumatic events such as mergers and disk instabilities. In the top left panel of Figure 3.12, we look at the fraction of $>10^{10} M_{\odot}$ galaxies of each type which have undergone a recent merger, with "recently" being defined as within three dynamical times (where $t_{\rm dyn} = 2\pi r_{\rm disk}/v_{\rm disk}$). We see that SFSs are more likely to have experienced a recent merger at all redshifts, while very few QDs have undergone a recent merger. SFDs and QSs fall in between. All types of galaxies are more likely to have experienced a recent merger at higher redshift. In the top right panel, we see that almost no galaxies at any redshift have avoided ever having a merger in their lifetime.

In the middle row, we restrict our attention to major mergers with a mass ratio >1:3 (the mass used to calculate this ratio is the combined baryonic (cold gas+stellar) and dark matter mass within 2 halo scale radii; see S08) and see that basically no QDs have undergone recent major mergers, while the fraction of SFDs with recent major mergers is only slightly higher (no more than $\sim 5\%$). This is because it is very unlikely to experience a major merger and still retain enough of a disk to be considered disk-dominated within a dynamical time of the merger. QSs are slightly more likely to have undergone a recent major merger than SFDs, while 65-80% (depending on redshift) have undergone a non-recent major merger. This is simply because very

soon after a major merger, the merger-triggered starburst would cause the spheroid-dominated galaxy to be classified as an SFS. After some time has passed and star formation has been quenched, it would be classified as a QS. For this same reason, SFSs are the least likely to have undergone a non-recent major merger; if the major merger wasn't recent, they're unlikely to still be star forming. SFSs are still most likely to have had a recent major merger and that likelihood increases somewhat towards higher redshift. The disk-dominated classes are actually more likely to have had a non-recent major merger than never to have had one at all, after which they must have regrown a substantial disk component. Unsurprisingly, the disk-dominated populations are more likely to have never had a major merger than the spheroid-dominated populations.

In the bottom row, we see that the fraction of all types which have undergone a recent disk instability peaks at $z \sim 1.5$. We note that this is in qualitative agreement with the peak of the clumpy fraction of galaxies (in the mass range $9.8<\log(M_*/M_\odot)<10.6$) found in Guo et al. (2015). We cannot make a quantitative comparison with these results as we have no way to estimate clumpiness in our models, but clumpy galaxies are expected to be associated with minor mergers and disk instabilities (Dekel et al. 2009).

Our star forming classes are more likely than our quiescent classes to have undergone a recent disk instability, but the fraction of SFSs plummets towards higher redshift, signaling the fact that mergers seem to be the dominant bulge-growing channel at high redshift, with disk instabilities increasing in importance as mergers become less frequent, as has been speculated in previous works (Parry et al. 2009; De Lucia et al. 2011; Fontanot et al. 2012). QSs are much more likely to have never had a disk instability, or to have had one longer ago (since it has likely been a while since they had a disk). QDs are just as likely to have had a disk instability recently, not recently, or not at all, suggesting that disk instabilities don't play a huge role in their evolution. Finally, a significant fraction of all types (40-60%) have never experienced a disk instability. This fraction increases steeply towards high redshift, presumably because the merger rate increases

and it is less likely for a galaxy to go undisturbed long enough to develop an instability on its own.

We note that there is a large amount of uncertainty in the highest redshift bin for our quiescent classes. There are very few galaxies classified as quiescent and so we suffer from small number statistics in that bin.

3.3.2 Individual Galaxy Histories

To illustrate how individual galaxies evolve, we now inspect the evolutionary tracks of four galaxies selected from the SAM, which end up in the four different quadrants of the sSFR-n plane at $z = 0$. Here we use bulge-to-total mass ratio as our proxy for morphology, since the tracks in the sSFR-morphology plane are much easier to see this way (and because the results are very similar: see Appendix B). Figure 3.13 shows the evolutionary path of a galaxy with a fairly quiet history that ends up as an SFD. This galaxy has a mass of $\sim 10^{10.8} M_{\odot}$ at $z = 0$. The top panel is its track in the sSFR-morphology plane, color coded by the age of the universe. The bottom and middle panels are the evolution with time of the morphology and sSFR respectively. We see that this galaxy has a few mergers early on after which its evolution is entirely due to accretion of new material, allowing it to continue forming stars. The decrease in B/T following the merger events is due to the regrowth of a disk component.

Figure 3.14 is a somewhat striking example of a galaxy being pummeled repeatedly by mergers until it is almost entirely bulge dominated, after which it finds itself unable to form more stars because of the black hole it has grown over the course of its traumatic history; the black hole is now keeping any remaining gas too hot for star formation through radio-mode feedback. This can also be effected by one (or more) big major merger(s). In both cases, it is likely that the system will make an appearance as an SFS for a time before quickly evolving into the QS quadrant. Once a galaxy falls into this quadrant, it tends to stay there, except for very rarely when it collides

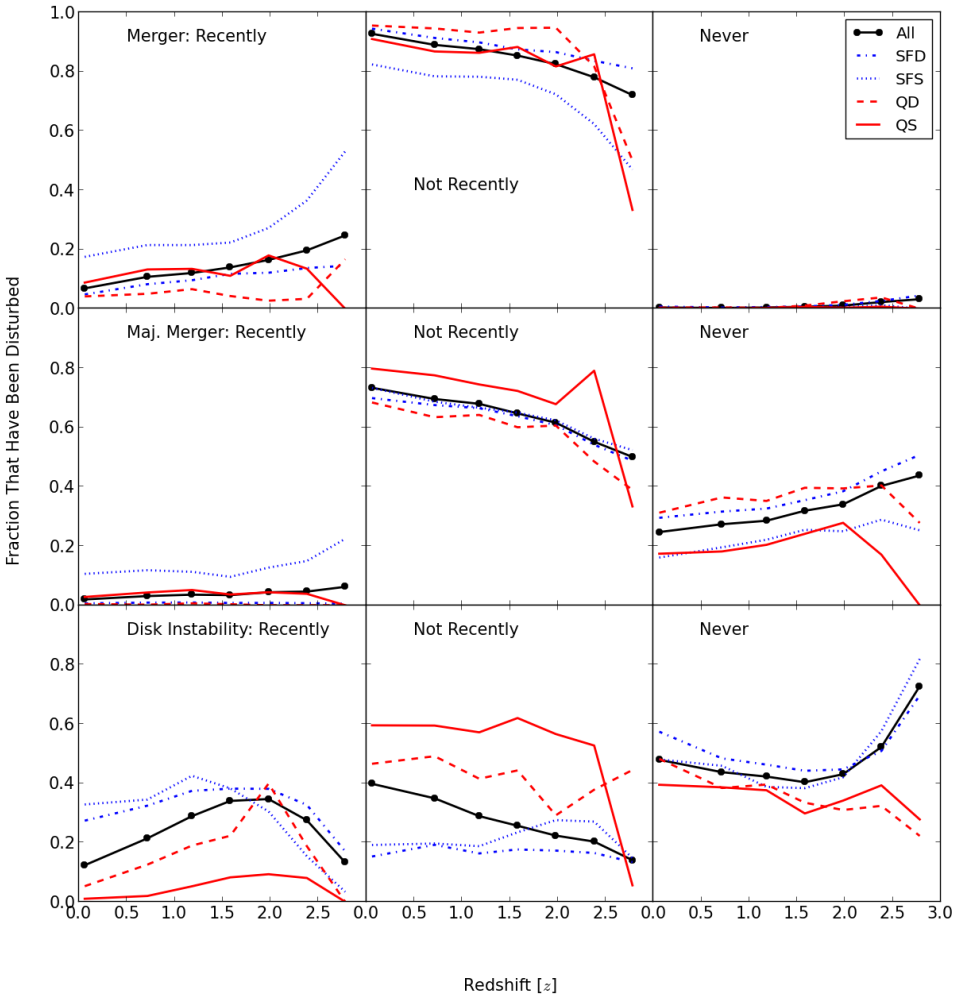

Figure 3.12: Top row: Left panel: Fraction of model galaxies in each quadrant which have undergone a recent ($<3t_{\rm dyn}$) merger with mass ratio >1:10. Middle panel: Fraction which have undergone a merger on a timescale $>3t_{\rm dyn}$. Right panel: Fraction which have never undergone a merger. Middle row: Same as top row, but for major mergers (>1:3). Bottom Row: Same as top and middle rows, but for disk instabilities. The fraction of galaxies that have suffered a recent merger declines with cosmic time from $z \sim 2$ to the present, while the fraction that have experienced a recent disk instability peaks at around $z \sim 1.5$–2.

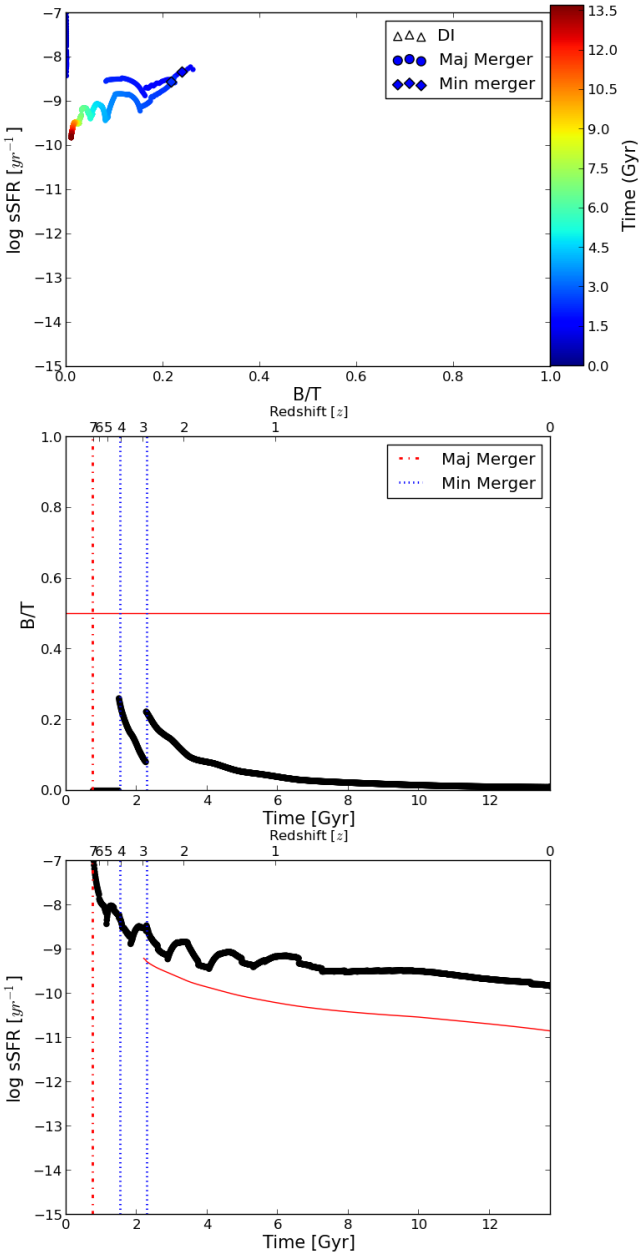

Figure 3.13: Evolution of sSFR and B/T mass ratio for a galaxy which is classified as a star forming disk-dominated galaxy with a mass of $\sim 10^{10.8} M_{\odot}$ at $z = 0$. Top panel: Evolutionary track in the sSFR-B/T plane, color coded by age of the universe. Minor mergers (<1:3), major mergers (>1:3) and DIs are indicated by diamonds, circles and triangles, respectively. Middle panel: Evolution of B/T mass ratio with time. The red dash-dotted line indicates a major merger and the blue dotted lines indicate minor mergers. The solid red line is our division between disk-dominated and spheroid-dominated. Bottom panel: Evolution of sSFR with time. The solid red line is our division between star forming and quiescent. The galaxy remains disk dominated, due to its quiet accretion history, and the SFR gradually declines due to the declining cosmological accretion rate.

with a gas-rich galaxy, at which point it might briefly return to the SFS quadrant before quickly using up all of its new gas and falling back down again. This can be seen in the very short spikes of star formation accompanying the last two mergers in the bottom panel. This galaxy is far more massive than the SFD above, with a stellar mass of $\sim 10^{11.8} M_{\odot}$, which is due to all of the merger events it has experienced and is consistent with many of the most massive galaxies in the universe being QSs. We note that the QS population in the models is much more concentrated toward lower Sérsic index than that from the observations, as can be seen in Figure 3.6. Our model is still not producing enough very bulge-dominated galaxies. As the most massive bulges are believed to be the result of mergers, this may indicate that we are still underestimating the role of merging.

Figure 3.15 shows the evolution of a galaxy that ends up as an SFS. Its final mass is $\sim 10^{11} M_{\odot}$, which is more massive than the SFD considered above because of its more active merger history. We see here what a major merger can do in terms of bulge growth: the first major merger this galaxy experiences gives it a substantial bulge component. After each bulge growth episode, the galaxy begins to regrow a disk, causing B/T to decrease steadily. This is the case for many galaxies in the SAM, as long as they have the gas to form new stars or continue to accrete new gas from the IGM. Changes in sSFR between merger events for this system are largely due to the interplay between "normal" star formation and new gas accretion. If this galaxy had not undergone a major merger recently, it would not have been considered an SFS, as the steady regrowth of its disk would have caused it to be classified as disk-dominated instead.

The SFS quadrant is more of a way station than a destination in galaxy evolution, with galaxies either quickly evolving back towards the SFD quadrant by regrowing their disks, or evolving downwards into the QS quadrant as they quench (this system is very close to being classified as a QS). This can be seen in Figure 3.6, where the SFS quadrant appears more to be made up of the tails of populations in the SFD and QS quadrants than to be a distinct

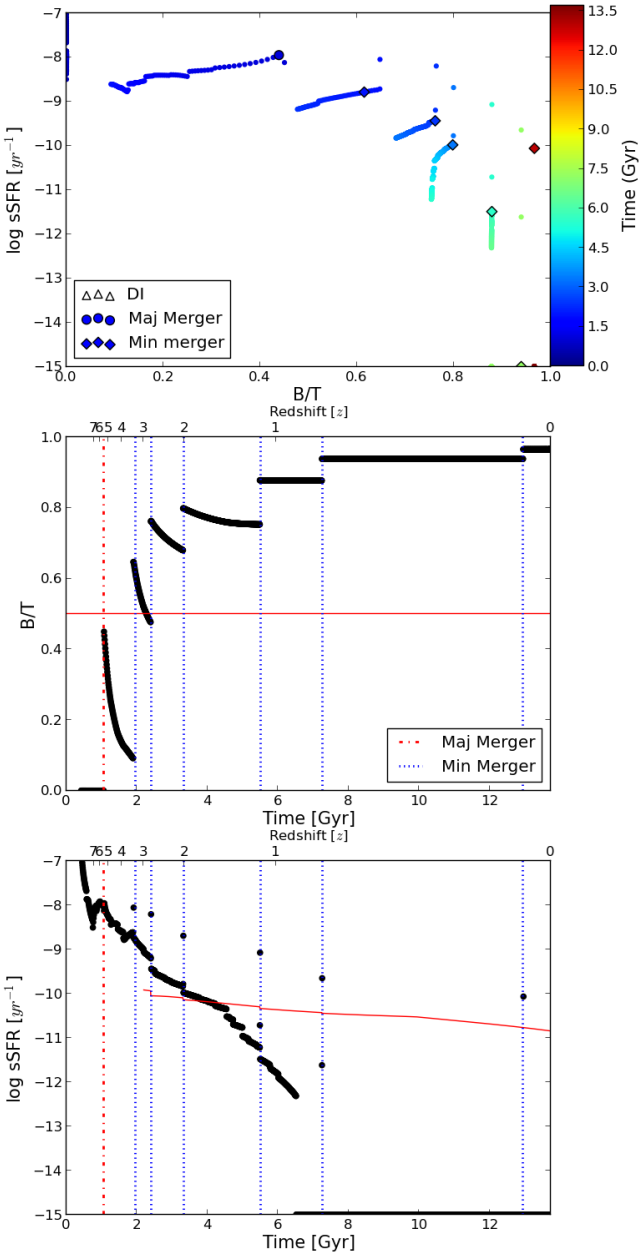

Figure 3.14: Same as previous figure, but for a galaxy which is classified as a quiescent spheroid-dominated galaxy at $z = 0$ with a mass of $\sim 10^{11.8} M_{\odot}$. Although this galaxy has suffered one major merger at very high redshift ($z = 5.5$), the build-up of its dominant spheroid occurs through a sequence of multiple minor mergers. This is quite typical. The build-up of the spheroid is accompanied by growth of the SMBH, leading to strong radio-mode feedback that shuts down cooling and, eventually, quenching of star formation.

population. This is something upon which the models and observations appear to agree, and is an explanation for why the evolution of the overall spheroid-dominated fraction is less steep than for the quiescent fraction: there is high turnover in the SFS quadrant so the fraction in that state is relatively constant, meaning that the buildup of the spheroid-dominated population relies mainly on the steady buildup of QSs. Meanwhile the quiescent fraction is built up by the steady growth of both the QS and QD populations. This interpretation seems to be corroborated by the CANDELS-based study of Rizer et al. (in prep.), in which visual morphological classifications are used. They find that while their QS population builds up steadily, their SFS population remains relatively constant, suggesting that bulge growth is leading to star formation quenching in many cases.

Figure 3.16 represents one possible path to becoming a quiescent disk-dominated galaxy. Some quiescent disks in our model are galaxies with quiet histories such as the one seen in Figure 3.13 above, but which have run out of gas (perhaps because they are more massive and have a harder time accreting new material) or can't form stars with the gas they do have (see below for a brief discussion). However, many of our disk-dominated quiescent galaxies really aren't very disk-dominated but in fact are systems which have had a somewhat more eventful history similar to that of a QS. These end up as QDs by one of two ways. In the first case, the events which lead to star formation quenching and bulge formation do not form enough of a bulge for the system to be considered spheroid-dominated. However, the galaxy still falls into the QD quadrant in the same way we expect SFSs to migrate sometimes to the QS quadrant after a traumatic event. In the second case, the galaxy *does* become an SFS, but retains gas to regrow a disk sufficient to be considered disk-dominated before falling into quiescence.

We see a mixture of these two fates in Figure 3.16; while its bulge growth episode was not enough to make it spheroid-dominated, the event which caused the bulge growth was enough to cut this galaxy off from new gas, causing it to become quiescent. We also see substantial

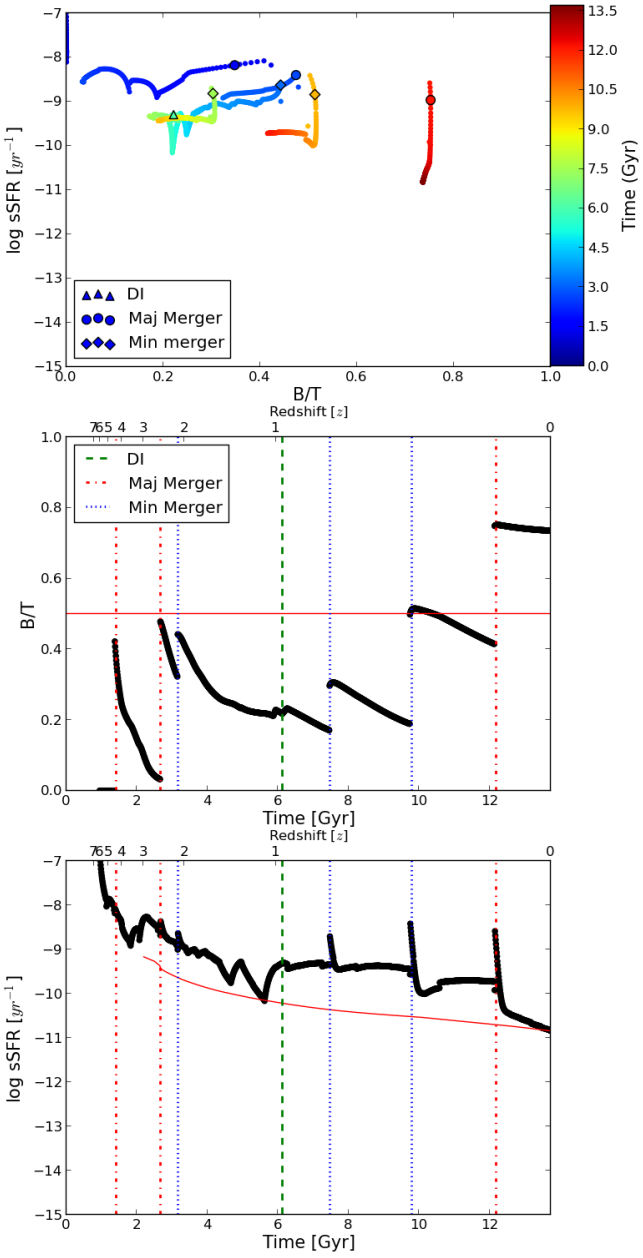

Figure 3.15: Same as previous figure, but for a galaxy which is classified as a star forming spheroid-dominated galaxy at $z = 0$ with a stellar mass of $\sim 10^{11} M_{\odot}$. This galaxy has had an extremely active history, with multiple major mergers, several minor mergers, and a disk instability. A recent major merger triggered a strong burst of star formation. This galaxy would probably appear morphologically disturbed.

disk growth in its decreasing B/T. This combination of both scenarios causes this galaxy to be somewhat rare: a QD which is both very disk-dominated and very quiescent. This galaxy is very massive at $z = 0$ with a stellar mass of $\sim 10^{11.7} M_{\odot}$. QDs are often quite massive due either to their merger histories or prolonged star formation which has led the galaxy to be unable to accrete new gas due to virial shock heating. In general, the average B/T for QDs is only slightly higher than for SFDs. However, as QDs with lower star formation rates are considered, the average B/T becomes larger, as these systems are the result of the QS-like paths described above. The very disk-dominated QDs are likely to have relatively higher sSFRs. This does bring up a larger point about dividing lines in general: some galaxies which fall below our dividing line are still forming stars, albeit at a slower rate than the majority of galaxies of their mass. They are "quenched" in the sense that their star formation rate is lower than expected, but they are not truly "quiescent" as is the case for some of our galaxies, which have had their star formation completely turned off. There is also the possibility, mentioned above, that some of our quiescent galaxies might begin to form stars again due to a wet merger or new gas accretion. In the case of a wet merger, this is likely to be short-lived, but in the case of new gas accretion, it can lead to a whole new life for a galaxy. Having clarified that, however, we believe this is happening in both the models and the observations, so it should not bias our results.

It appears that the QDs are much like the SFSs in that the population is a combination of tails of the SFD and QS populations. Curiously, the gas fractions of QDs in the SAMs are *not* systematically smaller than those of SFDs of the same mass. It appears that the quenching leading to very disk-dominated QDs has two possible origins, as mentioned above: a low gas accretion rate, or an extended low surface-density gas disk which is inefficient at making stars. In the models considered here, only gas that is above a critical surface density is allowed to participate in star formation; galaxies with larger than average angular momentum form more extended disks, which have a larger fraction of their gas sitting below this critical surface density.

There is observational evidence in the local universe for these gas rich but relatively quiescent disks (Lemonias et al. 2014; Schiminovich et al. 2010). Thus while the SFSs may be understood as a transient population, a step in the path from SFD to QS, it seems that QDs may be a static population.

In addition, our model QDs on average have smaller stellar and black hole masses than our QSs. They are also more likely to be satellites than QSs. In our lowest redshift bin, about 75% of model QSs are central galaxies, while only 50% of QDs are. The *very* disk-dominated QDs ($B/T < 0.1$) don't exist in our model before $z \sim 2$. When compared with the rest of the QDs, they have even smaller black hole masses, as they likely have not undergone any events which would have triggered AGN feeding. They are also even more likely to be satellites; in our lowest redshift bin, only 25% of very disk-dominated QDs are central galaxies. We note that the likelihood of being a satellite galaxy is not the only reason that QDs tend to have smaller stellar and black hole masses; this trend is observed even when only central galaxies are considered.

What these analyses and evolutionary tracks show is that the transformative processes which affect galaxies take them all over the map (and the sSFR-n plane). It is likely too simplistic to tell a simple story about two star forming disk galaxies colliding or one of them buckling under its own weight and triggering feedback which produces a nice, dead elliptical galaxy. These processes (mergers, disk instabilities, accretion of new gas) likely work together, sometimes in tandem and sometimes at cross purposes. It appears that a complex history with multiple transformative events is the norm rather than the exception and galaxy histories don't necessarily look like the arrows in Figure 3.11.

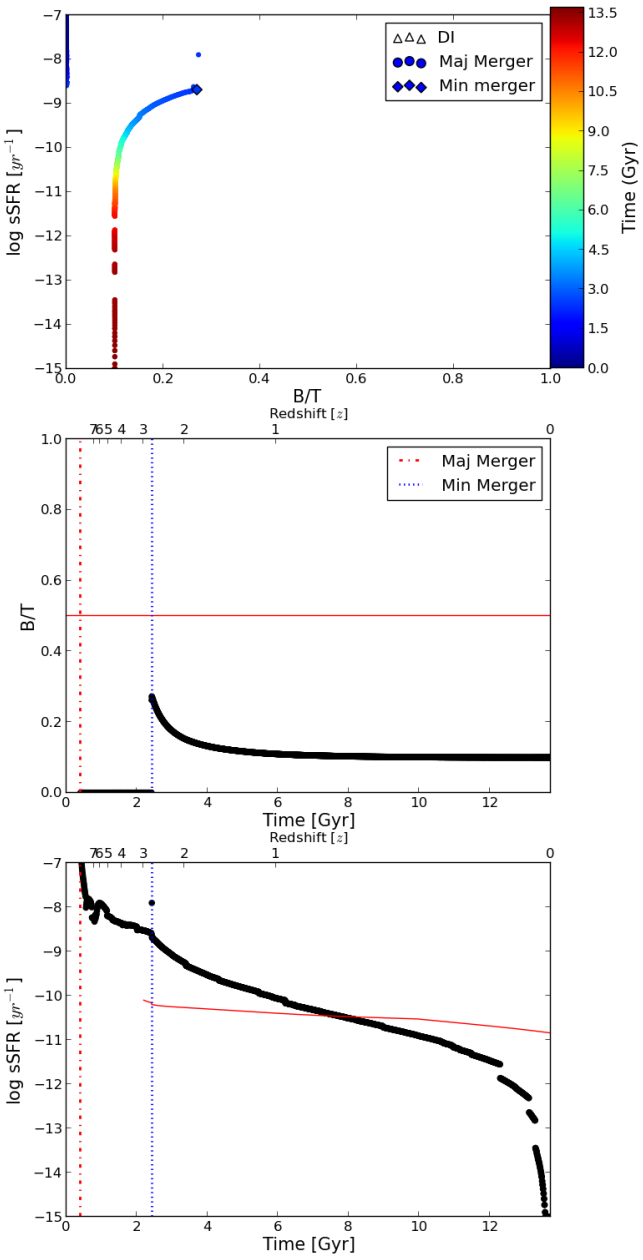

Figure 3.16: Same as previous figure, but for a galaxy which is classified as a quiescent disk-dominated galaxy at $z = 0$ with a stellar mass of $\sim 10^{11.7} M_{\odot}$.

3.3.3 How Might a Different Implementation of Disk Instability Change Our Results?

As mentioned in Chapter 2, our treatment of disk instabilities is based on rather dated simulations of isolated disk galaxies which are not in a cosmological context, and may not capture all of the relevant physics. Some of the questions associated with disk instabilities include: 1) What is the most relevant criterion for determining the onset of a disk instability? 2) What happens to the gas and stars in the disk when it becomes unstable? 3) How efficiently do disk instabilities feed a nuclear black hole?

As an aside, we have so far elided over a possibly important distinction. There are two kinds of physical mechanisms that are commonly referred to as "disk instabilities" in the literature, although in one case this is something of a misnomer, as we explain below. In "violent disk instabilities" (VDI; Dekel et al. 2009), the disk becomes globally unstable, leading to the formation of clumps of stars and gas, which may migrate to the center of the galaxy, building the spheroid. As the giant clumps orbit within the disk, even if they disrupt before reaching the center, they may drive inflows of gas into the galaxy nucleus, via the same sort of physics as merger-induced nuclear inflows, again leading to growth of the spheroid through in situ star formation, and feeding of the black hole (Bournaud et al. 2011). The second kind of "disk instability" involves the secular transfer of angular momentum outwards, and mass inwards, again leading to the building of a central compact and dynamically hot structure, and is accompanied by the formation of a bar (Kormendy & Kennicutt 2004). The term "instability" is a misnomer here, as the disk essentially remains in dynamical equilibrium. The relatively crude morphological statistics used in this analysis are not able to distinguish between edge-on bars and bulges, so some of the 'spheroids' we count in the observations may actually be bars. In addition, the nuclear structures that are formed via this secular process do not have the same properties as

"classical" bulges, and are sometimes called "pseudobulges". See Kormendy & Kennicutt (2004) for a detailed discussion of the differences between classical bulges and pseudobulges; the most germane for our purposes here is that pseudobulges do not obey the same scaling relationships with the SMBH mass as classical bulges (Kormendy & Ho 2013), suggesting that black hole feeding and/or feedback may operate differently.

One major limitation of our approach is that we based the disk instability criterion on the properties of the stellar disk only, and only stars are moved from the disk to the spheroid when the disk is deemed unstable. This is not what is seen in modern cosmological hydrodynamic simulations, in which VDI are ubiquitous at high redshift (Ceverino et al. 2010; Mandelker et al. 2014), and as mentioned above are associated with strong nuclear inflows of gas as well as stars. In addition, VDI can lead to significant quenching even in the absence of associated AGN feedback (Gammie 2001; Dekel & Burkert 2014; Forbes et al. 2014), which is not accounted for in our current models. Perhaps this could lead to a higher fraction of quiescent galaxies at high redshift, in accord with observations. Additional complications are the possible stablizing effects of a pre-existing bulge or central mass concentration, and possible triggering of disk instabilities by minor mergers.

P14 attempted to model a scenario closer to the modern VDI picture with their **"Stars+Gas DI"** model. They found that the results were very similar to the **"Stars DI"** model which is why we consider only that model here (this implementation of DI is similar to the one that is most commonly applied in other SAMs in the literature). In addition, the P14 **"Stars+Gas DI"** model is still somewhat arbitrary and simplified.

3.3.4 Other Possible Model Improvements

Aside from our treatment of disk instabilities, there are several ways in which we could improve our model in order to better capture what we believe is occuring in real galaxies. Our

implementation of satellite stripping does not account for any change in morphology of satellites and many which are not destroyed are stripped of their gas and remain disk dominated. Only central galaxies are supplied with new gas in our accretion and cooling model, so this may artificially increase our fraction of quiescent disk-dominated galaxies. While this effect dominates at low stellar masses and should not be as important in the mass range we consider in this work, $M_* > 10^{10} M_\odot$, it is worth noting (and is the reason we neglected satellites when determining the typical model main sequence star formation rate above). We do point out that the same analysis done for the model excluding satellite galaxies leads to very similar results; the largest difference is in the low redshift QD fraction, which in the lowest bin decreases from $\sim 25\%$ to $\sim 17 - 18\%$.

While our merger prescription is based on numerical hydrodynamic simulations of binary mergers (Hopkins et al. 2009b), we treat all mergers as discrete events, while in the real universe there may be a complex interplay between merger events if the galaxy has not had time to relax between them (Moster et al. 2014). This could have an effect on both the star formation rates and the morphologies of our post-merger remnants, especially of those that have had somewhat active merger histories.

In addition, in our current models galaxies are primarily kept quiescent by the "maintenance mode" type of AGN feedback, which becomes important only at relatively late times. Winds driven by radiatively efficient accretion ("bright mode" feedback) are assumed to be able to remove cold gas from the ISM but have no effect on the hot gas surrounding galaxies. However, recent cosmological simulations have shown that momentum-driven winds associated with bright mode accretion actually modify the hot gas profile and significantly retard cooling over long timescales (Choi et al. 2014, 2015) (also see Chapter 5 of this thesis). Including this physics might also help us to produce more quenched galaxies at high redshift, and could also suppress the re-formation of disks via cooling.

Finally, there is the issue of putting the models and observations on the same footing when it comes to quantitative comparison of morphologies; we would like to improve the way we assign morphology to our model galaxies, namely by using the masses (or luminosities) and sizes of our disk and bulge components to generate mock images which can then be processed like real observations (including noise, point-spread function, etc) and assigned morphological classifications. This way each galaxy would have its profile measured separately and other effects such as inclination angle could be taken into account. In the next Chapter, as described in Chapter 2, we move slightly closer to equal footing, but still have not generated mock images. Comparing the observed and predicted fractions of morphologically disturbed galaxies would also be interesting, but obviously requires us to be able to quantify this in the SAM in a way that can be compared with observations. This may be possible using our merger statistics in combination with a library of numerical simulations, as in Lotz et al. (2011); see also recent work by Snyder et al. (2015a).

3.4 Summary and Conclusions

We have studied the coevolution of star formation rate and morphology from $z \sim 3$ to the present by examining the buildup of galaxies in the four quadrants of the sSFR versus Sérsic index (n) plane. We have compared galaxies with stellar mass $>10^{10} M_{\odot}$ from the "Santa Cruz" semi-analytic model outlined in S08, S12 and P14 with galaxies observed as part of the GAMA and CANDELS surveys. Our conclusions are as follows:

- Our models qualitatively reproduce the increasing fraction of quiescent galaxies since $z \sim 2$ seen in observations, and produce excellent quantitative agreement with observations at $z \lesssim 1.2$. At higher redshift, the models underproduce the fraction of quiescent galaxies relative to observations.

- Our model in which spheroids are built solely through mergers (noDI) predicts an evolution in the fraction of spheroid dominated galaxies that is much too mild compared with observations. This model also underproduces spheroid-dominated galaxies at $z \lesssim 2$ compared with observations. Adding a channel for bulge growth via disk instabilities (DI model) leads to much better agreement with the observed evolution of the spheroid-dominated fraction, although still produces slightly flatter evolution than observed.

- The quiescent fraction is largely unaffected by the inclusion of disk instabilities, with changes <10%. We note, however, that our current disk instability model may be underestimating the change in quiescent fraction, especially at high redshift.

- Our models further qualitatively reproduce the observed evolutionary behavior of four classes of galaxies defined by both star formation activity and morphology: star forming disk-dominated, quiescent spheroid-dominated, star forming spheroid-dominated and quiescent disk-dominated. In both the observations and in our models, the fraction of star forming disks decreases over time while the fraction of quiescent spheroids increases. In the observations, the fractions of both star forming spheroids and quiescent disks remain nearly constant from $z \sim 3$–0. Models predict a stronger decrease in star forming spheroids and a stronger increase in quiescent disks with redshift than is seen in the observations, but the predicted fractions are not off from the observed fractions by more than ~ 0.2 and in most cases are off by less.

- In our models, star forming-disk dominated galaxies are galaxies which have had very quiet histories. They have avoided major mergers and if they have experienced any merger or disk instability activity, they have recovered by accreting new gas and regrowing a disk.

- Again in our models, quiescent spheroid-dominated galaxies are likely to have either undergone at least one extreme major merger or many smaller mergers or disk instabilities.

In either case they have built up a substantial bulge component and AGN feedback has made it impossible for them to accrete significant amounts of new gas, eventually leading to cessation of star formation.

- Star forming spheroid-dominated galaxies seem to be a short-lived population. Truly spheroid-dominated star forming galaxies are indicators of a recent trauma, as they are still experiencing a post-trauma starburst. At this point, they can regrow a disk with their remaining gas reservoir or through the accretion of new gas. In the absence of new gas, they can deplete their gas reservoirs and become quiescent.

- Quiescent disk-dominated galaxies are a combination of two populations: disk-dominated galaxies which have stopped accreting gas (in some cases due to environmental effects) and galaxies with extended low-surface density gas disks, which are inefficient at forming stars.

Despite the room for possible improvements to our model described above, the qualitative similarity between the buildup of our model populations with those of observed galaxies gives us confidence that we are beginning to capture the complicated interplay of several processes, including AGN feedback and bulge growth, which lead to the diversity of galaxies and their evolution over time.

Chapter 4

The Relationship Between Star-Formation Activity and Galaxy Structural Properties

4.1 Introduction

Out to $z \sim 3$, galaxies can be split into star-forming and quiescent populations based on the bimodality observed in their colors and derived star formation rates (Baldry et al. 2004; Bell et al. 2004b; Brinchmann et al. 2004; Kauffmann et al. 2003; Strateva et al. 2001; Brammer et al. 2011; Ilbert et al. 2013). As described in Chapters 1 and 3, when focusing specifically on the galaxies classified as star-forming, a strong correlation is observed between the star formation rate and stellar mass of galaxies at a fixed redshift (the SFR-M_* correlation) (Noeske et al. 2007; Daddi et al. 2007; Elbaz et al. 2007; Rodighiero et al. 2011). This correlation is also sometimes referred to as the "star-forming main sequence" (SFMS). This stands in contrast to the less rigidly defined quiescent population, for which there is no such strong correlation.

The SFR-M_* correlation can be defined by a (redshift-dependent) normalization and slope, with a straight line in log-log space providing a reasonable fit, although there is evidence that the slope of the main sequence may flatten above a mass of $\sim 10^{10} M_\odot$ (Whitaker et al. 2012b, 2014). It is still unclear whether this flattening is simply due to the fact that more of the stellar mass in high mass galaxies is likely to be in a non-star-forming bulge component, as suggested by Abramson et al. (2014) or Tacchella et al. (2015), or whether there is something else going on. It has also been suggested that the presence of non star-forming bulges in star-forming galaxies may

increase the scatter in the SFR-M_* relation around the main sequence (Whitaker et al. 2015). In any case, many studies have examined the SFR-M_* correlation and found that it holds over at least four orders of magnitude in mass and exists out to $z \sim 6$ (see Speagle et al. (2014) and references therein, as well as Salmon et al. (2015)). The value of the slope in the SFR-M_* plane is measured to be ~ 1 (Rodighiero et al. 2011) and the relationship has an intrinsic $1-\sigma$ scatter of only $\sim 0.2-0.4$ dex (Whitaker et al. 2012b; Kurczynski et al. 2016). In general, SFMS galaxies at high redshift have much higher SFRs than galaxies on the main sequence today (Sobral et al. 2014), and the evolution of the normalization of the SFMS appears to be independent of galaxy environment (Peng et al. 2010).

The small scatter of the SFR-M_* correlation leads us to believe that the evolution of star forming galaxies is dominated by relatively steady star formation histories, rather than being highly stochastic and bursty. This places constraints on the duty cycle of processes such as galaxy mergers or disk instabilities, which may trigger starburst and quenching events that drive galaxies above or below the main sequence. Furthermore, observations show that since $z \sim 2$ there has been a build-up of quiescent galaxies, while the mass density of galaxies on the SFMS has remained relatively constant, implying that galaxies are being moved *off* of the SFMS into the quiescent population, and remaining there permenantly or at least over rather long timescales (Bell et al. 2004b; Borch et al. 2006; Bell et al. 2007; Faber et al. 2007). As the processes which move galaxies off of the main sequence are often associated with morphological change, it is interesting to examine the correlation between distance from the SFR-M_* relation, or some other measure of quiescence, and galaxy structural properties.

In Chapter 3, we defined a redshift dependent SFMS by which to judge galaxies in order to divide them into star-forming and quiescent populations. We split the sSFR-Sérsic index plane into four quadrants in star-formation activity and morphology: star-forming disk-dominated

galaxies, star-forming spheroid-dominated galaxies, quiescent disk-dominated galaxies, and quiescent spheroid-dominated galaxies. After dividing galaxies up, we examined the evolution of the fraction of galaxies in each of these categories with redshift. In order to constrain which processes were responsible for moving galaxies between these different categories, we did the same analysis on a sample of model galaxies generated from the "Santa Cruz" semi-analytic model described in Somerville et al. (2008a) with updates as described in Somerville et al. (2012) and Porter et al. (2014a). In addition to prescriptions for the main physical processes believed to be important for shaping galaxy properties (described in Chapter 2), the model includes bulge formation due to mergers and disk instabilities, and concurrent growth of supermassive black holes and AGN feedback, allowing us to predict how model galaxies evolve in the SFR-Sérsic index plane. The SAM is a useful tool for studying the evolution of large populations of galaxies, as it can generate large cosmologically representative samples with modest computational resources, allowing us to efficiently test the effects of various physical processes. In Chapter 3, we found that our prescriptions for quenching and morphological transformation were able to transform galaxies in a manner in qualitative agreement with the observations as long as bulge growth due to disk instabilities was included. Bulge growth due to mergers and disk instabilities and subsequent AGN feedback produced roughly the right fraction of galaxies in each of our four subpopulations. Models in which bulge growth occured only due to mergers did not produce as many spheroid-dominated galaxies as seen in observations.

Our goal in this chapter is to study the structural properties of model galaxies *continuously* across and off the main sequence, rather than using the main sequence to sort our galaxies into bins based on their SFRs and morphologies as in Chapter 3 and Pandya et al. (2016). The latter explicitly examines galaxies with intermediate star-formation and structural properties. We learned in Chapter 3 that our model could broadly produce the right fractions of different types of galaxies and the evolution of these fractions, and now we will examine more closely

if it can produce both "typical" main sequence galaxies, as well as match how the structural properties of galaxies change as they move farther from the main sequence. In this way, we hope to continue to build our understanding of the physical processes which drive the correlation between star formation, quenching, and galaxy structural properties, specifically testing a model where AGN feedback and bulge growth often go hand in hand.

Many observational studies have examined the structure of galaxies across the main sequence and come to several conclusions: 1) The main sequence is made up of kinematically and morphologically disk-dominated galaxies which have the largest radial sizes for their stellar masses (Williams et al. 2010; Wuyts et al. 2011; Bluck et al. 2014; van der Wel et al. 2014b) (although it is true that the easy morphological distinction between disk-dominated and spheroid-dominated galaxies begins to break down at higher redshift, especially at high mass). 2) Galaxies lying above the main sequence are often morphologically disturbed and seem to be undergoing a starburst (Wuyts et al. 2011; Elbaz et al. 2011; Salmi et al. 2012). Elbaz et al. (2011) suggests that some of these may also include heavily obscured AGN. Of course, morphological disturbance above the main sequence is not universal; see Barro et al. (2016). 3) Compact star-forming galaxies (cSFGs, as defined in Barro et al. (2013)) on or just below the main sequence at z $\sim$ 2-3 suggest that bulge growth precedes quenching (Barro et al. 2014; Williams et al. 2014; Fang et al. 2015). Fang et al. (2015) even found that at z $\sim$ 2-3, cSFGs dominate the high mass end of the main sequence. 4) Quiescence is almost always associated with a bulge component or high central stellar mass density or velocity dispersion(Franx et al. 2008; Bell et al. 2012; Wake et al. 2012; Fang et al. 2013; Bluck et al. 2014; Lang et al. 2014; Woo et al. 2015b; Teimoorinia et al. 2016). Estimates of galaxy black hole masses derived from central velocity dispersions also point to black hole mass being very correlated with quiescence (Bluck et al. 2016).

On the simulation side, Snyder et al. (2015b) investigated the relationship between optical morphology, stellar mass and star formation rate for a sample of simulated galaxies from the

Illustris simulation (Vogelsberger et al. 2014). They found that their model, which includes feedback from accreting supermassive black holes, was able to produce the population of quiescent bulge-dominated galaxies at $z \sim 0$ needed to reproduce the distribution of observed morphologies. Tacchella et al. (2016) examined how galaxies in the VELA simulations (Ceverino et al. 2014) oscillate around the main sequence due to clumpy inflows and violent disk instabilities, leading to compaction and minor quenching episodes.

We compare our model predictions with galaxies observed with the Cosmic Assembly Near-infrared Deep Extragalactic Legacy Survey (CANDELS; Grogin et al. 2011; Koekemoer et al. 2011) and the Galaxy and Mass Assembly Survey (GAMA; Driver et al. 2011). In order to assure high levels of completeness and robust measurements of structural parameters, we consider only galaxies with stellar mass $M_*>10^{10}M_\odot$, for both the models and observations. We consider several structural properties, including Sérsic index, size, stellar mass density and star-formation rate density. In Section 2 we describe our fit to the main sequence and examine the evolution of star formation in galaxies which are star-forming or quiescent at z=0. In Section 3, we examine the distribution of structural properties across the SFR-M_* plane, as in Wuyts et al. (2011, hereafter W11). We also examine how some quantities on which we currently do not have direct observational constraints, such as bulge-to-total luminosity ratio, black hole mass, and dark matter halo mass, vary across this plane. We next consider how these structural properties change as a function of linear distance from the main sequence, again as studied by W11, in Section 4. In Section 5, we investigate the distribution of distances from the main sequence in bins of galaxy structural properties following the analysis of Bluck et al. (2014). A secondary goal of the this chapter will be to compare our results to those of W11 and Bluck et al. (2014), the inspirations for several of our plots, where appropriate, and we discuss this in Section 6, along with a comparison between our model predictions and some other theoretical predictions in the literature. In Section 6 we also discuss what our model tells us about the universe in the

cases where our model and the observations agree, and what the universe is telling us about our model in the cases where they don't. We summarize our results and conclude in Section 7.

4.2 Evolution of Star-forming and Quiescent Galaxies in the SAM

We define the main sequence much as we did in Chapter 3, although this time we use log(SFR) instead of log(sSFR). As described in Chapter 3, we decide to define our own stellar mass and redshift dependent main sequence line that is determined by the mean star formation rates of galaxies. The star formation rates of observed galaxies are systematically slightly higher than those of model galaxies, so this line is calculated separately for observed and model galaxies. While this already means that our model galaxies are not behaving exactly as observed galaxies, we do not think it impedes our goal of examining galaxy properties relative to the main sequence; as we judge quantities in this work as a function of distance from the main sequence line, we don't expect the disparity in absolute star formation rates to affect our results.

While the SFR-M_* correlation is known to have some dispersion, in order to judge distance from the main sequence, we define it with a single line, as has been done in W11 and Bluck et al. (2014). We also note that while the observed main sequence slope is known to flatten toward higher stellar mass (Whitaker et al. 2012b; Schreiber et al. 2015; Lee et al. 2015), here we extrapolate the slope derived for lower stellar mass galaxies to higher mass. We do this following the interpretation that the decrease in slope at higher stellar mass is due to the higher probability the galaxies of larger mass are already starting to quench and move off of the main sequence. Here, we try to define a more "pristine" version of the main sequence, which we expect on theoretical grounds based on the fact that models without quenching have an unbroken linear SFR-M_* correlation (see Renzini & Peng (2015) for another alternative to defining an unbiased main sequence). Throughout this work, distance from the main sequence is given in units of

log(SFR).

Figure 4.1 shows the evolution of the average star formation rate of galaxies from our model with cosmic time. The blue lines correspond to galaxies that are considered star-forming at $z = 0$ according to the prescription described in Chapter 3 (meaning their SFRs are greater than 25% of the main sequence SFR described above), while the red lines correspond to quiescent galaxies at $z = 0$ (with SFR $< 25\%$ of the main sequence SFR). Galaxies have been split into two mass bins at z=0, with final stellar masses $\sim 10^{10} M_{\odot}$ ($10^{9.9}$-$10^{10.1} M_{\odot}$) or $10^{11.5} M_{\odot}$ ($10^{11.4}$-$10^{11.6} M_{\odot}$), representing the two ends of the mass range we are considering. We see evidence for the SFR-M_* correlation in the higher SFR for star-forming galaxies of higher stellar mass (right panel) versus that of the lower stellar mass galaxies in the left panel. We also see an overall decrease in the SFRs of massive galaxies with cosmic time after an early peak at $\sim$ 2-3 Gyrs. The SFRs of the less massive galaxies are only now beginning to decrease. We see the same type of behavior for the quiescent galaxies, with the higher mass quiescent galaxies exhibiting an earlier and stronger peak.

The scatter in SFR for quiescent galaxies is in general larger than that for star-forming galaxies because the mechanism that leads to the most intense quenching, AGN feedback, is associated with significant mass growth due to the major and minor mergers that trigger it. This is not as apparent in the low mass panel, but only because we have artificially put a floor at log(SFR)=-2.0. Otherwise, the mean quiescent SFR becomes much less well-behaved.

This difference in average star formation histories between star-forming and quiescent galaxies is indicative of the SFMS at work in our model. As discussed in Chapter 3, and mentioned above, the SFR-M_* correlation in our model does not behave exactly as that observed in the universe; while the slope and normalization of our model main sequence is not quite the same as the observed SFR-M_* correlation, we do reproduce a relationship between SFR and stellar mass. Galaxies tend to stay near this sequence until something happens to move them off of it, and

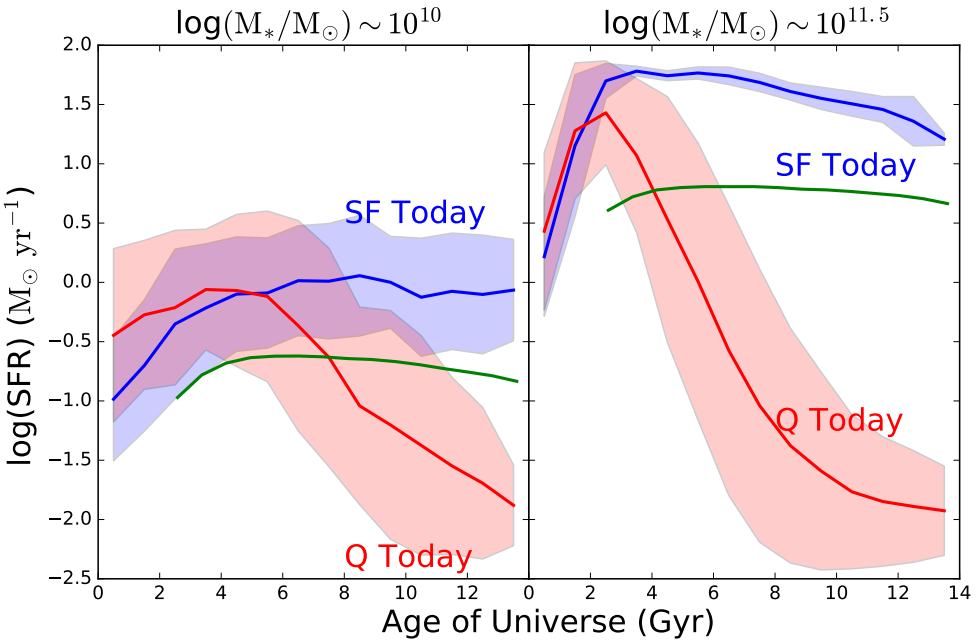

Figure 4.1: Evolution of the mean SFR for model galaxies that are star-forming or quiescent in the present day, split into two mass bins. The blue lines indicate star-forming galaxies at $z = 0$, while red indicates quiescent galaxies at $z = 0$. The shaded regions correspond to the $1-\sigma$ scatter in SFR for each of the curves. The green lines indicate the time-dependent star formation cut off line, below which galaxies are considered quiescent at a given age of the universe. Left panel: Galaxies with stellar masses $\sim 10^{10} M_{\odot}$ at $z = 0$. Right panel: Galaxies with stellar masses $\sim 10^{11.5} M_{\odot}$ at $z = 0$. We see the main sequence of star formation manifested in the higher SFRs of more massive galaxies. We also see evidence of downsizing in the SFRs of more massive galaxies, which peak earlier than those of less massive galaxies. This is true for both galaxies that are star-forming today, and for quiescent galaxies which peak at early times before falling below our quiescence threshold.

the diversity of processes responsible, as well as the varying severity of these processes, leads to the larger spread in average star formation histories of galaxies that are quiescent today. Later, we will examine different galaxy properties as a function of distance from this star-forming main sequence, but first we will look at how different galaxy properties are distributed in the SFR-M_* plane.

4.3 Distribution of Properties in the Star formation Rate-Stellar Mass Plane

Here we examine how the median Sérsic index, effective radius, SFR density, and stellar mass density vary across the SFR-M_* plane for both our model and the observations. We note again here that for the rest of this work we impose a floor on log(SFR) so that all log(SFR)<-2.0 are set equal to -2.0. This is mainly to deal with quiescent model galaxy SFRs which would be far below the plots otherwise.

4.3.1 Number Density in SFR-M_* Plane

In Figure 4.2, we show the distribution of galaxies in the SFR vs stellar mass plane. The number density is shown in greyscale with contours overlaid in red. We also show the main sequence fits we derive for both the model and observations in the three redshift bins of interest, as well as comparisons with the main sequence derived in Whitaker et al. (2012b) and Whitaker et al. (2014). We see immediately where the GAMA survey begins to become incomplete below a stellar mass of $10^{10} M_{\odot}$, which is why we have cut at this mass. We find that the distribution of galaxies is somewhat different in the model than in the observations. At all redshifts, most quiescent galaxies in our models have SFR that are below our floor value $\log(SFR) = -2.0$, while in the observations there is a cloud of galaxies with SFR that are low enough to qualify them as 'quiescent' but well above our floor value.

This may be due to limitations in our modeling of gas inflows and AGN feedback (for example, we may not resolve short timescale rejuvenation events), or it could be due to the difficulty of obtaining accurate observational estimates of SFR for quiescent galaxies (while there is no explicit floor on detected SFRs in CANDELS or GAMA, the errors at low absolute SFR can become quite large and a natural floor is set based on the upper limits of detection in the photometric

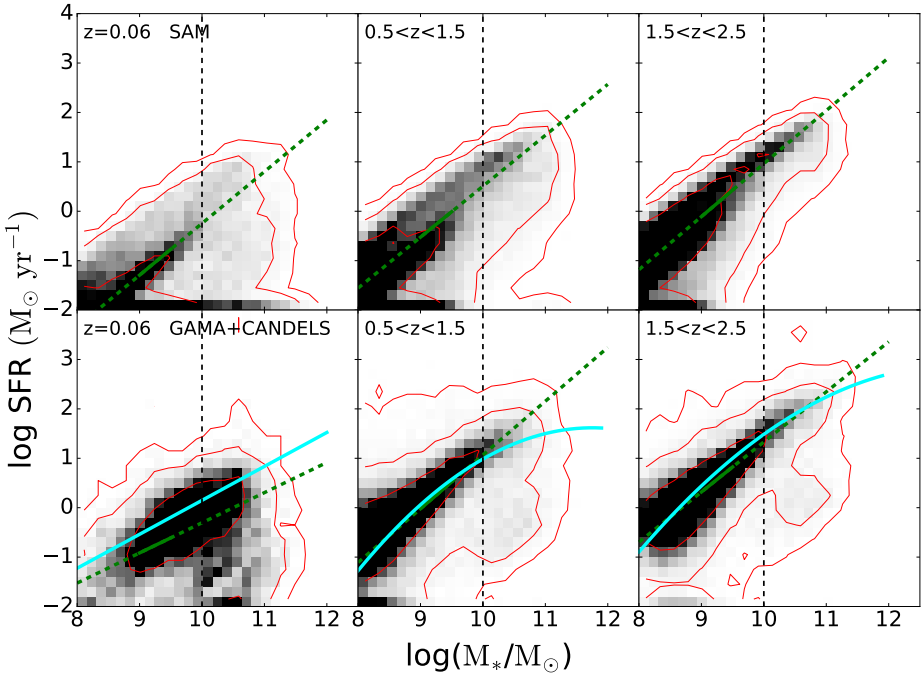

Figure 4.2: The distribution of model (top) and observed (bottom) galaxies with stellar mass $>10^8 M_\odot$ in the plane of SFR vs stellar mass in the redshift bins $z \sim 0.06$ (left panels), $0.5 < z < 1.5$ (middle panels), and $1.5 < z < 2.5$ (right panels). The greyscale indicates population density with contours overlaid in red. The green lines show our fits to the main sequence of star formation, which are based on the mass range 10^9 to $10^{9.5} M_\odot$ (solid green) and extrapolated to higher and lower mass (dashed green). The cyan lines indicate the main sequence fits found in Whitaker et al. (2012b) (lowest redshift bin) and Whitaker et al. (2014) (two higher redshift bins). The fits in Whitaker et al. (2014) are for smaller redshift bins, so we averaged the coefficients of the fits that fell within our larger bins. We see, as mentioned above, where the main sequence slope becomes more shallow at higher stellar mass. The dashed black lines show the stellar mass cut we use for the rest of this work. We note that the normalization and slope of the SFMS is slightly different in the models and in the observations, which is why we fit them separately. In addition, we note that the distributions of SFR for quiescent galaxies are quite different in the models and observations. We discuss this further in the main text.

band used to derive the SFR). Despite this difference, we see that the main sequence fits seem reasonable given the underlying distributions and continue with our analysis, although we will remark throughout when it seems this underlying difference is responsible for deviations between our model and the observations. We will also discuss possible reasons for this difference in our Discussion section.

4.3.2 Sérsic Index in SFR-M_* Plane

In Figure 4.3, we explore the distribution of Sérsic index in the SFR-M_* plane by examining a color map of the median Sérsic index in bins of SFR and M_* (as in the analysis of W11, to which we compare directly in Section 4.6.1). The Sérsic indices for our model galaxies (as well as their effective radii) are derived as described in Chapter 2. The top panel shows this distribution for galaxies from our model and the bottom panel shows galaxies from the GAMA and CANDELS surveys. We have estimated the 1-σ uncertainty on the median Sérsic index in each observational bin due to uncertainties in the estimates of galaxy properties in our observational sample. As in Chapter 3, we use quoted uncertainties in Sérsic index and effective radius, an assumed uncertainty of 0.25 log(SFR) for star-formation rates, and the redshift-dependent stellar mass uncertainty of Behroozi et al. (2013b). The uncertainty, dn, in almost all bins and across all redshifts is only $\sim 0.0 - 0.3$, except for at high redshift for low SFR galaxies, where dn$\sim$ 1.0. In our lowest redshift bin, there is also a small patch of low SFR massive ($>10^{11} M_{\odot}$) bins with dn$\sim$ 2.0. With this in mind we see that the model and observational distributions are qualitatively quite similar, although there are a few key differences.

Both the model and observations exhibit a pocket of high Sérsic index at low SFR and high mass, although this trend is more pronounced in the observations, especially in the two lower redshift bins. As noted before, more galaxies in the models "pile up" at SFRs below our floor value than in the observations, and these galaxies primarily have high Sérsic index

($n \sim 4$) characteristic of very spheroid-dominated galaxies. In the observations, high-Sérsic index (spheroid-dominated) galaxies are predominantly quiescent, but have higher SFRs than their model counterparts. In addition, the quiescent population is dominated by galaxies with higher Sérsic index in the observations than in the models (see also Figure 4.9).

Both the observations and model exhibit a smattering of high Sérsic index galaxies along the top edge of the SFR-M_* distribution, above the main sequence, although this is more apparent in the observations. In our models, we know that galaxies like these are star bursting as the result of a merger and appear as bulge-dominated. However, we see that many of the highly star forming galaxies above the main sequence in our model appear instead to be disk-dominated. The difference is especially apparent in the middle redshift bin, where some of the most massive, star-forming galaxies appear to have very strong disks. This is also true *on* the main sequence, where there appears to be a sharper transition to bulge-dominated systems along the observed main sequence (at $\sim 10^{11} M_\odot$ in our lowest redshift bin) than we see in the model.

In Figure 4.4, we show the distribution of Sérsic index across the SFR-M_* plane for our model without the prescription for bulge growth via disk instability. We see here how important the disk instability is in producing bulge-dominated galaxies. Without it we have very few truly bulge-dominated systems, even at low redshift far below the main sequence. Our main sequence is also completely dominated by disk galaxies, even at the high mass end, unlike in the observed sample. The distribution of galaxies in the SFR-M_* plane as compared with Figure 4.3 is relatively unchanged; the disk instability is much more important for building bulge components than it is for quenching galaxies (see also Chapter 3, where it is shown that the quiescent fraction of galaxies changes very little between the two models, while the spheroid-dominated fraction changes by a significant amount.)

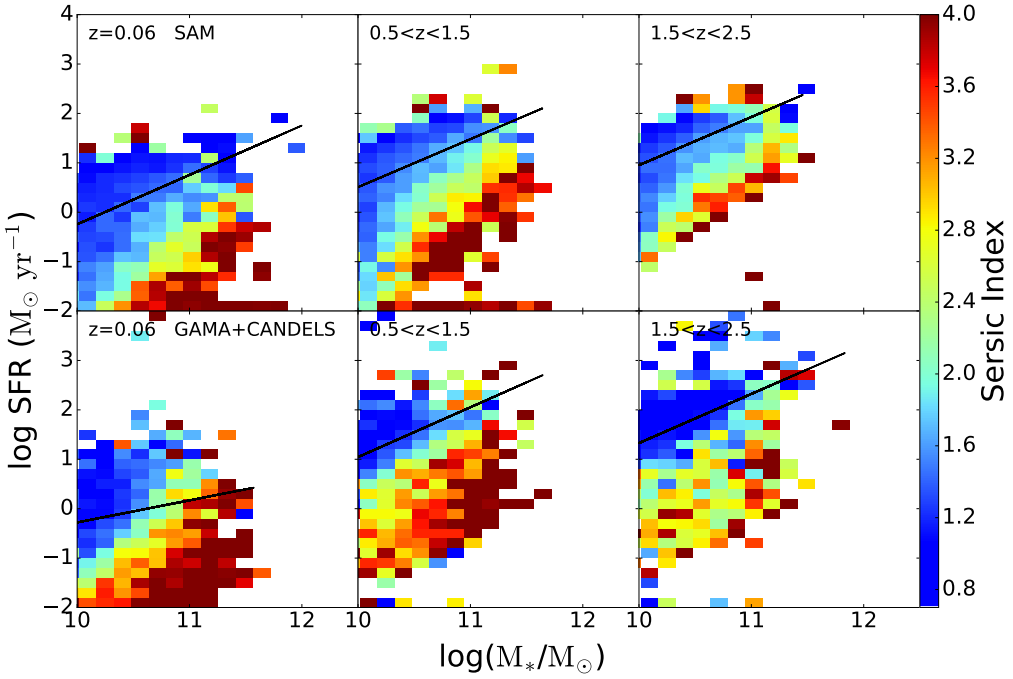

Figure 4.3: Distribution of median light-weighted Sérsic index in the SFR-M_* plane for (top) model galaxies and (bottom) observed galaxies in three redshift bins. The black lines indicate the star-forming main sequence fits. We find good qualitative agreement between the model predictions and the observations, although our model does not exactly reproduce the distribution of structural properties across the main sequence. In addition, massive high Sérsic-index ($n \sim 4$) galaxies are more strongly quenched in our models than in the observations.

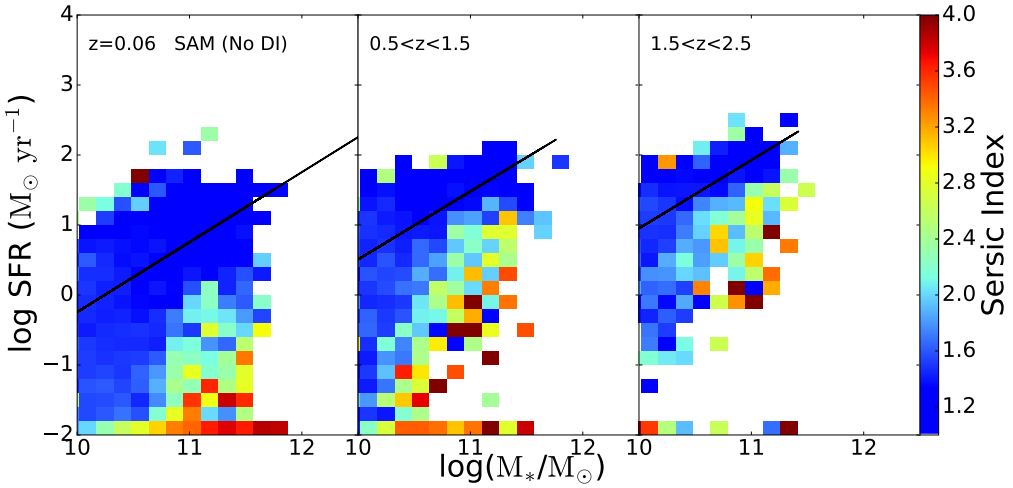

Figure 4.4: Distribution of Sérsic index in the SFR-M_* plane for model galaxies in three redshift bins, in a version of the model that does not include bulge growth due to disk instabilities. The black lines indicate the star-forming main sequence fits. Here we see how important the disk instability mechanism is to building bulges in our model galaxies. Without it, we have very few bins with a median Sérsic index $\gtrsim 3.5$.

4.3.3 Sizes and Surface Densities in SFR-M_* Plane

Figure 4.5 is the same as Figure 4.3, but for log effective radius. We calculate the uncertainty in each bin again as we did for Sérsic index and find that in general it is only ~ 0.05 dex. In our lowest redshift bin at very high stellar mass, the uncertainty can grow to be ~ 0.5 dex, but this affects very few bins. Again, the models qualitatively match the observations, although our model galaxies at low redshift tend to be too large. The main features are that there is a clear sequence from compact to extended galaxies from left to right, simply reflecting the size-mass relation. There is no clear correlation between size and location in the SFR-M_* plane for galaxies that are near the SFMS (see also Shanahan et al., in prep.). However, galaxies that are below the SFMS (quiescent galaxies) are more compact at almost every mass than SF galaxies (although at our highest masses, even galaxies below the main sequence tend to be quite extended; we will return to this in Section 4.4, as well as the issue of our large low redshift galaxies). These

observational trends are well known (see e.g. van der Wel et al. 2014b, and references therein) and our models qualitatively reproduce them. We discuss the quantitative comparison between our model predictions and observational results in more detail in Section 4.4.

Figure 4.6 is the same as Figures 4.3 and 4.5, but now looking at the distribution of median SFR surface density, $\Sigma_{\rm SFR}$, defined as $SFR/2\pi r^2$, where r is the effective radius. The uncertainty on these median values is generally less than ~ 0.5 dex. Here again we see very good qualitative agreement between our models and the observations, the biggest difference being the high density bins sitting above the main sequence that are much more pronounced in the observations than in the model. Whereas the model has no bins with a median $\log(\Sigma_{\rm SFR}) \gtrsim 1.0$ even at high redshift, the observations show several high SFR bins with $\log(\Sigma_{\rm SFR})$ as large as 1.5 all the way down to low redshift. This may reflect limitations in our modeling of starburst systems.

Figure 4.7 shows the distribution of the median stellar mass surface density, $\Sigma_{\rm M_*}$, defined as $M_*/2\pi r^2$ in the SFR-M_* plane. The uncertainties on the median values here are less than ~ 1.0 dex. We find that our agreement is very good in the lowest redshift bin. At higher redshifts, we see more compact systems in the observations, mainly below the main sequence at high stellar mass, than we produce in our model. This is most noticable in our highest redshift bin. The most compact systems are those with $n \sim 4$ in the quiescent cloud in Figure 4.3.

4.3.4 Model-only Properties in the SFR-$\rm M_*$ Plane

In Figure 4.8, we look at the distribution of some properties which are predicted for our models, but for which we do not currently have direct observational constraints. However, all of these quantities can in principle be observationally constrained. From top to bottom, these are bulge-to-total luminosity ratio (in observed F160W), bulge velocity dispersion, dark matter halo mass and black hole mass. The diagrams look extremely similar for all of these. As seen in previous studies, stellar mass is strongly correlated with all of these quantities, which also have significant

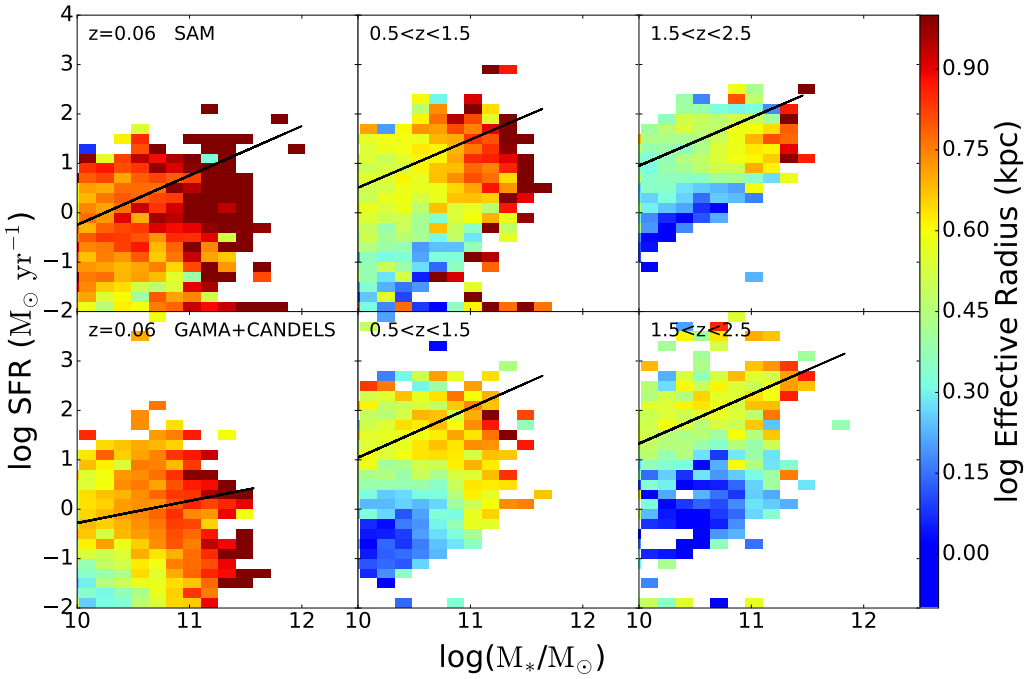

Figure 4.5: Distribution of log median effective radius in the SFR-M_* plane for (top) model galaxies and (bottom) observed galaxies in three redshift bins. The black lines indicate the star-forming main sequence fits. The agreement between model and observations is qualitatively quite good, although at low redshift, our model produces galaxies that are too large

.

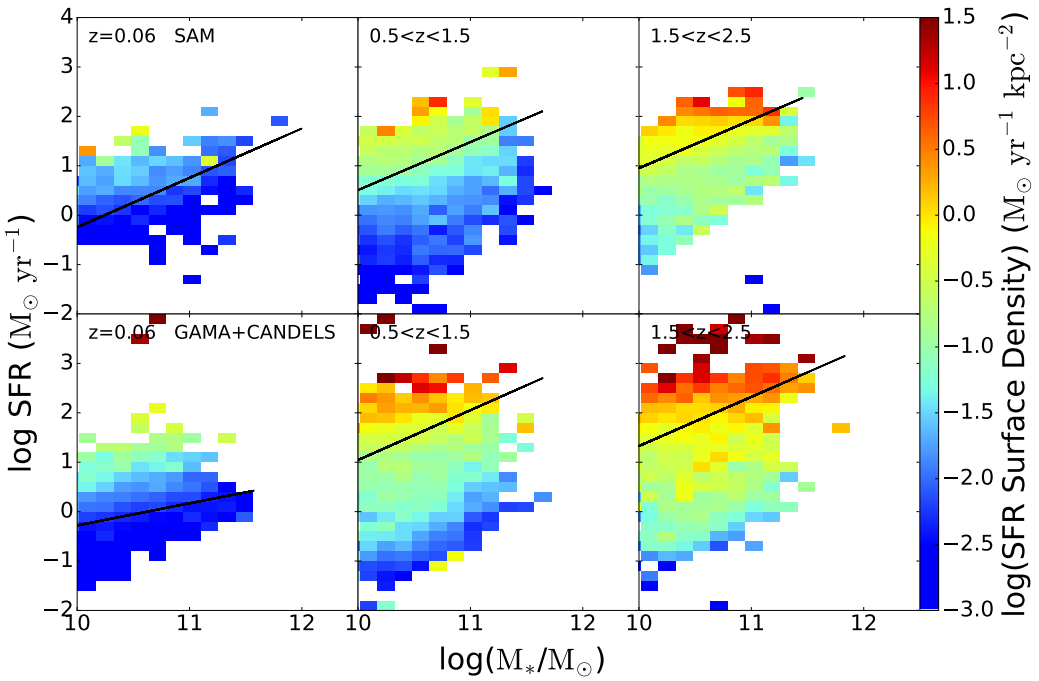

Figure 4.6: Distribution of median SFR density in the SFR-M_* plane for (top) model galaxies and (bottom) observed galaxies in three redshift bins. The main difference between the model and the observations in all redshift bins is the absence of the highest SFR density systems in the model as compared with the observations. This is due to the on average slightly larger radii of the model galaxies above the main sequence, where the most concentrated observed galaxies are.

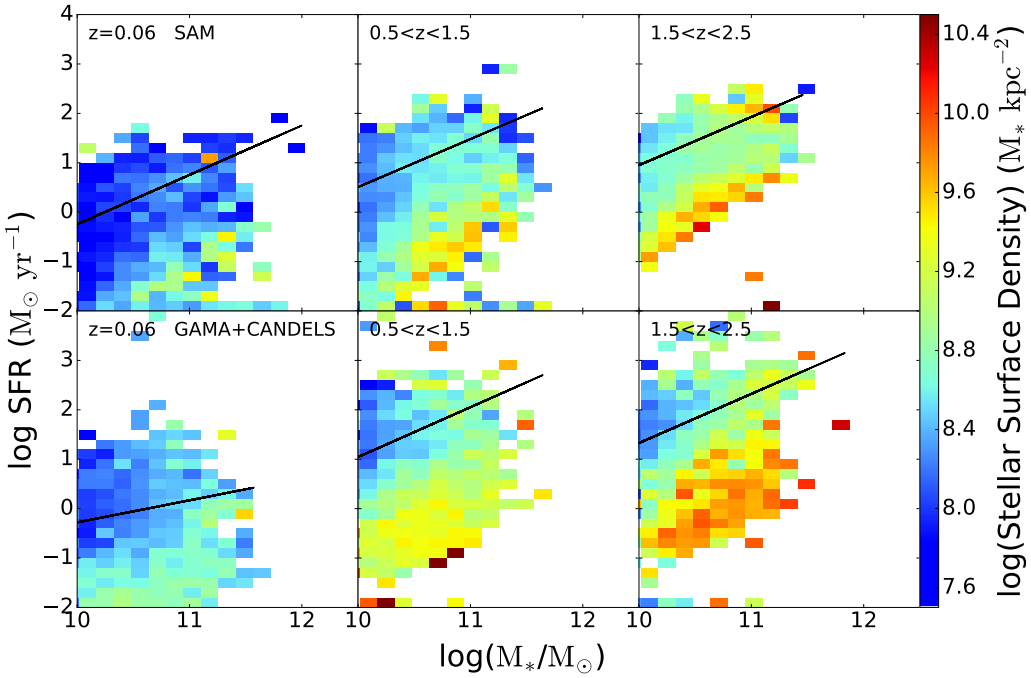

Figure 4.7: Distribution of median stellar mass density in the SFR-M_* plane for (top) model galaxies and (bottom) observed galaxies in three redshift bins. The black lines indicate the star-forming main sequence fits. The qualitative agreement between the models and observations is very good, although the models do not reproduce as prominent a population of high surface density, quiescent galaxies in the highest redshift bin as seen in the observed distribution.

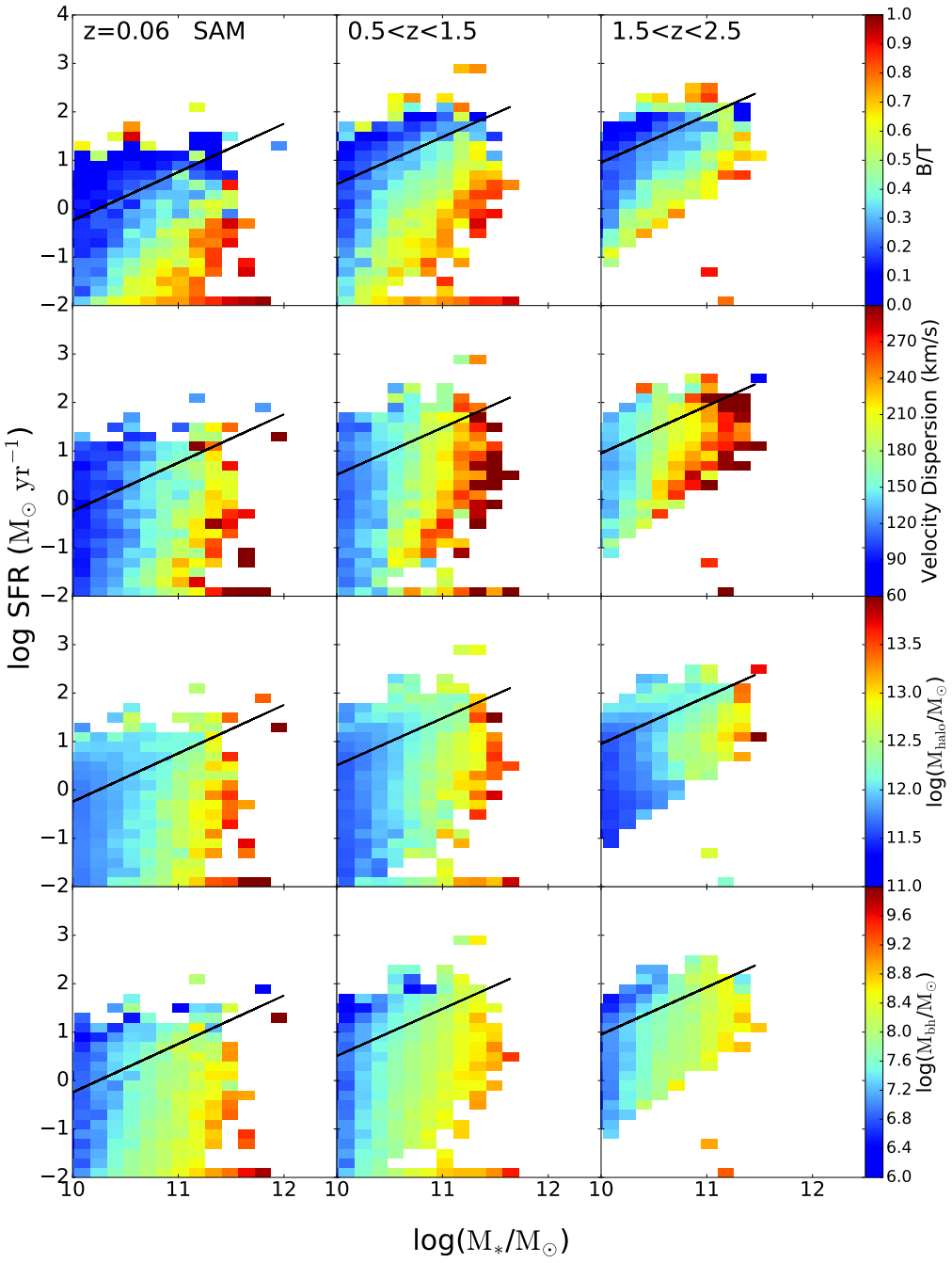

Figure 4.8: Distribution of (from top to bottom) bulge-to-total luminosity ratio in observed F160W, central velocity dispersion, halo mass, and black hole mass in the SFR-M_* plane for model galaxies in three redshift bins. The black lines indicate the star-forming main sequence line fits. Here we see the behavior of galaxy parameters which are native to our model, rather than the derived quantities we need to compare with observations. B/T and Sérsic index track each other very well. The other three quantities are strongly correlated with stellar mass.

correlations with one another. From this analysis, it is not possible to conclusively determine which property is the most fundamental causal factor in driving galaxy quiescence.

4.4 Distance from the Main Sequence

In order to be a bit more quantitative, we now examine the medians of the quantities investigated in the previous section as a continuous function of distance from the main sequence. We define ΔSFR as log(SFR)-log(SFR$_{MS}$), where log(SFR$_{MS}$) is the main sequence SFR for a galaxy's stellar mass and redshift. A ΔSFR of ~ 0 indicates galaxies on the main sequence, while a positive or negative ΔSFR indicates galaxies above (with a higher SFR than) or below (with a lower SFR than) the main sequence, respectively. The shaded region represents the distribution of the 25th-75th percentiles. We also include 1-σ error bars derived the same way as the uncertainties on the median quantities in the last section. We set a floor for ΔSFR at a value of -3 dex, below which there are very few galaxies in either the models or the observations. We also employ somewhat larger bins towards lower ΔSFR to combat very low number statistics.

Figure 4.9 shows median Sérsic index as a function of distance from the main sequence. In both the models and the observations, we see that the SFMS is dominated by galaxies with low Sérsic index (1.0-1.5), demonstrated by the minima of both the red and blue curves in all redshift bins near $\Delta SFR = 0$ (recall that the intrinsic width of the SFMS is $\sim 0.2 - 0.4$ dex). In the highest redshift bin, the SFMS population has slightly *lower* median Sérsic index (closer to a pure $n = 1$ exponential) in the observations, while in the models the median Sérsic index in this regime remains similar to the lower redshift bins. The trend towards increasing Sérsic index with decreasing ΔSFR seen in the observations is qualitatively reproduced in the models, as already noted, but the region below the SFMS ($\Delta SFR < 0$) is dominated by galaxies with higher values of Sérsic index in the observations, at least in the two lower redshift bins. In the

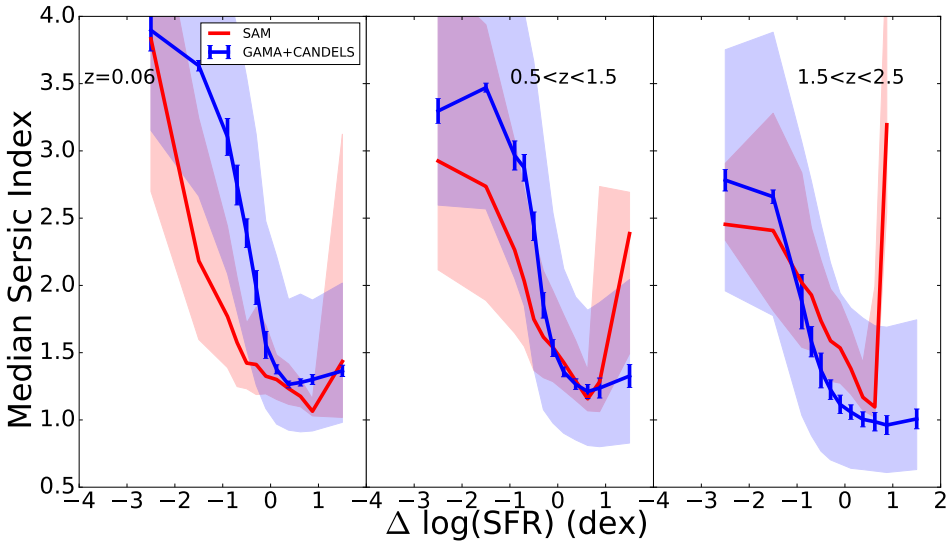

Figure 4.9: Median Sérsic index as a function of vertical distance from the fitted star-forming sequence for model galaxies (red) and observed galaxies (blue). The shaded region covers the 25th-75th percentiles of Sérsic index and the observations also have $1-\sigma$ error bars reflecting the uncertainties in galaxy parameter estimation. Below the SFMS, both the model and the observations exhibit an increase in Sérsic index with increasing distance from the SFMS.

highest redshift bin, the models produce fewer quiescent galaxies than are seen, as already noted and discussed (also in Chapter 3). For the observations, there is a very slight upturn in median Sérsic index in the starburst regime of the SFMS (Δ SFR $\gtrsim 0.6$; e.g. Rodighiero et al. (2011)) in the two lowest redshift bins. In the models, the highest ΔSFR bin is dominated by the few very highly star-forming, newly bulge-dominated systems, resulting in the large spike seen in all three redshift bins. These objects are rare in the model and subject to large statistical fluctuations in our relatively small samples, leading to the spikes as opposed to the gradual upturn of the observations. We also might expect the upturn in the observations to be larger (as seen in W11), but if the starburst is triggered by processes that cause morphological disturbance (such as mergers or disk instabilities), they are likely to have been excluded from our observational sample by our GALFIT quality cut.

In Figure 4.10, we see that our model in general produces galaxies whose sizes are in rough

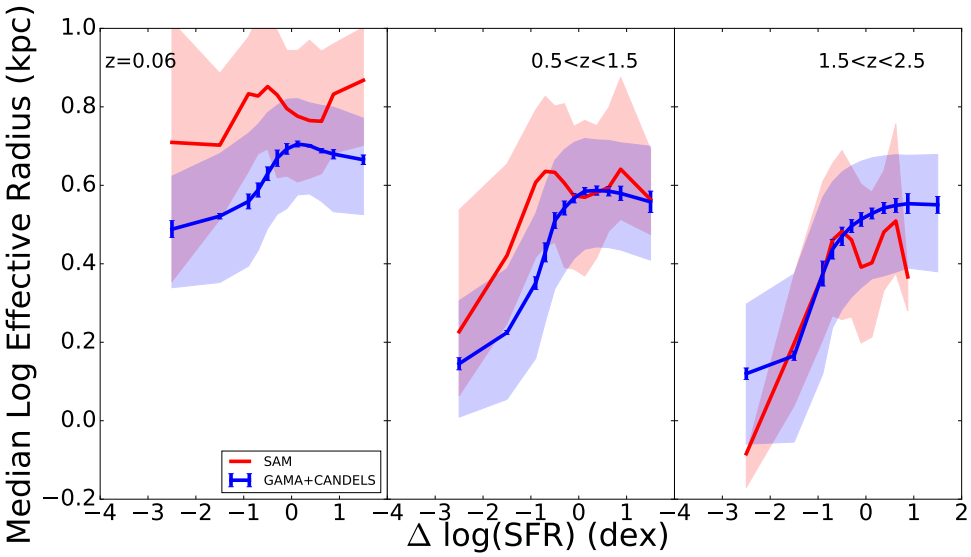

Figure 4.10: Median effective radius as a function of vertical distance from the fitted star-forming sequence for model galaxies (red) and observed galaxies (blue). The shaded region covers the 25th-75th percentiles of effective radius and the observations also have $1-\sigma$ error bars reflecting the uncertainty in galaxy parameter estimation. At low redshift, our model galaxies tend to be too large.

agreement with their observational counterparts in our two higher redshift bins, although in our lowest redshift bin, the model tends to produce galaxies which are too large regardless of distance from the main sequence. We also see that in the model, galaxies just above and below the main sequence tend to be slightly larger than galaxies directly on the main sequence; see the Discussion for more details. In our lowest redshift bin, and to a lesser extent in our middle redshift bin, the galaxies furthest below the main sequence tend to be especially large compared to observed galaxies; this will also be discussed later. In the observations, the largest galaxies live on the main sequence, with radial size decreasing monotonically below the main sequence with increasing distance from it.

Figure 4.11 shows good agreement between the median values of $\Sigma_{\rm SFR}$ at all distances from the main sequence in all three redshift bins, although model values fall slightly below observed values in our two higher redshift bins. In Figure 4.12, we see that the model produces galaxies

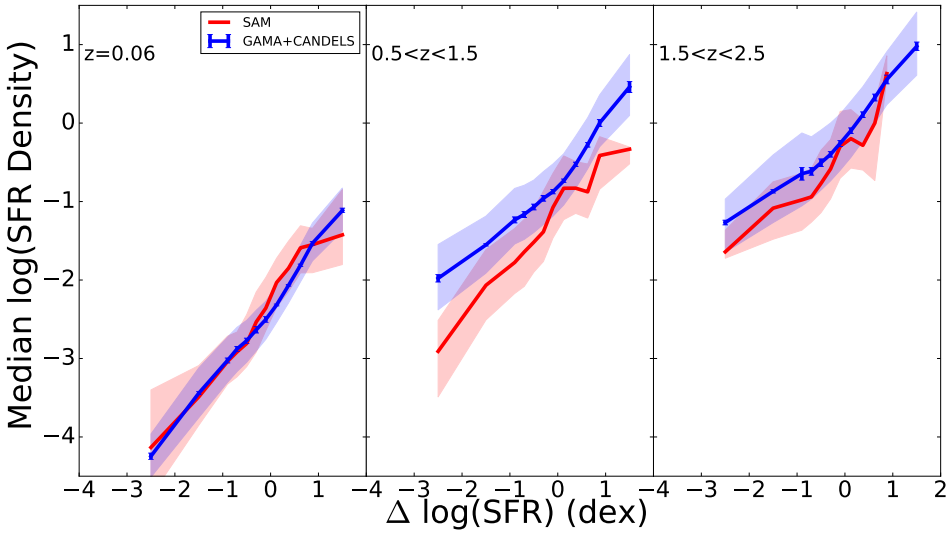

Figure 4.11: Median SFR density as a function of vertical distance from the fitted star-forming sequence for model galaxies (red) and observed galaxies (blue). The shaded region covers the 25th-75th percentiles of SFR density and the observations also have $1-\sigma$ error bars reflecting the uncertainty in galaxy parameter estimation. The agreement between models and observations is in general quite good, although in our higher redshift bins, the models produce slightly less dense systems.

whose stellar mass surface densities are in decent agreement with those observed on the main sequence. Below the main sequence, where the model galaxies tend to be too large, as noted above, the stellar mass surface density falls below that found in the observations.

4.5 Distribution of Distance as a Function of Galaxy Properties

Finally, we turn the tables and examine the distribution of ΔSFR in bins of various galaxy properties. Figure 4.13 shows the results for stellar mass, bulge-to-total mass ratio, and halo mass at low redshift, for our models and for the analysis of SDSS galaxies by Bluck et al. (2014). The structural and stellar mass measurements for the SDSS galaxies were carried out by Simard et al. (2011) (bulge-disk decompositions by light) and Mendel et al. (2014) (bulge, disk and total stellar mass). For this plot and the next, we extend our mass range down to $10^8 M_\odot$,

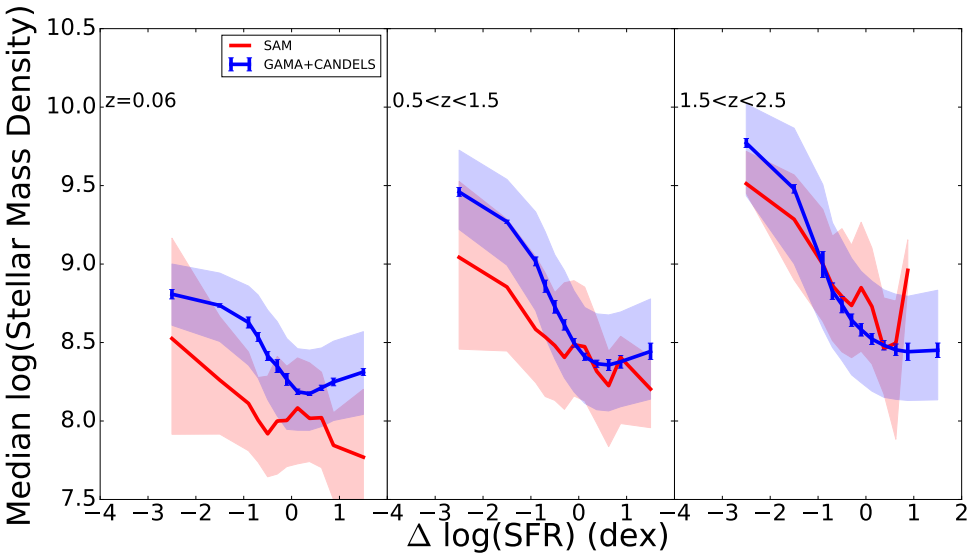

Figure 4.12: Median stellar mass density as a function of vertical distance from the fitted star-forming sequence for model galaxies (red) and observed galaxies (blue). The shaded region covers the 25th-75th percentiles of stellar mass density and the observations also have $1-\sigma$ error bars reflecting uncertainty in galaxy parameter estimation. The agreement between the models and observations is generally quite good, with the largest deviation being ~ 0.5 dex below the main sequence.

and use bulge-to-total stellar mass ratio as opposed to bulge-to-total luminosity ratio, to better compare with the results of Bluck et al. (2014). We see qualitatively similar trends, with the distributions for galaxies with larger values of these properties peaking below the main sequence. In the top left panel, we see a very extended model distribution for high mass galaxies. Our model distributions have less well-defined peaks both on and off the main sequence than those seen for the observed galaxies in the top right panel. B/T behaves the same way, although the model peaks are a bit more well-defined (but not as well as for the observations). The model distributions in bins of halo mass are well stratified, with higher halo mass galaxies peaking at successively lower ΔSFR. For the highest halo mass galaxies, this peak is right at our ΔSFR floor because these are most likely to be the most quiescent galaxies that live at the very bottom of our SFR-M_* plane plots. The observed high halo mass distribution in the bottom right panel peaks at a higher ΔSFR because those galaxies live in the quiescent cloud like our quiescent GAMA and CANDELS galaxies do. As mentioned above, the lack of a distinct peak below the main sequence in these distributions (and those throughout this section) is due to the fact that we have arbitrarily low SFRs in our model, while it becomes very difficult to measure very low SFRs observationally. In fact, for the SDSS data with which we are comparing here, an explicit floor on specific SFRs (at log(sSFR)=-12.0) has been introduced (see Brinchmann et al. (2004) for details).

In Figure 4.14, we see the same distributions for our higher redshift model galaxies. For all three galaxy properties, the distributions tend to collapse onto each other as we move to higher redshift, although stellar mass and halo mass remain somewhat stratified.

Now we return to the quantities we have been focusing on in the previous sections, comparing the distributions in bins of our model quantities with those from observed galaxies. We resume using our mass cut at $10^{10} M_{\odot}$ and revert back to using light-weighted B/T in order to derive the model Sérsic indices in the following plots. Figure 4.15 shows these distributions in bins

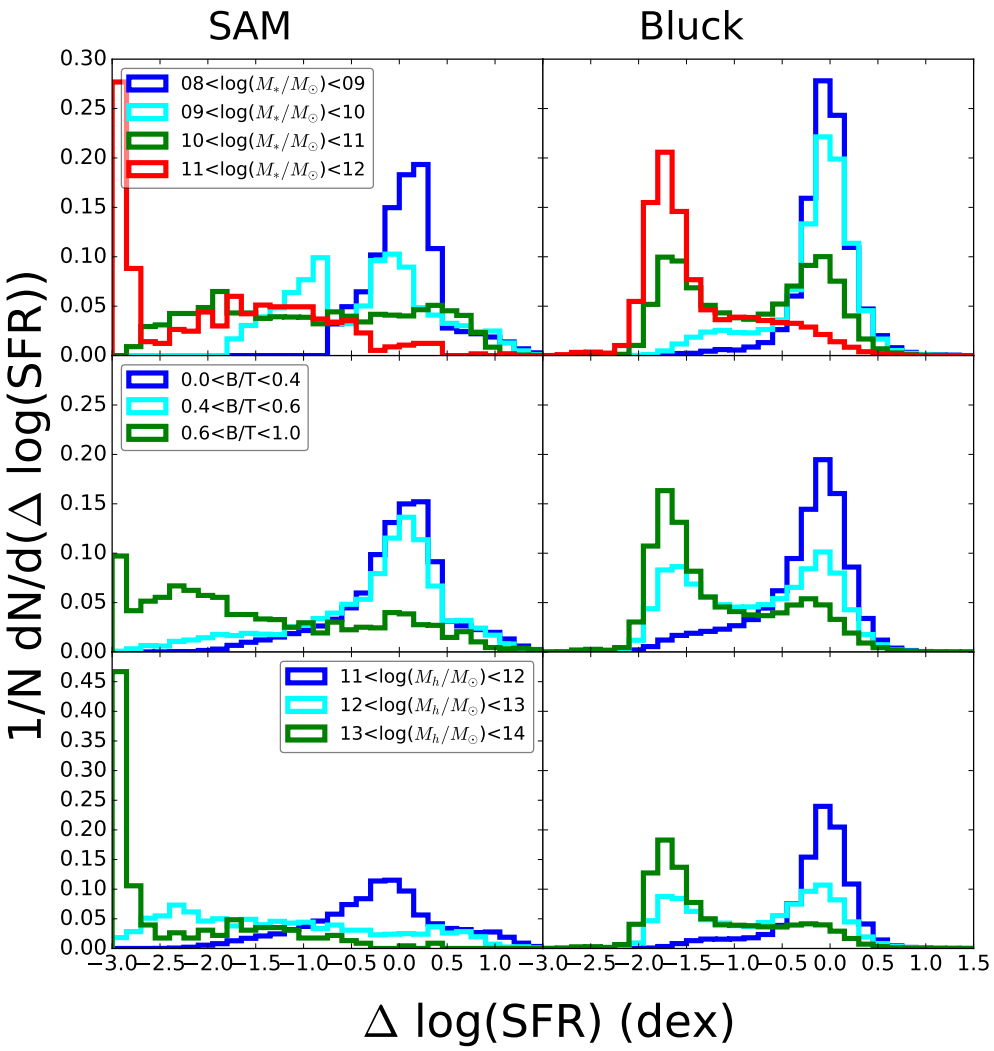

Figure 4.13: Distribution of $\Delta \log \mathrm{SFR}$ for different bins of galaxy properties (for galaxies with $M_*>10^8 M_\odot$) in our lowest redshift bin. Left: Model properties. Right: Galaxy properties used as part of the analysis of Sloan Digital Sky Survey galaxies that span the redshift range 0.02<z<0.2 in Bluck et al. (2014). Top panel: Stellar mass. Middle panel: Bulge-to-total stellar mass ratio (derived from bulge+disk decompositions for the observations). Bottom panel: Halo mass (derived from abundance matching for the observations). All three of these quantities behave as expected. The model and the observations qualitatively agree, although the distributions for the larger values of each galaxy parameter tend to peak farther below the main sequence in our models than in the observations.

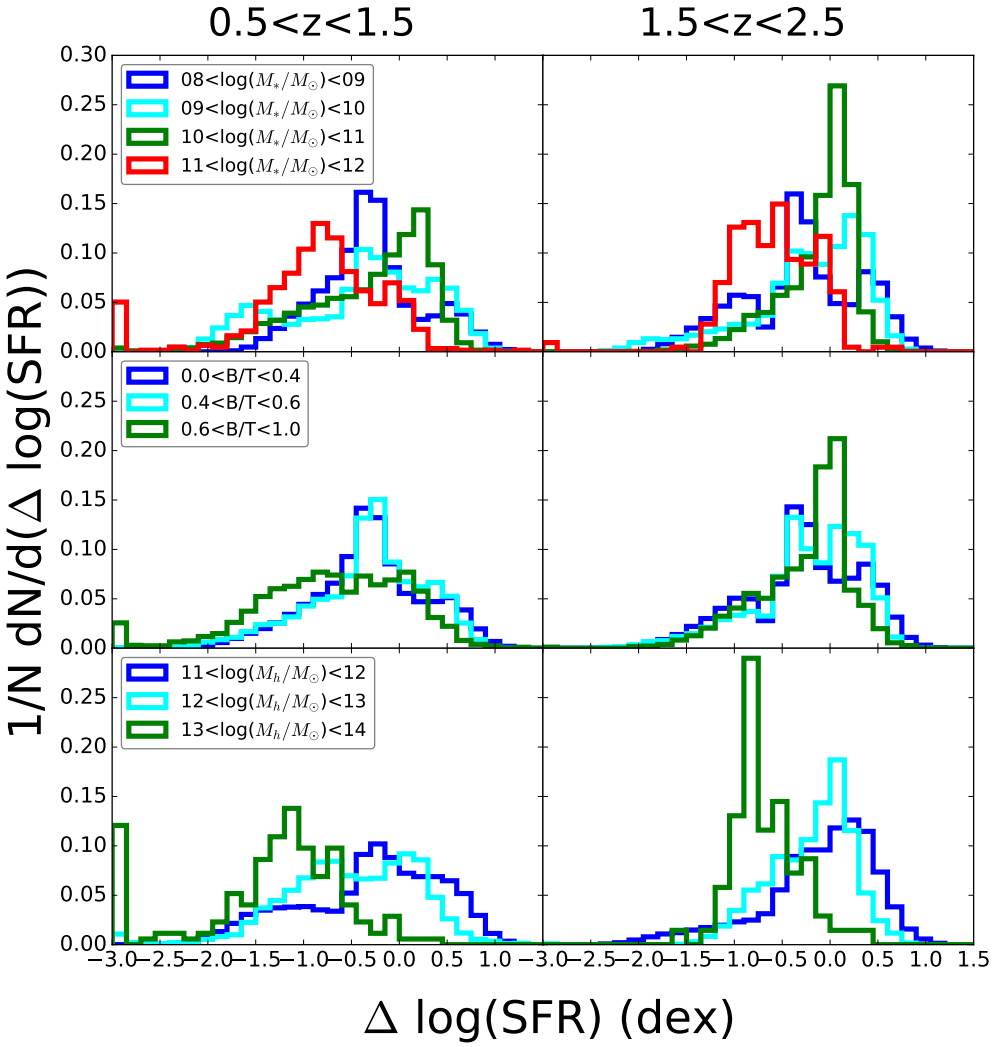

Figure 4.14: Distribution of $\Delta \log \mathrm{SFR}$ for different bins of model quantities (for galaxies with $M_*{>}10^8 M_\odot$) in our two higher redshift bins (redshift increasing left to right). Top panel: Stellar mass. Middle panel: Bulge-to-total stellar mass ratio. Bottom panel: Halo mass. We see that as we move toward higher redshift, the distributions in all bins of galaxy properties begin to pile up on the main sequence.

of Sérsic index, quartile of effective radius and SFR surface density for our lowest redshift bin. To assign a radius quartile, we divide galaxies into 1 dex mass bins (10^{10}-$10^{11}M_{\odot}$ and 10^{11}-$10^{12}M_{\odot}$) and see where they fall in the distribution of all sizes in their respective mass bins. We see that the qualitative agreement is good for all three quantities. Our model distributions tend to skew to lower ΔSFR as noted before. We also see that our model doesn't stratify in radius as well as the observations; we have some galaxies which are quite large for their stellar mass far below the main sequence and the distribution of large galaxies does not peak as strongly on the main sequence as it does for observations. We also see in the bottom panels that even our most dense star-forming systems aren't as high above the main sequence as those seen in the observations. These conclusions are consistent with those we reached by looking at the plots of median quantities above.

As we move towards higher redshift, the same trends persist. Figure 4.16 is the same as Figure 4.15 but for our middle redshift bin. The main difference we see is in the size distributions. While the observations show significantly different distributions in ΔSFR for the four radius quartiles, with the most compact galaxies being much more skewed towards large negative values of ΔSFR, the ΔSFR distributions in the models are much less well separated for the different radius quartiles. A similar result can be seen in Pandya et al. (2016), in which both model and observed galaxies have been split into star-forming, transition, and quiescent galaxies.

Finally, we look at high redshift in Figure 4.17. Here, the lack of model quiescent galaxies at this redshift asserts itself. While our model reproduces the separation in the distributions in bins for Sérsic index, the high Sérsic index bins do not peak as far below the main sequence as in the observations. This is also true for the distributions in bins of SFR density. Our model does not reproduce the separation of distributions in bins of size quartile, with model galaxies of all sizes living near the main sequence. The high-Sérsic index, small-radius, and low-SFR density peaks seen below the main sequence in the observations are the beginnings of the quiescent cloud

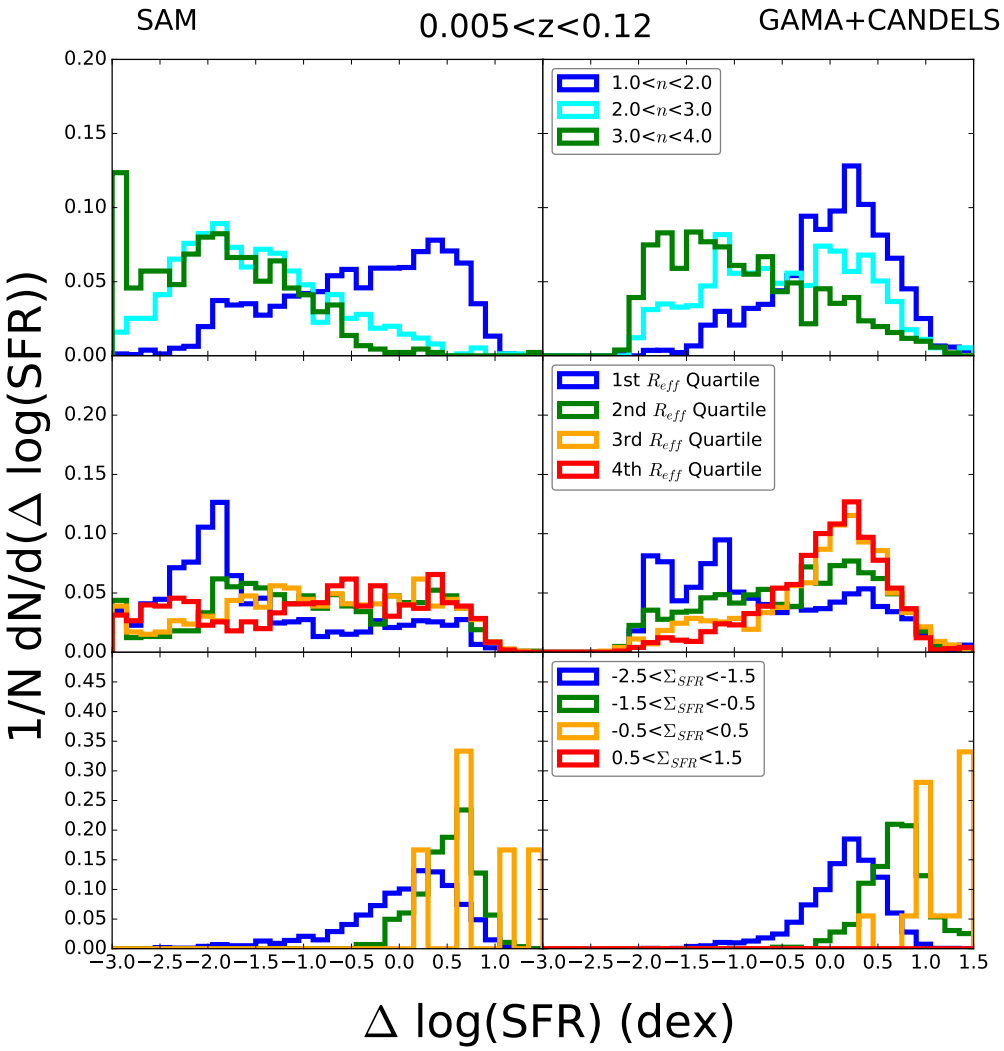

Figure 4.15: Distribution of $\Delta \log \mathrm{SFR}$ in our low redshift slice for different bins of model (left column) and observed (right column) galaxy properties. Top panel: Sérsic index. Middle panel: Quartile for effective radius for a given galaxy's 1 dex mass bin. Galaxies are divided into bins with $10^{10}<M_*/M_\odot<10^{11}$ and $10^{11}<M_*/M_\odot<10^{12}$. The first quartile is the smallest for each mass bin and so on. Bottom panel: SFR Density. The agreement for all three quantities is very good, although our model distributions tend to have tails to lower ΔSFR than the observations.

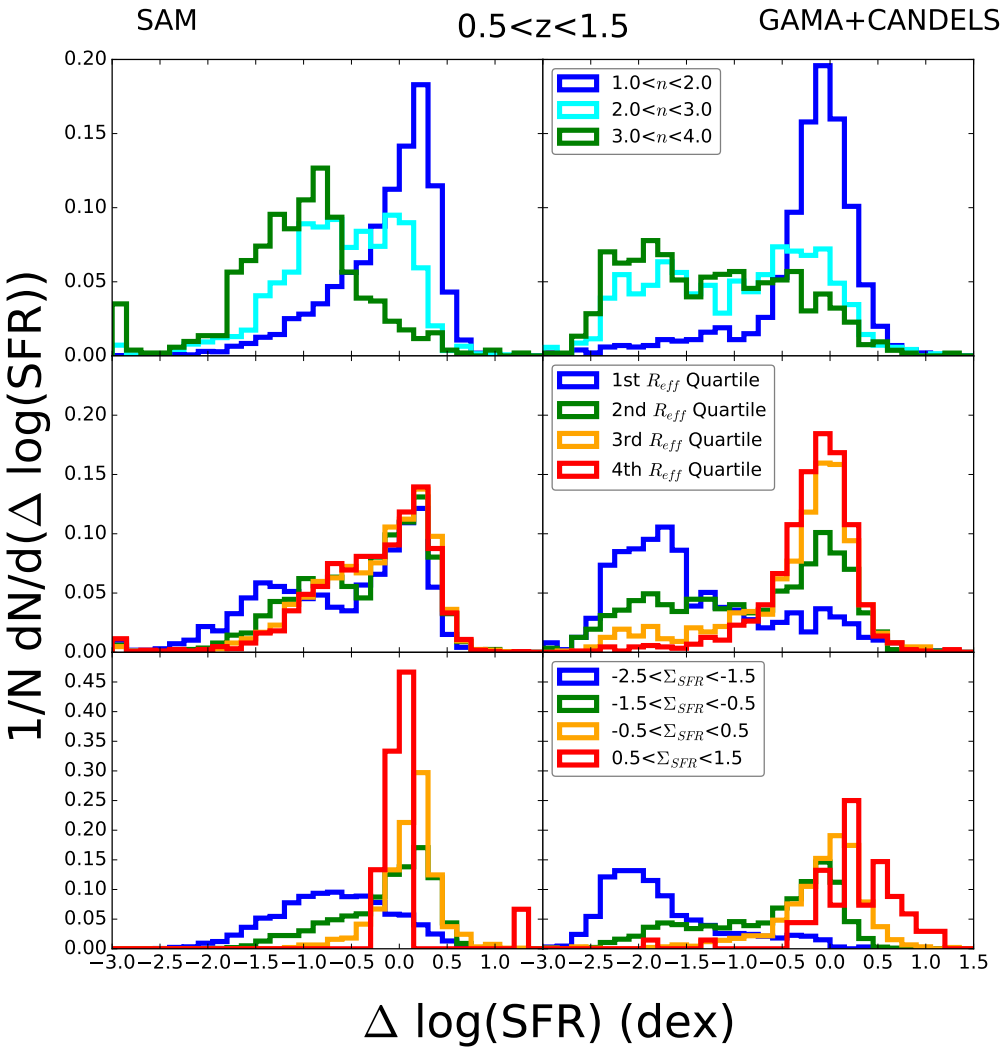

Figure 4.16: Distribution of $\Delta \log \mathrm{SFR}$ in our middle redshift slice for different bins of model (left column) and observed (right column) galaxy properties. Top panel: Sérsic index. Middle panel: Quartile for effective radius falls into for a given galaxy's 1 dex mass bin. Galaxies are divided into bins with $10^{10}<M_*/M_\odot<10^{11}$ and $10^{11}<M_*/M_\odot<10^{12}$. The first quartile is the smallest for each mass bin and so on. Bottom panel: SFR Density. Our agreement is again very good for Sérsic index and SFR density, but the models' $\Delta \log \mathrm{SFR}$ distributions are not as well differentiated for different radius quartiles the observed distributions.

which our model has trouble reproducing.

4.6 Discussion

Our study has demonstrated a significant correlation between galaxy structural properties and their star formation activity relative to a local star forming main sequence. These correlations have been seen many times before both in the nearby Universe and out to high redshift. However, our study is novel in several respects. 1) We take particular care to carry out the analysis of the GAMA survey of nearby galaxies and the CANDELS survey out to $z \sim 2.5$ in a consistent manner. 2) We carry out our analysis on the WFC3 images from the full five fields of CANDELS for the first time. 3) We make detailed comparisons between these observations and a statistically representative sample of model galaxies from a cosmological model of galaxy formation and evolution. The latter point is key, as an observed *correlation* can never prove *causation*, while if we see similar correlations in models, we can at least suggest a plausible story for a causal picture. For a short discussion on progenitor bias and how this might affect the causal picture, see Section 4.6.2.

In this section, we compare and constrast the results of our analysis with previous results in the literature, and discuss what we have learned about galaxy evolution in the Universe and in our models.

4.6.1 Comparison with Literature Results

Comparison with the Observational Analysis of Wuyts et al.

The study by W11 was a primary inspiration for this work, and our observational analysis is deliberately very similar. For the most part, our conclusions are also very similar. Here we summarize the most important differences between the two studies. The structural measurements

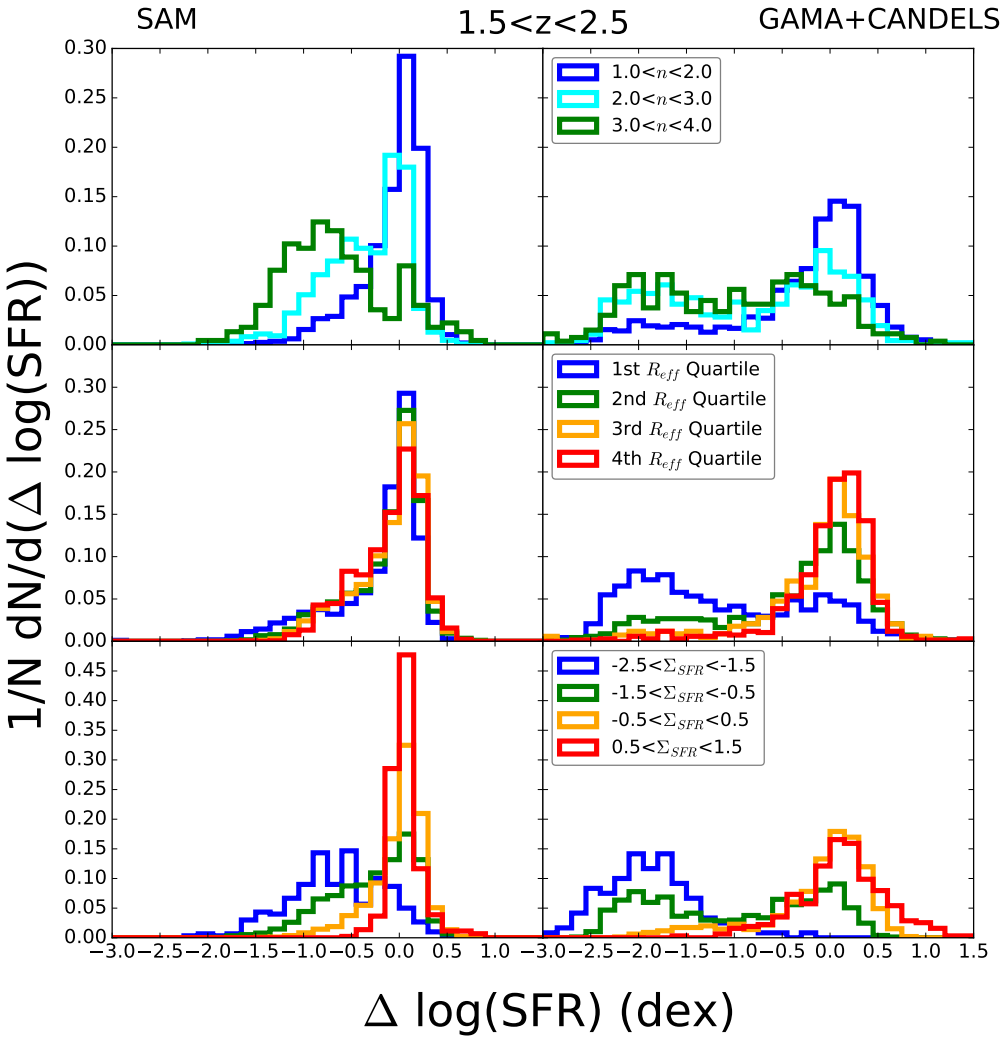

Figure 4.17: Distribution of $\Delta \log \mathrm{SFR}$ in our highest redshift slice for different bins of model (left column) and observed (right column) galaxy properties. Top panel: Sérsic index. Middle panel: Quartile for effective radius for a given galaxy's 1 dex mass bin. Galaxies are divided into bins with $10^{10}<M_*/M_\odot<10^{11}$ and $10^{11}<M_*/M_\odot<10^{12}$. The first quartile is the smallest for each mass bin and so on. Bottom panel: SFR Density. The main disagreement in all panels is that our model distributions do not have a large enough quiescent population with SFR well below the main sequence.

used in W11 were based on the ACS I_{814} image in the 1.48 deg^2 COSMOS field, the H_{160} image in the CANDELS UDS and GOODS-S fields, and the z_{850} image in the GOODS-N field. Similarly, the catalogs used in W11 were selected in different filter bands and for different depths, as summarized in Table 1 of W11. In contrast, our structural measurements are all derived from the CANDELS H_{160} image and are based on H_{160}-selected catalogs with uniform depth for all five CANDELS fields. W11 computed their own photometric redshifts and stellar masses based on compilations of ground and space-based data from the literature for each of their fields, while we use the CANDELS team photo-zs and stellar masses for all five fields.

In spite of these differences, the main results of our analysis are very much in agreement with those of W11 overall. Here we highlight a few differences and some possible reasons for them. Comparing the bottom row of our Figure 4.3 and Figure 4.9 with Figure 1 and 2 of W11, one of the main differences we notice is the more pronounced population of galaxies with high Sérsic index, $n \sim 3.5 - 4$, *above* the SFMS in W11. There are two possible reasons for this[1]. First, our GALFIT quality cut eliminates galaxies with highly uncertain Sérsic index fits. W11 did not make such a cut and so includes star bursting systems that may have disturbed morphologies and may not be well-fit by a single Sérsic profile. If we remove this cut, we also see more star bursting systems above the main sequence in our observational sample. Secondly, the COSMOS ACS observations used by W11 cover a much larger area than the CANDELS WFC3 footprint and includes more rare objects such as starburst galaxies and massive, quiescent, very bulge-dominated galaxies. Comparing our Figure 4.5 and 4.10 with W11 Figure 3 and 8, W11 saw a slightly stronger decrease in size for galaxies above the main sequence than we do. Similarly, W11 see more galaxies with very high SFR density ($\log \Sigma_{\rm SFR} > 1$; Figure 4 and 8) which again are missing from our sample. These compact, starbursting objects are likely the same ones that we have just discussed.

[1]Note also that Figure 2 and 8 of W11 plot a slightly different mass range than our corresponding figures.

Comparison with other observational studies

We find that we are in qualitative agreement with several observational studies that have been done on the relationship between star formation and galaxy structural properties. As shown above, we find a similar segregation in the SFR-M_* plane due to bulge mass or B/T stellar mass ratio as found in Bluck et al. (2014), the inspiration for the plots in our Section 5. We are also in qualitative agreement on this front with Lang et al. (2014) who found this type of segregation in CANDELS/3D-HST data (see also a comparison with our model in that work). Omand et al. (2014) found a simple dependence of quiescent fraction on B/T by flipping the type of analysis done here; they looked at the quiescent fraction in bins across the stellar mass-bulge fraction plane and found complementary behavior to what we have found. Wake et al. (2012), Teimoorinia et al. (2016) and Bluck et al. (2016) all find strong dependence of star formation on central velocity dispersion at low redshift, as we see in the left panel of the second row of our Figure 4.8. Woo et al. (2013) sees segregation in the SFR-M_* plane due to halo mass, which we also see quite strongly in the bottom panel of Figure 4.13. Our results are also in qualitative agreement with those of Woo et al. (2015b) who examined the distribution of sSFR for galaxies in bins of $\Sigma_{1\mathrm{kpc}}$ (analogous to our Sérsic index) with fixed halo mass and vice versa.

Comparison with other theoretical studies

Many studies based on semi-analytic models have shown that bulge-dominated galaxies in massive halos tend to be red and quiescent (Bower et al. 2006; Croton et al. 2006; Somerville et al. 2008a; Kimm et al. 2009; Lang et al. 2014), in general qualitative agreement with our results. As shown by e.g. Kimm et al. (2009) and Lang et al. (2014), different SAMs produce different relative degrees of correlation of the fraction of quenched galaxies with halo mass and bulge mass, reflecting differences in the physical recipes responsible for quenching star formation in

the models. However, we are not aware of any other SAM-based comparison that has examined the continuous distribution of galaxy structural properties in the SFR-M_* plane as we have done here.

Such an analysis has been done for the Illustris numerical hydrodynamical simulations at $z = 0$, by Snyder et al. (2015b). The top left panel of their Figure 5 is strikingly similar to our redshift zero panel from Figure 4.3, although it should be kept in mind that their color coding is based on a different metric representing how bulge-dominated the galaxy is (Gini-M_{20}). Similarly, in their Figure 10 Snyder et al. (2015b) show that quiescent galaxies are more compact at a given mass than star forming galaxies, although they note that the sizes of galaxies in Illustris are systematically too large. Snyder et al. (2015b) show that quenching in the Illustris simulations is clearly associated with the growth of a massive SMBH as well as a massive halo, very similar to what we find in our SAMs. Snyder et al. (2015b) have not presented a detailed comparison with observations. In another Illustris-based analysis, Sparre et al. (2015) showed that their simulations were lacking in extreme starburst galaxies (outliers above the SFMS), similar to what we find in our SAMs. The predicted population of extreme starbursts is likely quite sensitive to numerical resolution as well as the treatment of the interstellar medium and feedback.

In another type of study, Zolotov et al. (2015) and Tacchella et al. (2016) analyzed the star formation rates and sizes of a set of high resolution "zoom-in" simulations. These 26 moderately massive halos are not representative of a cosmological sample, and have not been run past $z = 1$, but they attain considerably higher resolution and contain arguably more physical "sub-grid" recipes for processes such as star formation and stellar feedback than large cosmological volumes like Illustris. Zolotov et al. (2015) and Tacchella et al. (2016) emphasize that in their simulations, mergers and violent disk instabilities can lead to rapid gas inflow, building a compact, dense nucleus. They find that this "compactification" phase is in general soon followed by a rapid

decrease in SFR due to the decreasing inflow rate relative to the stellar-driven outflows. These authors also emphasize the role of building up a massive halo that can support a virial shock in driving the onset of quenching. However, these simulations do not include AGN feedback. This is likely the reason that, as noted by these authors, galaxies in these simulations do not "fully quench". It can be seen in Fig. 8 of Tacchella et al. (2016) that the simulations contain very few galaxies that are more than 1 dex below the SFMS, while the CANDELS observations show a significant population of such "strongly quenched" galaxies even at $1.5 < z < 2.5$. Figure 8 of Tacchella et al. (2016) shows that within ± 0.5 dex of the SFMS, galaxies in their simulations have a weak dependence of structural properties (stellar mass density, radius, Sérsic index) as a function of main sequence residual. This is in qualitative agreement with our SAM predictions, and with the CANDELS observations. It also suggests that in order to create the strong outliers from the SFMS seen in observations, additional physical processes (such as AGN feedback) accompanied by fairly dramatic structural transformation are likely needed.

4.6.2 Interpretation of Results

Overall, our model's agreement with observations is qualitatively very good, although there are some recurring issues which manifest many times in the above analysis. We now discuss both sides of this coin: What does our model tell us about the Universe when the two agree with each other, and what does the Universe tell us about our model when they don't?

What Our Model Tells Us About the Universe

The broad agreement between our model and the observations is extremely encouraging and suggests a plausible physical scenario that can explain the observed correlations. In this picture, relatively smooth accretion of gas fuels star formation and builds up rotationally supported disks. The radial size of the disk that forms is roughly proportional to the angular momentum of the

gas, which (on average) traces that of the dark matter halo. Relatively minor perturbations, such as minor mergers or disk instabilities, cause galaxies to oscillate around the SFMS as suggested in Tacchella et al. (2016), and seen also in our models. As long as galaxies remain in this relatively smooth undisturbed growth phase, their structural properties do not show a strong correlation with their distance from the SFMS.

Eventually, either through many small perturbations or a few larger ones (see e.g. Figure 14 of Chapter 3), a galaxy can build up a sufficiently massive black hole that AGN feedback prevents further significant cooling, perhaps also rapidly removing the star forming ISM through powerful winds. In the models presented here, bulge growth and black hole growth are explicitly linked, and both are fed through a combination of major and minor mergers and disk instabilities. It is certainly not clear that the details of the implementation of these processes are correct in our simulations or any existing ones, but it is not unexpected that the build up of a dense central nucleus and rapid feeding of a SMBH should go together. In our models, this linked growth of a compact, dense structure in the centers of galaxies and the engine that drives feedback (the SMBH) is the causal driver of the strong correlations between structure and SFR for galaxies that are below the SFMS. It is plausible that this is also the case in the real Universe. We note also that although there is general consensus that what is sometimes called 'halo quenching' (the build up of a halo massive enough to sustain a virial shock) is *not by itself sufficient to cause strong and long-duration quenching* (Choi et al. 2015; Pontzen et al. 2017), it is certainly reasonable to suppose that any sort of AGN feedback will have an easier time stopping the accretion of hot, low density, isotropically distributed gas than that of dense, cold, filamentary gas. Because the fraction of accretion via the "hot mode" versus "cold mode" increases strongly with increasing halo mass (Birnboim & Dekel 2003; Dekel & Birnboim 2006; Kereš et al. 2005), it may therefore be that some combination of halo mass and black hole mass is in fact the best indicator of whether the conditions for quenching are met (see Terrazas et al., in prep.; also

Snyder et al. (2015b) and Woo et al. (2015b)). This will be an interesting issue to explore in simulations with more detailed treatment of AGN feedback.

Our model also suggests the existence of some rather radially large galaxies in the two lowest redshift bins (most prominent in the left panel and below the main sequence in the middle panel of 4.10). These galaxies do not appear to be present in existing catalogs from GAMA or CANDELS, but an interesting question is whether these objects could be missed due to their very low surface brightness. The recent discovery of "ultra diffuse galaxies" in the Coma and Virgo cluster (van Dokkum et al. 2015a,b; Koda et al. 2015; Mihos et al. 2015), as well as extremely large disk galaxies (Ogle et al. 2016), have raised the question of whether there might be more large, diffuse galaxies out there than previously thought. Using the effective soft surface brightness limit of GAMA (23.5 mag/arcsec^2 in the r-band (Baldry et al. 2012)), we estimate that over 17% of model galaxies in our lowest redshift bin with effective radii >10 kpc and at least 1.5 dex below the main sequence would be undetected. About two-thirds of these are disk galaxies, and the rest are spheroid dominated. A detailed comparison between our model predictions and the observed populations of ultra-diffuse galaxies is beyond the scope of this work, but it is intriguing that our models predict there may be a population of large diffuse galaxies.

What the Universe Tells Us About Our Model

Unfortunately (or perhaps fortunately) the universe does not take our suggestions on how to run itself, so here we discuss how our model is failing to reproduce the observations and what we may be able to learn from this. As discussed above, our most quenched galaxies, which are the result of intense AGN feedback after building a massive black hole, have SFRs which are lower than those in the quiescent cloud of observed galaxies. This probably indicates that our treatment of AGN feedback is too simple. Real galaxies likely undergo short duty-cycle bouts of quenching and rejuvanation, which our simple model does not resolve. Also, although

the observed population of compact, high-central density starburst systems well above the SFMS fits into our theoretical merger-based picture, we have trouble actually producing enough of these systems when compared with the observations. This is a direct result of the treatment of star formation enhancement in merger-triggered bursts implemented in our SAMs, which was based on a now rather out-of-date set of hydrodynamic simulations of binary mergers. As noted above, other hydro simulations, such as the Illustris simulation, have had similar trouble producing "extreme" starbursts which we would expect to see far above the main sequence (Sparre et al. 2015). We expect future simulations with higher resolution and a more detailed treatment of the ISM will help us understand how this population is produced.

The slight peaks in radial size above and below the main sequence apparent in Figure 4.10 appear to be due to highly star-forming galaxies which still have a significant disk component and disk-dominated galaxies which are slowly fading off of the main sequence, respectively. Examples of the disky highly star-forming galaxies can be found in the upper-rightmost occupied bins of the top middle panels of Figures 4.3 and 4.5. These galaxies, while likely starbursts, still have fairly low Sérsic indices and large sizes. A few galaxies like this are enough to cause the peak seen in Figure 4.10, as we start to see fewer galaxies that far above the main sequence overall. The large galaxies just below the main sequence appear to be due to a slight difference in the 2D size distributions seen in Figure 4.5. In the observational panels, we see that in the two higher redshift bins, for a given mass, as we move below the main sequence we only see sizes equal to or less than the sizes seen on the main sequence. In the model, however, at high stellar masses, especially, it is possible to encounter sizes larger than those found on the main sequence. Because this occurs at high mass and because the corresponding bins in Figure 4.3 are fairly disk-dominated, it seems that these are fairly massive disks which have fallen below the main sequence but which are not yet quiescent. While we expect galaxies to be kept on the main sequence by these cycles of activity and relative dormancy, it appears that perhaps this cycle

is affecting the sizes of our galaxies too strongly, as there is no sign of this size behavior in the observations.

As noted above, we also find that our model produces quiescent galaxies that are somewhat larger than those observed, and this discrepancy increases with decreasing redshift (see Figure 4.10). The systematic nature of this discrepancy in our lowest redshift bin suggests the need to refine overall how sizes are computed.

Finally, while it is possible that some of the large model galaxies in our lowest redshift bin might be missed observationally due to selection effects, this is likely not the full cause of the disagreement, especially for galaxies on the main sequence. Because disk galaxies are the largest galaxies for their mass range, it would be easy to assume that most of our very large galaxies are disk-dominated ones that escaped merging and were allowed to grow out of control. However, more than half of our model galaxies with sizes >20 kpc are in fact spheroid-dominated. This is doubtless due to the limitations of the relatively simple modeling of the sizes of disks and spheroids in our SAMs. A clue is that the sizes of our largest galaxies, regardless of morphology, are correlated with abnormally low halo concentrations. While the average halo concentration of our low redshift sample is ~ 8.5, when limiting to galaxies with effective radii >20.0 kpc we find an average halo concentration of ~ 7.0. A more detailed investigation of the size-mass relation in our model and its evolution will be presented in Somerville et al. (in prep.).

Progenitor Bias

Lilly & Carollo (2016) have suggested that the correlations between star formation and structural properties might be explained by progenitor bias. For galaxies at any epoch, quiescent galaxies represent systems that left the main sequence at an earlier epoch when the universe was denser and galaxy sizes were characteristically smaller. Because of this, quiescent galaxies will be systematically smaller than galaxies that have continued to grow while on the main sequence,

regardless of any relationship between quenching mechanism and galaxy structure. As noted above, we have been careful to make the distinction between correlation and causation in this work, but can look to our model for guidance. While progenitor bias exists in our model, as characteristic galaxy sizes grow with cosmic time, we find that we are unable to reproduce basic statistical galaxy properties like the stellar mass function, luminosity functions or stellar mass-to-halo mass relationship without including some form of feedback. Meanwhile, on the observational side, Bluck et al. (2016) have found that high central velocity dispersion is a good predictor for the fraction of green valley galaxies as well as for quiescent galaxies. Green valley galaxies aren't as likely to have left the main sequence a long time ago like quiescent galaxies, suggesting that feedback is a better explanation for these systems than progenitor bias. In light of this, while we acknowledge that progenitor bias may be a factor in the structural correlations observed here, we believe our model still represents a plausible explanation for our observations.

4.7 Summary and Conclusions

In this work, we have investigated the correlation of galaxy structural properties with their location in the plane of star formation rate and stellar mass. We studied structural properties such as morphology as represented by Sérsic index, radial size, and mean stellar surface density as a continuous function of a galaxy's distance from the mean star forming main sequence at its observation time. We carried out a parallel analysis on the GAMA survey of nearby galaxies, the CANDELS survey which can measure galaxy structural properties to $z \sim 3$, and a semi-analytic model that tracks the evolution of galaxy properties within a cosmological framework. We focus on the population of galaxies with stellar mass $>10^{10} M_{\odot}$, for which these surveys are highly complete and the measurement of structural properties is robust.

Our main findings are as follows:

- Within ± 0.5 dex of the SFMS, we find a weak dependence of galaxy structural properties on the distance from the MS. Below the main sequence, we see a rapidly steepening dependence such that galaxies with larger negative MS residuals had higher median Sérsic index, smaller size, and higher stellar surface density. These trends are seen in both nearby galaxies (GAMA) and out to $z \sim 2.5$ (CANDELS), and are qualitatively very similar in the theoretical models.

- Our observational results are very similar overall to the results of an earlier study by Wuyts et al. (2011, W11). One difference between our results and those of W11 is that we do not find a significant population of galaxies with high Sérsic index ($n \sim 3.5$–4) in the extreme starburst region above the SFMS. Similarly, we do not see as large a population of galaxies with small radii above the SFMS. We suspect that these galaxies are removed from our sample due to our requirement of being well fit by a single component Sérsic profile.

- The good qualitative agreement between our model results and the observations suggests a plausible causal explanation for the observed correlations; namely, that central spheroids and black holes grow together, and black holes play a major role in quenching star formation in galaxies.

- Quantitatively, our models disagree with the observations in some important respects. Our models do not produce as large a quiescent population at high redshift ($z > 1.5$) as seen in the observations (as already noted in Chapter 3), and the SFR for the model quiescent galaxies are lower than those of observed quiescent galaxies. This suggests the need to refine our modeling of AGN feedback. Moreover, the Sérsic indices of galaxies below the SFMS are systematically lower (more disk-like) in the models, while on and below the SFMS, especially at low redshift, the sizes of our galaxies are too large. As a result, there is not as large a separation between the sizes for the star forming and quiescent populations

in the models as there is seen in the observations. This suggests that we also need to refine our determination of galaxy sizes in the model.

Chapter 5

Momentum-driven Winds from Radiatively Efficient Black Hole Accretion and Their Impact on Galaxies

5.1 Introduction

It has been estimated by studying absorption lines associated with active galactic nuclei (AGN) across a large range of luminosities that upwards of 60% of AGN exhibit outflows, meaning that outflows are an important part of the process of supermassive black hole (SMBH) growth and accretion (Ganguly & Brotherton 2008). This AGN-outflow connection could even be universal if the typical covering fraction of outflows were $\sim 60\%$. Evidence of these outflows being potentially very powerful comes in the form of observations of broad absorption line quasars, which make up $\sim 20\%$ of the observed QSO population (Knigge et al. 2008). These systems show evidence of outflows being launched at velocities as fast as 10,000 km/s or more in the vicinity of the SMBH (Crenshaw et al. 2003; Moe et al. 2009; Dunn et al. 2010; Tombesi et al. 2010, 2013, 2015). There is also evidence for winds driven by AGN in low redshift systems (Cicone et al. 2014; Cheung et al. 2016). However, it is quite difficult to constrain the size and extent of outflows, and therefore the mass outflow rate, based on absorption line observations (Arav et al. 2012; Maiolino et al. 2012; Arav et al. 2013; Chamberlain & Arav 2015). Recently, integral field unit (IFU) observations have been used to more fully map the gas around AGN and gain insight into the kinematics of AGN-driven winds. These studies have revealed that outflows can act on large scales and entrain large quantities of gas on their way out, although it is difficult to say for sure

how much of a role AGN play in driving these winds as opposed to stellar feedback processes (Tremonti et al. 2007; Prochaska & Hennawi 2009; Alatalo et al. 2011; Rupke & Veilleux 2011; Sturm et al. 2011; Rupke & Veilleux 2013; Zakamska & Greene 2014; Perna et al. 2015).

The overall effect that these outflows have on their host galaxies, specifically on the gas cycle and future star formation rate, is unclear, although in general outflows are important for the regulation of galaxy growth (Lilly et al. 2013). Some observational studies have investigated the relationship between AGN activity and star formation in galaxies, but the results have been controversial. Some studies conclude that winds can remove enough gas to cause negative feedback on star formation (Rupke & Veilleux 2013), although it is not clear if the gas will remain outside of the galaxy, and that the presence of a strong AGN and a suppression of star formation are correlated (Page et al. 2012). However, other studies find that AGN preferentially live in galaxies on or even above the star-forming main sequence (Santini et al. 2012; Rosario et al. 2013a,b) where they can drive powerful outflows (Genzel et al. 2014), or even that AGN are stimulating star formation (positive feedback) (Feain et al. 2007; Zinn et al. 2013). The disagreement between different observational studies originates from the different selection criteria used by various works and the different timescales on which galaxies and their central supermassive black holes operate (see Harrison (2017) for details).

On the theoretical side, AGN feedback is often invoked to explain many observed properties of galaxy populations. It is believed that almost all galaxies with a bulge component host a supermassive black hole (SMBH) at their center (Magorrian et al. 1998). The mass of these central SMBHs is also known to be correlated with several properties of their host galaxies, specifically the mass, velocity dispersion and luminosity of their bulge components (Kormendy & Richstone 1995; Ferrarese & Merritt 2000; Gebhardt et al. 2000; Tremaine et al. 2002; Marconi & Hunt 2003; Häring & Rix 2004). Meanwhile, there is a bimodality in the colors of the galaxy population (Baldry et al. 2004; Bell et al. 2004a) and the growth of these two populations

suggests that blue, star-forming galaxies are being transformed into red, quiescent galaxies, with the dearth of galaxies between the two peaks in color or star-formation rate space indicating a fast transition timescale for a significant fraction of transitioning galaxies (Bell et al. 2004a; Faber et al. 2007; Pandya et al. 2016).

With these phenomena in mind, as well as the large amounts of energy which can be released by an accreting SMBH (Lynden-Bell 1969), AGN feedback becomes an appealing explanation for this galaxy "quenching," as well as for explaining the origin of the various black hole scaling relations mentioned above. It has also frequently been invoked to solve the overcooling problem in massive galaxies, suppressing the late formation of stellar mass and bringing theoretical predictions into alignment with the observed high-mass ends of the stellar mass function and stellar mass-halo mass relation (Somerville et al. 2015; Naab & Ostriker 2016, and references therein).

Theorists generally categorize AGN feedback into two broad types: "radiative" mode and "jet" mode (Heckman & Best 2014). Radiative mode is associated with radiatively efficient accretion, relatively high accretion rates (above a few hundredths of the Eddington rate), and is thought to be fueled by a classical optically thick, geometrically thin accretion disc (Shakura & Sunyaev 1973). The hard radiation field emanating from the accretion disc can Compton- and photo-heat as well as photo-ionize and photo-dissociate gas. In addition, radiation pressure on dust and free electrons can drive outflows, and this is likely the origin of the broad absorption line winds discussed above (Proga & Kurosawa 2009; Gaskell et al. 2016). When accretion rates drop lower than about $\simeq 0.01$ of the Eddington rate, the accretion becomes radiatively inefficient, with most of the energy instead emerging as highly collimated relativistic jets. These jets are often observed at radio frequencies, giving rise to the term "radio mode" feedback. The jets appear to be able to heat the diffuse hot halo gas via giant bubbles (seen in X-ray observations), sound waves, and weak shocks (see Fabian 2012; Heckman & Best 2014, for reviews).

Phenomenologically, theorists often speak of "ejective" feedback, in which star formation is

quenched due to the removal of the ISM from the galaxy, and "preventative" feedback, in which star formation is eventually choked off by the lack of fuel, as the inflow of fresh or recycled gas is suppressed. As noted by Peng et al. (2015) and others, the implications and effects of these two types of mechanisms for various aspects of galaxy evolution will differ in important ways. It is often assumed that "radiative" mode (also known as "quasar mode" and "bright mode") feedback works in a solely ejective manner, while "jet" mode (or radio mode) is solely preventative. (As a result, jet mode feedback is sometimes also referred to as "maintenance mode"). Indeed, these assumptions are built into the implementations of AGN feedback in most semi-analytic models, such as the one used in Chapters 3 and 4. However, the work presented here will call into question the first assumption, while observations of powerful outflows in systems with giant radio jets seems to challenge the second (Torresi et al. 2012).

Many previous simulations have included prescriptions for AGN feedback, although usually the radiative mode of feedback is implemented via deposition of thermal energy, while mechanical feedback is reserved for lower Eddington ratios and is associated with the jet mode of feedback (Springel et al. 2005; Di Matteo et al. 2012; Dubois et al. 2013; Vogelsberger et al. 2014; Hirschmann et al. 2014; Khandai et al. 2015; Schaye et al. 2015; Steinborn et al. 2015; Barai et al. 2016; Weinberger et al. 2017). Although such simulations can be successful at reproducing galaxy properties, it is unclear whether just depositing thermal energy associated with the radiative mode of black hole accretion can drive winds similar to those seen in observations. Moreover, thermal energy input leads to halo X-ray luminosities in disagreement with observations. If no winds are launched, the thermal energy that is radiated away is concentrated in the center of the galaxy, resulting in halo X-ray luminosities that are too low (Bogdán et al. 2015), while if there are only weak winds, the radiating hot gas that gets pushed into the halo results in X-ray luminosities that are too high when compared with observations (Choi et al. 2012, 2014; Schaye et al. 2015).

The motivation behind the work presented here is that outflowing hot, shocked gas on scales below those that can be explicitly resolved in cosmological simulations can impart momentum to gas, which cannot be radiated away. The physics is similar to the momentum boost occuring at the end of the Sedov-Taylor phase in a supernova explosion. Of the simulations that have modeled AGN feedback, relatively few have included a momentum-driven prescription associated with efficient black hole accretion. Momentum-driven wind scalings were adopted in the "Santa Cruz" semi-analytic model and resulted in more efficient galaxy quenching, again seen in Chapters 3 and 4 (Somerville et al. 2008a). In terms of hydrodynamical simulations, Debuhr et al. (2011a) and Debuhr et al. (2011b) investigated momentum-driven winds via radiation pressure in galaxy merger simulations. More recently, Anglés-Alcázar et al. (2014) implemented various wind models, including momentum-driven, in cosmological zoom simulations and found that including winds produced realistic disc galaxies at $z \sim 2$. Hopkins et al. (2016) has investigated the interplay between stellar and AGN feedback in isolated galaxies. They injected momentum flux around the accreting black hole and found powerful outflows that strongly suppressed star formation by removing gas. Eisenreich et al. (2017) investigated the effect of the AGN prescription used in this work on the metal content of a series of idealized elliptical galaxies. None of these hydrodynamical works, however, were in a cosmological context. In terms of cosmological simulations, the kinetic feedback model of Weinberger et al. (2017) was shown to bring the baryon content of galaxies in the *Illustris* simulation into better agreement with observations (Pillepich et al. 2017), although their mechanical feedback prescription is associated only with low black hole accretion rates.

Switching gears from examining the effect of an AGN feedback prescription on galaxy population statistics as in the last two chapters, in this chapter we focus on a series of hydrodynamical cosmological zoom simulations. In these simulations, in addition to thermal energy, we also deposit momentum associated with radiatively efficient accretion into the gas particles surrounding

the black hole, and, further, model photo-ionization and photo-heating by this radiation. The prescriptions for momentum and radiation feedback from AGN (MrAGN) presented in Choi et al. (2012, 2014, 2015) have been implemented into SPHGAL (Hu et al. 2014), an updated version of the Smoothed Particle Hydrodynamics code GADGET-3 (Springel 2005). The code has also recently been modified to include updated treatments of many physical processes, including an improved treatment of stellar and supernova feedback (Núñez et al. 2017), chemical enrichment and metal line cooling (Aumer et al. 2013), photoelectric heating, and X-ray heating by the meta-galactic X-ray background. These updates are described in detail in Choi et al. (2017), and an overview can be found in Chapter 2.

We address several questions: 1) what are the histories of inflow and outflow for these galaxies? 2) how much of the material ejected by winds is removed permanently and how much comes back, and on what timescales? and 3) how do these winds affect the host galaxy? We compare simulations including both AGN feedback and feedback due to stars and supernovae (MrAGN) to a matched set of simulations that include only stellar and supernova feedback (NoAGN). In this way we can attempt to isolate the effect of the AGN-driven winds on the gas cycle in these halos, which have virial masses of $\sim 10^{12} - 10^{13.4} M_{\odot}$, and consider how the answers to the questions posed above differ in the MrAGN vs. NoAGN cases. In this way we will narrow our focus from the last two chapters and study the effect of AGN feedback on the gas in individual galaxies. In Section 2, we describe our methods for matching galaxies between runs and particle tracking, and in Section 3 we present our results. In Section 4 we discuss our results. We summarize in Section 5.

5.2 Methods

5.2.1 Galaxy Matching

In order to compare MrAGN galaxies with their NoAGN counterparts, and also to examine inflowing and outflowing gas in our simulations, we must first find the center of our haloes of interest and make sure that we are tracking the same progenitor back with redshift in both runs. We utilize two different codes to track the halo centers: ROCKSTAR (Behroozi et al. 2013a) and GTRACE, a tool built specifically for analyzing GADGET snapshots. In 24 of our 30 pairs, at least one of these tools found the center of the same progenitor in both runs by $z = 1$. Going back to $z = 2$, we have 23 matched pairs and by $z = 3$ we have 21 matched pairs. There are brief periods when the center even of these matched pairs is lost, such as when a satellite of comparable mass approaches the main progenitor, but this is generally only for a short time and can be easily identified when a relatively stable quantity, such as stellar mass, suddenly dips as can be seen in Figure 5.1 below. We exclude the six galaxies for which the found centers do not correspond to the same progenitors by $z = 1$.

5.2.2 Particle Tracking

With the centers found, we track the flow of particles across two shells: one at 10% of the virial radius and one at the virial radius. We refer to the former as the "galaxy radius" $r_{\rm g}$ and the latter as the "halo radius" $r_{\rm h}$. The tracking begins when there is a reliable center found for both the MrAGN and NoAGN runs; for our three case study galaxies, for which it is important to track over the same period (as we display cumulative quantities), this tracking begins at z $\sim$ 4, give or take one timestep ($\sim$ 0.115 Gyr at $z \sim 4$). Almost all of the rest of our galaxies are tracked by z=3, as mentioned above. At each timestep the gas particles which are inside both of these radii are catalogued. In the next timestep any particle that was inside (outside) the radius of

interest in the last timestep and is now outside (inside) that radius and has a positive (negative) radial velocity is considered outflowing (inflowing). The inflowing and outflowing mass at each timestep is stored, and the inflow and outflow rate can be calculated by using the timestep between snapshots. We also keep track of whether a gas particle is accreting or outflowing for the first time, or if it has done so previously. Finally, we keep track of how long it takes for individual gas particles to be recycled, as well as the maximum radial displacement experienced by the particle during each recycling event (see Übler et al. (2014) for a similar treatment of gas particles in disc galaxies). Unless otherwise specified, stellar and gas masses of the galaxy are calculated within 10% of the virial radius.

5.3 Results

Here we present the results of our analysis, first examining the detailed histories of a few representative galaxies, then looking at broader trends in galaxy and inflow/outflow properties for the entire set of galaxies. We note again that outflows are driven by both stars and supernovae and AGN. Our analysis also captures inflow and outflow due simply to thermal motions of gas. This is more apparent in our NoAGN galaxies, as will be mentioned below.

5.3.1 Case Studies

When examining the histories of individual galaxies in terms of their basic properties and the properties of their inflows and outflows, some broad classes emerge, mainly as a result of galaxy mass. Below we present three galaxies representative of their mass bins: "high mass" m0163 ($M_{*,\mathrm{final}} \sim 10^{11.4} M_\odot$ and $M_{\mathrm{h,final}} \sim 10^{13.1} M_\odot$), "intermediate mass" m0329 ($M_{*,\mathrm{final}} \sim 10^{11.3} M_\odot$ and $M_{\mathrm{h,final}} \sim 10^{12.7} M_\odot$), and "low mass" m0501 ($M_{*,\mathrm{final}} \sim 10^{11.2} M_\odot$ and $M_{\mathrm{h,final}} \sim 10^{12.5} M_\odot$). We study the baryon cycles in these halos in detail, and use them as exemplars of more general trends that we discuss later.

Galaxy Property and Gas Flow Histories

Halo m0163 has a history characteristic of the more massive end of our population. It has a final halo mass of $\log(M_{\rm h}/M_\odot) \sim 13.1$ and a final stellar mass of $\log(M_*/M_\odot) \sim 11.4$ in the MrAGN run. Figure 5.1 shows the evolutionary histories of different galaxy, black hole, inflow and outflow properties. In panels (a) and (e) we see that the halo mass (shown multiplied by the universal baryon fraction, 0.1658) is largely unaffected by AGN feedback, while the final stellar mass is reduced by roughly 0.4 dex. While the cold gas mass (T$<2\times10^4$ K) decreases only mildly in the NoAGN run, all of the cold gas within r_g is removed or heated by AGN feedback in the MrAGN run. The hot gas mass of the MrAGN galaxy is only slightly smaller than that for the NoAGN galaxy, due to removal of some of the hot gas from the halo. We can also see the growth of the black hole in the MrAGN run, which reaches a final mass of $\log(M_*/M_\odot) = 9.2$. The green dashed lines denote mergers for which the halo ratio is greater than 1:10.

Panels (b) and (f) show that as the cold gas mass decreases, the star formation rate falls just as drastically, which is partially responsible for the smaller final stellar mass found in the MrAGN run. Star formation continues at a nearly constant rate in the NoAGN run (several tens of solar masses per year). We also see the black hole accretion rate (BHAR), which gradually increases from $\sim$ 4 Gyrs until about 12 Gyr after the start of the simulation. After this point, black hole accretion itself is quenched.

Panels (c), (d), (g) and (h) show the inflow and outflow rates for both runs on galaxy scales $r_{\rm g}$ and halo scales $r_{\rm h}$. In the MrAGN run, the inflow rate at $r_{\rm g}$ is suppressed relative to the NoAGN run value of $\sim 50\ M_\odot$/yr to only 1-2 $M_\odot$/yr, and overcome by the outflow rate after the two early merger events at $\sim$ 3-5 Gyrs (just after $z \sim 2$). The outflow rate continues to mirror the inflow rate thereafter at $\sim$ 10-30 $M_\odot$/yr. At $r_{\rm h}$, this same spike in outflow rate occurs after a slight delay, due to material that was caught up in the initial outflow at $r_{\rm g}$ and eventually

Table 5.1: The final halo, stellar, black hole and hot gas masses, the cumulative gas inflow and outflow masses that crossed shells at the galaxy radius and the halo radius, and the cumulative inflow mass at the halo radius divided by the final halo mass times the universal baryon fraction for our three example galaxies, both for our MrAGN run and our NoAGN run. All masses are given in units of log solar masses.

Galaxy	Halo Mass	Stellar Mass	BH Mass	Hot Gas Mass	Inflow_g	Outflow_g	Inflow_h	Outflow_h	$M_{\text{in,h}}/f_\text{b}M_{\text{h},0}$
m0163 (Mr)	13.1	11.4	9.2	11.9	11.2	11.2	12.2	11.9	0.90
m0163 (No)	13.1	11.8	N/A	12.1	11.8	11.5	12.3	11.6	1.00
m0329 (Mr)	12.7	11.3	9.2	11.2	10.9	10.7	11.9	11.7	0.85
m0329 (No)	12.8	11.7	N/A	11.7	11.5	10.9	12.0	11.1	1.05
m0501 (Mr)	12.5	11.2	9.3	7.3	11.0	10.8	11.5	11.4	0.57
m0501 (No)	12.6	11.5	N/A	11.4	11.4	10.8	11.8	10.9	1.00

crosses the virial radius, pushing out even more material on its way. This results in outflow rates of as much as $\sim 300 M_\odot$/yr. The outflow rate at r_h, however, rarely overtakes the inflow rate, even in the MrAGN run. In the NoAGN run, inflow dominates at almost all times at both radii. The outflow rate at r_g in the NoAGN case steadily rises, eventually reaching an equilibrium with the inflow rate at a value higher than is seen in the MrAGN case. This is due to the fact that we have more gas in the central region in the NoAGN case which is cycling in and out of the galaxy due to thermal motions. The inflow rate at r_h is largely unaffected by AGN feedback, while the outflow rate in the MrAGN run is enhanced relative to the NoAGN case. This means that the AGN feedback acts mostly in an ejective way at this halo mass ($\sim 10^{13.1} M_\odot$) at halo scales, rather than preventatively. See Table 5.1 for the cumulative inflow and outflow gas masses that cross both shells over the duration of the simulation. Already apparent from Table 5.1 is the importance of preventative feedback, as represented by the cumulative mass in baryons that accreted onto the halo divided by the final halo mass times the universal baryon fraction.

Figure 5.2 is the same as Figure 5.1, but now for galaxy m0329. This galaxy falls near the middle of our mass range, with a final halo mass of $\log(M_\text{h}/M_\odot) \sim 12.7$ and a final stellar mass of $\log(M_*/M_\odot) \sim 11.3$ in the MrAGN run. We see again the difference between the stellar mass (again ~ 0.4 dex) and cold gas mass in the MrAGN run versus those in the NoAGN run.

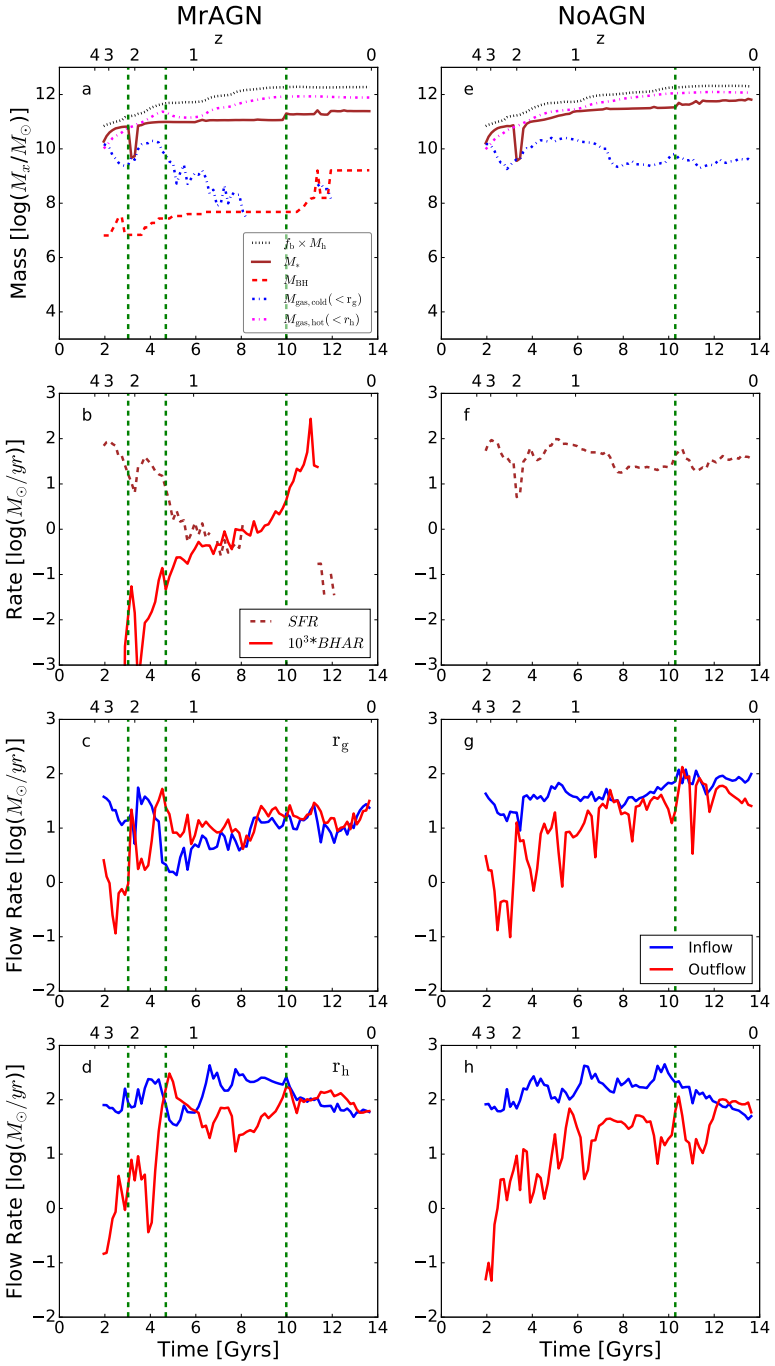

Figure 5.1: Baryon cycle history of the main progenitor galaxy in halo m0163. Left Column: Results for MrAGN run. Right Column: Results for NoAGN run. Top row: Evolution of galaxy properties – Baryon fraction times halo mass, stellar mass, black hole mass (for MrAGN run), cold gas mass within the galaxy radius (T<2×10^4K) and hot gas mass within the halo radius (T>2×10^4K). Second row: Evolution of star formation rate and black hole accretion rate (for MrAGN run; black hole accretion rate is scaled up by a factor of 1000). Third row: Inflow and outflow rates at the galaxy radius. Fourth row: Inflow and outflow rates at the halo radius. Green vertical dashed lines indicate halo merger events for which the halo mass ratio is 1:10 or greater. The final stellar mass in the MrAGN run is smaller due to the decrease in cold gas supply and thus star formation rate. AGN feedback does not affect the inflow of gas into the halo, but does mildly affect the inflow rate of gas at galactic scales. It also enhances outflows on both scales at early times.

The galaxy in the MrAGN run has a steeply decreasing cold gas mass, resulting in a steeply decreasing SFR. In the case of m0329, this also corresponds to an increasing black hole accretion rate. The suppression of inflow at both radii of interest is more pronounced than for m0163; the inflow rate at $r_{\rm g}$ is significantly (and permanently) decreased from >10 $M_\odot$/yr to 1-2 $M_\odot$/yr following a strong outflow event at $\sim 4-6$ Gyrs, concluding at $z \sim 1$. The inflow rate at $r_{\rm h}$ is also more noticeably decreased after this outflow event than it was for the more massive halo m0163; the final inflow rate at $r_{\rm h}$ is ~ 1.7 times larger in the NoAGN run than in the MrAGN run. This suggests that as we look at smaller halo masses and therefore shallower potential wells, *preventative feedback*, where AGN feedback not only removes material but also prevents new material from accreting, becomes more important (see the rightmost column of Table 5.1). The outflow rates at both radii match or exceed the inflow rates at almost all times after the initial outflow event in the MrAGN run. In the NoAGN case, inflows and outflows behave much as they did for m0163, with inflow always dominating.

Finally, Figure 5.3 is the same as Figures 5.1 and 5.2, but now for galaxy m0501. This galaxy is less massive than m0329 with a final halo mass of $\log(M_{\rm h}/M_\odot) \sim 12.52$ and a final stellar mass of $\log(M_*/M_\odot) \sim 11.22$ in the MrAGN run, and has a history more characteristic of the low mass galaxies in our suite. In the top four panels, the galaxy properties of m0501 evolve very similarly to those already examined for m0163 and m0329, except for hot gas in the MrAGN run, which is much more strongly affected. When focusing on the inflow and outflow properties, m0501 is very different. In the NoAGN case, things are much the same, with inflow dominating outflow at both radii at almost all times. In the MrAGN case, several bursts of outflow of between 10-30 $M_\odot$/yr dominate over inflow at $r_{\rm g}$ at around 4 Gyrs. This outflow is powerful enough to halt inflow, after which the outflow stops as well because the gas within $r_{\rm g}$ has been completely depleted. At $r_{\rm h}$, we see this outflow, having swept up gas in the halo and now removing ~ 100 $M_\odot$/yr, peak at a slightly later time and once again halt inflow across the virial radius. This outflow

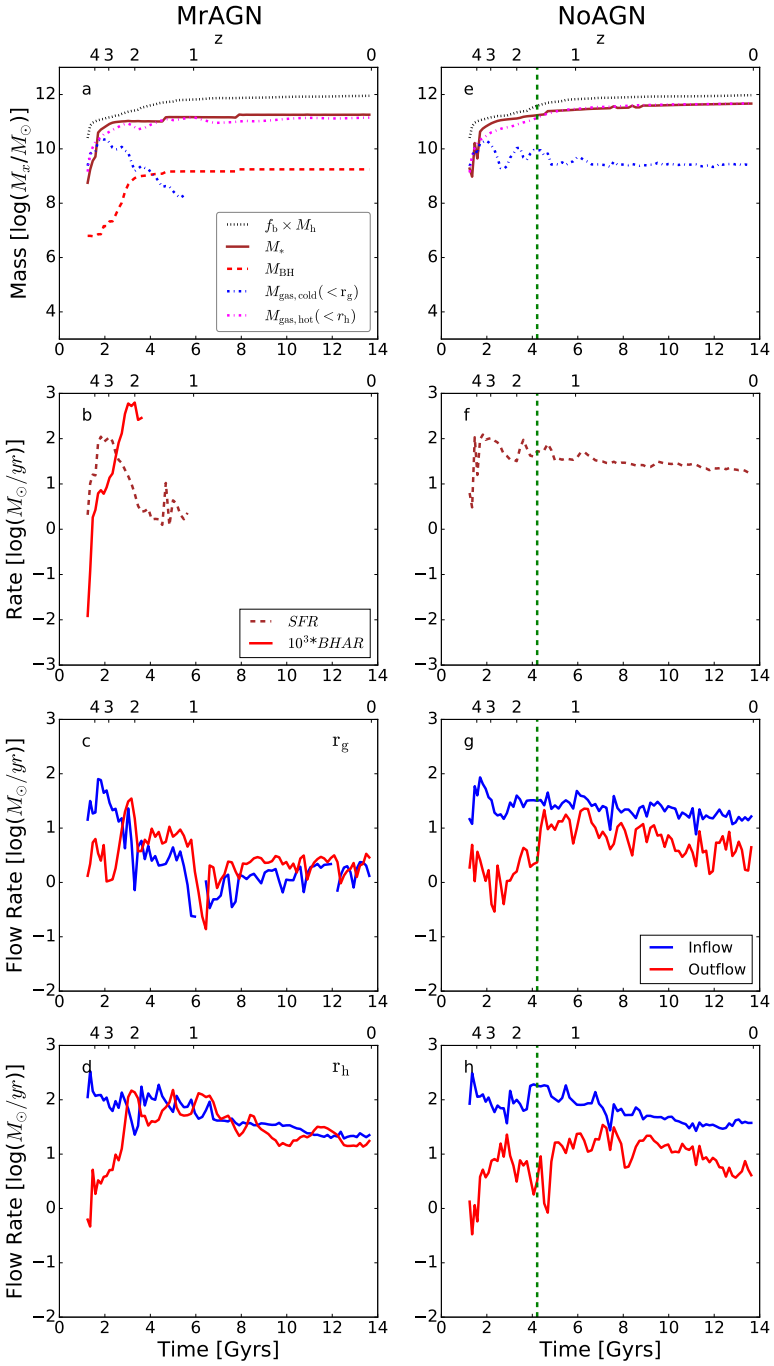

Figure 5.2: Same as Figure 5.1, but for halo m0329. Inflow in the MrAGN case is more noticeably suppressed at late times at both radii of interest than in the more massive halo m0163. Following an initial outflow event at $\sim 4-6$ Gyrs, outflow dominates inflow at the galaxy radius by a small amount, but consistently. In the NoAGN case inflow dominates outflow at all times at both radii.

then also tapers off as it has cleared most of the galaxy's halo gas as well. This is an extreme case where AGN feedback acts in both an ejective and a preventative way on dark matter halo scales. This is fairly rare, occurring only in 4 of our 30 MrAGN galaxies. These galaxies all have relatively small halo masses for our sample (the most massive has $M_{\rm h} \sim 10^{12.5} M_{\odot}$) and all contain a relatively large black hole mass for their halo mass, although they still sit on the $M - \sigma$ relation.

Gas Morphology and Velocity Structure

In Figure 5.4 we show vector maps of the gas velocities in m0163 overlaid onto color maps of the gas temperature for both runs at four different redshifts. The luminance of the gas in the images corresponds to its density. At $z \sim 3$ and $z \sim 2$, the images of the two runs look very similar to each other, with the main velocity features being filaments of gas funneling into the forming galaxy. At z $\sim$ 1, however, the two runs look very different. The galaxy in the MrAGN run is going through a large bout of outflow, which can be seen in panels (c) and (d) of Figure 5.1 at $\sim$ 5 Gyrs. Meanwhile, in the NoAGN run, the bulk of the velocity features are still due to inflowing material onto the galaxy. At $z \sim 0$, while the two runs look very similar, the MrAGN run exhibits a more diffuse hot gas halo. While gas has been heated by stellar and supernova feedback, the NoAGN run still exhibits somewhat ordered motions and inflows as opposed to the MrAGN run, in which we see material being pushed out of and away from the galaxy.

In Figure 5.5, the galaxy m0329 in the MrAGN run is undergoing a major outflow by $z \sim 2$, in contrast to its NoAGN counterpart, which is dominated by filamentary accretion. At $z \sim 1$, while the NoAGN galaxy also appears to be undergoing feedback as demonstrated by the bulk of hot gas, there is no strong outflow signature as we see again in the MrAGN case. Even in the MrAGN run, however, there is still a strong filamentary inflow feature outside of the outflow sphere of influence. When this inflowing gas reaches the outflow, some of it is heated and/or

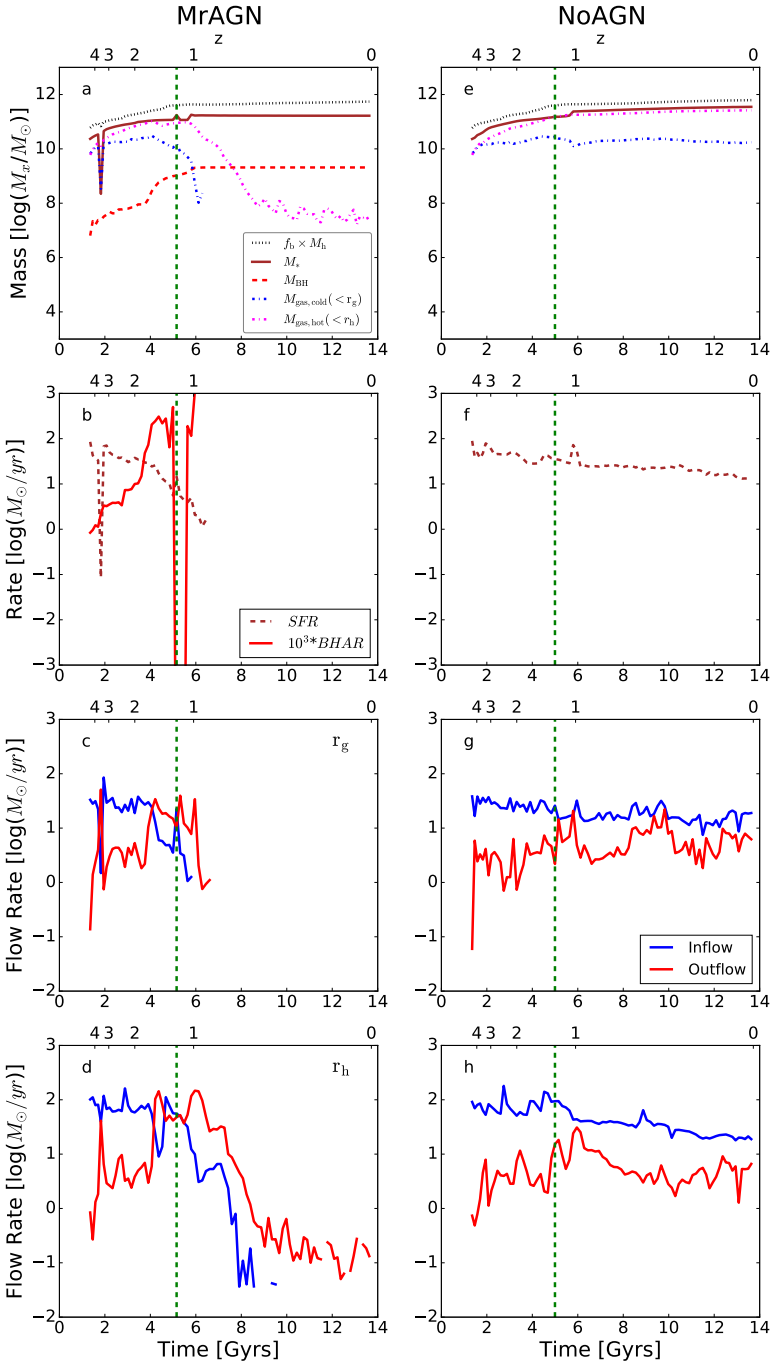

Figure 5.3: Same as Figures 5.1 and 5.2, but for halo m0501. While the NoAGN case is similar to the previous galaxies, the MrAGN case is exceptional in that AGN feedback completely clears the galaxy of gas and prevents any new gas from accreting for several billion years, even on the scale of the halo.

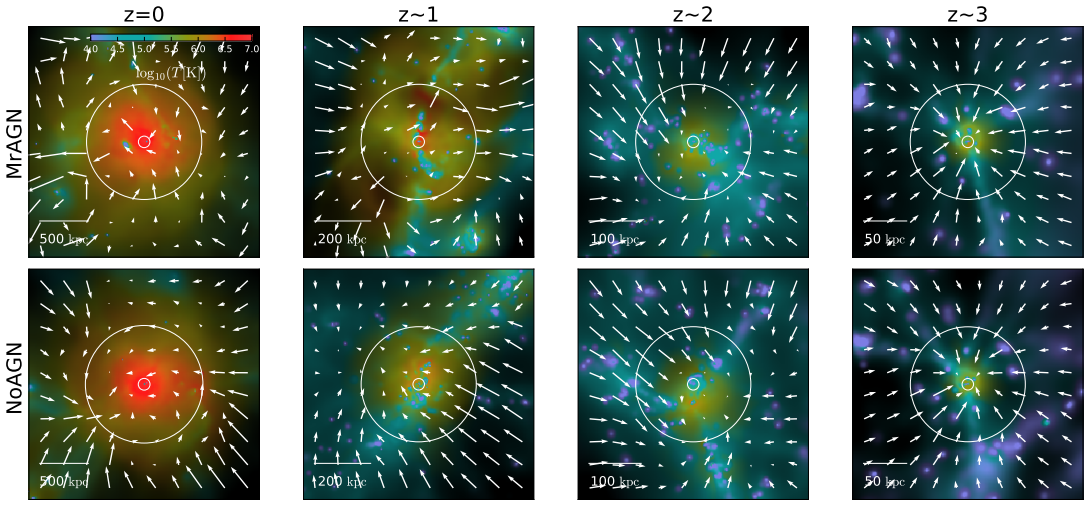

Figure 5.4: Gas temperature and velocity vector maps for galaxy m0163. Images created using `pygad` (Röttgers 2017). The color of the gas images in each panel corresponds to gas temperature, while the luminance corresponds to gas density. The velocity vectors are calculated for a slice with a thickness of the halo radius at the redshift of interest, with contributing gas velocities weighted by their densities. The arrow lengths are normalized by the number of spatial bins so as not to overlap, and then normalized by the average arrow length. Stars in these galaxies are not shown. Top row: Results for MrAGN run. Bottom row: Results for NoAGN run. The velocity vectors are overlaid onto gas temperature maps at four redshifts. White circles denote the current galaxy radius and the halo radius. At $z \sim 3$, the two runs are nearly identical and dominated by accretion along filaments. At $z \sim 2$, the two runs are still very similar, with the bulk velocity flow due to gas inflowing onto the central galaxy. At $z \sim 1$, the MrAGN run is undergoing a bout of outflow, while the NoAGN run is still steadily accreting gas. At $z \sim 0$, though the remnants appear similar, the gas in the MrAGN run is more diffuse.

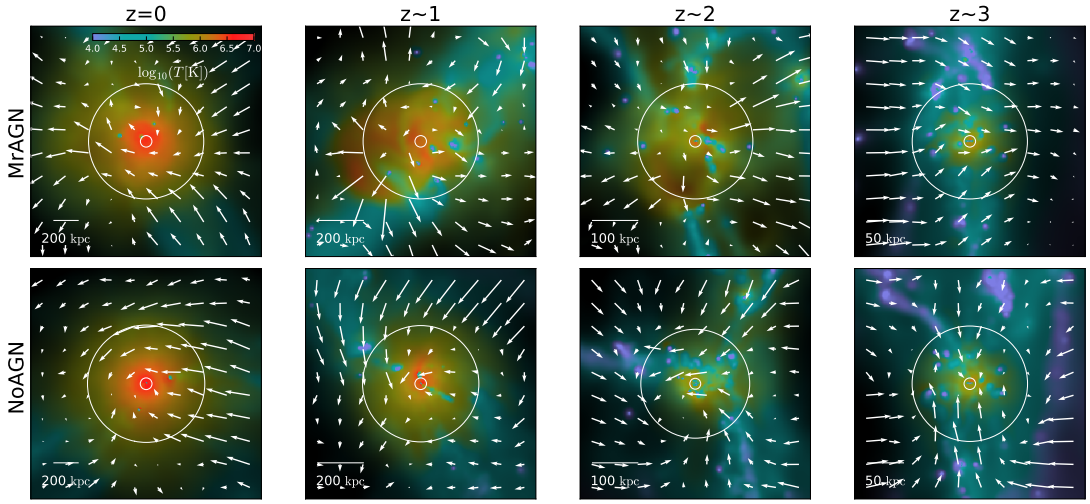

Figure 5.5: Same as Figure 5.4, but for halo m0329. At $z \sim 3$ and $z \sim 0$ the two galaxies look very similar, while at $z \sim 2$ and $z \sim 1$ we see the MrAGN galaxy at the height of its AGN-driven outflow activity in stark contrast to the NoAGN case.

turned around. At $z \sim 0$ we again end up with two galaxies with similar (to the eye) gas contents, although we know from Figure 5.2 that there is more to the story.

Figure 5.6 shows that the two runs of m0501 are very similar until $z \sim 1$, at which point a large AGN-driven outflow occurs in the MrAGN case. This outflow goes on to clear the galaxy of gas and eventually destroy the filament supplying the galaxy with gas, halting accretion even at the virial radius. At $z \sim 0$ there is basically no gas left to track in the MrAGN run, whereas in the NoAGN run, the gas has actually settled into a cold disc on galactic scales. Our mechanical AGN feedback is very efficient at removing gas from the lower mass galaxies of our sample.

Recycling Fractions

In Figure 5.7, two different measures of the instantaneous recycling fraction are plotted. The blue curves represent the fraction of inflowing material across r_g that was previously within the galaxy, while the green curves represent the currently outflowing material across r_g that will return to the galaxy at some future time. The future recycling fraction necessarily falls towards

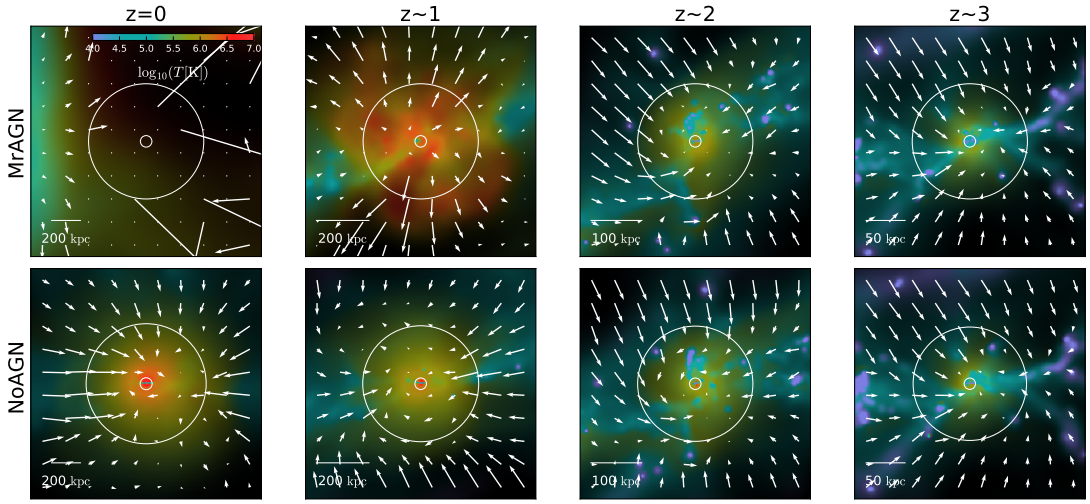

Figure 5.6: Same as Figures 5.4 and 5.5 but for halo m0501. Between $z \sim 1$ and $z \sim 0$, AGN-driven outflows drive the gas completely out of the galaxy in the MrAGN run, even destroying the gas filament which was supplying the galaxy with new gas.

zero at late times, as outflowing material runs out of time to fall back in before the end of the simulation. From top to bottom we see both the MrAGN and NoAGN runs for m0163, m0329, and m0501. In m0163, much of the outflowing material at early times in the MrAGN run (50-70%) is destined to come back until the first big bout of outflow at $\sim$ 4 Gyrs, after which there are only a few isolated incidents of outflowing material that will eventually fall back in. This decrease in the future recycling fraction also corresponds with the black hole accretion rate starting to increase, as can be seen in panel (c) of Figure 5.1. As a result, the fraction of inflowing material that is recycled never rises much above $\sim$ 20%. The future recycling fraction in the NoAGN run remains very large, between 60 and 90% for a large portion of the galaxy's history. As a result, the inflowing recycling fraction by the end of the simulation is almost 70%. In the MrAGN run, of the total $10^{11.2} M_{\odot}$ of gas that accreted onto the galaxy throughout its history, $10^{10.1} M_{\odot}$, or $\sim$ 8% was contributed by recycled material. By comparison, in the NoAGN run, 31% of the total $10^{11.8} M_{\odot}$ was recycled material. Conversely, the fraction of the cumulative outflow mass that was destined to come back when it left is 8.1% for the MrAGN run and 67.8%

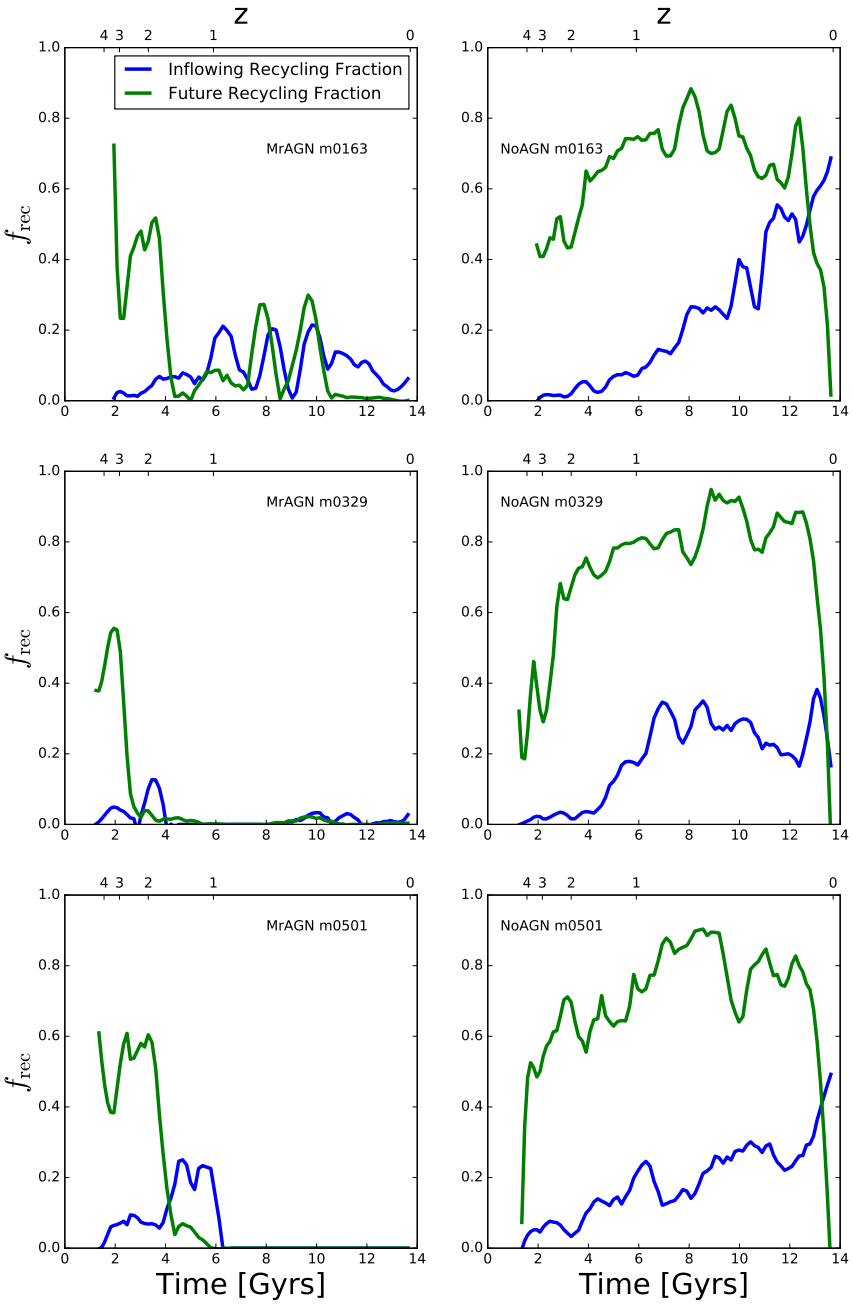

Figure 5.7: Two different measures of instantaneous recycling fraction for our case study galaxies. The green curves show the fraction of ejected material that will return at some future time. The blue curves show the fraction of currently inflowing material that was previously inside the galaxy. Left panel: MrAGN. Right panel: NoAGN. Top panels: m0163. Middle panels: m0329. Bottom panels: m0501. In all cases, both recycling fractions are much higher in the NoAGN runs.

for the NoAGN run.

m0329 behaves similarly to m0163, but there are some differences. The drop in future recycling fraction is more extreme than in m0163, with the inflowing recyling fraction rarely rising above a few percent. In the NoAGN galaxy, the future recycling fraction still reaches heights of 90% and greater, but the inflowing recycling fraction doesn't exceed 40%. This is partially because less material is being recycled than in m0163, but also because outflowing material falls back in on shorter timescales, leading to a more consistent inflowing recycling fraction. The total contribution of recycled material to the cumulative inflow mass in the MrAGN galaxy is $\sim 3\%$; in the NoAGN galaxy it is $\sim 16\%$. The fraction of the cumulative outflow mass contributing to the future recycling fraction is 5.1% for the MrAGN run and 78.0% for the NoAGN run.

m0501 shows similar trends, except that here there is no inflow or outflow in the MrAGN case after ~ 6 Gyrs. We can still see that the inflowing recycling fraction by $z = 0$ in the NoAGN case is $\sim 50\%$. The final total contribution of recycled material to the cumulative inflow mass is $\sim 9\%$ for the MrAGN galaxy and $\sim 17\%$ for the NoAGN galaxy. The fraction of cumulative outflow mass contributing to the future recycling fraction is 14.2% in the MrAGN run and 69.3% in the NoAGN run.

Accretion of Gas and Stars

The fraction of the $z = 0$ total galactic baryonic mass (M_{gas}+M_* within $r_{\rm g}$) of m0163 that is made up of accreted stars (formed in separate halos which have merged with the main progenitor, as opposed to being formed in situ) is $\sim 63\%$ in the MrAGN run and $\sim 33\%$ in the NoAGN run. These fractions are shown in the far left bars of the top row of Figure 5.8. Accreted stars make up a larger fraction of the final baryonic mass of the MrAGN galaxy than of the NoAGN galaxy because of the reduction of in situ star formation in the former. Also plotted is the total gas mass that has accreted since z ~ 4 divided by the total baryonic mass at $z = 0$, in bins of the

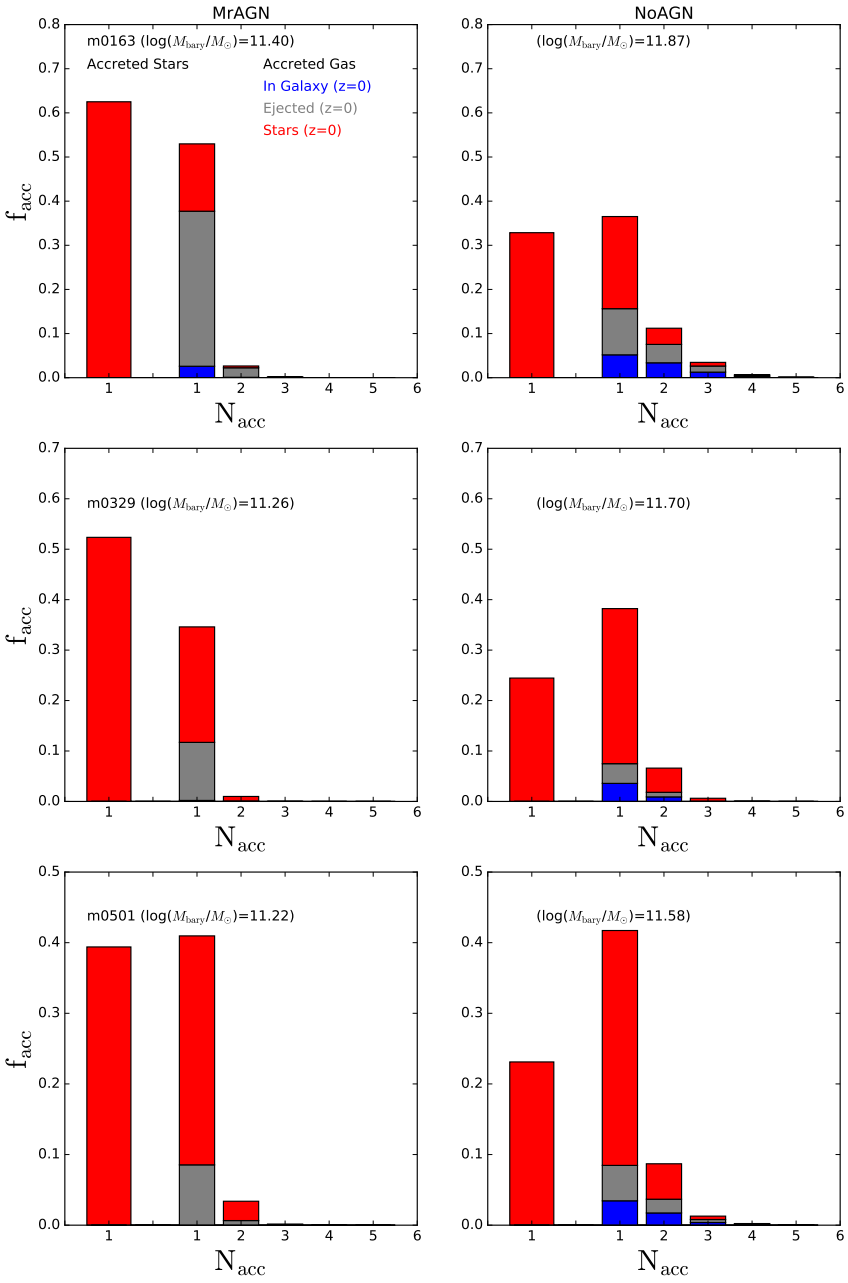

Figure 5.8: The total mass of accreted stars and gas which accreted onto the galaxy N times divided by the total baryonic mass of the galaxy at $z = 0$. The baryonic mass is given in each panel. Left panels: MrAGN. Right panels: NoAGN. Top panels: m0163. Middle panels: m0329. Bottom panels: m0501. The far left bar indicates the mass of accreted stars, which only ever accrete once, divided by the final total baryonic mass within the galaxy radius. The rest of the bars indicate gas particles which accreted N times. These bars are subdivided into the gas particle's fate at $z = 0$: blue if it is still gas within the galaxy, grey if it is gas outside of the galaxy and red if it is now a star particle. Accreted stars make up a larger fraction of the final baryonic mass of MrAGN galaxies than of NoAGN galaxies. Gas in the NoAGN run is more likely to accrete several times, and accreted gas is more likely to remain in the galaxy or form stars than in the MrAGN run, in which a significant fraction of accreted gas ends up being ejected.

number of times the gas particle accreted onto the galaxy. This is further subdivided into the fates of the accreted gas particles. Gas in the NoAGN run is more likely to be accreted several times and is also more likely to remain as gas in the galaxy or to form stars. In the MrAGN galaxy, gas is more likely to accrete fewer times, and the gas that is accreted is more likely to be outside of the galaxy by $z = 0$. The fraction of total accreted gas that is ejected from the galaxy by $z = 0$ in the MrAGN run is 67.1% as compared with 31.4% in the NoAGN run.

For m0329, the fraction of the $z = 0$ baryonic mass that was accreted as stars is again larger for the MrAGN galaxy than the NoAGN galaxy ($\sim$ 53% versus $\sim$ 24%). Also apparent is that practically none of the accreted gas remains as gas within the MrAGN galaxy at $z = 0$, whereas some of this gas remains in the NoAGN run, while a larger fraction is turned into stars. 32.6% of all accreted gas is ejected by $z = 0$ in the MrAGN run, while only 10.7% is ejected in the NoAGN run. These trends continue for m0501, which again has a larger accreted stellar fraction in the MrAGN run ($\sim$ 39% versus $\sim$ 24%). There is a slight preference for more recycling events in the NoAGN galaxy, and again none of the accreted gas in the MrAGN galaxy remains within the galaxy by $z = 0$. 20.8% of accreted gas is ejected in the MrAGN run, while the rest is converted into stars. This figure is relatively small when compared with the 14.4% in the NoAGN run, but this is because m0501 never has an opportunity to accrete any more gas that would be affected by future AGN feedback.

Recycling and Ejection Timescales

Figure 5.9 shows distributions of timescales of gas recycling and gas ejection events for our case study galaxies. Every time a gas particle crosses a shell at r_g, the time is recorded. The time is recorded again if it flows back into the galaxy. This may happen multiple times for a single gas particle, each of which is recorded as a separate recycling event and is included in the distribution. If the gas particle outflows but never comes back, the ejection timescale is recorded

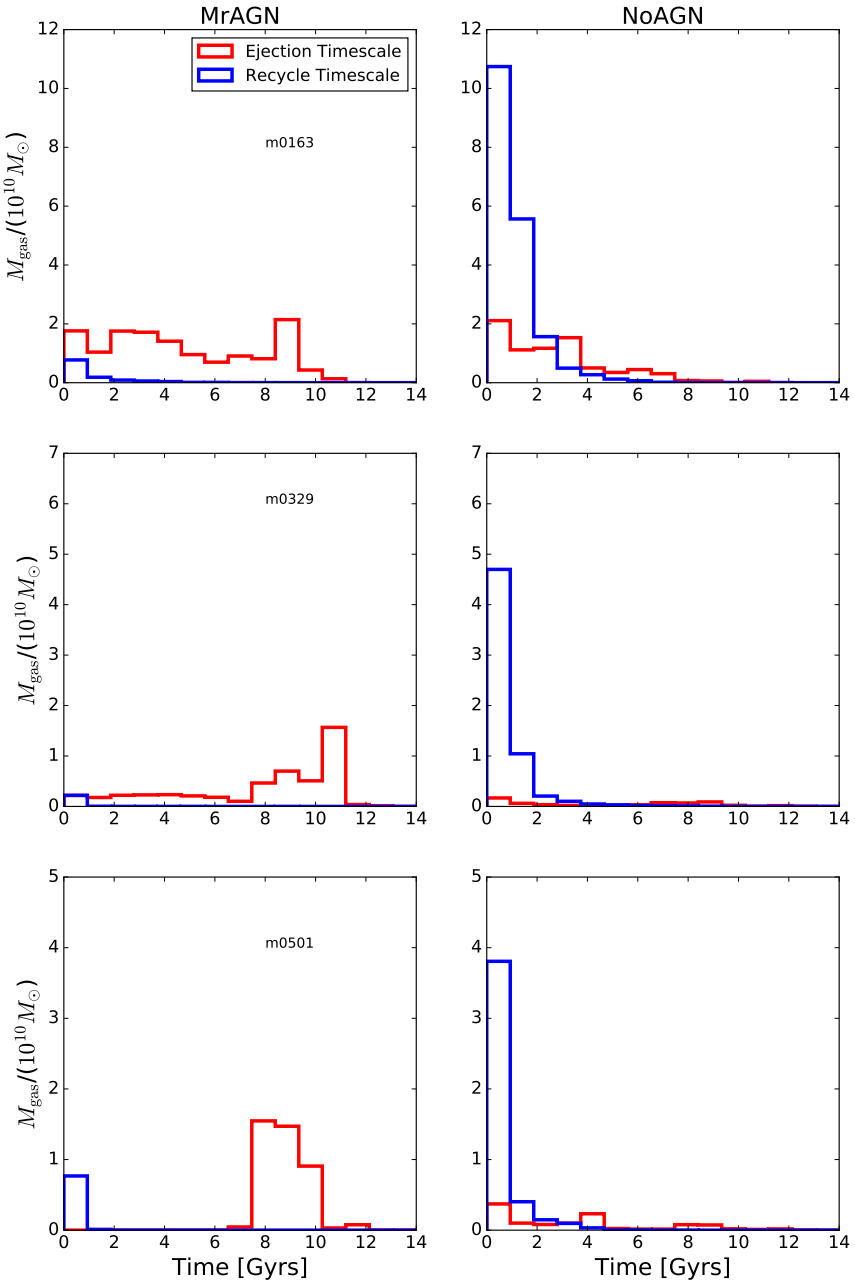

Figure 5.9: Distribution of timescales of recycling and ejection events for our case study galaxies. Top row: m0163. Middle row: m0329. Bottom row: m0501. Left panels: MrAGN runs. Right panels: NoAGN runs. The blue histograms show the distribution of the time spent outside the galaxy by gas that has been ejected past the galaxy radius and later came back. The red histograms show the distributions of the time since ejection for gas particles that have exited the galaxy at the galaxy radius and have not yet returned. There are more recycling events in the NoAGN runs. Recycled gas particles in higher mass NoAGN galaxies like m0163 tend to have longer recycling timescales than those in lower mass galaxies. Ejected gas particles in lower mass MrAGN galaxies like m0501 are more likely to have been ejected at early times by a powerful bout of AGN feedback than those in higher mass galaxies.

as the age of the universe minus the time of ejection. The top row shows us that in the MrAGN run of m0163, there is far less recycling on short timescales than in the NoAGN counterpart. This appears to be because of a few very long-term (seemingly permanent) ejection events that occurred 8-10 Gyrs ago. Those gas particles were then not available to be recycled by stellar and supernova feedback processes as in the NoAGN run. At later times (ejection timescales $\lesssim$2 Gyrs), the ejection distributions look very similar. This is most likely due to random motions of gas particles in both runs which have not had time to return to the galaxy.

The NoAGN run of m0329 also has many more recycling events than its MrAGN counterpart. This time, however, there are consistently more ejection events of longer timescales in the MrAGN case, and these are not only gas particles outflowing at early times as for m0163. The AGN activity more consistently removes material throughout this galaxy's history, again removing gas that would have contributed to the short-timescale recycling events due to stellar and supernova feedback. We also see the preference for shorter timescale recycling in the NoAGN galaxy as compared with m0163, which is responsible for the relatively constant inflowing recycling fraction seen in the middle row of Figure 5.7.

A cumulative gas mass of $\sim 4 \times 10^{10} M_{\odot}$ in the MrAGN run of m0501 is ejected in a series of outflows between 7 and 12 Gyrs ago. The NoAGN run is dominated by recycling events, with far fewer gas particles being ejected ($<10^{10} M_{\odot}$) relative to being recycled on short timescales ($>4 \times 10^{10} M_{\odot}$).

Recycling and Ejection Displacements

Figure 5.10 shows the distribution of maximum displacements of gas particles, again both for completed recycling events and ejection events in which the particle is still outside of the galaxy at the end of the simulation. When a particle is tagged as outflowing, its current radius is recorded (usually just outside of $r_{\rm g}$. We keep track of its subsequent radius and store the maximum

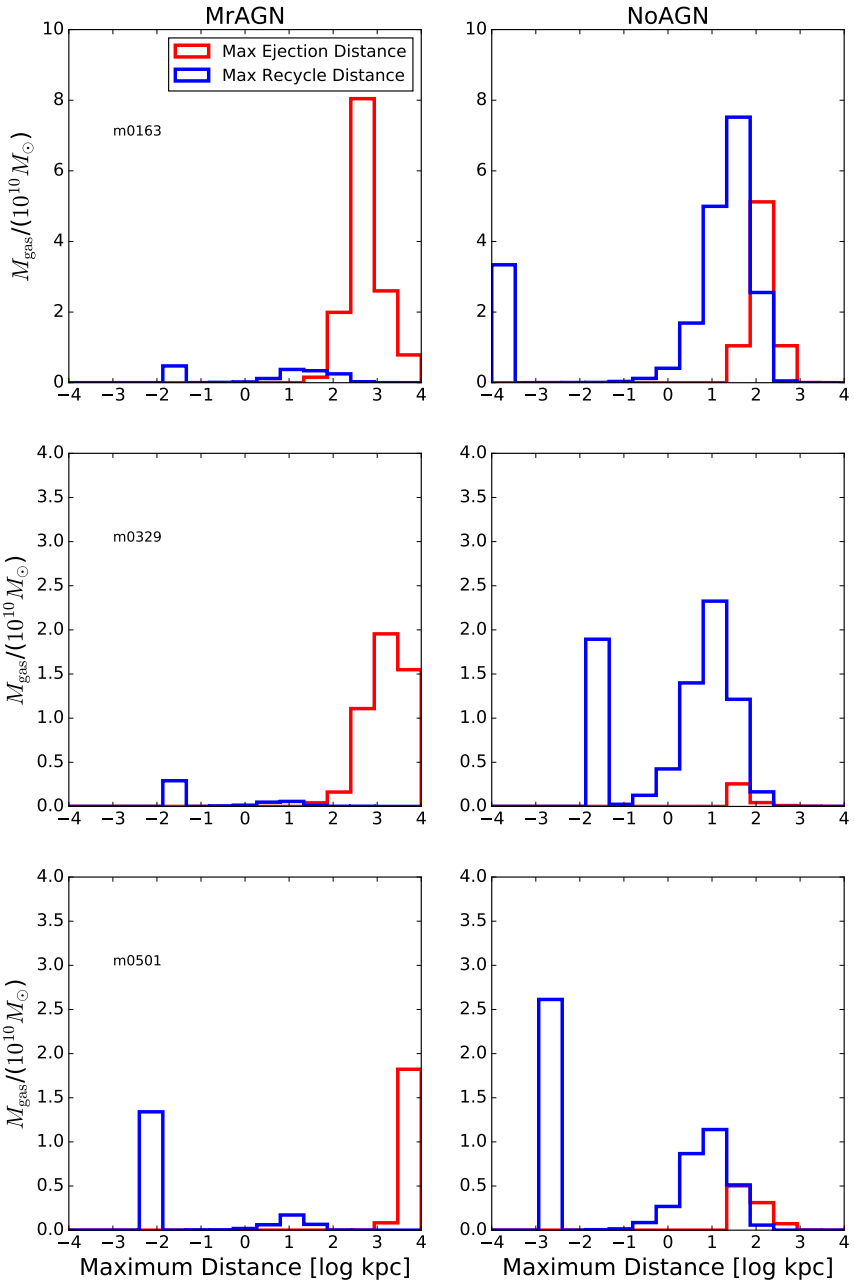

Figure 5.10: Distribution of displacements for recycling and ejection events in our case study galaxies. Displacement is measured from the particle's initial radius outside of the galaxy radius, recorded when the particle is first tagged as outflowing. Top row: m0163. Middle row: m0329. Bottom row: m0501. Left panels: MrAGN runs. Right panels: NoAGN runs. The blue histograms show the distribution of the maximum distance traveled by gas particles that have been ejected past the galaxy radius and later come back. The red histograms show the distributions of the maximum distance for gas particles that have exited the galaxy past the galaxy radius and have not yet returned. Recycled particles which only ever travel back inwards from their initially recorded radius outside the galaxy are counted in our lowest bin. Gas particles ejected by AGN feedback travel much farther than those ejected by stellar and supernova feedback, and this trend becomes more extreme towards lower halo masses.

radius reached during a given recycling or ejection event. We then subtract the initial radius to get the maximum displacement experienced by a given gas particle. For m0163, we see once again that there is far more mass ejected ($\sim 10^{11} M_{\odot}$) than recycled ($<10^{10} M_{\odot}$) in the MrAGN run, due to a larger number of gas particles which are part of outflows at early times and never re-accrete onto the galaxy. It is also evident that the outflowing gas particles removed by AGN feedback travel much larger distances than those removed by stellar and supernova feedback. In some cases, gas particles travel several Mpc, while in the NoAGN run only the very tail of the distribution reaches ~ 1 Mpc.

The distribution of maximum displacements for gas particles in the MrAGN run of m0329 is even more extreme than for m0163, with gas particles being driven out beyond the zoom region of our simulation. While we keep track of these distances, here we cap the particles' displacements at the boundaries of our zoom region. That this prescription for AGN feedback can launch gas so far is something we will return to in the Discussion. Ejected particles in the NoAGN case can travel several hundred kpc, but only the extreme tail of the distribution exhibits radii larger than this. In both cases, the recycled material is restricted to these smaller displacements as well.

In m0501, with the halo depleted and the surrounding filament destroyed there is nothing to stop ejected gas from traveling tens of Mpc in the MrAGN run. In contrast, ejected particles in the NoAGN run mostly only travel 100-200 kpc. In both runs, recycled gas particles are restricted to smaller radii, as is expected.

5.3.2 Broad Trends in Galaxy and Outflow Properties

In the last section, we focused on three individual example galaxies and found that the strength of gas outflows and inflows depend on halo mass. We now turn to the broad trends and scaling relations for galaxy and outflow properties that can be extracted from our complete suite of

galaxies. In the following plots, each point represents a single galaxy at the specified redshift. Some galaxies do not have a matched pair or reliable center by $z = 3$, or in some cases $z = 2$, and so these are not plotted at high redshift.

Galaxy Properties

Figure 5.11 shows the gas and stellar mass of all of our galaxies versus halo mass for four different redshifts. The full cold gas mass and stellar mass histories of our three case study galaxies can be found in Figures 5.1, 5.2 and 5.3. At $z = 3$, before most major AGN activity (when supermassive black holes are still fairly small), galaxies in both runs have very similar gas content and fall on a fairly tight relation between gas mass and halo mass. At $z = 2$, AGN feedback begins to kick in and MrAGN galaxies start to drop below the NoAGN relation. By $z = 1$, much of the gas affected by star formation and stellar feedback has fallen back into the galaxies, while in the MrAGN runs, much of this gas is lost. At $z = 0$, galaxies in the two runs fall on distinct relations, with some of the lowest halo mass galaxies having no gas left within r_g. The middle row tells a similar story about the cold gas content (defined as gas with $T<2\times10^4$K), except for two important differences. The relationship between cold gas and halo mass for NoAGN galaxies has more scatter than the total gas mass to halo mass relation. Secondly, by $z = 0$ none of the MrAGN galaxies has any cold gas left at all. Finally, the bottom panels show the stellar mass of the central galaxy versus the halo mass, and reveal a more gradual separation of the two relations due to the permanent removal and/or heating of cold gas causing the buildup of stars in the MrAGN runs to lag behind that of the NoAGN runs. The solid black curves are an estimate of the stellar-mass halo mass relation from the abundance matching analysis of Moster et al. (2013). The dashed black curve is the $z = 0$ abundance matching estimate of Kravtsov et al. (2014). Our MrAGN galaxies are a very good match to the Kravtsov et al. (2014) estimate, which used improved photometric techniques and took into account intracluster light to measure

stellar masses.

Inflow and Outflow Properties

Next we turn to inflow and outflow properties. Again, the full inflow and outflow histories of our case study galaxies have been presented above; here we present snapshots of these quantities at the specified redshifts for our entire sample of galaxies. Figure 5.12 illustrates that at $z = 3$, the inflow rates for MrAGN and NoAGN galaxies are very similar and dependent on halo mass. By $z = 2$, the higher mass MrAGN galaxies begin to have inflow suppressed by $\gtrsim$1 dex as their AGN turn on. By $z = 1$, this phenomenon is widespread and the inflow rate is again broadly dependent on halo mass. At $z = 0$, the highest mass galaxies are again accreting at a rate comparable to their NoAGN counterparts, while the rest of the MrAGN galaxies continue to have their inflow rates suppressed by up to 1.5 dex. This again shows the importance of preventative feedback, especially in lower mass galaxies.

At r_h the evolution is very similar, although the suppression of inflow at this larger scale is much less pronounced. At $z = 1$ and $z = 0$ it is the lower mass MrAGN galaxies that have their inflow suppressed (although now by $\sim$ 0.5 dex), while more massive galaxies have inflow rates closer to their NoAGN counterparts. However, as shown in Table 5.1, the cumulative inflowing mass at r_h expressed as a fraction of the universal baryon fraction times the halo mass at $z = 0$ is smaller in MrAGN galaxies than in NoAGN galaxies, even at larger masses. Still, the effect is more pronounced at lower masses. At both scales there is not much evolution in the inflow rates of NoAGN galaxies. At both radii we see evidence of downsizing: AGN feedback occurs in more massive galaxies first, as evidenced by the initial decrease in inflow rate for the most massive galaxies at z $\sim$ 2, and more strongly affects lower mass galaxies at later times.

Figure 5.13 is the same as Figure 5.12, but now for the outflow rate. At r_g the outflow rates of MrAGN galaxies at z = 3-1 are comparable to the outflow rates of NoAGN galaxies, and

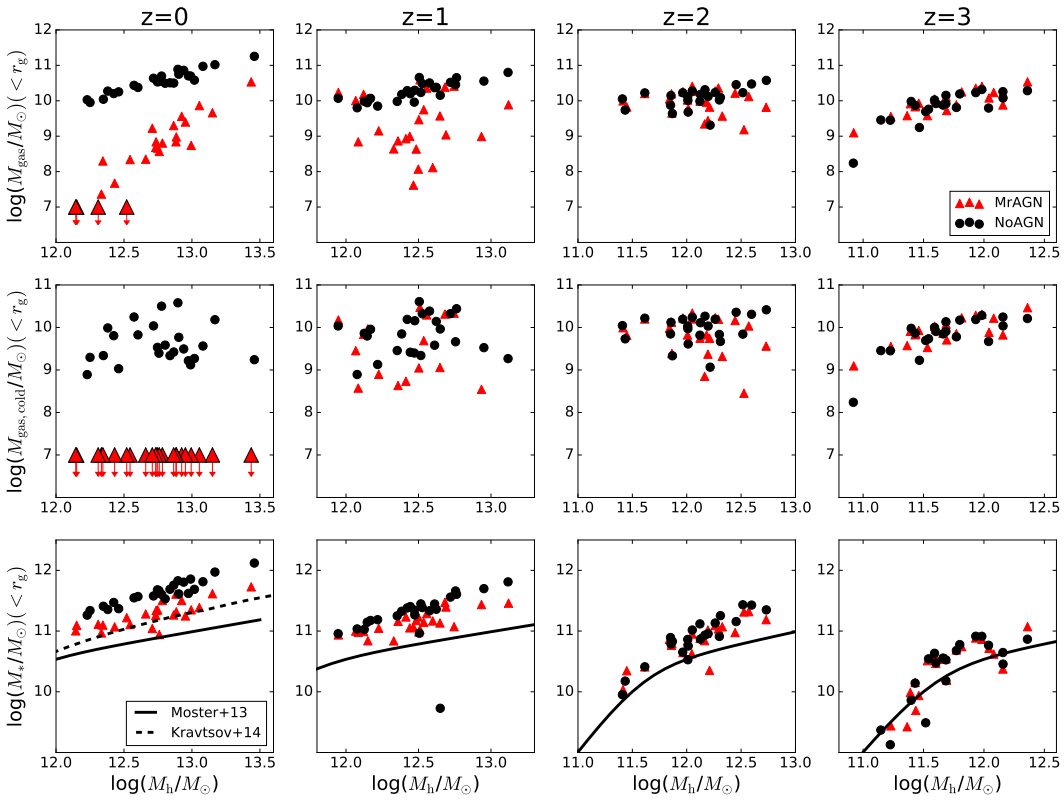

Figure 5.11: Gas and stellar content of all galaxies at four redshifts vs. halo mass. Top row: Total mass of gas within 10% of R_{vir}. Middle Row: Cold gas mass ($T<2\times10^4$ K) with 10% of R_{vir}. Bottom Row: Stellar mass. The solid black curves are the abundance matching estimates from Moster et al. (2013) and the dashed black curve is the $z = 0$ abundance matching estimate of Kravtsov et al. (2014). Black circles denote galaxies in the NoAGN runs, while red triangles denote galaxies in the MrAGN runs. Quantities plotted at $10^7 M_\odot$ with downward arrows are galaxies for which the y-axis value is 0. By $z = 0$, all MrAGN galaxies have significantly less gas (and in some cases no gas), and all have been cleared of cold gas completely. All MrAGN galaxies also have lower stellar masses, as was seen in the individual galaxy histories shown above.

at z=0 are slightly lower. At r_h, however, we see elevated outflow rates, first for more massive galaxies at $z = 2$, then for most galaxies by $z = 1$. The outflow rates of MrAGN galaxies remain slightly elevated by $z = 0$ for many galaxies. This confirms what was shown earlier for the case studies; outflowing gas driven by AGN feedback is less likely to fall back into the galaxy and is more likely to travel out past the virial radius.

Figure 5.14 again shows the outflow rates of our MrAGN galaxies at four different redshifts, this time versus the bolometric luminosity of their AGN. Higher luminosity AGN tend to be correlated with larger outflow rates. The blue and green dashed lines represent scaling relations presented in Fiore et al. (2017) for molecular and ionic winds, respectively, found for a sample of AGN galaxies containing outflows. While the measurements of outflow velocity were conducted at several different radii in the galaxies used to define these relationships, we are encouraged that our MrAGN galaxies occupy a realistic portion of the outflow rate-bolometric luminosity plane, and thus qualitatively agree with observed winds.

Figure 5.15 further quantifies the fraction of gas that has crossed a shell at r_g that eventually crosses a shell at r_h as a function of halo mass. Whenever a gas particle is tagged as outflowing past r_g, its radius is tracked and, if it later crosses r_h, it is considered expelled. At each redshift shown, we have divided the cumulative mass that has been expelled by the cumulative mass of gas that has been considered outflowing past r_g up until that redshift. These cumulative masses may include certain gas particles multiple times if they are recycled. At $z = 3$, when galaxies are small, this ratio is similar for MrAGN galaxies and NoAGN galaxies. At $z = 2$, we see the effect of AGN turning on in higher mass galaxies as in Figures 5.12 and 5.13. At later redshifts, once AGN feedback kicks in for all galaxies, this ratio is much larger for MrAGN galaxies than NoAGN galaxies, as gas particles ejected by AGN feedback tend to travel much farther. Interestingly, there does not appear to be much of a consistent trend with halo mass for this quantity.

In Figure 5.16, we examine different types of loading factors by plotting outflow rates versus

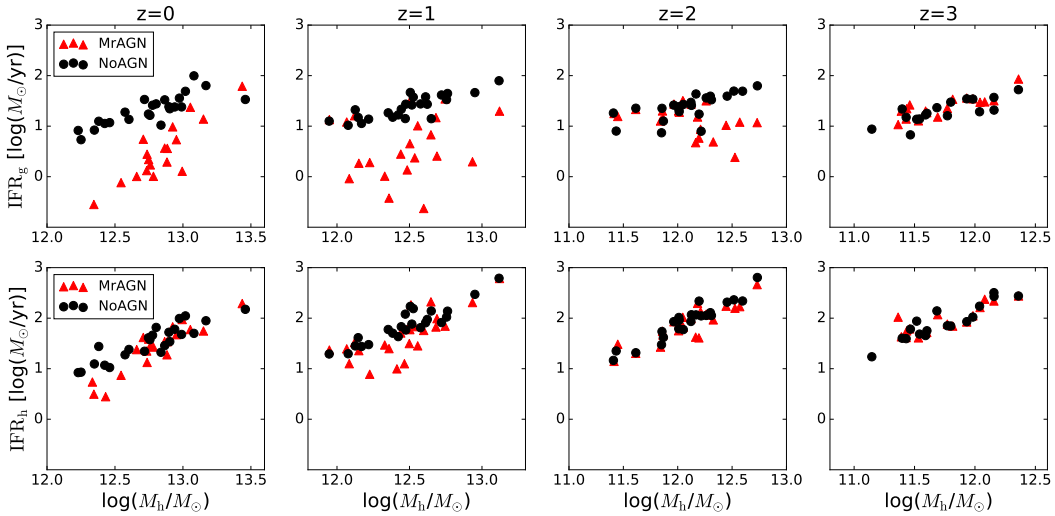

Figure 5.12: The inflow rate of gas at the specified redshift. Top row: Inflow across the galaxy radius. Bottom row: Inflow across the halo radius. Black circles denote galaxies in the NoAGN runs, while red triangles denote galaxies in the MrAGN runs. The inflow rate at the galaxy radius for MrAGN galaxies is decreased by as much as 1.5 dex by $z = 0$. We see evidence of downsizing in the initial decrease of inflow for high mass galaxies at z=2 when their AGN begin to switch on. At the halo radius, the inflow rate is only suppressed for lower mass halos.

inflow rates, both measured at $\mathrm{r_g}$ (top row), SFR (middle row) and BHAR (bottom row). In the top row, we consider outflow rate versus inflow rate. At $z = 3$, the two runs sit on top of each other at loading factors less than unity. By $z = 2$, the loading factors of MrAGN galaxies tend to be larger by as much as ten times, and by $z = 1$ as much as a hundred times, with some galaxies having outflow rates larger than their inflow rates. This is due to a combination of both higher outflow rates and lower inflow rates for MrAGN galaxies. By $z = 1$, almost every MrAGN galaxy has a loading factor greater than unity, while the NoAGN galaxies all sit below this line. Now, however, this difference is almost entirely due to the suppressed inflow rates of MrAGN galaxies. Finally, at $z = 0$, it appears that outflow and inflow are regulating each other in the case of the MrAGN galaxies, while the NoAGN galaxies hit a floor in inflow rate, as stellar and supernova feedback and gravitational heating do not suppress inflow as efficiently as AGN feedback does. Turning to outflow rate versus star formation rate, at $z = 3$, 2 and 1, this loading factor follows

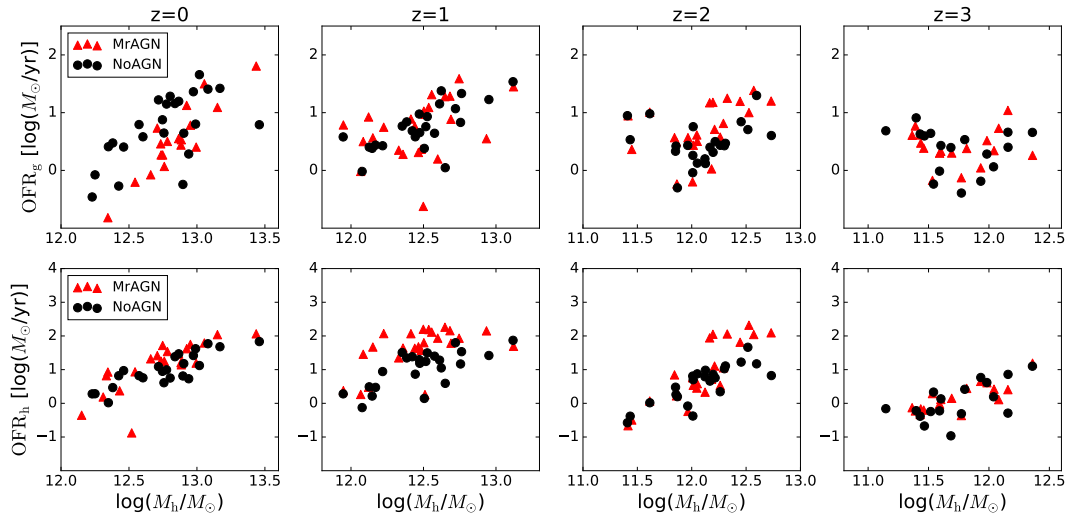

Figure 5.13: The outflow rate of gas at the specified redshift. Top row: outflow across the galaxy radius. Bottom row: outflow across the halo radius. Black circles denote galaxies in the NoAGN runs, while red triangles denote galaxies in the MrAGN runs. The outflow rate at the galaxy radius for MrAGN galaxies is not appreciably different from that of NoAGN galaxies, except at z=0, when it is slightly lower. At the halo radius, we see an elevated outflow rate for MrAGN galaxies, mainly at $z = 2$ and $z = 1$. We again see evidence for downsizing, with the most massive galaxies experiencing enhanced outflows at the halo radius before lower mass galaxies.

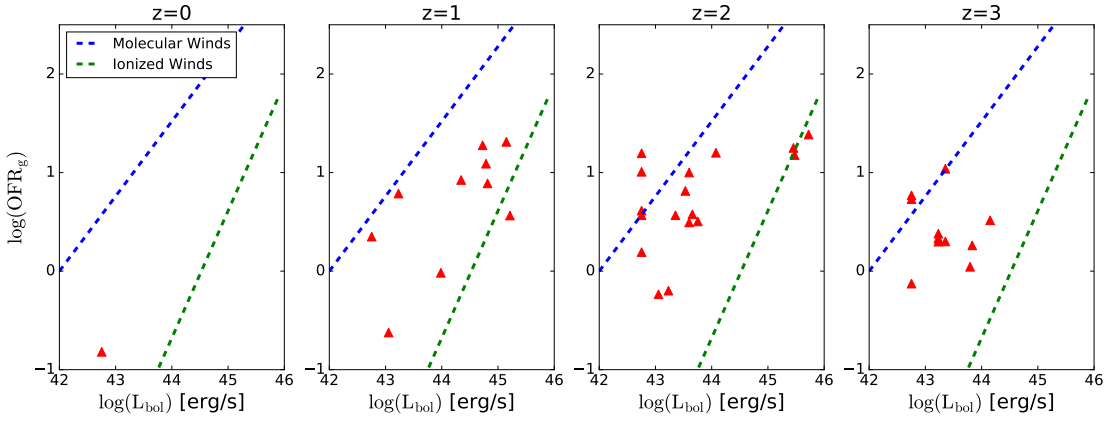

Figure 5.14: The outflow rate of gas across r_g versus the bolometric luminosity of the galaxy's AGN. MrAGN galaxies are shown as red triangles. The dashed blue and green lines are scaling relations found for AGN-driven molecular and ionized outflows, respectively, and presented in Fiore et al. (2017). These scaling relations were derived for outflows at a number of different radii, and there is large uncertainty on some of the values used to derive the relations, but the outflows in our galaxies and the behavior of the AGN appear to be physical and qualitatively agree with values found in the literature and compiled in Fiore et al. (2017).

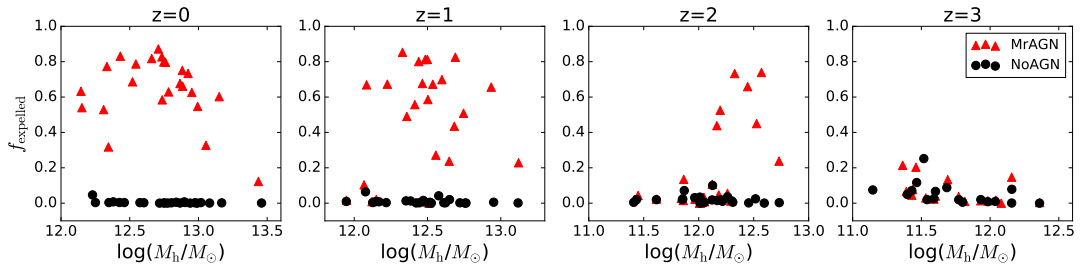

Figure 5.15: The fraction of the cumulative mass which has crossed a shell at the galaxy radius and which has subsequently crossed a shell at the halo radius by the specified redshift. Black circles denote galaxies in the NoAGN runs, while red triangles denote galaxies in the MrAGN run. We see that a much larger fraction of gas that outflows past the galaxy radius eventually crosses the halo radius in the MrAGN runs.

a similar pattern as outflow rate/inflow rate. At $z = 2$, the outflow rates of MrAGN galaxies are higher than NoAGN galaxies, while their SFRs are lower. At $z = 1$, the difference in loading factor is due almost entirely to the decreased SFRs of MrAGN galaxies. At $z = 0$, the one MrAGN galaxy still forming stars has a much lower SFR than any of the NoAGN galaxies, but also a very low outflow rate. Finally, the bottom panels show that the outflow rates of MrAGN galaxies are 100 times or more greater than their black hole accretion rates at $z = 3$, although this value falls slightly with redshift. There are also fewer galaxies with appreciable black hole accretion rates as we go from $z = 2$ to $z = 0$.

In Figures 5.17 and 5.18, we examine, very broadly, the kinematics of outflowing material. Figure 5.17 shows the kinetic energy outflow rate for particles which have crossed a shell at r_g since the last timestep versus stellar mass. The kinetic energy outflow rate is calculated by summing the total kinetic energy of all of the outflowing particles and dividing by the time between snapshots. At $z = 3$, the MrAGN galaxies and NoAGN galaxies are very similar, but by $z = 2$, some of the MrAGN galaxies have much more kinetic energy in outflowing particles. By $z = 1$ this trend is even clearer, and the MrAGN galaxies have started to become displaced to lower stellar masses as well. At $z = 0$, the kinetic energy in outflowing particles is once again similar in the two runs, but the outflows have left their mark on the MrAGN galaxies, which

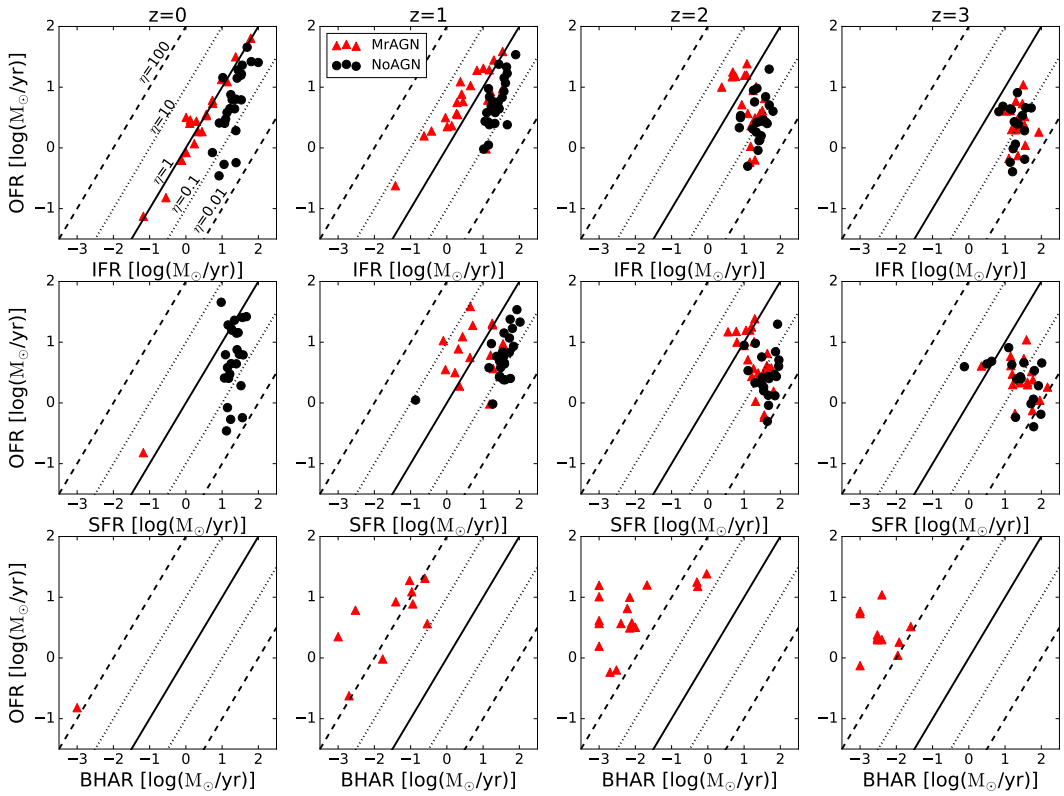

Figure 5.16: Outflow rate at the galaxy radius versus: inflow rate at the galaxy radius (top row), star formation rate (middle row), and black hole accretion rate (bottom row, for MrAGN runs). Black circles denote galaxies in the NoAGN runs, while red triangles denote galaxies in the MrAGN runs. Black lines specify constant mass loading factors, η. Top row: η=outflow rate/inflow rate. Middle row: η=outflow rate/star formation rate. Bottom row: η=outflow rate/black hole accretion rate. At $z = 2$ and $z = 1$ the MrAGN galaxies tend to have higher loading factors than the NoAGN galaxies, although by $z = 0$, there is only one MrAGN galaxy that still exhibits star formation or black hole accretion.

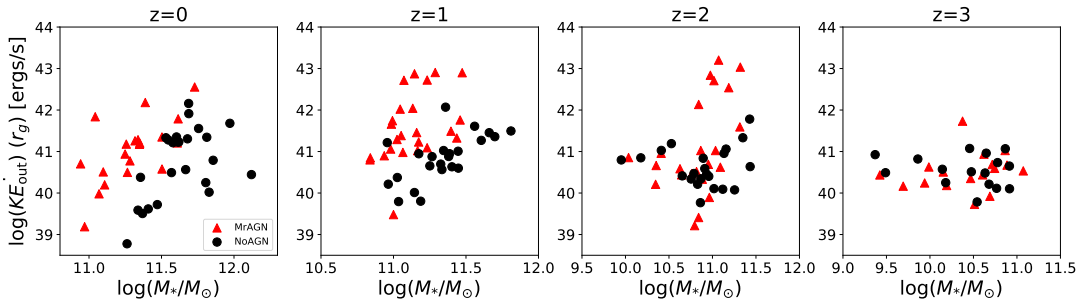

Figure 5.17: Kinetic energy outflow rate of all gas particles which have crossed a shell at the galaxy radius since the last timestep vs. stellar mass. The kinetic energy outflow rate is calculated by summing the total kinetic energy of all of the outflowing particles and dividing by the time between snapshots. Black circles denote galaxies in the NoAGN runs, while red triangles denote galaxies in the MrAGN runs. At $z = 3$ and $z = 0$, the total kinetic energy of outflowing particles is very similar between the two runs, although the stellar masses of MrAGN galaxies are characteristically lower at z=0. At $z = 2$ and $z = 1$, MrAGN galaxies have more kinetic energy in outflows by as much as two orders of magnitude.

have smaller stellar masses.

Figure 5.18 instead illustrates the average radial velocity of the same outflowing gas considered in Figure 5.17. At $z = 3$, 2 and 1, the trends are quite similar to those seen in the last figure. Large outflow velocities begin to be seen at $z = 2$ and at $z = 1$, and almost all MrAGN galaxies have outflowing material with significant radial velocities. At $z = 0$, whereas the total kinetic energy of outflowing particles for MrAGN and NoAGN galaxies were very similar, the radial velocities of those outflowing gas particles are characteristically larger in the MrAGN run. The similarity in kinetic energies is due to the fact that there is less mass in outflowing gas in the MrAGN galaxies; much more gas has already been removed permanently by AGN feedback. In the NoAGN run, the same gas is allowed to outflow and re-accrete. We will now investigate gas recycling in more detail.

Gas Recycling

Figure 5.19 depicts the ratio of the inflow rate of recycled material at r_g at the specified redshift to the inflow rate of new material. This is related to the inflowing recycling fraction depicted

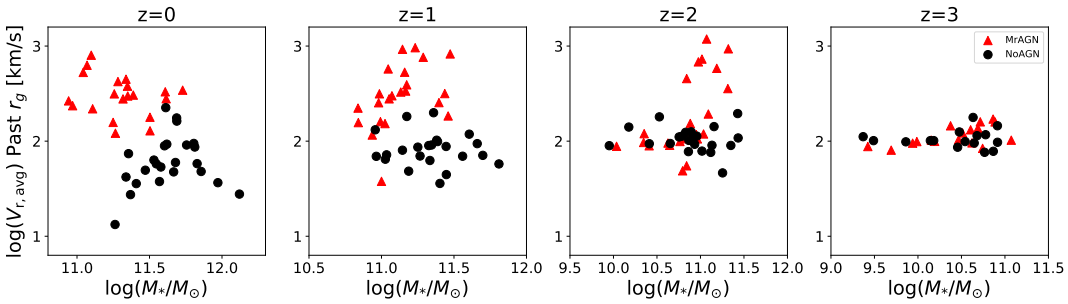

Figure 5.18: Average radial velocity of all gas particles just crossing a shell at the galaxy radius at the specified redshift vs. stellar mass. Black circles denote galaxies in the NoAGN runs, while red triangles denote galaxies in the MrAGN runs. For redshifts of 2 and less, the average radial velocity of gas outflowing past the galaxy radius in MrAGN galaxies is much higher than that of gas in NoAGN galaxies.

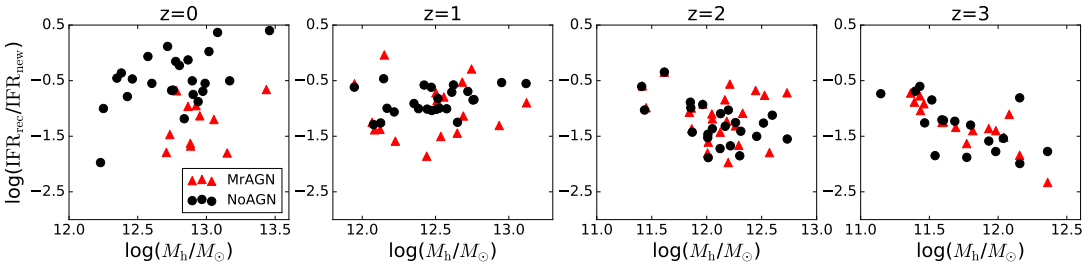

Figure 5.19: Instantaneous inflow rate at the galaxy radius composed of recycled accretion divided by the inflow rate of new gas at the specified redshift. Black circles denote galaxies in the NoAGN runs, while red triangles denote galaxies in the MrAGN runs. While MrAGN galaxies are almost always dominated by new accretion, NoAGN galaxies at $z = 0$ experience more recycled accretion, and are even dominated by recycled accretion in the large halo mass regime.

for our case studies. Down to $z = 1$, galaxies in both runs are more likely to accrete a larger portion of new gas regardless of halo mass. This remains true for galaxies in the MrAGN run to $z = 0$, but NoAGN galaxies experience more recycled accretion, with larger mass halos being dominated by recycling.

In Figure 5.20, we have taken the histograms like those shown in Figure 5.9 for all of our galaxies and turned them into cumulative timescale distributions. While we lose information on the relative number of recycling and ejection events, those properties are in line with those found for the example galaxies above. The cumulative distributions are color-coded by halo

mass, with purple corresponding to the least massive and yellow to the most massive. MrAGN galaxies have characteristically longer recycling timescales due to the more efficient and energetic feedback. This is especially true for more massive galaxies; while the feedback is strong enough to lengthen recycling timescales, it is harder to remove the gas completely from a very massive halo, resulting in gas that is gone for a long time but nevertheless comes back. We also find that ejection timescales are characteristically longer for MrAGN galaxies; in this case the longest timescales correspond to the less massive halos, which experienced strong early bouts of AGN feedback that removed gas permanently.

5.4 Discussion

In this section we will first compare our results with those from other simulations, then discuss our results in the context of several questions asked in this chapter's Introduction.

5.4.1 Comparison with Other Work

Other studies have examined the baryon cycle in simulations, although usually these have been focused on lower mass galaxies than the ones we study here. Despite this, we now discuss how our results compare with some of these studies.

Oppenheimer et al. (2010) examined a set of galaxies run with `GADGET-2` (Springel 2005) with various prescriptions for stellar driven winds, tied to the galaxies' star formation rate. They find that when galactic winds are included, the contribution of recycled material to accretion at late times (especially z<1) is very significant. These outflow models result in too many galaxies with $M_{\rm h} \gtrsim 2 \times 10^{12} M_{\odot}$ because the material that is removed is re-accreted, and they posit that AGN feedback may suppress this re-accretion. These results are consistent with our large NoAGN inflowing recycling fractions; even if our sample is not cosmologically representative, we confirm

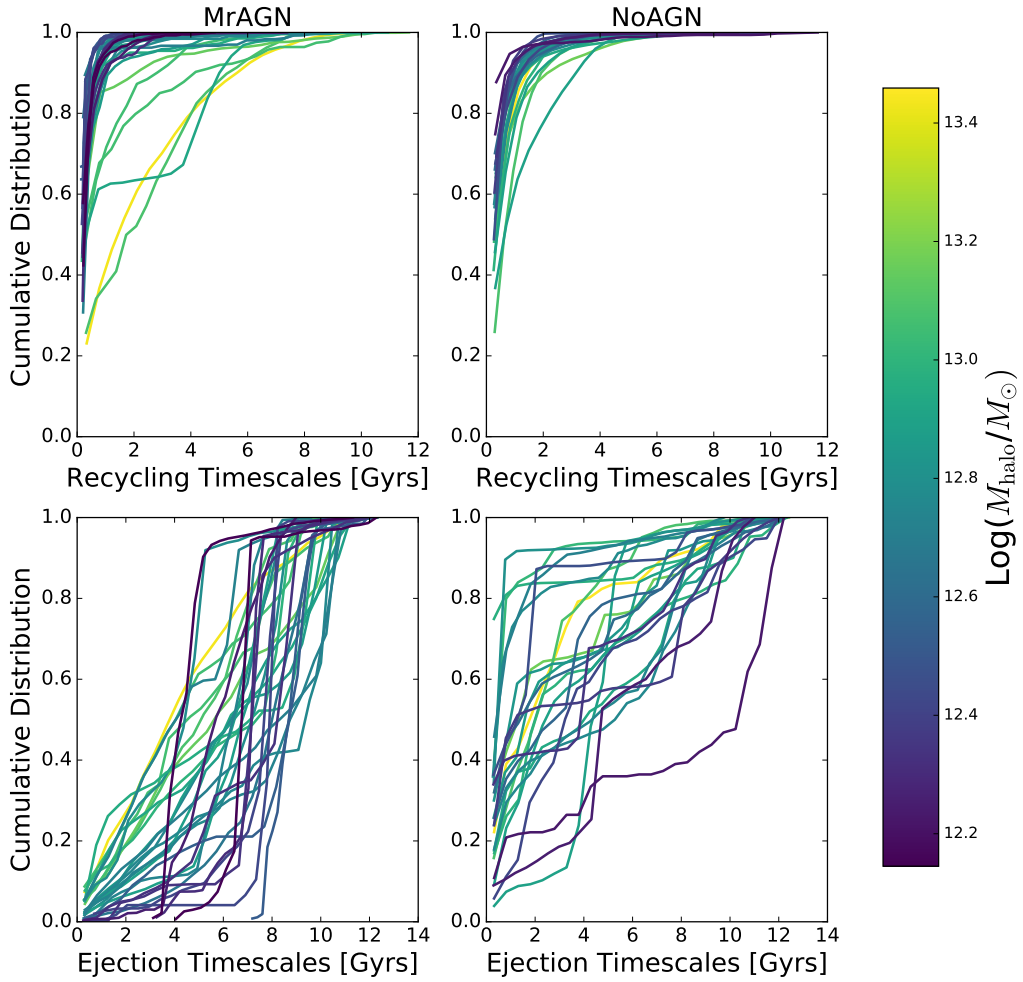

Figure 5.20: The normalized cumulative distribution of recycling (top row) and ejection (bottom row) event timescales by $z = 0$, color-coded by halo mass. Purple corresponds to lower halo mass, while yellow corresponds to higher halo mass. Left panels: MrAGN galaxies. Right panels: NoAGN galaxies. MrAGN galaxies have characteristically longer recycling timescales, especially for higher mass galaxies. MrAGN galaxies also have characteristically longer ejection timescales, often the result of large, early bouts of AGN feedback. The latter trend is strongest for lower mass galaxies.

their speculation that AGN feedback can suppress late re-accretion of gas.

Hirschmann et al. (2013) examine cosmological zoom simulations using the same stellar-driven wind model as Oppenheimer et al. (2010) and find the same large inflow rate at late times, leading to too much in situ star formation and galaxies which are too massive. They also found outflow rate versus SFR mass loading factors at high redshift ($z \sim 2-3$) as large as ~ 100, which is higher than we find in either our MrAGN or NoAGN runs.

Übler et al. (2014) examined a series of cosmological zoom simulations, also run with GADGET, with masses slightly below our mass range and overlapping with our lower mass galaxies. Much like this work, they compared two feedback models, one with weak feedback from massive stars, the other with strong feedback. They examined the baryon cycle around these galaxies and found that stronger stellar feedback produced disc galaxies with properties comparable to observations. Their strong feedback model is similar to our NoAGN model, and they find similar gas behavior. They find that at early times, some gas is ejected from the galaxies permanently, due to their shallower potential wells, while later the galaxies are dominated by accretion of recycled gas, like ours. Their Figure 6 is the inspiration for our Figure 5.8.

Christensen et al. (2016) carried out a study of outflows in 20 field galaxies run with the SPH code `GASOLINE` (Wadsley et al. 2004). They looked at galaxies with halo masses of $10^{9.5}$-$-10^{12} M_{\odot}$. They find that 50% of gas that leaves the galaxies is later re-accreted regardless of mass. Our results are in agreement with theirs in that we find that the future recycling fraction for our NoAGN galaxies is very similar for all galaxies, also regardless of mass. However, we also find that the cumulative inflowing mass of higher mass galaxies is more likely to be recycled ($\sim 25-35\%$) than in lower mass galaxies (as low as $\sim 7\%$). Our results also suggest that a very common recycling timescale for gas in our NoAGN galaxies is ~ 1 Gyr, in agreement with their results.

Barai et al. (2016) implemented mechanical AGN feedback similar to ours in a cluster-sized halo using GADGET-3. Although our analysis is quite different, they come to several similar conclusions. They find bipolar bubble-like outflows of heated gas out to hundreds of kiloparsecs, which is very similar to the structure of our outflows. They also find that kinetic feedback is far more efficient at affecting central gas and quenching star formation than thermal feedback.

Anglés-Alcázar et al. (2016) examined a suite of galaxies in the FIRE simulation (Hopkins et al. 2014), which span a lower range of halo masses than the ones we have looked at and also do not include AGN feedback. They find (for galaxies with stellar feedback) that galaxies with lower halo mass are more dominated by recycled accretion and become more so at low redshift, while higher mass halos are dominated by new accretion. We find that in general NoAGN galaxies are more dominated by recycled accretion at late times, although this is much more prevalent for the higher mass galaxies in our halo mass range. With our AGN feedback prescription we find that there is very little recycled accretion onto our galaxies, even at late times, regardless of galaxy mass.

Anglés-Alcázar et al. (2016) also find that in the absence of AGN feedback, the most massive galaxies have the shortest recycling timescales, although they do find that these same galaxies have larger recycling distances than lower mass galaxies. We find that our NoAGN galaxies are all dominated by relatively short recycling timescales and these timescales are longer for more massive halos. Recycled gas remains outside the galaxy for longer and travels farther in MrAGN galaxies than in NoAGN galaxies, and higher mass halos have the longest- and farthest-traveling recycled gas. This is because gas launched from lower mass galaxies is much more likely to be expelled from the halo.

Finally, Weinberger et al. (2017) implemented a prescription for AGN feedback into AREPO, the moving mesh MHD code (Springel 2010). They included thermal feedback for high-Eddington ratio black hole accretion and kinetic feedback for low-Eddington ratio accretion. Pillepich et al.

(2017) adopted this dual-mode feedback prescription and also implemented an improved model for galactic-scale, star formation-driven, kinetic winds in the *IllustrisTNG* simulation. They found that the interplay of the new AGN feedback prescription and the new galactic wind scalings resulted in realistic elliptical galaxies, with which we are in qualitative agreement, but it is unclear if they drive the powerful outflows associated with observed quasars.

Our NoAGN model is in broad agreement with several of the studies above which only include stellar and supernova feedback. We find similar trends in terms of inflow rate at late times and gas recycling. However, differences in our feedback prescriptions cause us not to agree on every detail. While our MrAGN model produces realistic galaxies in agreement with other studies which have included AGN feedback, our model is still unique in that we employ mechanical feedback at all black hole accretion rates.

5.4.2 Physical Interpretation

In this work, we have examined how the cycle of gas inflow and outflow is affected by our model for strong mechanical and radiation-driven AGN feedback. We have focused on 24 massive galaxies with halo masses of $M_{\rm vir} \sim 10^{12} - 10^{13.4} M_{\odot}$ at $z = 0$. For each of these galaxies, we have runs from two different models: MrAGN and NoAGN. The MrAGN model includes stellar feedback via UV heating, stellar winds and supernovae, AGN feedback via momentum-driven winds and X-ray heating, photoelectric heating, and cosmic X-ray background heating from a meta-galactic X-ray background. The NoAGN model is identical except that it does not include any AGN feedback. The MrAGN model has been shown to produce realistic galaxy properties for massive galaxies (Choi et al. 2015, 2017; Hirschmann et al. 2017).

We set out, in part, to answer several questions about the gas cycle in our suite of galaxies, which we will discuss here.

What are the histories of inflow and outflow like for these galaxies?

The inflow and outflow histories for both MrAGN and NoAGN galaxies are dependent upon halo mass (Figures 5.1, 5.2, 5.3, 5.12, 5.13). As demonstrated by our case studies, as well as our ensemble plots, the inflow rate at both halo and galactic scales is halo mass dependent and is naturally due to the depth of the galaxy's potential well. The outflow rates also appear to be partially mass-dependent, especially at halo scales. Outflow rarely overtakes inflow at either scale of interest, except at late times in massive halos (like m0163) where inflow and outflow reach rough equilibrium due to the high central gas density. The outflows driven by AGN activity appear to correlate with AGN luminosity in a way qualitatively similar to winds in the universe (Figure 5.14).

In MrAGN galaxies, halo mass governs not only the cosmological inflow rate as for NoAGN galaxies, but also the effectiveness of AGN feedback. The outflow rates at r_g for MrAGN galaxies are often comparable to those of NoAGN galaxies, except for when the AGN turns on, resulting in a spike in the outflow rate. From $z \sim 2$ to $z \sim 1$, the outflow rate at r_h is elevated in MrAGN galaxies relative to NoAGN galaxies, as material driven by AGN feedback travels farther than material driven by stellar and supernova feedback. We also see inflow suppressed at both radii, significantly and for almost all galaxies at r_g; after the AGN turns on, inflow and outflow tend to track each other (Figure 5.16, top row). The effect is more subtle and mainly significant for lower mass galaxies at r_h.

Both outflow enhancement and inflow suppression are seen first in higher mass galaxies at high redshift before manifesting in lower mass galaxies at later times, a result which corresponds to the phenomenon of "downsizing", or anti-hierarchical black hole growth (Hirschmann et al. 2012, 2014). In our simulations this is a result of the more massive halos receiving seed black holes at earlier times when the gas density in the black hole's vicinity is very high, resulting in

massive black holes at higher redshift feeding voraciously. This in turn results in more massive galaxies being affected by AGN feedback earlier. This is in agreement with many observational studies of the AGN population which conclude that the number density of the most luminous AGN peaks at high redshift, while less luminous AGN have almost constant number density and are more prevalent than high luminosity AGN at late times (Cristiani et al. 2004; Croom et al. 2004; Matute et al. 2006).

We also want to emphasize the increasing importance of so-called "preventative" feedback as we move to lower mass halos. While "ejective" feedback is important for removing gas and bouts of ejective feedback are seen in halos of all masses, the inflow of gas, both new and recycled, is far more suppressed in low mass halos than high mass halos. By $z = 1$-0, MrAGN galaxies have inflow at galactic scales suppressed by as much as ~ 1.6 dex, with lower mass halos most strongly affected. In fact, the lowest mass halos even have inflow suppressed at *halo* scales by up to ~ 0.5 dex. The cumulative mass of inflowing material onto the galaxy is lower by 0.4-0.6 dex for our MrAGN case studies, while the cumulative mass accreted onto the halo is suppressed by 0.1-0.3 dex. This is a result of outflowing material disrupting infall of new and recycled material by imparting momentum and energy. The infall is easier to halt in a shallower potential well. This mass-dependent preventative feedback is an interesting consequence of our mechanical feedback prescription. The strong outflows and their ability to clear out gas from the galaxy are not in and of themselves a surprise as the feedback prescription is designed to launch these winds, but their ability to sweep up gas that is on its way into the galaxy and in some cases turn it around is an interesting counterpoint to the usual theoretical method of putting in two separate feedback prescriptions, a "wind" mode and a "maintenance" mode; they are rather two sides of the same coin. Even if our AGN feedback model might not be perfect, since gas-free present day galaxies (such as m0501) may not be realistic, the ability of strong outflows to act in both ejective and preventative ways can be considered a general result and should be kept in mind.

How Much Gas is Removed Permanently and How Much Comes Back?

The main difference between the gas cycles in MrAGN and NoAGN galaxies is that while NoAGN galaxies remain recycling-dominated throughout their lives, MrAGN galaxies become ejection-dominated when their black holes begin feeding and their AGN turn on (Figure 5.7). While as much as 90% of the material in a given outflow episode might return to a NoAGN galaxy, this fraction is much smaller, at most 20%, for MrAGN galaxies. Even fractions this high are only seen in more massive galaxies whose potential wells are deep enough to retain some of the gas pushed out by AGN feedback. AGN-driven outflowing gas can travel larger distances than stellar and supernova-driven gas because it is launched with much higher velocities and is harder to slow down and turn around (Figures 5.17 and 5.18). MrAGN galaxies can have as much as 90% of the total outflowing material that is driven out past r_g cross the virial radius by $z = 0$ (Figure 5.15). NoAGN galaxies tend to have much smaller fractions of expelled material, around 1-2%. This results in NoAGN galaxies having much higher contributions of recycled gas to their inflow and outflow by $z = 0$, with larger contributions for larger halos (Figures 5.7 and 5.19).

Since gas in NoAGN galaxies is more likely to be recycled, each gas particle is more likely to accrete two or more times than gas particles in MrAGN galaxies, and the timescales of these recycling events tend to be shorter, and the distances traveled smaller, than for MrAGN gas particles (Figures 5.8, 5.9, 5.20). Again this seems to be due to the larger velocities associated with outflows driven by AGN feedback, which causes the recycling history of galaxies in the two runs to diverge when the black hole begins to feed. After that point, MrAGN galaxies rarely recycle outflowing material. The large distances traveled by gas particles has interesting implications for metal enrichment in the hot gas halo around galaxies and in the IGM (see the next chapter for a preliminary discussion).

How Are the Host Galaxies Affected?

Galaxies in our two runs tend to have different gas morphologies by $z = 0$ as a result of the different effects of feedback. In higher mass halos, the difference is mainly in the gas density and more diffuse hot gas halo around MrAGN galaxies as a result of more gas being removed from both the galaxy's inner regions and its gas halo (Figures 5.4, 5.5). In lower mass galaxies, however, the difference is much more stark. Lower mass MrAGN galaxies may be left only with diffuse hot gas (or may be depleted of gas completely) while their NoAGN counterparts develop substantial discs of cold gas by $z = 0$ (Figure 5.6). While the complete removal of gas may be too extreme, the cold gas disc, as well as the young stellar disc that accompanies it, are in conflict with observations in the mass range of our sample.

Beyond morphologies, AGN feedback is needed to quench our galaxies in order for them to resemble the observed high-mass galaxy population. Our feedback prescription accomplishes this by removing or heating the cold gas in the galaxy, which results in a steep decrease in star formation (Figures 5.1, 5.2, 5.3). In the case of lower mass galaxies, as mentioned above, even the hot gas within r_h is severely depleted by feedback (in m0501, this decrease is > 2 dex). This results in overall reduced in situ SFRs and thus smaller gas (by $\sim 0.5 - 2$ dex) and stellar (by ~ 0.2 dex) masses in MrAGN galaxies by $z = 0$ (Figure 5.11).

The effects of our implementation of AGN feedback bring our simulated galaxies into better agreement with observed galaxies in terms of morphology, star formation rate and stellar mass, but it may result in cold gas fractions which are too low.

5.5 Summary

Our study of two sets of 24 cosmological zoom galaxies both with and without mechanical and radiation-driven AGN feedback has led to the following main conclusions:

- Our model for mechanical and radiation-driven AGN feedback enhances galaxy-scale outflows and acts in an ejective way. Outflow rates at $r_{\rm g}$ are comparable between the two runs, but outflow rates at $r_{\rm h}$ can be enhanced by up to 1 dex in MrAGN galaxies at $z \sim$ 1-2. This is the result of larger outflowing gas velocities in the MrAGN runs, which cause a higher fraction of outflowing material at $r_{\rm g}$ to escape the galaxy's potential well and cross $r_{\rm h}$. This fraction is as high as 80% in MrAGN galaxies and only $\sim$ 5-10% in NoAGN galaxies.

- Our feedback model also suppresses inflow in MrAGN galaxies relative to NoAGN galaxies, effecting feedback in a preventative way as well, especially at the low mass end of our sample. At $r_{\rm g}$ the inflow rate can be suppressed by as much as 1.5 dex, while at $r_{\rm h}$, inflow rates can be suppressed by up to 0.5 dex in lower mass galaxies. This results in an overall smaller cumulative inflowing mass relative to the final halo masses of MrAGN galaxies versus their NoAGN counterparts (see Table 5.1 for these numbers for our case studies).

- Our NoAGN galaxies are recycling-dominated throughout their lives, such that most of the material removed from the galaxy returns ($\sim$ 68 - 78% for our case studies). By z=0, $\sim$ 50% of inflowing material into NoAGN galaxies is returning recycled material. Once their black holes begin to feed, MrAGN galaxies become ejection-dominated, with the majority of outflowing gas never returning to the galaxy (only about 8 - 15% returns in our case studies). The recycled inflowing fraction of MrAGN galaxies at z=0 can be as low as a few percent.

- Gas that *is* recycled in MrAGN galaxies tends to remain outside of the galaxy for longer ($\sim$ 2-3 Gyrs versus 1 Gyr) and to travel farther than recycled gas in NoAGN galaxies (up to several Mpcs). Accreted gas is more likely to undergo several recycling events in NoAGN galaxies than in MrAGN galaxies, and is more likely to remain in the galaxy (either as gas

or stars) until $z = 0$. Between $\sim$ 70 - 90% of accreted gas remains in our NoAGN case studies at $z = 0$ as compared with $\sim$ 30 - 50% in our two MrAGN case studies that have entire histories.

- Our model for AGN feedback succeeds in quenching galaxies and keeping discs from re-forming.

There are several further avenues of study which we plan to investigate in a series of future works.

One interesting point illustrated by our individual galaxy histories (Figures 5.1, 5.2, 5.3) is the weak correlation between AGN activity/outflow events and galaxy mergers. This is different from what has been seen in some other studies of simulations with AGN feedback, such as Tremmel et al. (2016). While it does sometimes appear that mergers and outflow events may be correlated, such as for m0163, it is difficult to say for sure. It is worth noting that the green dashed lines in Figures 5.1, 5.2 and 5.3 represent 1:10 or greater halo mass ratio mergers. The stellar or baryonic mass ratios and the time of the eventual galaxy mergers will be somewhat different, and this could contribute to the lack of correlation seen. It is also possible, especially in the early universe, to have several smaller satellites, none of which represents a 1:10 merger, interact with the central galaxy, the collective effect of which is disruption on par with a more major interaction. AGN activity may also be triggered by a very rich gas supply along filaments that does not take the form of galaxy interactions (Bellovary et al. 2013; Sanchez et al. 2016). This lack of a strong relationship between merger events and AGN activity is also being seen in other simulations of statistically complete galaxy populations, such as the Magneticum simulations (Steinborn et al., in preparation). In any event, a much closer look at how this AGN activity correlates with merger history is being reserved for a future work (Choi et al., in preparation).

We also plan to carry out a detailed comparison with observations on several fronts. We

plan to do a more in-depth study of the kinematics of these outflows beyond the very superficial discussion here, as well as the kinematics of the gas within the galaxy. This will include a theoretical study of the angular momentum, as well as a study of mock absorption lines to compare the kinematics of our simulated winds with those observed in the universe. We also plan to use these mock observations to compare with observed mass loading factors (again, only briefly touched on here), in order to see how realistic our outflows appear (especially in the case of our more extreme blowout events in lower mass galaxies) and how our interpretation of these events might change from different viewing angles and at different times.

The very large distances traveled by ejected gas (and even recycled gas in the MrAGN runs) has interesting implications for outflows enriching the surrounding halo and the IGM, as well as enriching other galaxies at very large distances, something which we have not studied here. We will present a preliminary study of the impact of AGN driven winds on metal enrichment in the next chapter. Finally, we also plan to explore the impact of AGN-driven outflows on nebular emission and absorption in different regions of a galaxy, producing spatially resolved emission and absorption line maps to improve the interpretation of modern integral-field spectroscopic observations (Hirschmann et al., in prep.).

Chapter 6

The Effect of Mechanical AGN Feedback on Chemical Enrichment

6.1 Introduction

As we have seen in Chapter 5, mechanical and radiation-driven AGN feedback can have a very strong effect on both the inflow and outflow of gas around a galaxy. If AGN in the universe are indeed affecting the baryon cycle in their host galaxies so strongly, this is likely to leave a signature on the metal content of those galaxies, especially in the hot halo gas component.

The hot halo can be the dominant baryonic component in massive elliptical galaxies, and is made up of both enriched material from inside of the galaxy, as well as pristine material that flows in from outside the dark matter halo and is shock heated (Gonzalez et al. 2007; Arnaud et al. 1992; Schindler & Diaferio 2008). Because of this, the enrichment of halo gas will be strongly affected by changes in the behavior of inflows and outflows like those observed between our two simulation runs.

Observations suggest that massive galaxies and groups exhibit negative abundance gradients, being more enriched at the center, with decreasing metal abundance corresponding to increasing radius (Finoguenov & Ponman 1999; Buote et al. 2003; Sato et al. 2009). However, the central metal excess extends out further than the optical emission from the central galaxy, suggesting that metal enriched gas is being distributed outside of the galaxy (David & Nulsen 2008). Some massive galaxies have halo gas whose metallicity is on the order of the metallicity within the

galaxy itself. AGN feedback has often been invoked to explain such redistribution of metal-enriched gas (Rebusco et al. 2006; Moll et al. 2007).

Meanwhile, simulations have had a hard time producing galaxies with enough metals in their halo components to agree with observations. Simulations tend to produce galaxies with metal excesses in their centers, and deficits in the outskirts when compared with observations (Valdarnini 2003; Romeo et al. 2005; Davé et al. 2008).

In this chapter, we will examine the differences in chemical enrichment of both the galaxy and the hot halo gas in the two simulation runs previously presented in Chapter 5. These simulations have already been shown to accurately model the X-ray luminosities of galaxies in our mass range, another property that other simulations have trouble matching (Choi et al. 2017). We also know that, in general, metals tend to follow the gas, which is profoundly affected by the addition of AGN feedback. We will track gas particles as we did in the previous chapter in order to discover the fate of outflowing metals. In Section 2 we present our results, and in Section 3 we discuss them. We conclude in Section 4.

6.2 Results

6.2.1 Case Studies

We begin again, as we did in Chapter 5, by examining in detail the history of metals in the representative galaxies m0163 ($M_{*,\mathrm{final}} \sim 10^{11.4} M_\odot$ and $M_{\mathrm{h,final}} \sim 10^{13.1} M_\odot$), m0329 ($M_{*,\mathrm{final}} \sim 10^{11.3} M_\odot$ and $M_{\mathrm{h,final}} \sim 10^{12.7} M_\odot$) and m0501 ($M_{*,\mathrm{final}} \sim 10^{11.2} M_\odot$ and $M_{\mathrm{h,final}} \sim 10^{12.5} M_\odot$).

Metal Mass and Metallicity Histories

Figure 6.1 shows the history of metallicity in galaxy m0163. In the top panels are shown the mass of metals contained in four different components: stars within r_g, gas within r_g, cold gas

($T < 2 \times 10^4 K$) within r_g, and hot gas ($T > 2 \times 10^4 K$) between r_g and r_h. The largest mass of metals is contained in stars, with a larger mass found in the NoAGN run, where star formation is allowed to continue all the way until redshift zero. The mass of metals in galactic gas is lower by more than 1 dex in the MrAGN run when compared with the NoAGN run, due both to the fact that fewer stars are born to enrich their surrounding gas, and to the removal of enriched gas from the galaxy by AGN feedback. The removal or heating of cold gas results in a strong decrease in the mass of metals contained in cold gas in the MrAGN run, in contrast to the NoAGN run, where about one third of the metals contained in gas at redshift zero are in cold gas particles. There is a slightly higher, although comparable, mass of metals (by $\sim 0.2 - 0.3$ dex) in the hot halo component of the MrAGN run than in the NoAGN run, although in both runs there are more metals contained in the hot halo gas than in the galactic gas.

In the lower panels are shown the average metallicities of gas by mass in units of solar metallicities, $Z_\odot = 0.0134$ (Asplund et al. 2009), in the same four components. The average metallicity of stars is once again larger in the NoAGN run, and the average metallicity of hot halo gas is larger in the MrAGN run. At times when there is still cold gas in the MrAGN run, the metallicity of cold gas in the NoAGN run is higher. In both runs, the metallicity of cold galactic gas tends to be much larger than the metallicity of hot halo gas, despite the mass of metals in hot halo gas being so much higher: the mass of hot halo gas in total is much larger than the mass of cold galactic gas.

Figure 6.2 is the same as Figure 6.1, but for galaxy m0329. Here the mass of metals is affected much more strongly by AGN feedback, with the total mass of metals in gas being severely decreased in the MrAGN run, while the mass of metals in the hot gas halo is about the same as that found in the NoAGN run. The bottom panels reveal that the average metallicities of these components behave very similarly to m0163.

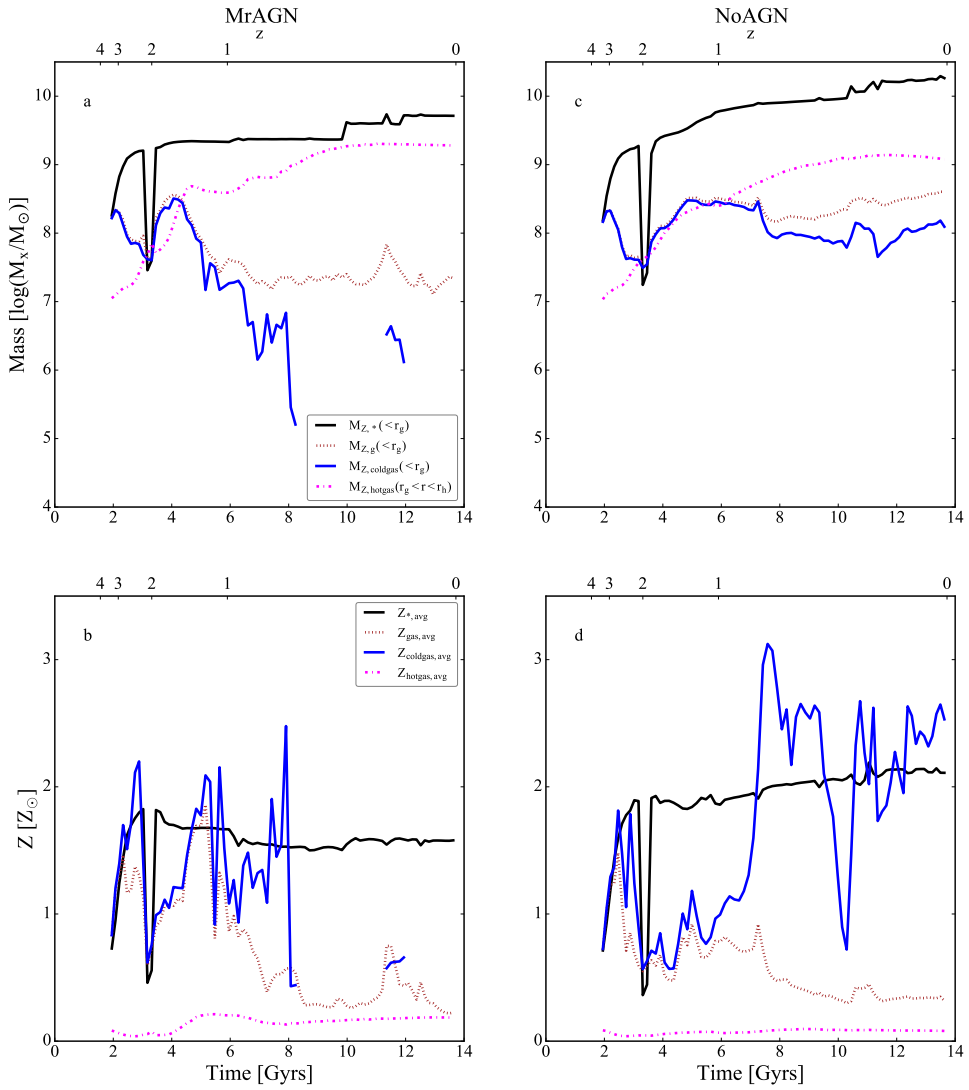

Figure 6.1: History of metals in galaxy m0163. Left Column: Results for MrAGN run. Right Column: Results for NoAGN run.

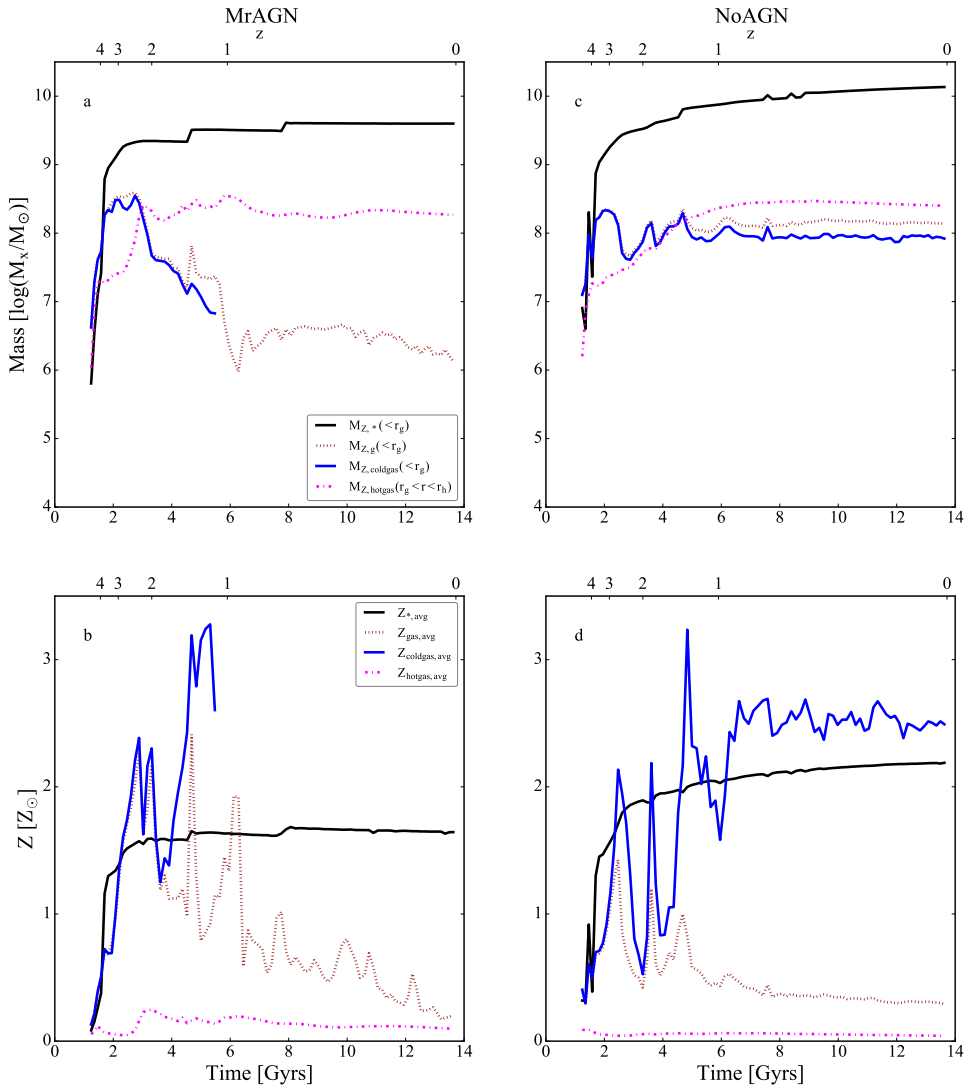

Figure 6.2: History of metals in galaxy m0329. Left Column: Results for MrAGN run. Right Column: Results for NoAGN run.

Finally, in Figure 6.3, we see the metal masses and average metallicities for these four components in galaxy m0501. All of the gas components are depleted by the strong outflow event between 4-6 Gyrs. However, while the mass of metals in the hot gas halo is greatly decreased by AGN feedback, the average metallicity of the hot gas halo increases drastically due to the influx of gas that was enriched within the galaxy being pushed out into the galactic halo.

Metal Maps

We now turn to the distribution of metals within and around our case study galaxies. Figure 6.4 is a metallicity map of the gas in galaxy m0163 in four different redshift slices. The metallicity is again shown in units of solar metallicities. At $z \sim 3$ and $z \sim 2$, the distribution of metallicity looks very similar between the two runs, but at $z \sim 1$, there is evidence of a large-scale, chemically enriched outflow depositing metals into the galactic halo. At z=0, the average halo gas metallicity is higher in the MrAGN run than in the NoAGN run. Figure 6.5 is the same as Figure 6.4, but for galaxy m0329. The behavior is very similar, except the outflow signatures can be seen as early as $z \sim 2$. Finally, Figure 6.6 is a metallicity map of galaxy m0501. At $z \sim 1$ we can see nearly all of the metals contained in gas within the galaxy being expelled as a result of the large galaxy-clearing outflow event that takes place between 4-6 Gyrs.

Metallicity Abundance Gradients

Again examining the distribution of metals, we turn to Figure 6.7, which is the radially averaged metal abundance gradient for all gas in m0163, shown at four different redshifts. At z=3 and z=2, the profiles exhibit a steep gradient and are very similar between the two runs. By z=1, however, the overall metal abundance beyond $0.1R_{500}$ is higher in the MrAGN run, and the gradient is more negative. At z=0, the abundance gradient in the NoAGN run has remained quite similar to that at z=1, while the gradient in the MrAGN run has flattened considerably

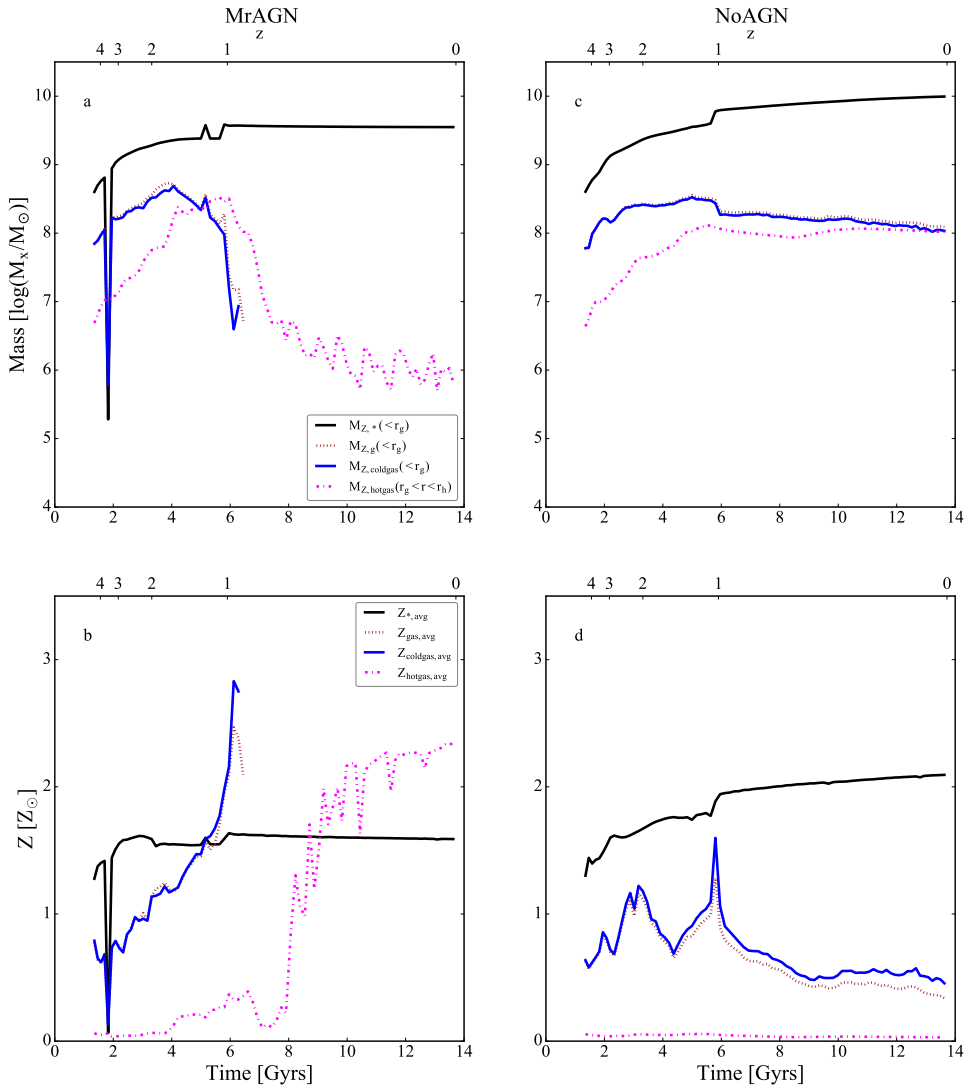

Figure 6.3: History of metals in galaxy m0501. Left Column: Results for MrAGN run. Right Column: Results for NoAGN run.

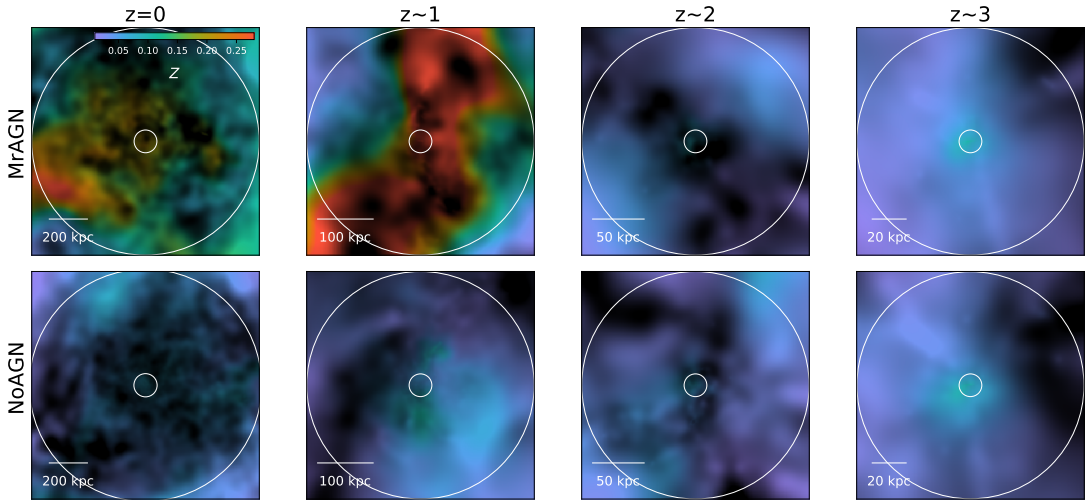

Figure 6.4: Metallicity maps for galaxy m0163, given in solar metallicities. Images created using `pygad` (Röttgers 2017). In the gas image, the color corresponds to gas metallicity, while the luminance corresponds to gas density. Top row: Results for MrAGN run. Bottom row: Results for NoAGN run. White circles denote the current r_g and r_h.

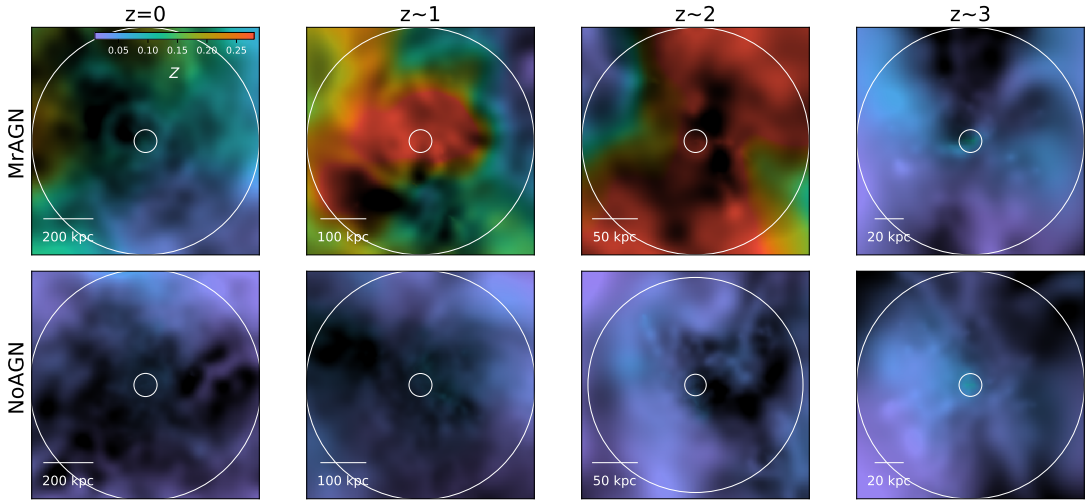

Figure 6.5: Metallicity maps for galaxy m0329, given in solar metallicities. Images created using `pygad` (Röttgers 2017). In the gas image, the color corresponds to gas metallicity, while the luminance corresponds to gas density. Top row: Results for MrAGN run. Bottom row: Results for NoAGN run. White circles denote the current r_g and r_h.

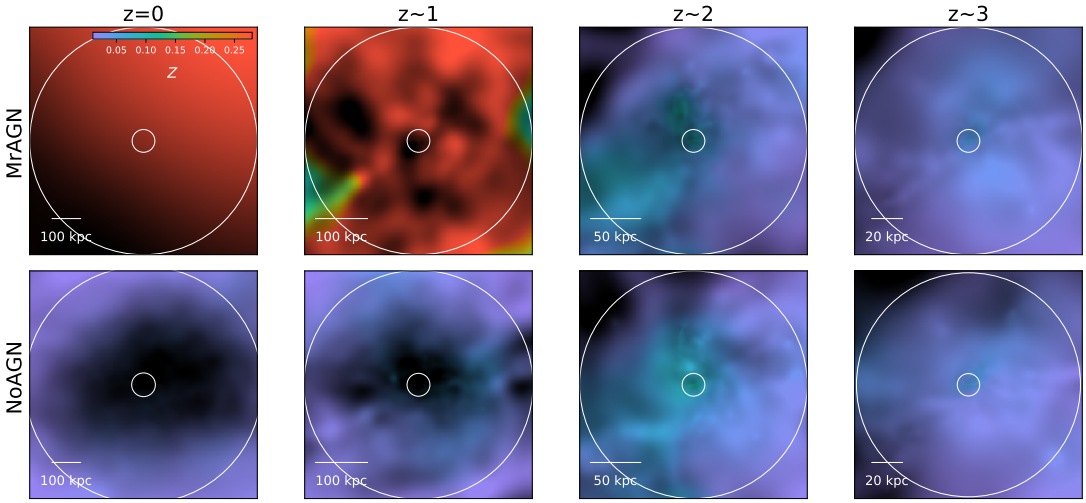

Figure 6.6: Metallicity maps for galaxy m0501, given in solar metallicities. Images created using `pygad` (Röttgers 2017). In the gas image, the color corresponds to gas metallicity, while the luminance corresponds to gas density. Top row: Results for MrAGN run. Bottom row: Results for NoAGN run. White circles denote the current r_g and r_h.

out to R_{500}.

In order to make a comparison with observations, in Figure 6.8, we present a stacked metal abundance gradient for all of our halos with $M_{halo}>8 \times 10^{12} M_{\odot}$. Overplotted at z=0 is a fit to the metal abundance gradients of stacked non cool-core groups at low redshift presented in Johnson et al. (2011). The flatter average MrAGN gradient is in better agreement with these

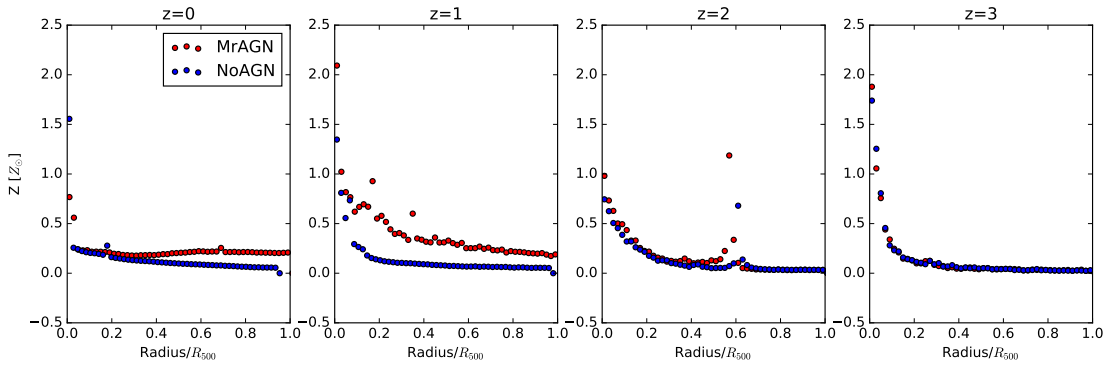

Figure 6.7: Gas metal abundance gradient for all gas in m0163 at four redshift snapshots.

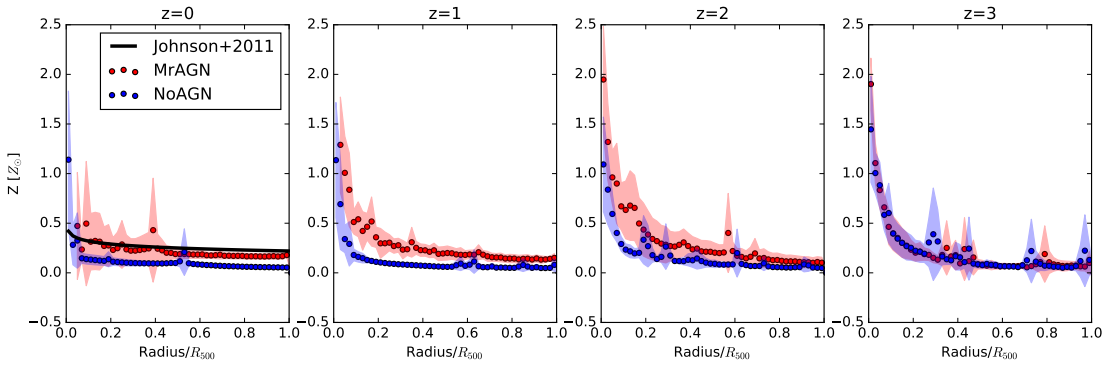

Figure 6.8: Average gas metal abundance gradient for all gas in halos with $M_{halo}>8 \times 10^{12} M_\odot$ at four redshift snapshots. In black at z=0 is shown a fit to a stacked analysis of non cool-core clusters from Johnson et al. (2011). Shaded regions represent the standard deviation from the mean.

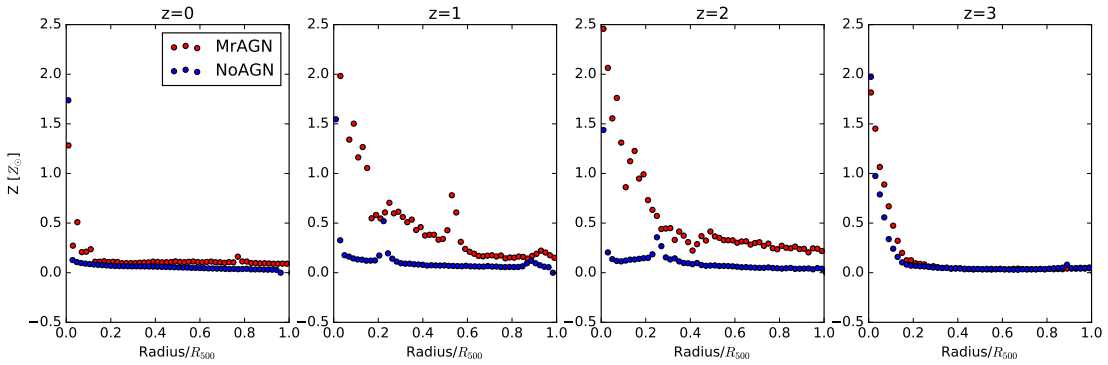

Figure 6.9: Gas metal abundance gradient in m0329 at four redshift snapshots.

results at $r > 0.5R_{500}$ than the average NoAGN gradient.

In Figure 6.9, we see that the two abundance gradients diverge earlier for m0329 than for m0163, by z=2, due to a slightly earlier onset of AGN feedback. At z=1-2, the metallicity is higher and the gradient is steeper in the MrAGN run. At z=0, the abundance gradient in the MrAGN run is only slightly higher than in the NoAGN run, although the MrAGN gradient is still marginally flatter.

In Figure 6.10, we see a large increase in metallicity at about the time of the major burst of AGN-driven outflow seen in Chapter 5. By z=0, there isn't any gas left to contain metals in the

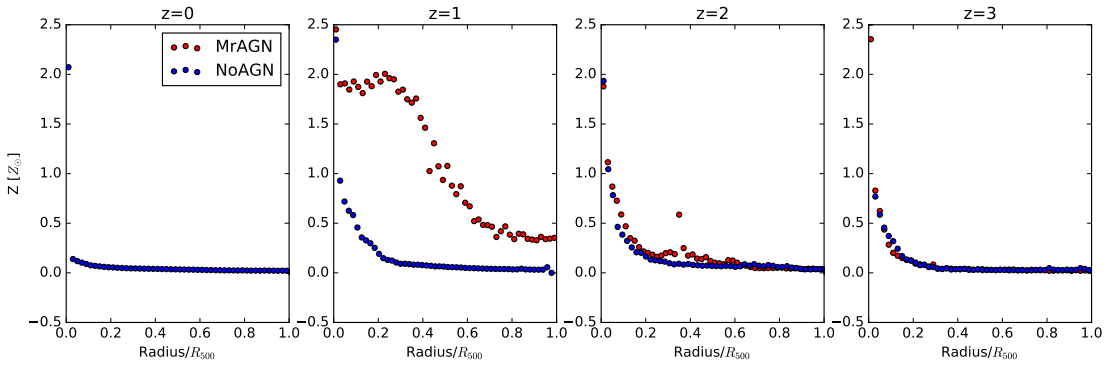

Figure 6.10: Gas metal abundance gradient in m0501 at four redshift snapshots.

MrAGN run.

Outflow Enrichment

Turning explicity to outflowing gas, the top panel of Figure 6.11 shows the evolution of the ratio of the average metallicity of outflowing gas to the average metallicity of gas within the galaxy m0163 with time. The outflowing gas in the MrAGN run is more enriched relative to the rest of the gas in the galaxy than the outflowing gas in the NoAGN run, and the metallicity at certain times can be even higher than the average metallicity of all of the gas left behind. In both runs, this ratio increases with time, due to the repeated recycling of enriched material. These same trends can be seen for m0329 as well, although the effect is even more pronounced, especially at late times. This is also true for m0501, although, after $\sim$ 6 Gyrs, there is no more outflowing gas to track.

6.2.2 Broad Trends

We now turn to properties of our simulated sample at large. In Figure 6.12 is plotted iron abundance of the hot gas halo versus the total X-ray luminosity of our galaxies. We define hot gas as having $T > 10^6$K in order to make a comparison with observations. The small grey

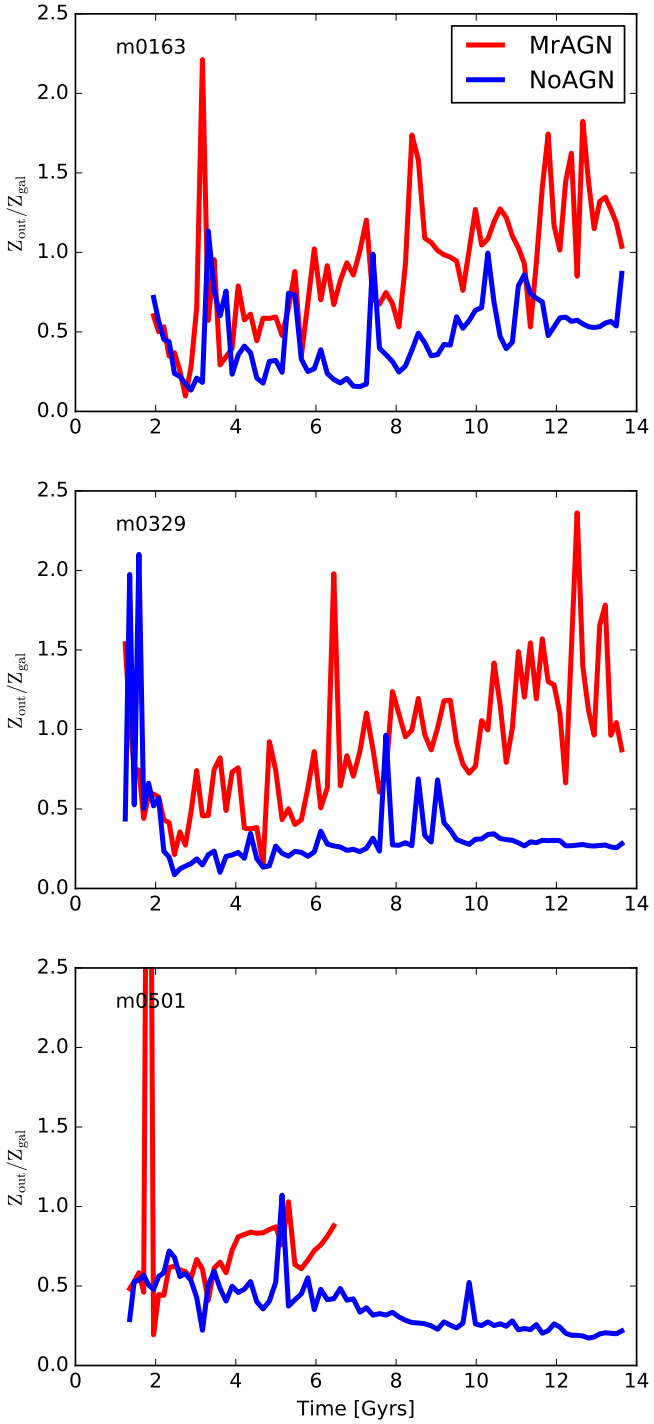

Figure 6.11: The average metallicity of outflowing gas versus the average metallicity of gas within the galaxy as a function of cosmic time in our three case study galaxies.

points represent a sample of elliptical galaxies presented in Crain et al. (2013) and collected from Humphrey & Buote (2006) and Athey (2007). As demonstrated in Choi et al. (2017), our AGN feedback prescription decreases the X-ray luminosity of our galaxies, bringing them into better agreement with observations. This also has an effect on the hot halo iron abundances; galaxies whose X-ray luminosities are more strongly suppressed also tend to have higher iron abundances which are also in better agreement with observations than those in the NoAGN case. While we do not capture the apparent correlation between X-ray luminosity and iron abundance (and indeed have a few outliers at small X-ray luminosity due to a more severe removal of gas from the halo), our MrAGN run is at least in better qualitative agreement with observations.

Figure 6.13 shows the iron abundance of gas within R_{500} versus the temperature of gas at R_{500}. Plotted in grey circles is a homogenized dataset of groups and clusters compiled by Yates et al. (2017). Our MrAGN galaxies once again occupy a more reasonable portion of the diagram than our NoAGN galaxies, although once more, the trend of abundance with gas temperature is not reproduced by our model.

Figures 6.14 and 6.15 show the masses of gas and metals contained in both the galaxy and the halo of all of our galaxies at z=0. We further present the masses of gas and metals in cold gas ($T < 2 \times 10^4 K$) and hot gas ($T > 2 \times 10^4 K$). In the top row of Figure 6.14, the overall gas mass inside galaxies is greatly reduced in the MrAGN run when compared with the NoAGN run, especially at low mass where the difference can be as great as 2 dex. Most of this gas is hot, so the hot gas in the right panel behaves almost identically. We see that there is no cold gas in the MrAGN galaxies in the middle panel. In the bottom row, we see that the mass of gas in the halo can be decreased by as much as 1 dex in lower mass galaxies, and again most of the gas is hot. The masses of cold gas in the halo are actually comparable between the two runs.

Turning to Figure 6.15, the mass of metals in MrAGN galaxies is reduced, but by a slightly smaller percentage than the total gas mass in Figure 6.14. Meanwhile, the mass of metals in the

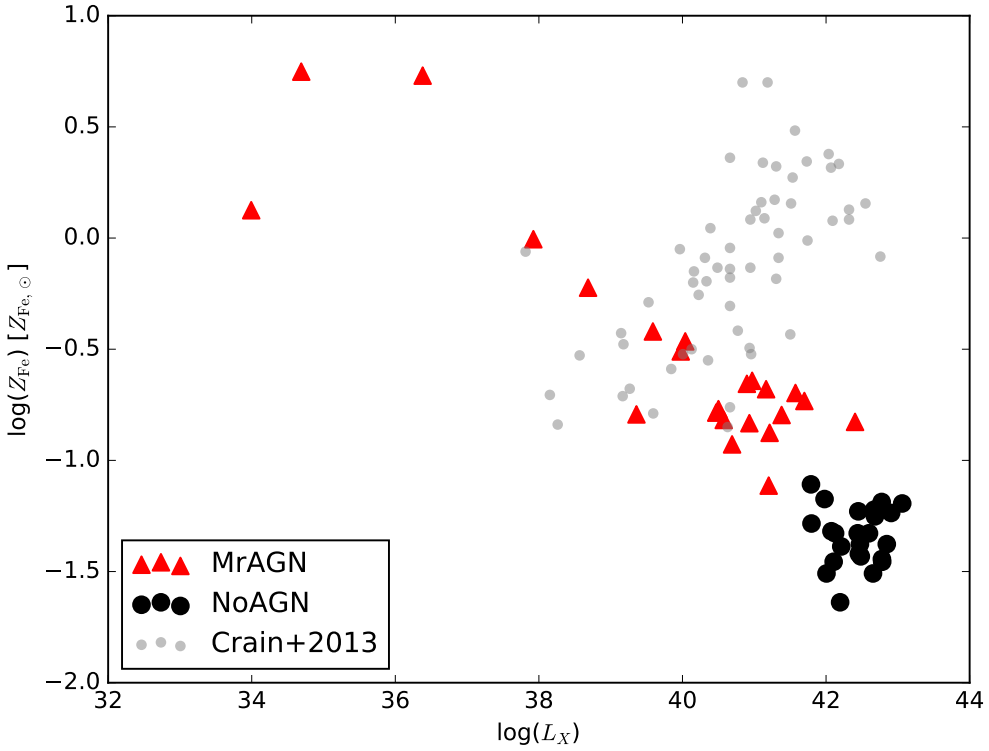

Figure 6.12: The iron abundance of our galaxies' hot gas halos versus their total X-ray luminosities. Black circles denote galaxies in the NoAGN runs, while red triangles denote galaxies in the MrAGN runs. Small grey circles denote a sample of galaxies presented in Crain et al. (2013) comprised of observations collected from Humphrey & Buote (2006) and Athey (2007).

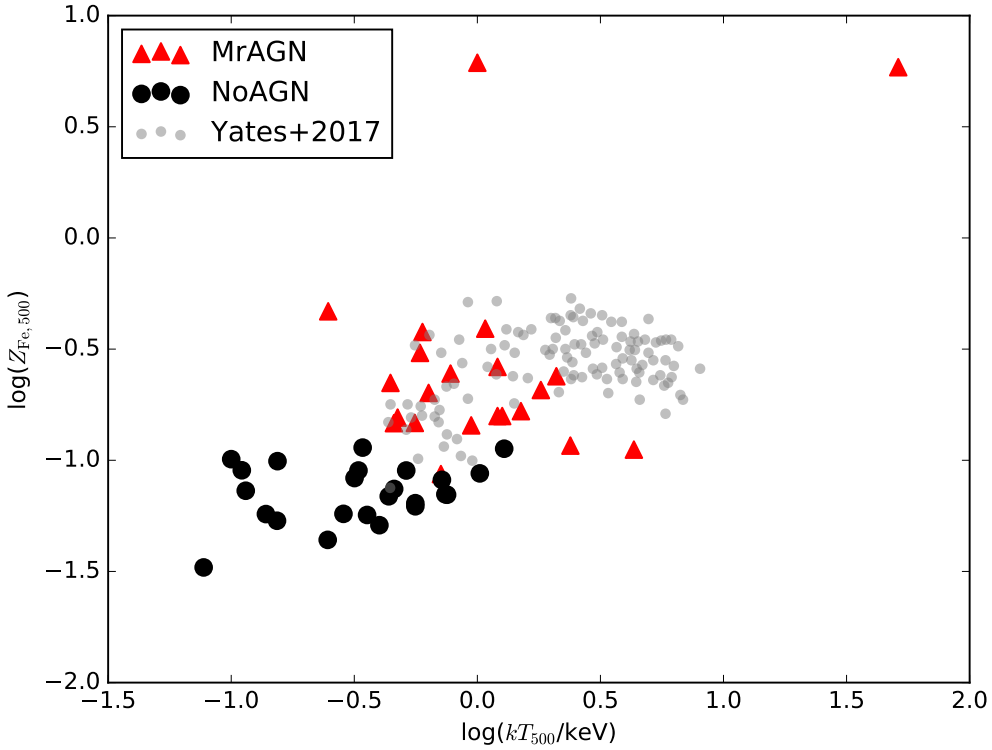

Figure 6.13: The iron abundance within R_{500} versus the gas temperature at R_{500} in our galaxies. Overplotted in grey points is a compilation of observations from Yates et al. (2017).

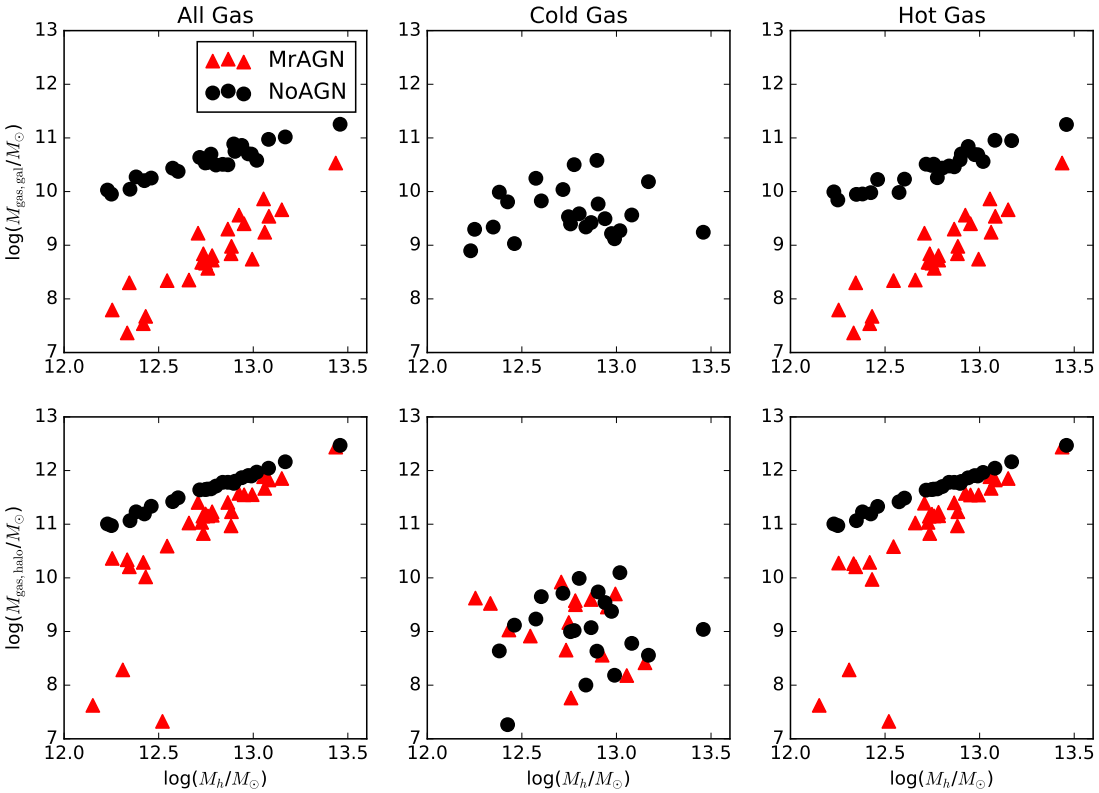

Figure 6.14: The total, cold ($T < 2 \times 10^4 K$), and hot($T > 2 \times 10^4 K$) galaxy and halo gas masses of our zoom galaxies. Top: galaxy gas. Bottom: Halo gas. Left column: Total gas. Middle column: Cold gas. Right column: Hot gas.

halo is very similar in all three phases between the two runs, despite the smaller mass of gas in the halo found in the MrAGN run. In Figure 6.16, both of these trends manifest as slightly higher gas metallicities both within the galaxies and in the halos. In lower mass galaxies, the trend can be very pronounced.

In Figure 6.17, we examine the average metallicity of gas specifically in the galaxy halos in units of solar metallicities. In all cases, the metallicity in the MrAGN cases is higher, with some low mass galaxies exhibiting metallicities that are twice solar. The green dashed line represents current estimates of the metallicity of the CGM in galaxy groups (Edge & Stewart 1991; Tamura et al. 2004). While our AGN galaxies are in general closer to matching this line, the metallicities

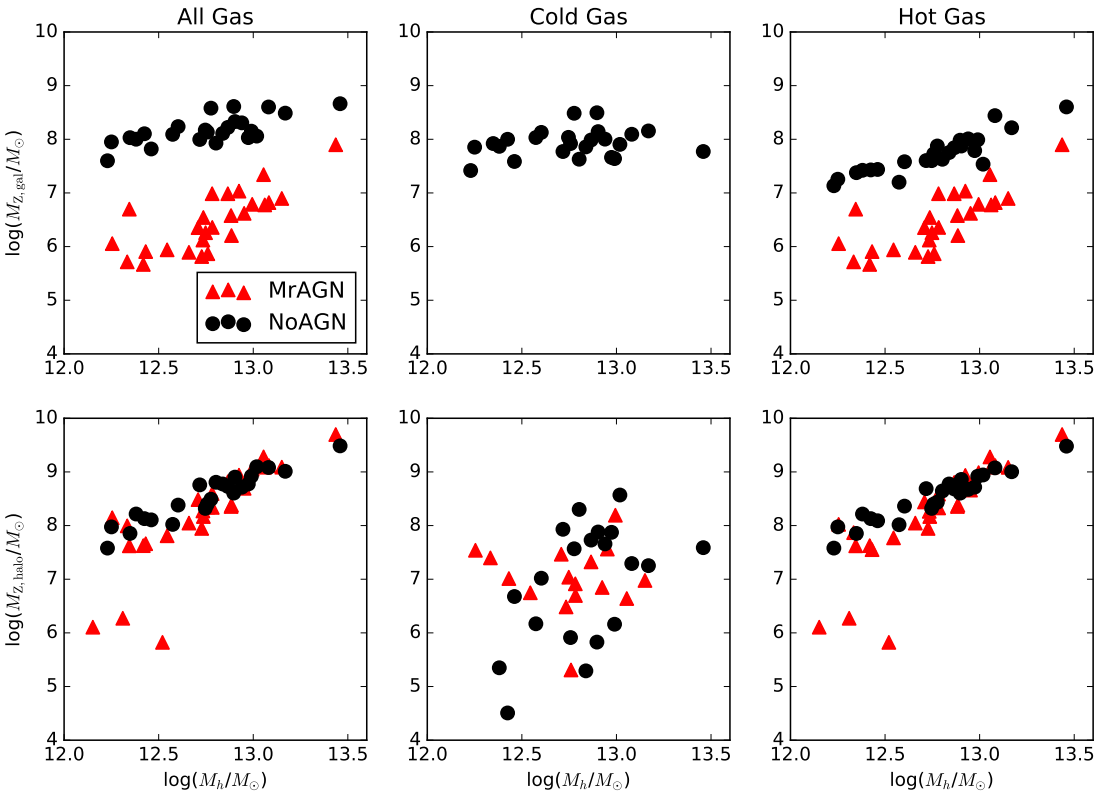

Figure 6.15: The total, cold ($T < 2 \times 10^4 K$), and hot($T > 2 \times 10^4 K$) galaxy and halo metal masses of our zoom galaxies. Top: galaxy metals. Bottom: Halo metals. Left column: Total metals. Middle column: Cold metals. Right column: Hot metals.

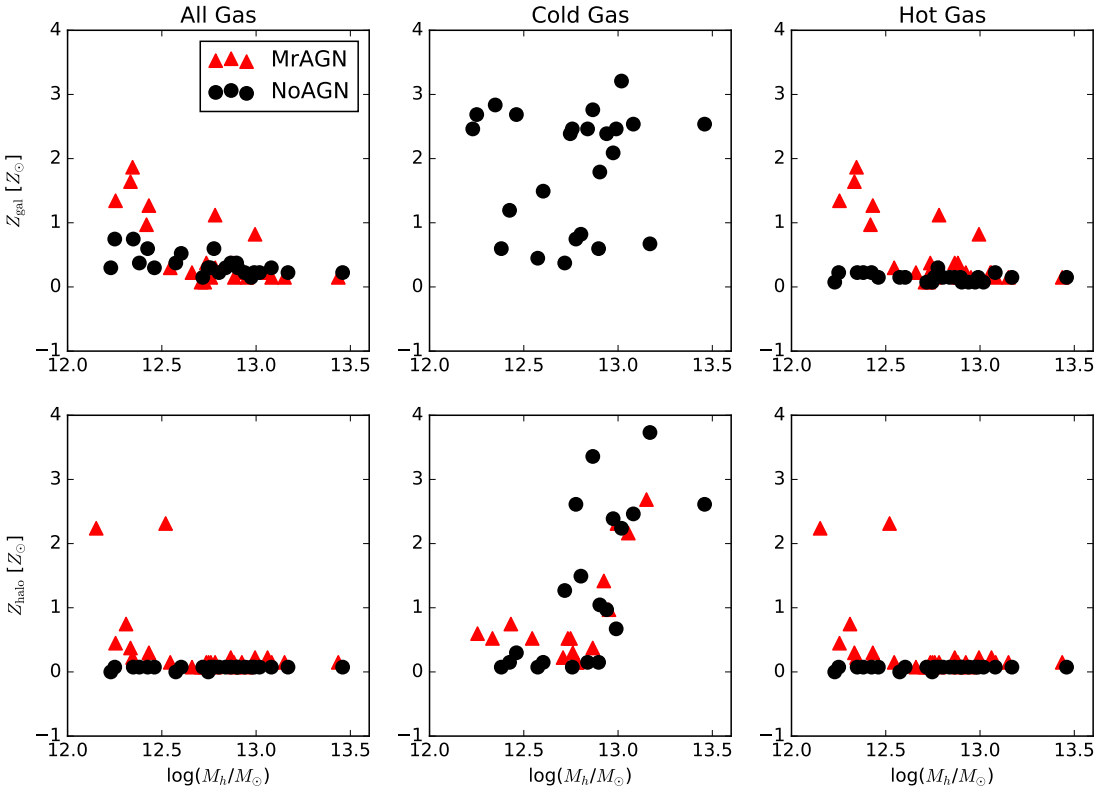

Figure 6.16: The total, cold ($T < 2 \times 10^4 K$), and hot($T > 2 \times 10^4 K$) galaxy and halo gas metallicities of our zoom galaxies. Top: galaxy metallicity. Bottom: Halo metallicity. Left column: Total gas metallicity. Middle column: Cold gas metallicity. Right column: Hot gas metallicity.

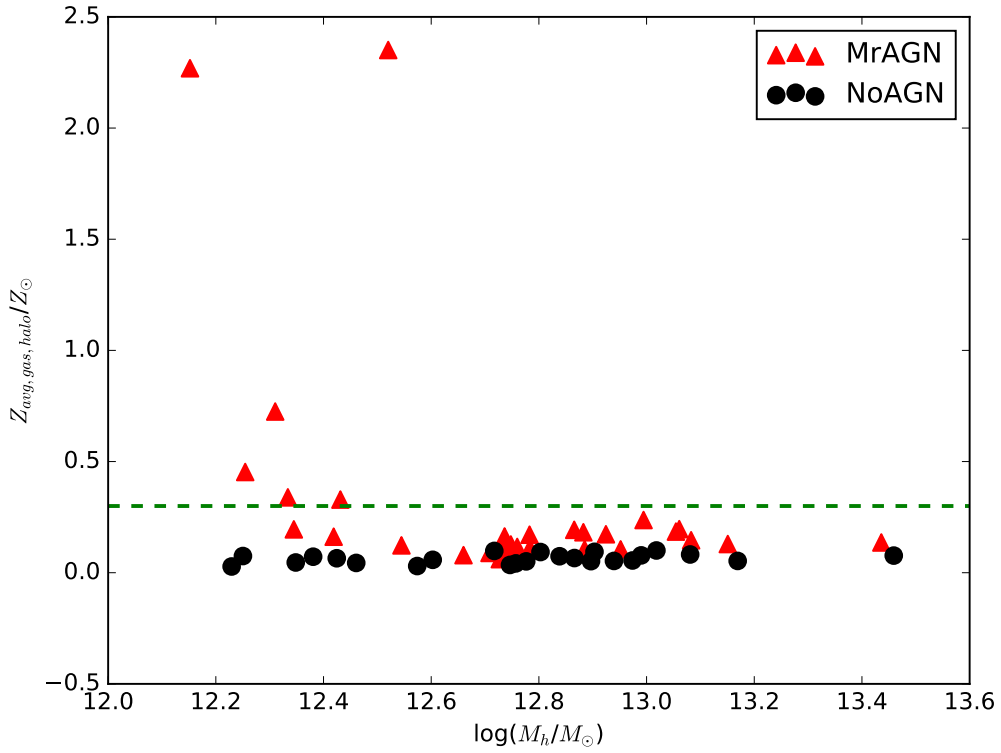

Figure 6.17: Average metallicity of halo gas in units of solar luminosities.

are still slightly too small.

Figure 6.18 shows the ratio of average metallicity of halo gas to the average metallicity of gas within the galaxy. In all cases, this ratio is higher for the MrAGN runs, with the disparity between runs being greatest for higher mass galaxies, where the ratio approaches and even slightly exceeds unity.

We see in Figure 6.19 that the fraction of metal mass in the halo that arrived directly via outflows is only about 20% at most even in the MrAGN run. While AGN feedback increases the average metallicity of galactic halos, it doesn't achieve this only by depositing metals into the halo, but by a combination of deposition of metals and removal of gas that was already present in the halo. We will discuss this further below. We might expect the effect to be stronger, but

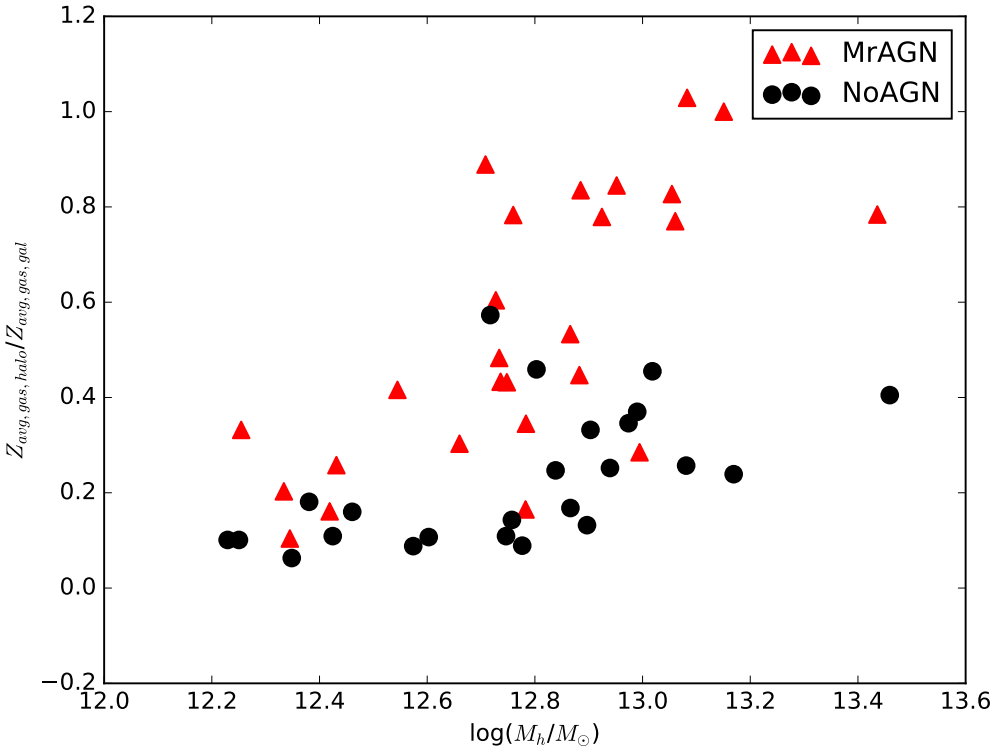

Figure 6.18: Ratio of average metallicity of halo gas to average metallicity of gas within the galaxies.

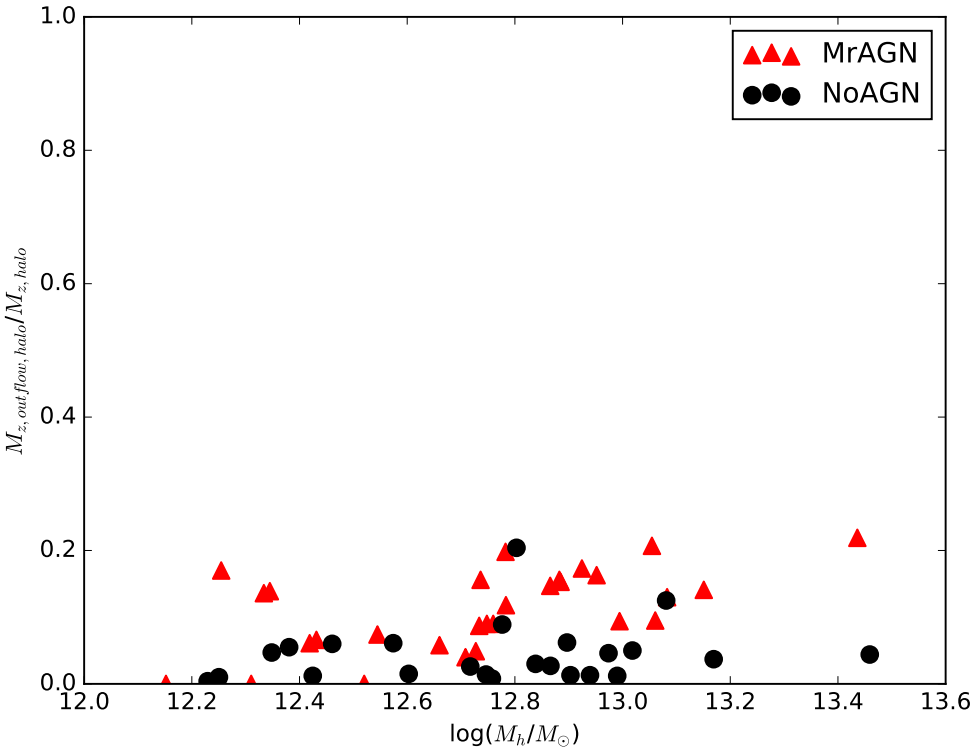

Figure 6.19: Fraction of metal mass in halo that comes from outflows.

in fact we know from Chapter 5 that much of the enriched gas driven from the galaxy actually ends up beyond the halo. Figure 6.20 shows the percentage of all of the metals which have been driven from each galaxy that are in a set of radial bins at z=0. In MrAGN galaxies, the vast majority of metals driven from the galaxy reside as far as or farther than 2 virial radii from the galaxy center. Towards higher mass, a larger fraction of gas exists in the halo. In NoAGN galaxies, a much larger fraction of metals is back in the galaxy, with most of the rest occupying the halo.

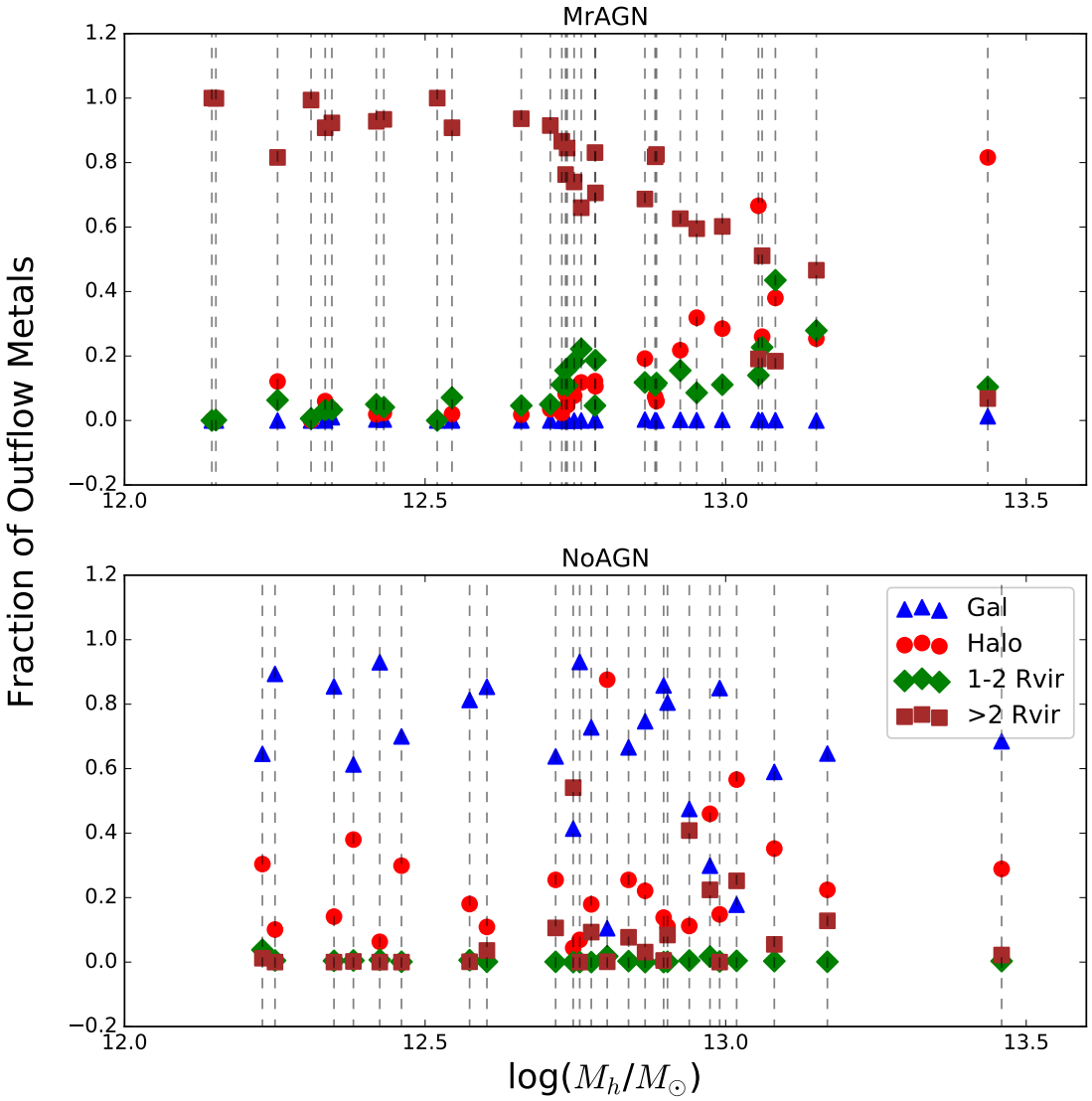

Figure 6.20: The fraction of metals which have flown out of the galaxy that occupy a set of radial bins at z=0. Each black dotted line represents a galaxy. Blue triangles denote the fraction of outflowing metals which are now back in the galaxy. Red circles denote outflowing metals now in the halo. Green diamonds denote outflow metals between one and two virial radii, and brown squares denote metals at distances greater than two virial radii.

6.3 Discussion

6.3.1 Metal Content of the Galaxy (r<$r_{\rm g}$)

We first discuss the metal content of gas within $r_{\rm g}$. At high redshift ($z \sim 3$), before AGN feedback becomes prevalent, both runs of galaxies form stars and experience the same baryon cycles, leading to the same chemical enrichment. When AGN feedback kicks in in the MrAGN runs ($z \sim 1-2$), the two types of galaxies diverge. Outflows driven by AGN feedback remove chemically enriched gas from the MrAGN galaxies (Figures 6.4, 6.5, 6.6, 6.11). However, even enriched particles are made up of more pristine gas than enriched gas, and so the total mass of gas in the MrAGN galaxies decreases faster than the total mass of metals, resulting in MrAGN galaxies having higher average galactic gas metallicities than NoAGN galaxies at $z \sim 1-2$ despite having smaller total galactic gas metal masses (Figures 6.1, 6.2, 6.3, 6.14, 6.15, 6.16). As time goes on, the outflowing gas is characteristically more metal-rich, so the galactic metal mass falls like the total metal mass, resulting in galactic metallicities for higher mass MrAGN galaxies at $z \sim 0$ very similar to those found in NoAGN galaxies, despite the diminished gas and metal reservoirs found within $r_{\rm g}$ (Figures 6.1, 6.2, and the inner radii in Figures 6.7, 6.9). The AGN feedback leaves more of a signature on the metal content within $r_{\rm g}$ in our lower mass galaxies, where more gas is removed from within the galaxy, and the contribution of the metals left behind leads to higher average metallicities.

6.3.2 Metal Content of the Halo ($r_{\rm g}$<r<$r_{\rm h}$)

In Section 2, we found that the gas halos of our MrAGN galaxies had higher average metallicities than those of our NoAGN galaxies, but that a relatively small fraction of the metals in our MrAGN halos were actually directly deposited by outflows from the central galaxy (6.19). While outflows from within $r_{\rm g}$ are important for seeding metals into the halo, this is only part of the

story. In addition, as we found in the previous Chapter, our AGN feedback prescription is capable of removing gas from the halo as well as the galaxy. In terms of metal enrichment, this removal of gas from the halo, combined with the addition of metals from within the galaxy, allows for a relatively small mass of injected metals to account for a boost in the average metallicity of MrAGN halos. A majority of the metals ejected from the galaxy by AGN feedback actually ends up far outside of the halo (Figure 6.20).

As discussed in the last Chapter, the halo gas mass of MrAGN galaxies can be smaller than that of NoAGN galaxies by as much as ~ 1 dex. However, here we find that the mass of metals in the halo is almost identical between the two runs, thanks to the injection of metals from AGN-driven winds (Figure 6.14). This results in an overall higher metallicity in the halos of MrAGN galaxies, which even approach the gas metallicities of the galaxies themselves (Figures 6.1, 6.2, 6.3, 6.4, 6.5, 6.6, 6.12,6.13, 6.17, 6.18). This disparity in metallicity between the halos of MrAGN and NoAGN runs tends to be strongest in lower mass galaxies, due to the severe depletion of gas that occurs in these systems, coupled with almost all of the metals within the galaxy being driven out into the halo or beyond. This results in an overall higher metal abundance in MrAGN halos, as well as a flatter slope in the metal abundance gradients of our higher mass halos, a signature which we can see in observations of groups (Figure 6.7).

6.4 Conclusions

In this Chapter, we have investigated the effect of mechanical and radiation-driven AGN feedback on the metal content of our suite of cosmological zoom simulations. We have found that:

- Our prescription for AGN feedback is capable of moving large amounts of metals from the galaxy into the halo and beyond.
- The deposition of metals is in fact not enough to appreciably raise the average metallicity

of halo gas. Instead, the removal of gas from the halo by galactic outflows, combined with the deposition of metals, results in the increase of metallicity observed.

- The overall effect is a very slight decrease in the metallicity of gas within MrAGN galaxies, and a notable increase in the metallicity of their gas halos.

- The metal abundance gradients of our higher mass MrAGN galaxies exhibit higher overall metallicities and flatter slopes, but in lower mass galaxies, the majority of the expelled metals end up far beyond the halo.

Chapter 7

Conclusions

In this thesis, we have studied the effect of AGN feedback on galaxies from z$\sim 0-3$, both in terms of how it shapes the galaxy population at large, and how it affects the gas in individual galaxies. In order to do this we have used different types of models of galaxy formation and evolution as well as observations of the star formation and structural properies of real galaxies. First, in Chapter 2, we described the models used in the rest of the work: a semi-analytic model to generate large populations of galaxies shaped by various physical processes, and a hydrodynamical simulation in order to study in particular the gas in and around galaxies affected by AGN feedback.

In Chapter 3, we divided galaxies up by their star formation rates and Sérsic indices in order to study the co-evolution of these properties in the presence of AGN feedback. We carried out this study both on simulated galaxies and observed galaxies in order to test our model. We found that our models qualitatively reproduce the fraction of quiescent galaxies since z$\sim$ 2, but that our model with bulge growth due only to mergers failed to reproduce the spheroid-dominated fraction of galaxies. An additional channel for bulge growth through disk instabilities is required to produce roughly the right fraction. Our model further qualitatively reproduced the fraction of galaxies in our four star formation rate-and-morphologically defined bins, capturing the decrease in the fraction of star forming disk-dominated galaxies with time and the corresponding increase in quiescent spheroid-dominated galaxies. However, we predicted stronger evolution in the fraction of star forming spheroid-dominated galaxies and quiescent disk-dominated galaxies than is

seen in observations. We found that, in our model, star forming disk-dominated galaxies were the result of very quiet histories, absent of mergers or disk instabilities, while quiescent spheroid-dominated galaxies were likely to have undergone at least one major merger or several minor mergers or disk instabilities. Star forming spheroid-dominated galaxies were a short-lived population of post-trauma galaxies undergoing a starburst, while quiescent disk-dominated galaxies were galaxies which had either stopped accreting new gas or whose low surface density gas disks were inefficient at forming stars. In general the qualitative similarity between the buildup of our model population and observed galaxies supported the idea that AGN are a viable way to explain galaxy quenching and its correlation with morphology.

In Chapter 4, we extended our analysis to more broadly look at the correlation of galaxy structural properties with their location in the plane of star formation rate and stellar mass, as well as with their distance from the main sequence of star formation. We carried out this analysis on a sample of SAM galaxies, as well as galaxies from the CANDELS and GAMA surveys. We found in the observations that near the main sequence, there is a very weak dependence of galaxy structural properties on distance from the main sequence. Below the main sequence, we found that galaxies farther from the main sequence showed a steepening dependence such that their median Sérsic indices and stellar surface density increased while their effective radii decreased. We found these trends for both nearby and high-redshift galaxies, and found qualitatively similar results for our model galaxies. Agreement with our model suggested that the observed correlation between star formation and morphology can be explained by a causal relationship: central spheroids and black holes grow together, and black holes play a major role in quenching star formation in galaxies. However, we also found discrepancies between our model and the observations which suggest the need to improve our prescriptions for galaxy sizes and AGN feedback at early times.

In Chapter 5, we shifted focus to examine how individual galaxies are affected by AGN

feedback. We achieved this by studying two sets of 24 cosmological zoom galaxies both with and without mechanical and radiation-driven AGN feedback. This prescription for AGN feedback was meant to drive winds analogous to those observed around AGN in the universe. We found that this model both enhances gas outflow events and suppresses gas inflow events. In higher mass galaxies, the effect is mainly ejective, with more gas being driven out of the halo than in our corresponding runs without AGN. However, in lower mass galaxies, the effect becomes more preventative, even supressing inflow at halo scales. We also found that while our galaxies without AGN were recycling-dominated throughout their lives, our galaxies with AGN became ejection-dominated once their AGNs turned on. This model for AGN feedback also succeeded in quenching star formation in galaxies and preventing disks from reforming, much like the simple prescription for AGN feedback in our semi-analytic model did for our SAM galaxies.

Finally, in Chapter 6, we studied how AGN feedback affects the metal content of galaxies and their halos. We found that while the gas-phase metallicity of gas within $r_{\rm g}$ is very similar between the two runs, the halo gas metallicity is appreciably larger in MrAGN galaxies. This is due to a combination of two effects, both a result of the outflows discussed in Chapter 5. These winds simultaneously clear the gas halo of relatively pristine gas, which can be entrained by outflows and moved beyond $r_{\rm vir}$, and desposit metal-rich gas from within the galaxy into the halo, boosting the metallicity of the halo gas in the process. This has a strong effect on the abundance gradients of our higher mass MrAGN galaxies, causing them to have higher normalization and flatter slopes than those found in our NoAGN sample. At lower mass, a very large fraction of metals which have been entrained in outflows from the galaxy end up at vast distances from the galaxy by z=0.

Throughout this thesis, we have examined the ways in which galaxies are affected by AGN feedback. We have used models of galaxy formation and evolution to see how both individual

galaxies and the galaxy population as a whole evolve with time when subject to energy and momentum injection by their central supermassive black holes. We have found that AGN feedback in a semi-analytic model can qualitatively reproduce the demographics of galaxies observed in the universe, as well as correlations between star formation and galaxy morphology. We have also found that AGN feedback that is capable of driving strong winds like those observed in the universe is also capable of having a profound effect on the gas cycle and metal content of individual galaxies, bringing simulated galaxies into broader agreement with observations of galaxies in the universe around us. Taken as a whole, this work supports the argument that AGN feedback is a vital aspect of galaxy evolution, both in terms of producing the diversity of galaxies in the universe, and in deeply affecting individual galaxies.

Appendix A

Conversion from B/T to Sérsic Index in Chapter 3

As part of Chapter 3, we compare the morphologies of model galaxies to observed galaxies. To do this, we convert bulge-to-total stellar mass ratios (B/T), which our model naturally outputs, to Sérsic indices from single component fits, which are directly comparable to observations. To do this, we use a lookup table generated from synthetic galaxies which are made up of an exponential ($n = 1$) disk and a bulge with n=4. A Sérsic index and effective radius are derived by fitting to the two-component profile for a wide range of B/T and $r_{\rm bulge}/r_{\rm disk}$ (which we hereafter refer to as "rbd"). The lookup table takes in B/T and rbd and outputs a Sérsic index and effective radius for the composite system. Since the values are discrete, we have interpolated between the table values to generate our Sérsic indices. Appendix A of Lang et al. (2014) illustrates that the relationship between B/T and n derived from these synthetic galaxies matches well with the relationship derived from CANDELS galaxies with 2-component bulge+disk fits. Here we present the mapping between B/T and Sérsic index in order to illustrate the relationship between the two. Then, in the next section, we will show that the results of the analysis presented in the main text are largely unchanged when done in terms of B/T rather than Sérsic index. We also refer the reader to Figure A6 in Lang et al. (2014), where this analysis is done for the observed galaxies with bulge-disk decompositions. They carry out their analysis in terms of both bulge-to-total stellar mass ratio and H-band light ratio. We have used the lookup table generated in terms of the mass ratio, but we would expect results in terms of light ratio to be qualitatively

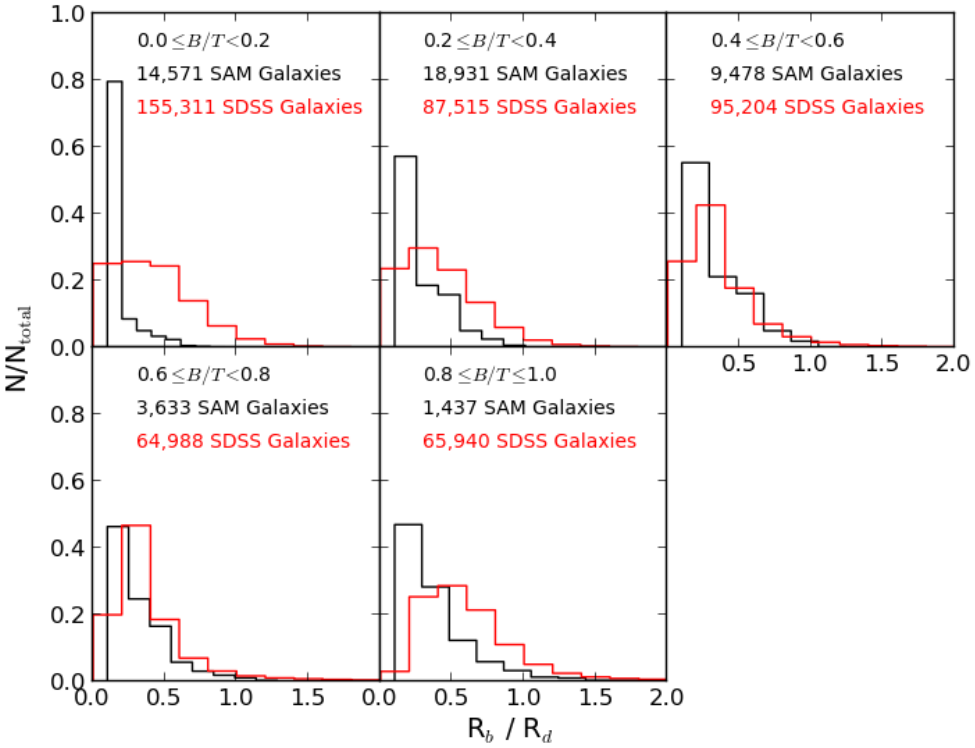

Figure A.1: Distribution of rbd values for SAM galaxies with $0.06 < z < 0.12$ and galaxies from SDSS with bulge-disk decompositions from Simard et al. (2011) in bins of B/T.

similar (see Appendix B of Lang et al. 2014).

To test the SAM predictions for the bulge and disk sizes, we use the r-band bulge+disk decompositions of SDSS galaxies performed by Simard et al. (2011). We trimmed the original catalog of 1,123,718 galaxies down to 618,186 galaxies by applying the following selection cuts: $0.005 < z < 0.12$, $0.0 \leq B/T \leq 1.0$, $0.5 \leq n_{\rm pure} \leq 8.0$, $M_r > -99$, $M_{\rm r,err} > -99$, $M_{\rm r,pure} > -99$, $M_{\rm r,pure,err} > -99$, $r_{\rm bulge,eff} > 0$, $r_{\rm disk,eff} > 0$, and $r_{\rm pure,eff} > 0$, where the subscript "pure" refers to single-component (pure) Sérsic fits (which were also computed for the galaxies). The bulge+disk decompositions were fit simultaneously in the r- and g-band in order to minimize errors, and the assumed model was a de Vaucouleurs bulge ($n_{\rm bulge} = 4$) with a pure exponential disk. The fits

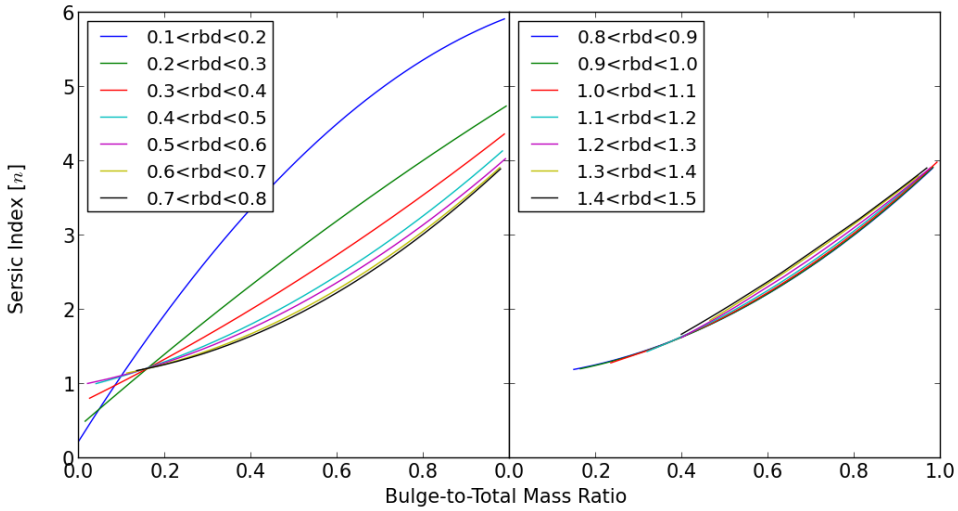

Figure A.2: Fit to the relationship between B/T and Sérsic index in bins of bulge radius/disk radius. For compact bulges, the Sérsic index is a function of both B/T and rbd. As rbd increases, the relationship becomes degenerate.

were done using the Galaxy Image 2D (GIM2D) program; see Simard et al. (2002) and Simard et al. (2011) for further details about the fitting procedure and outputs. In general, the model predictions and observational results are similar, except in the lowest B/T bin, where our model predicts more compact bulges relative to the disk sizes than is seen in the observations. This excess is seen to a lesser degree in the other B/T bins as well. However, as the discrepancy is the largest for disk-dominated galaxies (where the radial size of the bulge component will have little impact on our results), we conclude that our model should produce reasonable predictions for the composite Sérsic indices in most cases. In the future, it will be interesting to compare the SAM results with the sizes and B/T ratios obtained from multi-component bulge-disk decompositions, which are starting to become available.

Figure A.2 shows the best fit curves to the relationship between B/T and n in bins of rbd. If rbd<0.4, for a given B/T a larger rbd will lead to a lower Sérsic index (unless the galaxy also has very low B/T, in which case n is mostly concentrated between $\sim 0.5-1.0$ anyway). Above

an rbd of ~ 0.4, there is a nearly one-to-one mapping between B/T and Sérsic index. However, as we saw in Figure A.1, in the SAMs and in nearby galaxies, most galaxies have rbd< 1. We see here that a split in B/T instead of n will lead to the selection of slightly different sets of galaxies because the bulge radius to disk radius ratio causes a spread in Sérsic index for a given bulge-to-total mass ratio and vice versa.

Appendix B

Results of Chapter 3 Using B/T

In this section we present the main (morphology-dependent) results of the analysis of Chapter 3 again, this time using B/T as our morphological parameter. These results may be able to be compared with future observational analyses, if bulge-disk decompositions are carried out, and may be more easily compared with predictions from other theoretical models. Our dividing line between star forming and quiescent remains the same, but our condition for spheroid domination is now $B/T > 0.5$. Figure B.1 shows the evolution of the spheroid-dominated fraction of galaxies as in Figure 3.4. The observed spheroid-dominated fraction is still derived using a Sérsic index $n = 2.5$ to make the cut. We can see that the evolution of model galaxies is similar to the evolution in Figure 3.4. However, splitting by B/T we predict more spheroid-dominated galaxies for $z < 2$ and fewer for $z \sim 3$. The predicted fraction does not vary by more than 0.1 at any redshift. This variation suggests that there are more galaxies at high redshift with smaller values of rbd than at low redshift.

The evolution of the quadrant fractions in Figure B.2 is extremely similar to that in Figure 3.9. The fraction predicted in each of the spheroid-dominated quadrants is slightly larger than in the Sérsic index case. Figure B.3 is like Figure 3.12. The only significant difference when splitting by B/T instead of n is in the disk instability plot. More SFSs and QSs have had recent disk instabilities as defined by B/T than by n. This is because the change in definition is not likely to affect galaxies that are very clearly disk-dominated or spheroid-dominated. The galaxies

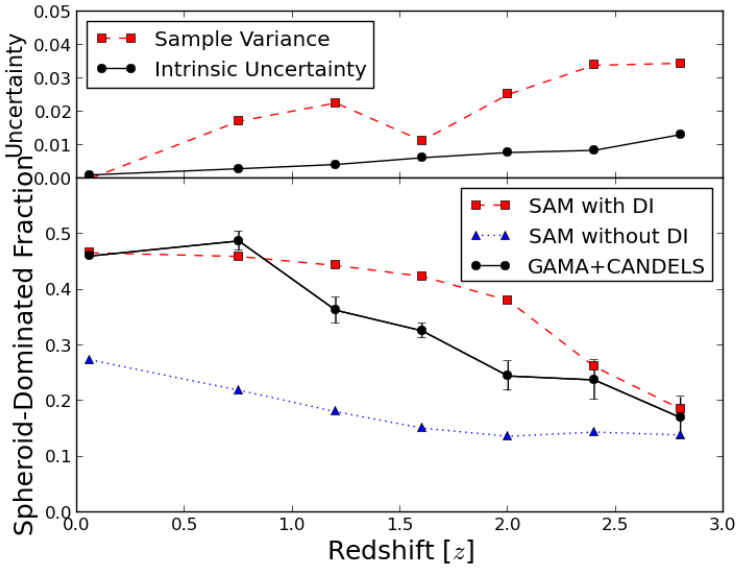

Figure B.1: The evolution of the spheroid-dominated fraction of galaxies with redshift, now with spheroid domination defined as $B/T > 0.5$. The observed galaxies are still split by Sérsic index at $n = 2.5$. Error bars are the $1 - \sigma$ uncertainties due to sample variance in the models and uncertainty in observed galaxy properties added in quadrature. The separate contributions are plotted in the top panel.

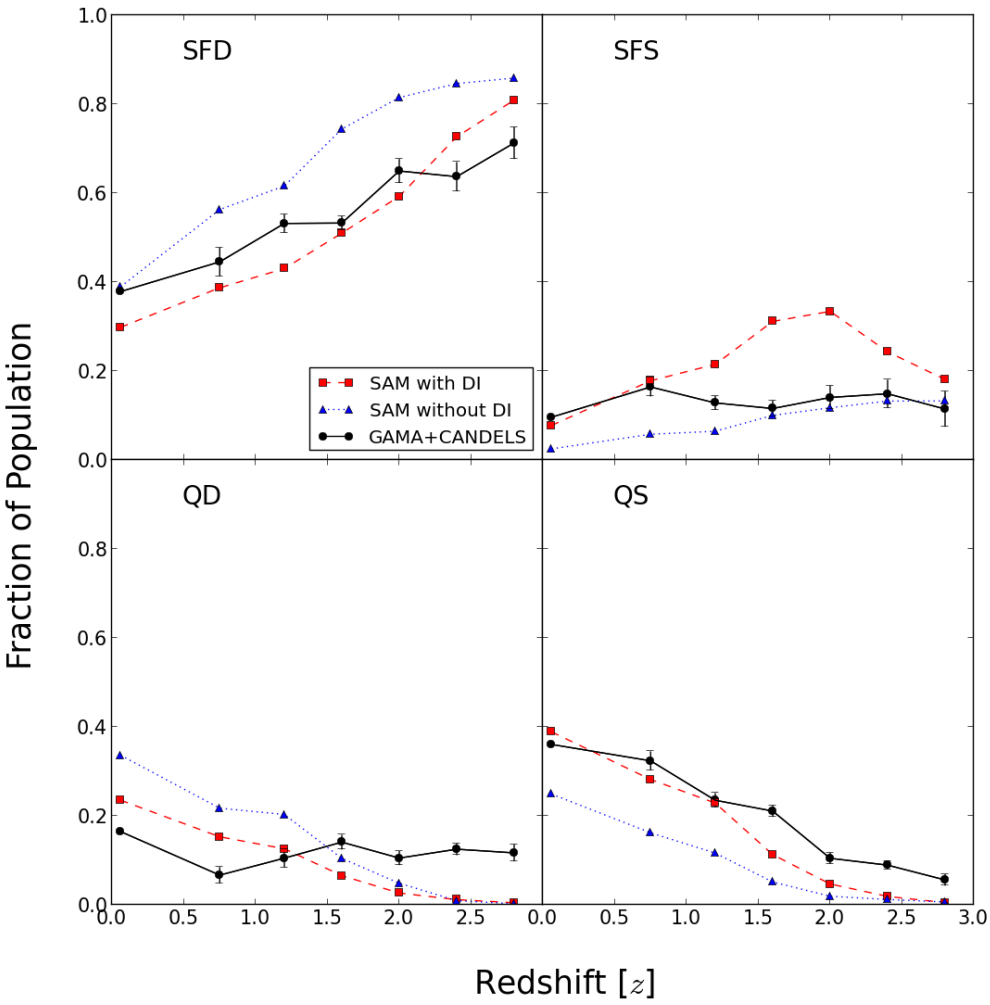

Figure B.2: Same as Figure 3.9, but now with model galaxies split by $B/T = 0.5$. Observed galaxies are still split by Sérsic index at $n = 2.5$. Top left: Star forming disk-dominated galaxies. Top right: Star forming spheroid-dominated galaxies. Bottom left: Quiescent disk-dominated galaxies. Bottom right: Quiescent spheroid-dominated galaxies.

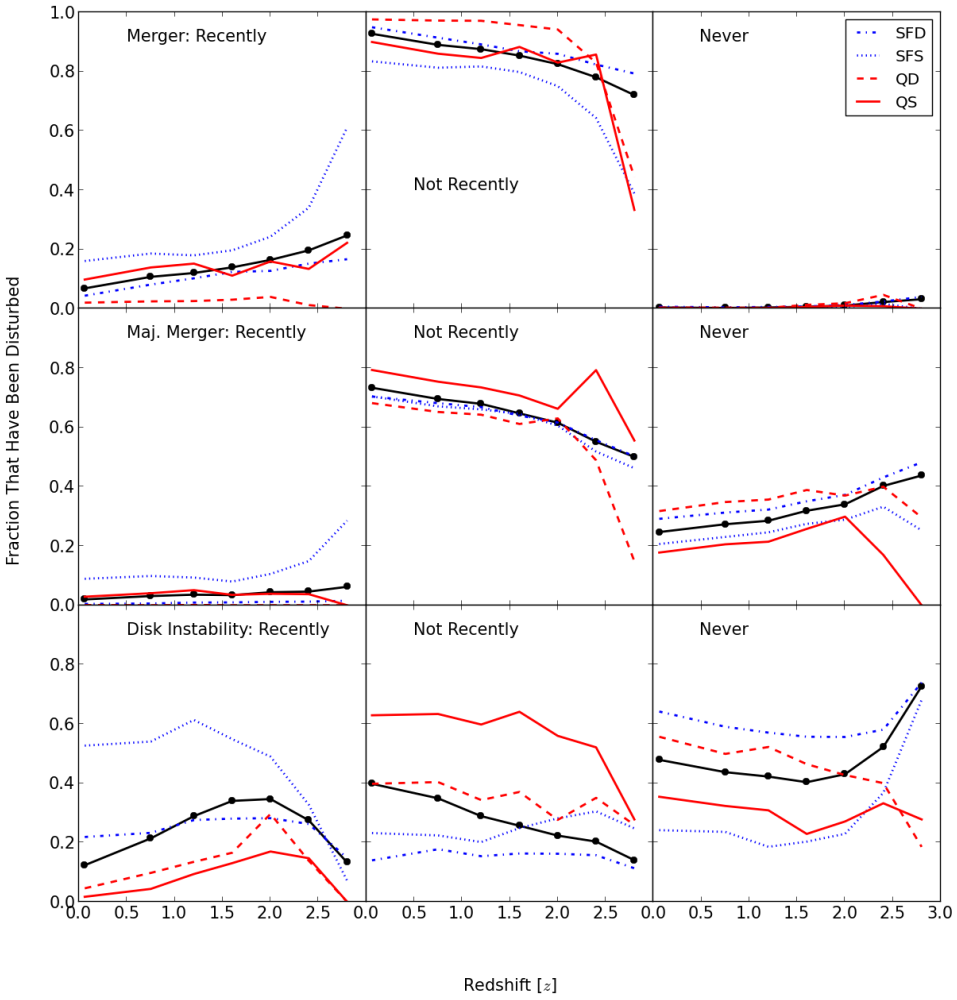

Figure B.3: Same as Figure 3.12, but with a morphology cut at $B/T = 0.5$. Top row: Left panel: Fraction of galaxies in each quadrant which have undergone a recent ($<3t_{\rm dyn}$) merger with mass ratio >1:10. Middle panel: Fraction which have undergone a merger on a timescale $>3t_{\rm dyn}$. Right panel: Fraction which have never undergone a merger. Fractions are now determined using the B/T cut. Middle row: Same as top row, but for major mergers with mass ratio >1:3. Bottom row: Same as top and middle rows but for disk instabilities.

that have intermediate Sérsic indices or $B/T \sim 0.5$ are the ones that are traded back and forth depending on definition (because of their rbd values), and a large fraction of these are created by the disk instability. This is also why the results for the DI model seem to be affected more strongly by morphological definition than the noDI model.

Bibliography

Abazajian K. N., et al., 2009, ApJS, 182, 543

Abramson L. E., Kelson D. D., Dressler A., Poggianti B., Gladders M. D., Oemler Jr. A., Vulcani B., 2014, ApJL, 785, L36

Alatalo K., et al., 2011, ApJ, 735, 88

Anglés-Alcázar D., Davé R., Özel F., Oppenheimer B. D., 2014, ApJ, 782, 84

Anglés-Alcázar D., Faucher-Giguère C.-A., Kereš D., Hopkins P. F., Quataert E., Murray N., 2016, preprint (`arXiv:1610.08523`)

Arav N., et al., 2012, A&A, 544, A33

Arav N., Borguet B., Chamberlain C., Edmonds D., Danforth C., 2013, MNRAS, 436, 3286

Arnaud M., Rothenflug R., Boulade O., Vigroux L., Vangioni-Flam E., 1992, A&A, 254, 49

Asplund M., Grevesse N., Sauval A. J., Scott P., 2009, ARA&A, 47, 481

Athey A. E., 2007, PhD thesis, PhD Thesis, 2007

Aumer M., White S. D. M., Naab T., Scannapieco C., 2013, MNRAS, 434, 3142

Baldry I., Balogh M., Bower R., Glazebrook K., Nichol R., 2004, AIP Conference Proceedings, 743, 106

Baldry I. K., et al., 2012, MNRAS, 421, 621

Balogh M., et al., 2004, MNRAS, 348, 1355

Barai P., Murante G., Borgani S., Gaspari M., Granato G. L., Monaco P., Ragone-Figueroa C., 2016, MNRAS, 461, 1548

Barro G., et al., 2011, ApJS, 193, 30

Barro G., et al., 2013, ApJ, 765, 104

Barro G., et al., 2014, ApJ, 791, 52

Barro G., et al., 2016, ApJL, 827, L32

Behroozi P. S., Wechsler R. H., Wu H.-Y., Busha M. T., Klypin A. A., Primack J. R., 2013a, ApJ, 763, 18

Behroozi P. S., Wechsler R. H., Conroy C., 2013b, ApJ, 770, 57

Bell E. F., 2008, ApJ, 682, 355

Bell E. F., et al., 2004a, ApJL, 600, L11

Bell E. F., et al., 2004b, ApJ, 608, 752

Bell E. F., Zheng X. Z., Papovich C., Borch A., Wolf C., Meisenheimer K., 2007, ApJ, 663, 834

Bell E. F., et al., 2012, ApJ, 753, 167

Bellovary J., Brooks A., Volonteri M., Governato F., Quinn T., Wadsley J., 2013, ApJ, 779, 136

Benson A. J., Devereux N., 2010, MNRAS, 402, 2321

Bernardi M., et al., 2003, AJ, 125, 1882

Birnboim Y., Dekel A., 2003, MNRAS, 345, 349

Blanton M. R., Moustakas J., 2009, ARA&A, 47, 159

Bluck A. F. L., Mendel J. T., Ellison S. L., Moreno J., Simard L., Patton D. R., Starkenburg E., 2014, MNRAS, 441, 599

Bluck A. F. L., et al., 2016, MNRAS, 462, 2559

Blumenthal G. R., Faber S. M., Flores R., Primack J. R., 1986, ApJ, 301, 27

Bogdán Á., et al., 2015, ApJ, 804, 72

Bondi H., 1952, MNRAS, 112, 195

Borch A., et al., 2006, A&A, 453, 869

Bournaud F., Dekel A., Teyssier R., Cacciato M., Daddi E., Juneau S., Shankar F., 2011, ApJ, 741, L33

Bower R. G., Benson A. J., Malbon R., Helly J. C., Frenk C. S., Baugh C. M., Cole S., Lacey C. G., 2006, MNRAS, 370, 645

Boylan-Kolchin M., Ma C.-P., Quataert E., 2008, MNRAS, 383, 93

Brammer G. B., van Dokkum P. G., Coppi P., 2008, ApJ, 686, 1503

Brammer G. B., et al., 2009, ApJ, 706, L173

Brammer G. B., et al., 2011, ApJ, 739, 24

Brennan R., et al., 2015, MNRAS, 451, 2933

Brennan R., et al., 2017, MNRAS, 465, 619

Brinchmann J., Charlot S., White S. D. M., Tremonti C., Kauffmann G., Heckman T., Brinkmann J., 2004, MNRAS, 351, 1151

Bruce V. A., et al., 2014, MNRAS, 444, 1001

Bruzual G., Charlot S., 2003, MNRAS, 344, 1000

Buitrago F., Trujillo I., Conselice C. J., Häußler B., 2013, MNRAS, 428, 1460

Bundy K., et al., 2006, ApJ, 651, 120

Buote D. A., Lewis A. D., Brighenti F., Mathews W. G., 2003, ApJ, 595, 151

Calzetti D., 2001, PASP, 113, 1449

Ceverino D., Dekel A., Bournaud F., 2010, MNRAS, 404, 2151

Ceverino D., Klypin A., Klimek E. S., Trujillo-Gomez S., Churchill C. W., Primack J., Dekel A., 2014, MNRAS, 442, 1545

Chabrier G., 2003, PASP, 115, 763

Chamberlain C., Arav N., 2015, MNRAS, 454, 675

Cheung E., et al., 2012, ApJ, 760, 131

Cheung E., et al., 2016, Nature, 533, 504

Choi E., Ostriker J. P., Naab T., Johansson P. H., 2012, ApJ, 754, 125

Choi E., Naab T., Ostriker J. P., Johansson P. H., Moster B. P., 2014, MNRAS, 442, 440

Choi E., Ostriker J. P., Naab T., Oser L., Moster B. P., 2015, MNRAS, 449, 4105

Choi E., Ostriker J. P., Naab T., Somerville R. S., Hirschmann M., Núñez A., Hu C.-Y., Oser L., 2017, ApJ, 844, 31

Christensen C. R., Davé R., Governato F., Pontzen A., Brooks A., Munshi F., Quinn T., Wadsley J., 2016, ApJ, 824, 57

Cicone C., et al., 2014, A&A, 562, A21

Cole S., Aragon-Salamanca A., Frenk C. S., Navarro J. F., Zepf S. E., 1994, MNRAS, 271, 781

Conselice C. J., et al., 2007, MNRAS, 381, 962

Conselice C. J., et al., 2011, MNRAS, 413, 80

Cox T. J., Dutta S. N., Di Matteo T., Hernquist L., Hopkins P. F., Robertson B., Springel V., 2006, ApJ, 650, 791

Crain R. A., McCarthy I. G., Schaye J., Theuns T., Frenk C. S., 2013, mnras, 432, 3005

Crenshaw D. M., Kraemer S. B., George I. M., 2003, ARA&A, 41, 117

Cristiani S., et al., 2004, ApJL, 600, L119

Croom S. M., Smith R. J., Boyle B. J., Shanks T., Miller L., Outram P. J., Loaring N. S., 2004, MNRAS, 349, 1397

Croton D. J., et al., 2006, MNRAS, 365, 11

Cullen L., Dehnen W., 2010, MNRAS, 408, 669

Daddi E., et al., 2007, ApJ, 670, 156

Dahlen T., et al., 2013, ApJ, 775, 93

Davé R., Oppenheimer B. D., Sivanandam S., 2008, MNRAS, 391, 110

David L. P., Nulsen P. E. J., 2008, ApJ, 689, 837

De Lucia G., Springel V., White S. D. M., Croton D., Kauffmann G., 2006, MNRAS, 366, 499

De Lucia G., Fontanot F., Wilman D., Monaco P., 2011, MNRAS, 414, 1439

Debuhr J., Quataert E., Ma C.-P., 2011a, MNRAS, 412, 1341

Debuhr J., Quataert E., Ma C.-P., 2011b, MNRAS, 412, 1341

Dehnen W., Aly H., 2012, MNRAS, 425, 1068

Dekel A., Birnboim Y., 2006, MNRAS, 368, 2

Dekel A., Burkert A., 2014, MNRAS, 438, 1870

Dekel A., Sari R., Ceverino D., 2009, ApJ, 703, 785

Di Matteo T., Khandai N., DeGraf C., Feng Y., Croft R. A. C., Lopez J., Springel V., 2012, ApJL, 745, L29

Dressler A., 1980, ApJ, 236, 351

Driver S. P., et al., 2009, Astronomy and Geophysics, 50, 12

Driver S. P., et al., 2011, MNRAS, 413, 971

Dubois Y., Gavazzi R., Peirani S., Silk J., 2013, MNRAS, 433, 3297

Dunn J. P., et al., 2010, ApJ, 709, 611

Durier F., Dalla Vecchia C., 2012, MNRAS, 419, 465

Edge A. C., Stewart G. C., 1991, MNRAS, 252, 414

Efstathiou G., Lake G., Negroponte J., 1982, MNRAS, 199, 1069

Eisenreich M., Naab T., Choi E., Ostriker J. P., Emsellem E., 2017, MNRAS, 468, 751

Elbaz D., et al., 2007, AAP, 468, 33

Elbaz D., et al., 2011, A&A, 533, A119

Ellison S. L., Patton D. R., Mendel J. T., Scudder J. M., 2011, MNRAS, 418, 2043

Emonts B. H. C., Piqueras-López J., Colina L., Arribas S., Villar-Martín M., Pereira-Santaella M., Garcia-Burillo S., Alonso-Herrero A., 2014, A&A, 572, A40

Faber S. M., et al., 2007, ApJ, 665, 265

Fabian A. C., 2012, ARA&A, 50, 455

Fall S. M., Efstathiou G., 1980, MNRAS, 193, 189

Fang J. J., Faber S. M., Koo D. C., Dekel A., 2013, ApJ, 776, 63

Fang G., Ma Z., Kong X., Fan L., 2015, ApJ, 807, 139

Feain I. J., Papadopoulos P. P., Ekers R. D., Middelberg E., 2007, ApJ, 662, 872

Ferrarese L., Merritt D., 2000, ApJ, 539, L9

Finoguenov A., Ponman T. J., 1999, MNRAS, 305, 325

Fiore F., et al., 2017, A&A, 601, A143

Flores R., Primack J. R., Blumenthal G. R., Faber S. M., 1993, ApJ, 412, 443

Fontanot F., Cristiani S., Santini P., Fontana A., Grazian A., Somerville R. S., 2012, MNRAS, 421, 241

Forbes J. C., Krumholz M. R., Burkert A., Dekel A., 2014, MNRAS, 438, 1552

Franx M., van Dokkum P. G., Schreiber N. M. F., Wuyts S., Labbé I., Toft S., 2008, ApJ, 688, 770

Galametz A., et al., 2013, ApJS, 206, 10

Gallazzi A., Charlot S., Brinchmann J., White S. D. M., 2006, MNRAS, 370, 1106

Gammie C. F., 2001, ApJ, 553, 174

Ganguly R., Brotherton M. S., 2008, ApJ, 672, 102

Gaskell C. M., Gill J. J. M., Singh J., 2016, preprint (`arXiv:1611.03733`)

Gebhardt K., et al., 2000, ApJ, 539, L13

Geha M., Blanton M. R., Yan R., Tinker J. L., 2012, ApJ, 757, 85

Genzel R., et al., 2014, ApJ, 796, 7

Gnedin N. Y., 2000, ApJ, 542, 535

Gonzalez A. H., Zaritsky D., Zabludoff A. I., 2007, ApJ, 666, 147

Grogin N. A., et al., 2011, ApJS, 197, 35

Guo Q., et al., 2011, MNRAS, 413, 101

Guo Y., et al., 2013, ApJS, 207, 24

Guo Y., et al., 2015, ApJ, 800, 39

Haardt F., Madau P., 2012, ApJ, 746, 125

Häring N., Rix H.-W., 2004, ApJ, 604, L89

Harrison C. M., 2017, preprint (`arXiv:1703.06889`)

Heckman T. M., Best P. N., 2014, ARA&A, 52, 589

Hirschmann M., Somerville R. S., Naab T., Burkert A., 2012, MNRAS, 426, 237

Hirschmann M., De Lucia G., Iovino A., Cucciati O., 2013, MNRAS, 433, 1479

Hirschmann M., Dolag K., Saro A., Bachmann L., Borgani S., Burkert A., 2014, MNRAS, 442, 2304

Hirschmann M., Charlot S., Feltre A., Naab T., Choi E., Ostriker J. P., Somerville R. S., 2017, preprint (arXiv:1706.00010)

Hopkins P. F., Hernquist L., Cox T. J., Di Matteo T., Robertson B., Springel V., 2006, ApJS, 163, 1

Hopkins P. F., Hernquist L., Cox T. J., Robertson B., Krause E., 2007, ApJ, 669, 45

Hopkins P. F., et al., 2009a, MNRAS, 397, 802

Hopkins P. F., Cox T. J., Younger J. D., Hernquist L., 2009b, ApJ, 691, 1168

Hopkins A. M., et al., 2013, MNRAS, 430, 2047

Hopkins P. F., Kereš D., Oñorbe J., Faucher-Giguère C.-A., Quataert E., Murray N., Bullock J. S., 2014, MNRAS, 445, 581

Hopkins P. F., Torrey P., Faucher-Giguère C.-A., Quataert E., Murray N., 2016, MNRAS, 458, 816

Hu C.-Y., Naab T., Walch S., Moster B. P., Oser L., 2014, MNRAS, 443, 1173

Humphrey P. J., Buote D. A., 2006, ApJ, 639, 136

Ilbert O., et al., 2013, AAP, 556, A55

Johnson R., Finoguenov A., Ponman T. J., Rasmussen J., Sanderson A. J. R., 2011, MNRAS, 413, 2467

Kauffmann G., White S. D. M., Guiderdoni B., 1993, MNRAS, 264, 201

Kauffmann G., et al., 2003, MNRAS, 341, 54

Kennicutt R. C., 1998, ApJ, 498, 541

Kereš D., Katz N., Weinberg D. H., Davé R., 2005, MNRAS, 363, 2

Khandai N., Di Matteo T., Croft R., Wilkins S., Feng Y., Tucker E., DeGraf C., Liu M.-S., 2015, MNRAS, 450, 1349

Kimm T., et al., 2009, MNRAS, 394, 1131

Klypin A. A., Trujillo-Gomez S., Primack J., 2011, ApJ, 740, 102

Knigge C., Scaringi S., Goad M. R., Cottis C. E., 2008, MNRAS, 386, 1426

Koda J., Yagi M., Yamanoi H., Komiyama Y., 2015, ApJL, 807, L2

Koekemoer A. M., et al., 2011, ApJ, 197, 36

Komatsu E., et al., 2009, ApJS, 180, 330

Komatsu E., et al., 2011, ApJS, 192, 18

Kormendy J., Ho L. C., 2013, ARAA, 51, 511

Kormendy J., Kennicutt Jr. R. C., 2004, ARAA, 42, 603

Kormendy J., Richstone D., 1995, ARAA, 33, 581

Kravtsov A. V., Gnedin O. Y., Klypin A. A., 2004, ApJ, 609, 482

Kravtsov A., Vikhlinin A., Meshscheryakov A., 2014, preprint (arXiv:1401.7329)

Kriek M., van Dokkum P. G., Labbé I., Franx M., Illingworth G. D., Marchesini D., Quadri R. F., 2009, ApJ, 700, 221

Kurczynski P., et al., 2016, ApJL, 820, L1

Laidler V. G., et al., 2007, PASP, 119, 1325

Lang P., et al., 2014, ApJ, 788, 11

Lange R., et al., 2015, MNRAS, 447, 2603

Lee K.-S., et al., 2012, AJ, 752, 66

Lee N., et al., 2015, ApJ, 801, 80

Lemonias J. J., Schiminovich D., Catinella B., Heckman T. M., Moran S. M., 2014, ApJ, 790, 27

Lilly S. J., Carollo C. M., 2016, ApJ, 833, 1

Lilly S. J., Carollo C. M., Pipino A., Renzini A., Peng Y., 2013, ApJ, 772, 119

Lintott C. J., et al., 2008, MNRAS, 389, 1179

Lintott C., et al., 2011, MNRAS, 410, 166

Liske J., et al., 2015, MNRAS, 452, 2087

Lotz J. M., Jonsson P., Cox T. J., Croton D., Primack J. R., Somerville R. S., Stewart K., 2011, ApJ, 742, 103

Lynden-Bell D., 1969, Nature, 223, 690

Madau P., Dickinson M., 2014, ARA&A, 52, 415

Magorrian J., et al., 1998, AJ, 115, 2285

Maiolino R., et al., 2012, MNRAS, 425, L66

Mandelker N., Dekel A., Ceverino D., Tweed D., Moody C. E., Primack J., 2014, MNRAS, 443, 3675

Marconi A., Hunt L. K., 2003, ApJL, 589, L21

Martig M., Bournaud F., Teyssier R., Dekel A., 2009, ApJ, 707, 250

Martin D. C., et al., 2005, ApJ, 619, L1

Matute I., La Franca F., Pozzi F., Gruppioni C., Lari C., Zamorani G., 2006, A&A, 451, 443

McGrath E. J., Stockton A., Canalizo G., Iye M., Maihara T., 2008, ApJ, 682, 303

McIntosh D. H., et al., 2014, MNRAS, 442, 533

Mendel J. T., Simard L., Palmer M., Ellison S. L., Patton D. R., 2014, ApJS, 210, 3

Mihos J. C., et al., 2015, ApJL, 809, L21

Mo H. J., Mao S., White S. D. M., 1998, MNRAS, 295, 319

Mo H., van den Bosch F. C., White S., 2010, Galaxy Formation and Evolution

Moe M., Arav N., Bautista M. A., Korista K. T., 2009, ApJ, 706, 525

Moll R., et al., 2007, A&A, 463, 513

Morris A. M., et al., 2015, AJ, 149, 178

Mortlock A., et al., 2015, MNRAS, 447, 2

Moster B. P., Naab T., White S. D. M., 2013, MNRAS, 428, 3121

Moster B. P., Macciò A. V., Somerville R. S., 2014, MNRAS, 437, 1027

Muzzin A., et al., 2013a, ApJS, 206, 8

Muzzin A., et al., 2013b, ApJ, 777, 18

Naab T., Ostriker J. P., 2016, preprint (`arXiv:1612.06891`)

Nayyeri H., et al., 2017, ApJS, 228, 7

Noeske K. G., et al., 2007, ApJ, 660, L43

Núñez A., Ostriker J. P., Naab T., Oser L., Hu C.-Y., Choi E., 2017, ApJ, 836, 204

Nyman L.-A., et al., 1992, A&AS, 93, 121

Oemler Jr. A., 1974, ApJ, 194, 1

Ogle P. M., Lanz L., Nader C., Helou G., 2016, ApJ, 817, 109

Omand C. M. B., Balogh M. L., Poggianti B. M., 2014, MNRAS, 440, 843

Oppenheimer B. D., Davé R., Kereš D., Fardal M., Katz N., Kollmeier J. A., Weinberg D. H., 2010, MNRAS, 406, 2325

Oser L., Ostriker J. P., Naab T., Johansson P. H., Burkert A., 2010, ApJ, 725, 2312

Oser L., Naab T., Ostriker J. P., Johansson P. H., 2012, ApJ, 744, 63

Ostriker J. P., Peebles P. J. E., 1973, ApJ, 186, 467

Ostriker J. P., Choi E., Ciotti L., Novak G. S., Proga D., 2010, ApJ, 722, 642

Page M. J., et al., 2012, Nature, 485, 213

Pandya V., et al., 2016, preprint (`arXiv:1611.03869`)

Parry O. H., Eke V. R., Frenk C. S., 2009, MNRAS, 396, 1972

Peletier R. F., Balcells M., 1996, AJ, 111, 2238

Peng C. Y., Ho L. C., Impey C. D., Rix H.-W., 2002, AJ, 124, 266

Peng Y.-J., et al., 2010, ApJ, 721, 193

Peng Y., Maiolino R., Cochrane R., 2015, Nature, 521, 192

Perna M., et al., 2015, A&A, 583, A72

Peterson B. M., 2008, NewAR, 52, 240

Pillepich A., et al., 2017, preprint (arXiv:1703.02970)

Pontzen A., Tremmel M., Roth N., Peiris H. V., Saintonge A., Volonteri M., Quinn T., Governato F., 2017, MNRAS, 465, 547

Porter L., Somerville R., Primack J., Johansson P., 2014a, MNRAS, 444, 942

Porter L. A., Somerville R. S., Primack J. R., Croton D. J., Covington M. D., Graves G. J., Faber S. M., 2014b, MNRAS, 445, 3092

Prochaska J. X., Hennawi J. F., 2009, ApJ, 690, 1558

Proga D., Kurosawa R., 2009, in Hubeny I., Stone J. M., MacGregor K., Werner K., eds, American Institute of Physics Conference Series Vol. 1171, American Institute of Physics Conference Series. pp 295–303 (arXiv:0912.0565)

Prugniel P., Simien F., 1997, A&A, 321, 111

Read J. I., Hayfield T., 2012, MNRAS, 422, 3037

Rebusco P., Churazov E., Böhringer H., Forman W., 2006, MNRAS, 372, 1840

Renzini A., Peng Y.-j., 2015, ApJL, 801, L29

Robertson B., Cox T. J., Hernquist L., Franx M., Hopkins P. F., Martini P., Springel V., 2006, ApJ, 641, 21

Rodighiero G., et al., 2011, ApJ, 739, L40

Romeo A. D., Portinari L., Sommer-Larsen J., 2005, MNRAS, 361, 983

Rosario D. J., et al., 2013a, A&A, 560, A72

Rosario D. J., et al., 2013b, ApJ, 771, 63

Röttgers B., 2017, Astrophysics Source Code Library

Rupke D. S. N., Veilleux S., 2011, ApJL, 729, L27

Rupke D. S. N., Veilleux S., 2013, ApJ, 768, 75

Saitoh T. R., Makino J., 2009, ApJL, 697, L99

Salmi F., Daddi E., Elbaz D., Sargent M. T., Dickinson M., Renzini A., Bethermin M., Le Borgne D., 2012, ApJL, 754, L14

Salmon B., et al., 2015, ApJ, 799, 183

Sanchez N. N., et al., 2016, preprint (arXiv:1610.01155)

Santini P., et al., 2012, A&A, 540, A109

Sato K., Matsushita K., Ishisaki Y., Yamasaki N. Y., Ishida M., Ohashi T., 2009, PASJ, 61, S353

Sazonov S. Y., Ostriker J. P., Sunyaev R. A., 2004, MNRAS, 347, 144

Sazonov S. Y., Ostriker J. P., Ciotti L., Sunyaev R. A., 2005, MNRAS, 358, 168

Schawinski K., et al., 2014, MNRAS, 440, 889

Schaye J., et al., 2015, MNRAS, 446, 521

Schiminovich D., et al., 2007, ApJS, 173, 315

Schiminovich D., et al., 2010, MNRAS, 408, 919

Schindler S., Diaferio A., 2008, SSR, 134, 363

Schreiber C., et al., 2015, A&A, 575, A74

Sérsic J. L., 1963, Boletin de la Asociacion Argentina de Astronomia La Plata Argentina, 6, 41

Shakura N. I., Sunyaev R. A., 1973, A&A, 24, 337

Shen S., Mo H. J., White S. D. M., Blanton M. R., Kauffmann G., Voges W., Brinkmann J., Csabai I., 2003, MNRAS, 343, 978

Silk J., Rees M. J., 1998, A&A, 331, L1

Silverman J. D., et al., 2011, ApJ, 743, 2

Simard L., et al., 2002, ApJS, 142, 1

Simard L., Mendel J. T., Patton D. R., Ellison S. L., McConnachie A. W., 2011, ApJS, 196, 11

Smethurst R. J., et al., 2015, MNRAS, 450, 435

Snyder G. F., Lotz J., Moody C., Peth M., Freeman P., Ceverino D., Primack J., Dekel A., 2015a, MNRAS, 451, 4290

Snyder G. F., et al., 2015b, MNRAS, 454, 1886

Sobral D., Best P. N., Smail I., Mobasher B., Stott J., Nisbet D., 2014, MNRAS, 437, 3516

Somerville R. S., Davé R., 2015, ARA&A, 53, 51

Somerville R. S., Kolatt T. S., 1999, MNRAS, 305, 1

Somerville R. S., Primack J. R., 1999, MNRAS, 310, 1087

Somerville R. S., Primack J. R., Faber S. M., 2001, MNRAS, 320, 504

Somerville R. S., Hopkins P. F., Cox T. J., Robertson B. E., Hernquist L., 2008a, MNRAS, 391, 481

Somerville R. S., et al., 2008b, ApJ, 672, 776

Somerville R. S., Gilmore R. C., Primack J. R., Domínguez A., 2012, MNRAS, 423, 1992

Somerville R. S., Popping G., Trager S. C., 2015, MNRAS, 453, 4337

Sparre M., et al., 2015, MNRAS, 447, 3548

Speagle J. S., Steinhardt C. L., Capak P. L., Silverman J. D., 2014, ApJS, 214, 15

Spergel D. N., et al., 2007, ApJS, 170, 377

Springel V., 2005, MNRAS, 364, 1105

Springel V., 2010, MNRAS, 401, 791

Springel V., Di Matteo T., Hernquist L., 2005, MNRAS, 361, 776

Stefanon M., et al., 2017, ApJS, 229, 32

Steinborn L. K., Dolag K., Hirschmann M., Prieto M. A., Remus R.-S., 2015, MNRAS, 448, 1504

Strateva I., et al., 2001, AJ, 122, 1861

Sturm E., et al., 2011, ApJL, 733, L16

Sutherland R. S., Dopita M. A., 1993, ApJS, 88, 253

Tacchella S., et al., 2015, ApJ, 802, 101

Tacchella S., Dekel A., Carollo C. M., Ceverino D., DeGraf C., Lapiner S., Mandelker N., Primack Joel R., 2016, MNRAS, 457, 2790

Tamura T., Kaastra J. S., den Herder J. W. A., Bleeker J. A. M., Peterson J. R., 2004, A&A, 420, 135

Taylor E. N., et al., 2011, MNRAS, 418, 1587

Teimoorinia H., Bluck A. F. L., Ellison S. L., 2016, MNRAS, 457, 2086

Tinker J. L., Wetzel A. R., 2010, ApJ, 719, 88

Tombesi F., Cappi M., Reeves J. N., Palumbo G. G. C., Yaqoob T., Braito V., Dadina M., 2010, A&A, 521, A57

Tombesi F., Cappi M., Reeves J. N., Nemmen R. S., Braito V., Gaspari M., Reynolds C. S., 2013, MNRAS, 430, 1102

Tombesi F., Meléndez M., Veilleux S., Reeves J. N., González-Alfonso E., Reynolds C. S., 2015, Nature, 519, 436

Torresi E., Grandi P., Costantini E., Palumbo G. G. C., 2012, in International Journal of Modern Physics Conference Series. pp 396–399 (`arXiv:1112.2549`)

Tremaine S., et al., 2002, ApJ, 574, 740

Tremmel M., Karcher M., Governato F., Volonteri M., Quinn T., Pontzen A., Anderson L., Bellovary J., 2016, preprint, (`arXiv:1607.02151`)

Tremonti C. A., et al., 2004, ApJ, 613, 898

Tremonti C. A., Moustakas J., Diamond-Stanic A. M., 2007, ApJL, 663, L77

Trujillo-Gomez S., Klypin A., Primack J., Romanowsky A. J., 2011, ApJ, 742, 16

Übler H., Naab T., Oser L., Aumer M., Sales L. V., White S. D. M., 2014, MNRAS, 443, 2092

Valdarnini R., 2003, MNRAS, 339, 1117

Vogelsberger M., et al., 2014, MNRAS, 444, 1518

Wadsley J. W., Stadel J., Quinn T., 2004, New Astronomy, 9, 137

Wake D. A., van Dokkum P. G., Franx M., 2012, ApJL, 751, L44

Weinberger R., et al., 2017, MNRAS, 465, 3291

Whitaker K. E., et al., 2010, ApJ, 719, 1715

Whitaker K. E., Kriek M., van Dokkum P. G., Bezanson R., Brammer G., Franx M., Labbé I., 2012a, ApJ, 745, 179

Whitaker K. E., van Dokkum P. G., Brammer G., Franx M., 2012b, ApJ, 754, L29

Whitaker K. E., et al., 2014, ApJ, 795, 104

Whitaker K. E., et al., 2015, ApJL, 811, L12

White S. D. M., Rees M. J., 1978, MNRAS, 183, 341

Williams R. J., Quadri R. F., Franx M., van Dokkum P., Toft S., Kriek M., Labbé I., 2010, ApJ, 713, 738

Williams C. C., et al., 2014, ApJ, 780, 1

Williams C. C., et al., 2015, ApJ, 800, 21

Wong O. I., et al., 2012, MNRAS, 420, 1684

Woo J., et al., 2013, MNRAS, 428, 3306

Woo J., Dekel A., Faber S. M., Koo D. C., 2015a, MNRAS, 448, 237

Woo J., Dekel A., Faber S. M., Koo D. C., 2015b, MNRAS, 448, 237

Wuyts S., et al., 2011, ApJ, 742, 96

Yates R. M., Thomas P. A., Henriques B. M. B., 2017, MNRAS, 464, 3169

York D. G., et al., 2000, AJ, 120, 1579

Zakamska N. L., Greene J. E., 2014, MNRAS, 442, 784

Zinn P.-C., Middelberg E., Norris R. P., Dettmar R.-J., 2013, ApJ, 774, 66

Zolotov A., et al., 2015, MNRAS, 450, 2327

van Dokkum P. G., et al., 2009, PASP, 121, 2

van Dokkum P. G., Abraham R., Merritt A., Zhang J., Geha M., Conroy C., 2015a, ApJL, 798, L45

van Dokkum P. G., et al., 2015b, ApJL, 804, L26

van der Wel A., et al., 2011, ApJ, 730, 38

van der Wel A., et al., 2012, ApJS, 203, 24

van der Wel A., et al., 2014a, ApJ, 788, 28

van der Wel A., et al., 2014b, ApJL, 792, L6